Title
Behaviors of Silica Nanoparticle Deposition and Gold Coating on Polystyrene Particles

Author
Choi, Seongcheol

Publication Date
2021

UNIVERSITY OF CALIFORNIA SAN DIEGO

Behaviors of Silica Nanoparticle Deposition and Gold Coating on Polystyrene Particles

A Dissertation submitted in partial satisfaction of the

requirements for the degree

Doctor of Philosophy

in

Materials Science and Engineering

by

Seongcheol Choi

Committee in charge:

Professor Olivia A. Graeve, Chair
Professor James Friend
Professor Andrea R. Tao
Professor Rafael Vazquez-Duhalt
Professor Joseph Wang
Professor Sheng Xu

2021

The dissertation of Seongcheol Choi is approved, and it is acceptable in quality and form for publication on microfilm and electronically.

University of California San Diego

2021

DEDICATION

My lovely parents, Jooho and Kaya,
my lovely sister, Yumi,
my lovely wife, Narae,
my lovely son, Hyunwoo,
and my lovely daughter, Seoyeon

EPIGRAPH

If I have seen further,

it is by standing on the shoulders of giants.

— In the letter to Robert Hooke from Sir Isaac Newton in 1676

If quantum mechanics hasn't profoundly shocked you,

you haven't understood it yet.

— Niels Bohr

I took the one less traveled by,

And that has made all the difference.

— In "The Road Not Taken" by Robert Frost

TABLE OF CONTENTS

LIST OF FIGURES

LIST OF TABLES

ACKNOWLEDGEMENTS

First and foremost, I would like to express my deepest gratitude to my advisor, Professor Olivia A. Graeve. Her guidance, support, patience, enthusiasm, trust, respect, and motivation encouraged me to reach the end of my Ph.D. journey even in tough time. My research experience under her guidance has had a huge positive impact on many aspects of not only my professions but also my life. It has been my honor to study in her research group.

I am also grateful to the rest of my dissertation committee members: Professor Andrea R. Tao, Professor James R. Friend, Professor Joseph Wang, Professor Rafael Vazquez-Duhalt, and Professor Sheng Xu. I sincerely appreciate their valuable advice, insightful comments, and encouragement.

Most importantly, I would like to thank my parents and parents-in-law for their endless encouragement and unconditional support to complete my doctoral studies. Every single achievement I have done is only possible with you. Also, I appreciate my sister, sister-in-law, and brother-in-law encouraging and supporting me.

Lastly, I truly appreciate my wife. Her trust in me has always been a great encouragement for me to endure and keep forwarding in every struggled moment. I appreciate you for sharing all beautiful memories with me. Also, I thank our lovely son and daughter for coming to a mom and a dad from heaven.

Chapter 1, in part is currently being prepared for submission for publication of the material. Choi, Seongcheol; Vazquez-Duhalt, Rafael; Graeve, Olivia A. The dissertation author was the primary investigator and author of this material.

Chapter 2, in part is currently being prepared for submission for publication of the material. Choi, Seongcheol; Vazquez-Duhalt, Rafael; Graeve, Olivia A. The dissertation author was the primary investigator and author of this material.

VITA

2010	B.S. in Chemical Engineering, Inha University, South Korea
2012	M.E. in Chemical Engineering, Inha University, South Korea
2021	Ph.D. in Materials Science and Engineering, University of California San Diego

PUBLICATIONS

S. Choi, R. Vazquez-Duhalt, O.A. Graeve, Effect of initial reaction rate gradient and Casimir-Lifshitz force on gold coating behavior on positively charged polystyrene particles under potential distribution, *In Preparation*.

S. Choi, R. Vazquez-Duhalt, O.A. Graeve, Nonlinear charge regulation for the deposition of silica nanoparticles on polystyrene spherical surfaces. *Submitted.*

S. Choi, C. Cheung, O.A. Graeve, Fabrication of continuous linear pores in an SOFC anode using unidirectional carbon fibers as sacrificial templates. *J. Am. Ceram. Soc.* **2021**, 104(7):3030-3041.

ABSTRACT OF THE DISSERTATION

Behaviors of Silica Nanoparticle Deposition and Gold Coating on Polystyrene Particles

by

Seongcheol Choi

Doctor of Philosophy in Materials Science and Engineering

University of California San Diego, 2021

Professor Olivia A. Graeve, Chair

Development of fine and sophisticated nanosized composite colloidal particles has been intensively studied due to their huge potential to solve a lot of problems in a variety of fields. To have higher degree of freedom in designing nano-architecture on colloidal particles and controlling their unique properties, a more detailed understanding of chemical and physical phenomena in colloidal suspension is required. This dissertation discusses new mathematical approaches to describe in detail the behaviors of silica nanoparticle deposition and gold coating on submicron polystyrene (PS) colloidal particles in terms of colloidal science including surface chemistry and

surface physics. To consider realistic phenomena inside the colloidal suspension, the proposed models for these two topics are based on the non-linear relationship between surface charge density and surface potential which are regulated by free ions.

Chapter 1 presents the numerical analysis for the deposition behavior of monodispersed silica nanoparticles onto PS particles by using modified pairwise DLVO (Derjaguin, Landau, Verwey, and Overbeek) interaction force at different pH. This model includes an improved nonlinear charge regulation model considering redistribution of ions. To vindicate the model, silanol-terminated silica nanoparticles and *L*-lysine covered silica nanoparticles were separately deposited on polyallylamine hydrochloride-covered polystyrene (PAH/PS) particles. The morphological analysis of the experimental results shows that this modified DLVO force well describe the deposition behavior of the silica nanoparticles onto the PAH/PS particles.

Chapter 2 discusses the computational models to elucidate the gold coating behavior on the positively charged PAH/PS particles at different concentration of *L*-ascorbic acid in terms of the initial nucleation stage. This analysis focuses on the initial generation rate gradient of Au(I) complex ions and the Casimir-Lifshitz interaction force between particles under the potential gradient. To justify our models, a direct gold coating method was performed on the PAH/PS particles with a constant concentration of $HAuCl_4$ and various concentrations of *L*-ascorbic acid. The morphological analysis of the variation of gold coating shows that the computational results properly describe the morphological difference in gold coating by the trend of nucleation of gold along with the distance away from the PAH/PS particles.

Chapter 1

Nonlinear Charge Regulation for the Deposition of Silica Nanoparticles on Polystyrene Spherical Surfaces

1.1. Abstract

We describe the deposition behavior of monodispersed silica nanoparticles on polystyrene spherical particles by using modified pairwise DLVO (Derjaguin, Landau, Verwey, and Overbeek) interaction force profiles at pH values between two and twelve. Our modified model contains a new nonlinear charge regulation parameter that considers redistribution of ions, which allows us to realistically express the electrical double layer (EDL) interaction forces. Silanol-terminated silica nanoparticles (7.6 ± 0.4 nm), *L*-lysine-covered silica nanoparticles (7.8 ± 0.4 nm), and polyallylamine hydrochloride-covered polystyrene (PAH/PS) particles (348 ± 1 nm) were synthesized. Then, each type of silica nanoparticle was deposited on the PAH/PS particles at a range of pH values. Our new regulation parameter describes the realistic redistribution of charges governed by pH, total salt concentration, ionic strength of solution, and separation distance of particles. We find that this regulation parameter can be roughly approximated from the absolute values of theoretically calculated surface charge density and potential distributions, as well as experimentally measured ζ-potentials. Morphological analysis using electron microscopy of the experimental systems shows that the modified pairwise DLVO interaction forces exceptionally

describe the deposition behavior of the silica nanoparticles deposited on the PAH/PS particle substrates.

1.2. Introduction

The synthesis of organic/inorganic hybrid nanoparticles has been extensively studied for their applications in a variety of technologies, including battery systems, optics, biomedicine, and electronics [1-4]. For synthesis of these systems, it is typical for an inorganic material to be decorated on an organic substrate, resulting in countless options for different sizes, shapes, and types of materials, and providing many options for the design of hybrid materials. Generally, there are four strategies to prepare organic/inorganic hybrid nanoparticles, namely deposition of *ex situ* synthesized inorganic nanoparticles on a prepared organic substrate by either covalent or noncovalent bonding [2, 3, 5-8], *in situ* growth of inorganic nanoparticles by crystallization or precipitation on the polymer substrate [9-14], *in situ* synthesis of polymer particles in the presence of inorganic nanoparticles [15-18], and simultaneous synthesis of both polymer and inorganic nanoparticles [19, 20]. The first strategy can result in controlled size and shape of both the organic and inorganic components. However, the deposited inorganic particles can undergo aggregation depending on the pH, ionic strength, and separation distance of the nanoparticles, among others. These aggregated particles become irreversibly bound and manifest behaviors of the aggregates instead of the behaviors of single inorganic nanoparticles. Thus, to gain control in such systems, the deposition behavior and surface interactions of the inorganic nanoparticles must be explored.

One can normally discuss the aggregation behavior of colloidal particles in terms of interaction energies or forces based on the classical theory developed by Derjaguin, Landau, Verwey, and Overbeek (DLVO) [21-23]. This theory assumes that particle interactions are mainly dominated by van der Waals (vdW) and electrical double layer (EDL) forces. EDL forces are described by the Poisson-Boltzmann theory, which states that surfaces in aqueous solutions maintain constant charge or constant potential, an unrealistic scenario for most cases [24]. In addition, the classic EDL model and its derivatives fail to effectively describe the interaction energy or force of asymmetric systems such as oppositely charged surfaces [25]. For isolated particles in dilute solutions, the surface charge density and surface potential are regulated by the adsorbed ions on the surfaces, total salt concentration, pH and ionic strength of the solution, inducing protonation and deprotonation of the ionizable chemical groups on the surfaces. In practical cases, the charged surface density and surface potential vary when the colloidal particles approach each other, as this triggers redistribution of ions on the surfaces. This phenomenon in which the surface charge density is controlled by the redistributed ions is called charge regulation [25-31].

Studies have used the linearized Poisson-Boltzmann model, which introduces a parameter to describe the charge regulation behaviors for both symmetric and asymmetric surfaces in solution [26-32]. In this model, symmetric surfaces are described as having the same charge densities or potentials, while asymmetric surfaces bear different charge densities or potentials. The model expresses charge regulation by assuming that the value of the regulation parameter remains constant when the two surfaces approach each other. This is called the constant regulation approximation and valid for situations in which there is low ionic strength and low potential. Its derivation originates from the linearized Poisson-Boltzmann equation and Debye-Hückel approximation [33]. Although this model has been considered a leap forward, an extended model to describe more complex situations is still unavailable. This may include systems having asymmetric particles, for example, an EDL interaction between a slightly charged amine-functionalized polymer particle and a fully charged silica nanoparticle at high pH. To efficiently describe practical cases like this one, the EDL interaction force term should be governed by a charge regulation model that describes the redistribution of ions near the surface depending on pH, total salt concentration, ionic strength of solution, and separation distance.

In this study, we describe the deposition behavior of inorganic silica nanoparticles on oppositely charged submicron-sized polymeric particles, together with a generalized pairwise EDL interaction model that is valid for both symmetric and asymmetric cases. A regulation parameter as a function of pH and functional groups on particle surfaces is introduced for symmetric systems. Our analysis includes the development of (1) a nonlinear relationship between surface charge and surface potential under realistic charge regulation conditions and a nonlinear Poisson-Boltzmann model; and (2) a method to find the diffuse layer potential by considering the diameter of the dominant ionic component near the surfaces. To compare and verify that our model effectively describes a wide range of practical cases, including low and high ionic strength solutions and low and high surface potentials, two different monodisperse silica nanoparticles, silanol-terminated silica nanoparticles and *L*-lysine-covered silica nanoparticles, and uniform-sized polyallylamine hydrochloride (PAH)-covered polystyrene (PS) particles, were experimentally prepared. For the case of the silanol-terminated silica nanoparticles, we scrutinize the vdW and EDL interaction forces for (1) two silanol-terminated silica nanoparticles (symmetric system) and (2) silanol-terminated silica nanoparticles on PAH/PS particles (asymmetric system). For the case of the *L*-lysine-covered silica nanoparticles, we scrutinize the vdW and EDL interaction forces of (3) two *L*-lysine-covered silica nanoparticles (symmetric system) and (4) *L*-lysine-covered silica nanoparticles on PAH/PS particles (asymmetric system). Since the calculated values used in our analysis correspond to the force between two particles of interest, if the concentration of the particles is high, these two particles will also interact with other particles in the same system, resulting in a significant deviation between the experimental results and theoretical model. Therefore, dilute solutions are used in this work to minimize the error between the experiment and the model [24, 25].

1.3. Experimental Methodology

The procedure to prepare the PAH/PS particles covered with silanol-terminated silica nanoparticles or with *L*-lysine-covered silica nanoparticles is illustrated in Figure 1.1(a) and 1.1(b) respectively.

Materials: Styrene (≥99%, contains 1% of 4-tert-butylcatechol as a stabilizer), potassium persulfate (≥99.0%), tetraethyl orthosilicate (TEOS, 98%), *L*-lysine (≥98%), cyclohexane (99.5%, anhydrous), ammonium hydroxide solution (NH_4OH, 28.0-30.0%), ammonium chloride (NH_4Cl, ≥99.5%), hydrochloric acid (HCl, 37%), sodium hydroxide (NaOH, >98%, pellets), poly(allylamine) hydrochloride (PAH, M_w: 5,000-15,000 g/mol), and sodium chloride (NaCl, ≥99.5%) were purchased from Sigma-Aldrich (St. Louis, MO). All chemical reagents except styrene were used without further purification. Relevant pH adjustments for the solutions were controlled with either HCl or NaOH solutions. Deionized water was used for all experiments.

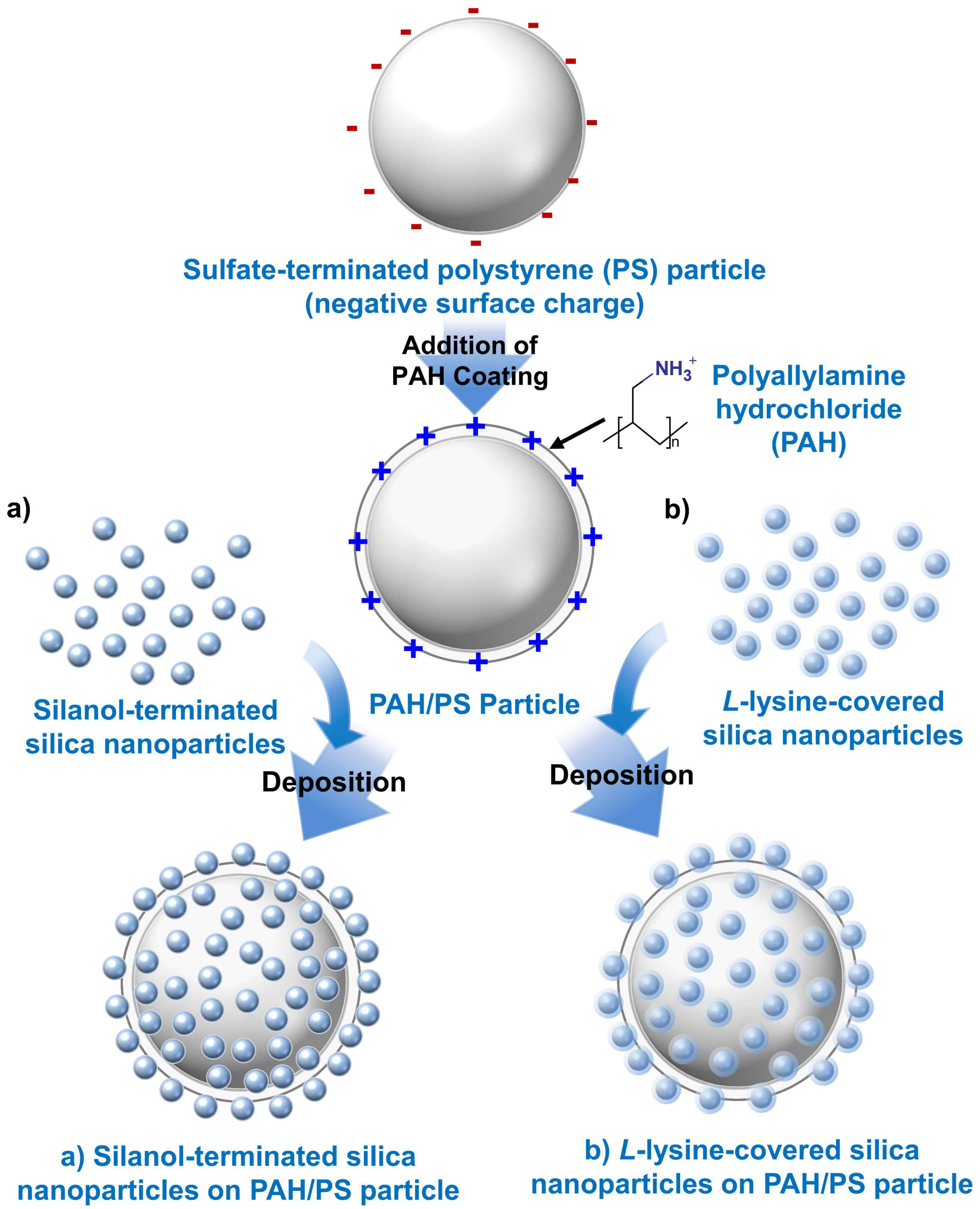

Figure 1.1. General schematic of the procedures used to prepare (a) silanol-terminated silica nanoparticles deposited on PAH/PS particles and (b) *L*-lysine-covered silica nanoparticles deposited on PAH/PS particles.

Synthesis of silanol-terminated silica nanoparticles: $NH_4Cl{\bullet}NH_3$ buffer solution of pH 9.0 was prepared by adding 10 mM NH_4Cl to 0.1 M NH_4OH solution. A volume of 350 mL of the

$NH_4Cl•NH_3$ buffer solution was heated to 60°C in a round flask, and a mixture of TEOS (100 mL) and cyclohexane (50 mL) was added [34, 35]. The solution was stirred vigorously for 24 h and then cooled to room temperature. The aqueous layer containing silanol-terminated silica nanoparticles on the bottom of the reactor was collected, filtered with water of pH 6.5 by using an aluminum oxide filter membrane (pore size: 0.02 μm, Anodisk, Whatman®, GE Healthcare, Chicago, IL), which has straight porous channels. Then, the filtered sample was diluted to 1.0×10^{-5} wt.% with water of the same pH and redistributed by ultrasonication for 15 min. The pH of this solution was 6.7.

Synthesis of L-lysine-covered silica nanoparticles: A mass of 28 mg of *L*-lysine was dissolved in 28 mL of water in a reactor at 78°C. Then, 2.0 g of TEOS were injected into the mixture, and the mixture was vigorously stirred for 24 h and cooled to room temperature [36-39]. To remove the impurities (*i.e.*, free *L*-lysine and ethanol) the solution was filtered using an aluminum oxide membrane. The filtered sample was diluted to 1.0×10^{-5} wt.% with water and redistributed by ultrasonication for 15 min. The measured pH of this solution was 7.3.

Synthesis of sulfate-terminated polystyrene particles: The styrene precursor was washed 4 times with a solution of 1.0 M NaOH to remove the 4-tert-butylcatechol inhibitor. Then, the washed styrene was dried with magnesium sulfate before use. The anionic polystyrene (PS) particles consisting of sulfate-ended chains were prepared by soap-free emulsion polymerization [40]. A mass of 10 g of purified styrene was vigorously mixed with 190 g of water in a three-necked flask for an hour under nitrogen atmosphere at 75°C. Then, 10 g of water containing 0.10 g of potassium persulfate were injected into the reactor to initiate the chain-growth polymerization and incubated for 24 h. The PS particle suspension was washed 7 times with excess water by a sequence of ultrasonication and centrifugation to eliminate impurities such as unreacted sulfate molecules, styrene monomers, dimers, and trimers. The concentration of the purified PS particle suspension was diluted to 0.10 wt.% with water, and then the solution was mixed by ultrasonication for 15 min. The measured pH of this solution was 7.2.

Physisorption of PAH on sulfate-terminated PS particles: In order to coat a PAH monolayer on the sulfate-terminated PS particles, 1.0 mL of 20 wt.% PAH water solution was poured into 30.0 mL of the 0.10 wt.% PS particle suspension, and then the mixture was vigorously stirred for 24 h at room temperature [41-45]. The solution was microfiltered 5 times with excess water by using a cellulose acetate membrane filter (pore size: 0.20 μm, Advantec MFS, Inc., Dublin, CA) to remove free PAH molecules. The purified sample was diluted to 1.0×10^{-5} wt.% with water, and the measured pH was 6.7.

Deposition of silica nanoparticles on PAH/PS particles: A 1.0 mL suspension of 1.0×10^{-5} wt.% silica nanoparticles was incorporated into 10 mL of the PS particle solution and vigorously stirred for 10 s. Then, the pH of each mixture was adjusted to 2, 4, 6, 8, 10, and 12 with 0.1 mM of HCl solution to lower the pH or 0.1 mM of NaOH to increase the pH of each mixture. After mixing for 6 h at room temperature, each sample was microfiltered 3 times with water of the same pH by using a cellulose acetate membrane filter.

Characterization: A field emission scanning electron microscope (FE-SEM, Zeiss Sigma 500, Carl Zeiss AG, Oberkochen, Germany) and a transmission electron microscope (TEM, JEOL 1200 EX II, JEOL Ltd., Tokyo, Japan) were used to observe the morphology of each sample. A drop of sample was placed on aluminum foil and dried in a vacuum oven at room temperature for a week to minimize the thermal effect on the pairwise EDL forces between all particles and to maintain the original morphology of the particles. Temperature is one of the controlling parameters of surface charge. If the sample is dried at higher temperature, charge redistribution occurs at the particle surfaces. The potential profile also changes and the modified value of the EDL force initiates the movement of the attached silica nanoparticles, changing the morphologies of the nanoparticles deposited on the PS particles. The samples for SEM were not sputter-coated since this may affect the original morphology of the silica nanoparticles deposited on the PS particles. The hydrodynamic size distributions and the ζ-potentials of all the particle suspensions were measured using dynamic light scattering (DLS, Nanotrac Wave II, Microtrac, Inc., Montgomeryville, PA) [46-57]. All particle suspensions were ultrasonicated for 10 min before the measurements using DLS.

1.4. Theoretical model

In this section, the modified pairwise DLVO interaction force model is discussed with the assumption that the total interaction force [$F_{\mathrm{DLVO}}(D)$] is a sum of the vdW force [$F_{\mathrm{vdW}}(D)$] and the EDL force [$F_{\mathrm{EDL}}(D)$]:

$$F_{\mathrm{DLVO}}(D)=F_{\mathrm{vdW}}(D)+F_{\mathrm{EDL}}(D) \tag{1.1}$$

where D is the separation distance between surfaces [21-23]. The modified model is valid for both symmetric and asymmetric spherical particles having low and high surface potentials, under low and high ionic strength of solutions at different pH values. In this study, the symmetric systems include solutions of silanol-terminated silica nanoparticles and *L*-lysine-covered silica nanoparticles, for which we analyze the surface interactions between two silanol-terminated silica nanoparticles and between two *L*-lysine-covered silica nanoparticles. The asymmetric systems include mixed solutions of PAH/PS particles with silanol-terminated silica nanoparticles and PAH/PS particles with *L*-lysine-covered silica nanoparticles.

1.4.1. vdW interaction force: London dispersion

The vdW force [$F_{\mathrm{vdW}}(D)$] between spheres used in this work only includes the simplified version of London dispersion interaction forces [$F_{\mathrm{London}}(D)$] with non-retarded Hamaker constants. The origin of London dispersion interaction forces is the fluctuation in electron distribution of an atom. This phenomenon induces a redistribution of electrons in an adjacent atom and creates temporary electric fields [58-62]. These instantaneous dipole-induced dipole attractive energies between all the atoms in one surface and all the atoms in the adjacent surface can be integrated, resulting in a pairwise London dispersion energy [$W_{\mathrm{London}}(D)$] between two plates. The London dispersion force [$F_{\mathrm{London}}(D)$] between spheres is defined by the Derjaguin approximation [25]:

$$F_{\mathrm{vdW}}(D) = F_{\mathrm{London}}\left(D\right) = -\frac{A_{ijk}}{6D^2}\left(\frac{R_i R_k}{R_i + R_k}\right) \tag{1.2}$$

where R_i and R_k are the radii of spheres *i* and *k*, respectively and A_{ikj} is the non-retarded Hamaker constant for media *i* and *k* interacting across medium *j*. Because we investigate the interaction between particles only at small distances, it is a good approximation to ignore the retardation effect, which decreases the interactions at large separations. Moreover, it is very convenient to use experimentally determined non-retarded Hamaker constants to calculate London dispersion interactions since this method does not consider the dielectric function of each medium over all frequencies. All the Hamaker constants used in this work are summarized in Table 1.1. Each medium *i* and *k* is denoted by integers from 1 to 4, with "1" representing a silanol-terminated silica nanoparticle, "2" an *L*-lysine-covered silica nanoparticle, "3" a PAH/PS particle, and "4" a water molecule. When both media *i* and *k* are separated by a water molecule, then *j* is "4". When both media *i* and *k* interact with each other across a vacuum, *j* is null. In this case, A_{ijk} is rewritten as A_{ik}, which can be defined by the simple classical Hamaker constant [25, 58, 62] as:

$$A_{ik} = \pi^2 C_{ik} n_i n_k \quad (1.3)$$

where C_{ik} is called the London or interaction constant of media i and k interacting across a vacuum, and n_i and n_k are atomic number densities for media i and k.

Table 1.1. List of non-retarded Hamaker constants for media i and k interacting across medium j.

Medium			Non-retarded Hamaker constant	
i	j	k	A_{ijk}	Value (J)
Silica	Vacuum	Silica	A_{11}	7.16×10^{-20} (a)
L-lysine/Silica	Vacuum	*L*-lysine/Silica	A_{22}	1.68×10^{-19} (b)
PAH/PS	Vacuum	PAH/PS	A_{33}	7.09×10^{-20} (a)
Water	Vacuum	Water	A_{44}	3.42×10^{-20} (a)
Silica	Water	Silica	A_{141}	6.83×10^{-21} (c)
Silica	Water	PAH/PS	A_{143}	6.72×10^{-21} (c)
L-lysine/Silica	Water	*L*-lysine/Silica	A_{242}	5.06×10^{-20} (c)
L-lysine/Silica	Water	PAH/PS	A_{243}	1.83×10^{-20} (c)

(a) Experimentally measured values [63].
(b) A roughly estimated value with an assumption that C_{11} and C_{22} are equal.
(c) Approximated values by using Equation (1.4).

The Hamaker constants of A_{11} for silanol-terminated silica nanoparticles, A_{33} for PS particles, and A_{44} for water molecules are obtained from experimental published results [63]. The A_{33} value for PS particles is also used for PAH/PS particles in this work because the atomic number densities for amorphous PS and PAH are very close. In order to calculate the unknown Hamaker constant A_{22} for *L*-lysine-covered silica nanoparticles, C_{22} and n_2 must be known. For purposes of simplifying the calculation, we roughly assume that C_{11} and C_{22} are equal. We measured the size of the *L*-lysine-covered silica nanoparticles as 7.8 nm and estimated the thickness of the *L*-lysine monolayer from literature [64] to calculate the atomic number density n_2. Now, with C_{22} and n_2, we can calculate A_{22} using Equation (1.3). The Hamaker constants of most condensed phases are found to lie in the range of 0.4 to 4×10^{-19} J [25]. As seen in Table

1.1, the non-retarded Hamaker constant for the *L*-lysine-covered silica nanoparticles, $A_{22} = 1.68 \times 10^{-19}$ J, is within this energy range. All the variables, including the density of amorphous silica [65], to compute A_{22} are listed in Table 1.2.

Table 1.2. Variables used to compute the Hamaker constant A_{22} for two *L*-lysine-covered silica surfaces in contact.

Description	Symbol	Value
Radius of silanol-terminated silica nanoparticles	R_1	7.6 ± 0.4 nm (a)
Radius of *L*-lysine-covered silica nanoparticles	R_2	7.8 ± 0.4 nm (a)
Radius of PAH/PS particles	R_3	348 ± 0.4 nm (a)
Density of amorphous silica	ρ_1	1.9×10^3 kg/m^3 [65]
Density of *L*-lysine	ρ_2	1.1×10^3 kg/m^3
Number density of atoms of silica nanoparticles	n_1	5.71×10^{28} m^{-3} (b)
Number density of atoms of *L*-lysine-covered silica nanoparticles	n_2	8.75×10^{28} m^{-3} (b)
London (interaction) constant of silica nanoparticles	C_{11}	2.22×10^{-78} J·m^6 (b)
London (interaction) constant of *L*-lysine-covered silica nanoparticles	C_{22}	2.22×10^{-78} J·m^6 (b)

(a) Experimentally measured values
(b) Computed values in present work

In order to approximate A_{141} for all four model systems, the following relation [25] was used:

$$A_{ijk} = \left(\sqrt{A_{ii}} - \sqrt{A_{jj}}\right)\left(\sqrt{A_{kk}} - \sqrt{A_{jj}}\right) \tag{1.4}$$

With this, we have all the variables necessary to calculate the pairwise vdW forces by using Equation (1.2) for symmetric and asymmetric spheres.

1.4.2. EDL interaction forces for symmetric and asymmetric systems

We introduce a regulation parameter p_i, based on the nonlinear Poisson-Boltzmann model, to the EDL interaction energy for either symmetric or asymmetric isolated plates. Then, these EDL energies are converted to EDL interaction forces between two spherical particles by using the Derjaguin approximation [25].

1.4.2.1. Ionic concentration profile

In situations in which two particles are far away, both the surface charge density (σ) and the surface potential (ψ_o) are regulated by the concentration of all the ionic species near the surface. Because the local density of each ion on the surface depends on pH and ionic strength of the solution, the concentration profile $C_{x,i}$ of ions *i* (H^+, Na^+, Cl^-, and OH^-) at distance *x* away from the surface is governed by a Boltzmann distribution [25] expressed by:

$$C_{x,i} = C_{\infty,i}\ e^{-\frac{z_i q \psi_x}{\mathrm{k_B} T}} \tag{1.5}$$

where $C_{\infty,i}$ is the bulk molar concentration of an ionic species *i*, z_i is valence of the ionic species *i*, *q* is the elementary charge, $\mathrm{k_B}$ is Boltzmann's constant, and *T* is the absolute temperature of the solution. The symbol ∞ represents that the point of interest is effectively far away from the surface. The ionic concentrations of bulk solution $C_{\infty,i}$ satisfy the electroneutrality balance [66, 67]:

$$\left[\mathrm{H}^+\right]_\infty + \left[\mathrm{Na}^+\right]_\infty = \left[\mathrm{Cl}^-\right]_\infty + \left[\mathrm{OH}^-\right]_\infty \tag{1.6}$$

Because the only salts we used are HCl for acidic solutions and NaOH for basic solutions, $\left[\mathrm{Na}^+\right]_\infty = 0$ for pH less than 7, $\left[\mathrm{Na}^+\right]_\infty = \left[\mathrm{Cl}^-\right]_\infty = 0$ for pH 7, and $\left[\mathrm{Cl}^-\right]_\infty = 0$ for pH higher than 7. In order to simplify our model, we ignore any potential dissolved CO_2 resulting from diffusion from air into the water solution. Even though the ionic form of CO_2, such as carbonic acid, bicarbonate, and carbonate, change pH and participate in the electroneutrality balance, their concentrations are low enough to be ignored.

1.4.2.2. Charge regulation by proton concentration on surface

When the surfaces are isolated in solution, the ionizable chemical species on the surface can release (deprotonation) or accept protons (protonation), thus being charged or uncharged, depending on the local concentration of protons near the surface [66-74]. These surface chemical species may include functional groups such as amines, carboxylic groups, and hydroxyl groups. When the chemical species on the surface possess extra protons, they are positively charged. If they satisfy the octet rule, they are neutral. When the chemical species are missing protons, they are negatively charged. The surface charge density (σ) of the ionizable surface sites can be expressed in terms of a maximum surface charge density (σ_{max}) and the fraction of ionized sites (α) [25] as:

$$\sigma = \alpha\sigma_{max} \tag{1.7}$$

We develop our discussion of a pH-dependent charge regulation model by deriving the first relation between surface charge density and surface potential for the following three symmetric surfaces: (1) silanol-terminated silica nanoparticles, (2) *L*-lysine-covered silica nanoparticles, and (3) PAH/PS particles.

We surmise that the following two equilibrium acid-base reactions [66-74] occur at the interface between the silanol-terminated silica nanoparticles and the water solution:

$$\mathrm{SiOH_2^+} \overset{K_{a_1}}{\rightleftharpoons} \mathrm{SiOH} + \mathrm{H^+} \tag{1.8a}$$

$$\mathrm{SiOH} \overset{K_{a_2}}{\rightleftharpoons} \mathrm{SiO^-} + \mathrm{H^+} \tag{1.8b}$$

where K_{a_1} and K_{a_2} are acid dissociation constants for Equations (1.8a) and (1.8b), respectively. Each constant is defined by:

$$K_{a_1} = \frac{[\mathrm{SiOH}]_0 [\mathrm{H}^+]_0}{[\mathrm{SiOH}_2^+]_0} \tag{1.9a}$$

$$K_{a_2} = \frac{[\mathrm{SiO}^-]_0 [\mathrm{H}^+]_0}{[\mathrm{SiOH}]_0} \tag{1.9b}$$

where $[\mathrm{SiOH}_2^+]_0$, $[\mathrm{SiOH}]_0$, and $[\mathrm{SiO}^-]_0$ are the surface site densities of SiOH_2^+, SiOH, and SiO^-, respectively, and $[\mathrm{H}^+]_0$ is the concentration of protons at the solid/liquid interface. The total ionizable site density $N_{\mathrm{total,silica}}$ of silanol groups at the solid/liquid interface is expressed as:

$$N_{\mathrm{total,silica}} = [\mathrm{SiO}^-]_0 + [\mathrm{SiOH}]_0 + [\mathrm{SiOH}_2^+]_0 \tag{1.10}$$

Equation (1.7), can be rewritten as:

$$\sigma = -q\mathrm{N_A}\left([\mathrm{SiO}^-]_0 - [\mathrm{SiOH}_2^+]_0\right) \tag{1.11}$$

where $\mathrm{N_A}$ is Avogadro's number. Using Equation (1.10) and substituting $[\mathrm{SiO}^-]_0$ and $[\mathrm{SiOH}_2^+]_0$ with rearranged Equations (1.9a) and (1.9b), one can rewrite the surface charge density as a function of all the equilibrium acid dissociation constants and the concentration of protons at the interface:

$$\sigma = -q\mathrm{N_A}N_{\mathrm{total,silica}} \frac{K_{a_1}K_{a_2} - [\mathrm{H}^+]_0^2}{K_{a_1}K_{a_2} + K_{a_1}[\mathrm{H}^+]_0 + [\mathrm{H}^+]_0^2} \tag{1.12}$$

Since the concentration of all ionic species of the salts is governed by a Boltzmann distribution (*i.e.*, Equation (1.5)) [25], $[\mathrm{H}^+]_0$ can be expressed as a function of $[\mathrm{H}^+]_\infty$:

$$\left[\mathrm{H}^+\right]_0 = \left[\mathrm{H}^+\right]_\infty e^{-\frac{q\psi_\mathrm{o}}{\mathrm{k_B}T}} \tag{1.13}$$

where ψ_o is surface potential. Replacing $\left[\mathrm{H}^+\right]_0$ in Equation (1.12) with Equation (1.13) yields surface charge density as a function of the acid dissociation constants, the concentration of protons at the interface, and the surface potential:

$$\sigma = -q\mathrm{N_A}N_\text{total, silica}\frac{K_{\mathrm{a}_1}K_{\mathrm{a}_2} - \left[\mathrm{H}^+\right]_\infty^2 e^{-\frac{2q\psi_\mathrm{o}}{\mathrm{k_B}T}}}{K_{\mathrm{a}_1}K_{\mathrm{a}_2} + K_{\mathrm{a}_1}\left[\mathrm{H}^+\right]_\infty e^{-\frac{q\psi_\mathrm{o}}{\mathrm{k_B}T}} + \left[\mathrm{H}^+\right]_\infty^2 e^{-\frac{2q\psi_\mathrm{o}}{\mathrm{k_B}T}}}$$

(1.14)

For the *L*-lysine-covered silica nanoparticles, we assume that the α-carboxyl group and α-amine group of the *L*-lysine shell are the only ionizable species contributing surface charge density [75-79], and this configuration is consistent over all the surfaces regardless of pH of the solution. At the interface between an *L*-lysine-covered silica nanoparticle and water, the following two equilibrium acid-base reactions are valid:

$$\alpha\text{-COOH} \overset{K_{\mathrm{a}_3}}{\rightleftharpoons} \alpha\text{-COO}^- + \mathrm{H}^+ \tag{1.15a}$$

$$\alpha\text{-NH}_3^+ \overset{K_{\mathrm{a}_4}}{\rightleftharpoons} \alpha\text{-NH}_2 + \mathrm{H}^+ \tag{1.15b}$$

where K_{a_3} and K_{a_4} are acid dissociation constants at equilibrium for Equations (1.15a) and (1.15b), respectively. These constants are written as:

$$K_{\mathrm{a}_3} = \frac{\left[\alpha\text{-COO}^-\right]_0\left[\mathrm{H}^+\right]_0}{\left[\alpha\text{-COOH}\right]_0} \tag{1.16a}$$

$$K_{\mathrm{a}_4} = \frac{\left[\alpha\text{-NH}_2\right]_0\left[\mathrm{H}^+\right]_0}{\left[\alpha\text{-NH}_3^+\right]_0} \tag{1.16b}$$

where $[\alpha\text{-COOH}]_0$, $[\alpha\text{-COO}^-]_0$, $[\alpha\text{-NH}_3^+]_0$, and $[\alpha\text{-NH}_2]_0$ are the surface site densities of $\alpha\text{-COOH}$, $\alpha\text{-COO}^-$, $\alpha\text{-NH}_3^+$, and $\alpha\text{-NH}_2$ of the *L*-lysine shell, respectively. The total density $N_{\text{total},L\text{-lysine}}$ of α-carboxyl groups and α-amine groups at the *L*-lysine shell/water interface is expressed as:

$$N_{\text{total},L\text{-lysine}} = [\alpha\text{-COOH}]_0 + [\alpha\text{-COO}^-]_0 + [\alpha\text{-NH}_3^+]_0 + [\alpha\text{-NH}_2]_0 \tag{1.17}$$

Because each *L*-lysine molecule has one α-carboxyl group and one α-amine group, the number of independent variables from Equation (1.17) can be reduced to:

$$\frac{N_{\text{total},L\text{-lysine}}}{2} = [\alpha\text{-COOH}]_0 + [\alpha\text{-COO}^-]_0 = [\alpha\text{-NH}_3^+]_0 + [\alpha\text{-NH}_2]_0 \tag{1.18}$$

Equation (1.7), can be rewritten as:

$$\sigma = -q\mathrm{N_A}\left([\alpha\text{-COO}^-]_0 - [\alpha\text{-NH}_3^+]_0\right) \tag{1.19}$$

Using Equation (1.18), substituting $[\alpha\text{-COOH}]_0$ and $[\alpha\text{-NH}_3^+]_0$ with the rearranged forms of Equation (1.16a) and (1.16b), and then incorporating Equation (1.13), results in the following surface charge density as a function of equilibrium acid dissociation constants, the concentration of a proton at the interface, and the surface potential:

$$\sigma = -q\mathrm{N_A}\frac{N_{\text{total},L\text{-lysine}}}{2}\left(\frac{K_{\mathrm{a}_3}}{K_{\mathrm{a}_3} + [\mathrm{H}^+]_\infty e^{-\frac{q\psi_0}{\mathrm{k_B}T}}} - \frac{[\mathrm{H}^+]_\infty e^{-\frac{q\psi_\mathrm{o}}{\mathrm{k_B}T}}}{K_{\mathrm{a}_4} + [\mathrm{H}^+]_\infty e^{-\frac{q\psi_\mathrm{o}}{\mathrm{k_B}T}}}\right) \tag{1.20}$$

For PAH/PS particles, we assume that the coated PAH layer on the PS particle follows solid-like behavior in the pH range between 2 and 12. At the interface between the coated PAH layer and water, the only acid-base reaction at equilibrium is defined by:

$$\mathrm{NH_3^+} \overset{K_{\mathrm{a}_5}}{\rightleftharpoons} \mathrm{NH_2} + \mathrm{H^+} \tag{1.21}$$

where K_{a_5} is an acid dissociation constant at equilibrium. This equilibrium constant can be written as:

$$K_{\mathrm{a}_5} = \frac{[\mathrm{NH_2}]_0 \left[\mathrm{H^+}\right]_0}{\left[\mathrm{NH_3^+}\right]_0} \tag{1.22}$$

where $[\mathrm{NH_2}]_0$ and $\left[\mathrm{NH_3^+}\right]_0$ are the surface site densities of $\mathrm{NH_2}$ and $\mathrm{NH_3^+}$ of the coated PAH layer, respectively. The total ionizable site density $N_{\mathrm{total,PAH/PS}}$ of the amine groups at the coated PAH layer/water interface is expressed as:

$$N_{\mathrm{total,PAH/PS}} = \left[\mathrm{NH_3^+}\right]_0 + [\mathrm{NH_2}]_0 \tag{1.23}$$

Thus, Equation (1.7) can be rewritten as:

$$\sigma = q\mathrm{N_A}\left[\mathrm{NH_3^+}\right]_0 \tag{1.24}$$

One can incorporate Equation (1.23) into Equation (1.24), substitute $\left[\mathrm{NH_3^+}\right]_0$ in the rearranged form of Equation (1.22), and use Equation (1.13) to derive the following surface charge density function in an acid dissociation constant, the proton concentration at the interface, and the surface potential:

$$\sigma = q\mathrm{N_A}N_{\mathrm{total,PAH/PS}} \frac{\left[\mathrm{H^+}\right]_\infty e^{-\frac{q\psi_o}{\mathrm{k_B}T}}}{K_{\mathrm{a}_5} + \left[\mathrm{H^+}\right]_\infty e^{-\frac{q\psi_o}{\mathrm{k_B}T}}} \tag{1.25}$$

The derived equations, namely Equation (1.14) for the silanol-terminated silica nanoparticles, Equation (1.20) for the *L*-lysine-covered silica nanoparticles, and Equation (1.25) for the PAH/PS particles, show the relation between surface charge density and surface potential with respect to pH of the solution. However, these charge regulation equations are still unrealistic because of the effects of total salt concentration and ionic strength of the solution, which also change as the pH of the solution is varied. Moreover, since both the surface charge density and surface potential are unknown in these equations, we need one more independent equation to solve the relation between surface charge density and surface potential at specific pH values.

1.4.2.3. Nonlinear charge regulation relation between surface charge density and surface potential

The surface charge is regulated by proton concentration on the surface and by all co-ions and counter-ions in solution, which affects the charge balance within the EDL and changes the proton concentration profile. Thus, the second relation between surface charge density and surface potential should be dependent on total ionic concentrations on the surface. The well-known Poisson equation describes a Laplacian of the potential as a function of the distance x away from the surface [25] and the ionic concentration profile $C_{x,i}$ as:

$$\nabla^2\psi = \frac{\mathrm{d}^2\psi}{\mathrm{d}x^2} = -\frac{z_i q C_{x,i}}{\varepsilon_\mathrm{o}\varepsilon_\mathrm{r}} \tag{1.26}$$

where ε_o is the permittivity of vacuum and ε_r is the relative permittivity of water at room temperature. Since the ionic concentration follows a Boltzmann's distribution, one can combine Equation (1.5) and Equation (1.26), resulting in the Poisson-Boltzmann equation [25]:

$$\frac{\mathrm{d}^2\psi}{\mathrm{d}x^2} = -\frac{q\mathrm{N_A}}{\varepsilon_\mathrm{o}\varepsilon_\mathrm{r}}\sum_i z_i C_{\infty,i} e^{-\frac{z_i q\psi_x}{\mathrm{k_B}T}} \tag{1.27}$$

This Poisson-Boltzmann equation governs the electrostatic potential distribution for a charged surface, which is immersed in an electrolyte solution [66, 67, 69, 70]. For two symmetric plates separated in isolation by the distance $D \rightarrow \infty$, the boundary condition of the electric field in the mid-plane between these surfaces is:

$$\left.\frac{\mathrm{d}\psi}{\mathrm{d}x}\right|_{x=D/2} = 0 \tag{1.28}$$

Differentiating Equation (1.5) and then integrating it between the concentrations of ions at the midplane $x = D/2$ at any point x [25] results in:

$$C_{x,i} = C_{\infty,i} + \frac{\varepsilon_{\mathrm{o}}\varepsilon_{\mathrm{r}}}{2\mathrm{k}_{\mathrm{B}}T}\left(\frac{d\psi}{dx}\right)_x^2 \tag{1.29}$$

From overall electroneutrality, the total charge of all the ions in the gap between the surfaces must be equal to the charge on the surfaces. This boundary condition yields a relation between the electric field at the surface and the surface charge density as:

$$E_{\mathrm{o}} = \frac{-\sigma}{\varepsilon_{\mathrm{o}}\varepsilon_{\mathrm{r}}} \tag{1.30}$$

where E_{o} is the electric field exerted between the two charged surfaces. One can incorporate Equation (1.30) into Equation (1.29) and express it as a function of the sum of all ionic species:

$$\sum_i C_{\mathrm{o},i} = \sum_i C_{\infty,i} + \frac{\sigma^2}{\varepsilon_{\mathrm{o}}\varepsilon_{\mathrm{r}}\mathrm{k}_{\mathrm{B}}T} \tag{1.31}$$

where $C_{\infty,i}$ is the concentration of an ionic species at the midpoint between any two isolated objects. Incorporating Equation (1.5) for $x = 0$ into Equation (1.31), the Grahame equation [25] is obtained:

$$\sigma = \sqrt{8\varepsilon_{\mathrm{o}}\varepsilon_{\mathrm{r}}\mathrm{k}_{\mathrm{B}}T\mathrm{N}_{\mathrm{A}}C_{\infty}\times 10^3}\ \sinh\left(\frac{q\psi_{\mathrm{o}}}{2\mathrm{k}_{\mathrm{B}}T}\right) \tag{1.32}$$

This equation shows that there is, indeed, a second relation between surface charge density and surface potential, which depends on the total concentration of salts C_{∞}. All the variables required [80-85] to compute the surface charge density and surface potential are listed in Table 1.3.

Table 1.3. Variables and constants used to calculate the EDL interaction force.

Description	Symbol	Value [(a)]
Distance away from the surface	x	m
Valence of ionic species *i*	z_i	
Surface charge density	σ	C/m^2
Potential at distance *x* away from the surface	ψ_x	V
Surface potential	ψ_o	V
Molar concentration of ionic component *i* at distance *x* away from the surface	$C_{x,i}$	M
Molar concentration of ionic component *i* on the surface	$C_{o,i}$	M
Bulk molar concentration of ionic species *i*	$C_{\infty,i}$	M
Distance between the surface of two particles	D	m
Elementary charge	q	$1.60217662 \times 10^{-19}$ C
Boltzmann constant	k_B	1.380649×10^{-23} J/K
Absolute temperature	T	298.15 K
Avogadro's number	N_A	6.022×10^{23} mol^{-1}
Acid dissociation constant of the reaction in Equation (1.8a)	K_{a_1}	$10^{1.9}$ [80, 81]
Acid dissociation constant of the reaction in Equation (1.8b)	K_{a_2}	$10^{-6.4}$ [81]
Acid dissociation constant of the reaction in Equation (1.15a)	K_{a_3}	$10^{-2.18}$ [82]
Acid dissociation constant of the reaction in Equation (1.15b)	K_{a_4}	$10^{-8.95}$ [82]
Acid dissociation constant of the reaction in Equation (1.21)	K_{a_5}	$10^{-8.9}$ [83]
Total ionizable site density of silanol groups at the solid/liquid interface	$N_{\text{total,silica}}$	1.99×10^{-6} mol/m^2 [81]
Total ionizable site density of α-carboxyl groups and α-amine groups at the *L*-lysine shell/water interface	$N_{\text{total},L\text{-lysine}}$	2.20×10^{-6} mol/m^2 [84]
Total ionizable site density of the amine groups at the coated PAH layer/water interface	$N_{\text{total,PAH/PS}}$	3.32×10^{-6} mol/m^2 [85]
Permittivity of vacuum	ε_o	8.854×10^{-12} F/m
Relative permittivity of water at room temperature	ε_r	78.4 [25]

[(a)] Only units are listed for parameters that represent variables.

By using the optimize.root() function from the SciPy package of Python, the solution of each pH-dependent charge regulation model [Equations (1.14), (1.20), and (1.25)] and the Grahame equation [Equation (1.32)] results in a pair of roots of σ and ψ_o with respect to pH of the solution for each symmetric surface. These relations between surface charge density and surface potential are valid for isolated surfaces and both low and high potential cases because the Grahame equation is based on a nonlinear Poisson-Boltzmann equation. However, the ionic strength of the solution is not considered in this model. Moreover, this charge regulation model does not describe the changes in surface charge density and surface potential for the two surfaces upon approach. Therefore, we should introduce a regulation parameter under this nonlinear charge regulation relation so that both the surface charge density and the surface potential are affected by the ionic strength of the solution and the separation distance.

1.4.2.4. Regulation parameter

Chan and Mitchell [86] determined that an approach to show the interaction energy per unit area $W_{\mathrm{EDL}}(D)$ between two identical surfaces may use the following three boundary conditions: (1) $W_{\mathrm{EDL,CP}}(D)$ for constant potential, (2) $W_{\mathrm{EDL,CR}}(D)$ for constant regulation, and (3) $W_{\mathrm{EDL,CC}}(D)$ for constant charge, with:

$$W_{\mathrm{EDL,CP}}(D) \le W_{\mathrm{EDL,CR}}(D) \le W_{\mathrm{EDL,CC}}(D) \tag{1.33}$$

The fraction of $W_{\mathrm{EDL,CC}}(D) - W_{\mathrm{EDL,CP}}(D)$, which contributes to the interaction energy of the regulating surfaces, is defined by:

$$p(D) = \frac{W_{\mathrm{EDL,CR}}(D) - W_{\mathrm{EDL,CP}}(D)}{W_{\mathrm{EDL,CC}}(D) - W_{\mathrm{EDL,CP}}(D)} \tag{1.34}$$

For large separations ($D \rightarrow \infty$), a local linearization of the charge and potential relation permits an arbitrary value and approximation of $p(D)$ [26, 32]:

$$p_i = \lim_{D\to\infty} P_i(D) = \frac{C_{\mathrm{dl},i}}{C_{\mathrm{dl},i} + C_{\mathrm{in},i}} \tag{1.35}$$

where p_i is the regulation parameter for plate i, $C_{\mathrm{dl},i}$ is the diffuse layer capacitance of the plate i, and $C_{\mathrm{in},i}$ is the inner layer capacitance of plate i. When the surface charge of two particles approaching each other is constant $p(D) = 0$ and when the surface potential of two particles approaching each other remains constant $p(D) = 1$. Thus, the constant regulation approximation allows one to describe the charge regulation behavior of two surfaces approaching each other with a single arbitrary regulation parameter between 0 and 1 [21, 22, 26-31]. This regulation parameter depends on the capacitance within the Stern layer of the EDL [29]. The diffuse layer capacitance is obtained from:

$$C_{\mathrm{dl},i} = \frac{\partial \sigma_{\mathrm{dl},i}}{\partial \psi_{\mathrm{dl},i}} = \varepsilon_0 \varepsilon_r \kappa \cosh\left(\frac{q\psi_{\mathrm{dl},i}}{2\mathrm{k_B}T}\right) \tag{1.36}$$

where $\psi_{\mathrm{dl},i}$ is the diffuse layer potential at the outer Helmholtz plane. The location of the outer Helmholtz plane is determined using a straightforward definition by Stern [87]:

$$\delta = 2r_{\mathrm{water}} + r_{\mathrm{hydrated\ ion}} \tag{1.37}$$

where δ is the distance at the outer Helmholtz plane away from the surface, r_{water} is the radius of a water molecule (0.138 nm), and $r_{\mathrm{hydrated\ ion}}$ is the radius of the dominant counter-ions near the isolated surface. The radii of hydrated ions [25] used are listed in Table 1.4. Once the co-ion and counter-ion profiles are known from the Boltzmann equation [Equation (1.5)], one can determine the dominant counter-ions near the solid/liquid interface, as listed in Table 1.5.

Table 1.4. Ionic radii, hydrated radii, and hydration numbers of ions in water.

Ion	$r_{\mathrm{hydrated\ ion}}$ (nm) [(a)]	Hydration number (±1) [(b)]
H_3O^+	0.28	3
Na^+	0.36	4
Cl^-	0.33	1
OH^-	0.30	3

[(a)] Radius of hydrated ion including hydration shell [25]

[(b)] Number of water molecules to fully hydrate ionic species [25]

Table 1.5. Dominant counterion species and distance at outer Helmholtz plane away from the surface of a particle with respect to pH of solution.

pH	Silanol-terminated silica nanoparticles		*L*-lysine-covered silica nanoparticles		PAH/PS particles	
	Dominant counterions [(a)]	δ (nm) [(b)]	Dominant counterions [(a)]	δ (nm) [(b)]	Dominant counterions [(a)]	δ (nm) [(b)]
2	Cl^-	0.61	Cl^-	0.61	Cl^-	0.61
4	H^+	0.56	Cl^-	0.61	Cl^-	0.61
6	H^+	0.56	H^+	0.56	Cl^-	0.61
8	Na^+	0.63	Na^+, H^+	0.61[(c)]	OH^-	0.66
10	Na^+	0.63	Na^+	0.63	OH^-	0.66
12	Na^+	0.63	Na^+	0.63	OH^-	0.66

[(a)] Dominant counterion species at outer Helmholtz plane.

[(b)] Distance at the outer Helmholtz plane away from the surface of a particle.

Now, we need the potential profile as a function of the distance *x* to calculate the diffuse layer potential. For a monovalent electrolyte, the form of the sum of all ionic species from Equation (1.29) can be rearranged [25] as:

$$\frac{d\psi_i}{dx} = \sqrt{\frac{8k_B T C_{\infty,i} N_A \times 10^3}{\varepsilon_o \varepsilon_r}} \sinh\left(\frac{q\psi_{x,i}}{2k_B T}\right) \tag{1.38}$$

One can integrate Equation (1.38) in *x* and obtain the potential profile $\psi_{x,i}$ at a distance *x* away from the surface:

$$\psi_{x,i} = \frac{2k_B T}{q} \ln\left[\frac{1+\left\{\tanh\left(\frac{q\psi_{o,i}}{4k_B T}\right)\right\} e^{-\kappa x}}{1-\left\{\tanh\left(\frac{q\psi_{o,i}}{4k_B T}\right)\right\} e^{-\kappa x}}\right] \tag{1.39}$$

where κ is the inverse Debye screening length [25] defined by:

$$\kappa = \sqrt{\frac{\sum_i q^2 z_i^2 C_{\infty,i} N_A \times 10^3}{\varepsilon_o \varepsilon_r k_B T}} \tag{1.40}$$

The potential profile of Equation (1.39) is governed by the surface potential based on the nonlinear charge regulation relation and the ionic strength of the solution. With the given conditions, δ is incorporated as x into Equation (1.39) to find the diffuse layer potential $\psi_{\mathrm{dl},i}$ of plate i.

The inner layer capacitance $C_{\mathrm{in},i}$ can be considered as two capacitors connected in series and defined by:

$$C_{\mathrm{in},i} = -\frac{\mathrm{d}\sigma_{\mathrm{in},i}}{\mathrm{d}\psi_{\mathrm{dl},i}} = \frac{C_{\mathrm{bi},i} C_{\mathrm{s},i}}{C_{\mathrm{bi},i} + C_{\mathrm{s},i}} \tag{1.41}$$

$C_{\mathrm{bi},i}$ is the binding capacitance expressed as:

$$C_{\mathrm{bi},i} = \frac{q^2 N_{\mathrm{total},i}}{4\mathrm{k_B}T\ \cosh^2\left(\frac{q\psi_{\mathrm{o},i}}{2\mathrm{k_B}T} - \frac{q\psi_{\mathrm{dl},i}}{2\mathrm{k_B}T}\right)} \tag{1.42}$$

where $N_{\mathrm{total},i}$ is the maximum ionizable site density on the surface i [26]. The ratio of the surface charge density to this potential drop yields the Stern capacitance $C_{\mathrm{s},i}$ defined by:

$$C_{s,i} = \frac{\sigma}{\psi_{\mathrm{o},i} - \psi_{\mathrm{dl},i}} \tag{1.43}$$

1.4.2.5. Generalized EDL interaction force

For any symmetric or asymmetric plates i and j separated in isolation by the distance $D \to \infty$, the Poisson-Boltzmann equation [Equation (1.27)] should be solved with the boundary condition of the electric field profile E_x of the plate i at its surface ($x = 0$) [21, 22, 29] as:

$$E_{x,i} = -\left.\frac{\mathrm{d}\psi_i}{\mathrm{d}x}\right|_{x=0} = -\frac{\sigma_i - C_{\mathrm{in},i}\left(\psi_{\mathrm{o},i} - \psi_{\mathrm{dl},i}\right)}{\varepsilon_{\mathrm{o}}\varepsilon_{\mathrm{r}}} \tag{1.44}$$

The linearization of the constant regulation approximation allows one to replace the inner layer capacitance $C_{\mathrm{in},i}$ of Equation (1.44) with the regulation parameter p_i of Equation (1.35). When the electrostatic potential is known, the interaction pressure Π between surfaces can be expressed as:

$$\Pi = \mathrm{k_B}T\sum_i C_{\infty,i}\left[e^{-\frac{z_i q\psi}{\mathrm{k_B}T}} - 1\right] - \frac{\varepsilon_\mathrm{o}\varepsilon_\mathrm{r}}{2}\left(\frac{\mathrm{d}\psi}{\mathrm{d}x}\right)^2 \tag{1.45}$$

The linearization of the Poisson-Boltzmann equation [Equation (1.27)] results in the Debye-Hückel approximation defined by:

$$\frac{\mathrm{d}^2\psi}{\mathrm{d}x^2} = \kappa^2\psi \tag{1.46}$$

which is valid for low potentials of ±25 mV for a monovalent electrolyte. The system with the Debye-Hückel approximation depends on the regulation parameter in Equation (1.35) and the boundary condition in Equation (1.45). The interaction pressure in Equation (1.45) can be written as:

$$\Pi = \frac{\varepsilon_\mathrm{o}\varepsilon_\mathrm{r}}{2}\left[\kappa^2\psi - \left(\frac{\mathrm{d}\psi}{\mathrm{d}x}\right)^2\right] \tag{1.47}$$

An integration of this pressure over the separation distance yields the pairwise EDL interaction energy between two plates *i* and *j*:

$$\begin{aligned} W_{\mathrm{EDL,planes}}(D) &= \int_D^\infty \Pi(D')\,\mathrm{d}D' = \\ &= \varepsilon_\mathrm{o}\varepsilon_\mathrm{r}\kappa\,\frac{2\psi_{\mathrm{o},i}\psi_{\mathrm{o},j}\;e^{-\kappa D} + \left[(2p_i - 1)\psi_{\mathrm{o},j}^2 + (2p_j - 1)\psi_{\mathrm{o},i}^2\right]e^{-2\kappa D}}{1 - (2p_i - 1)(2p_j - 1)\;e^{-2\kappa D}} \end{aligned} \tag{1.48}$$

where p_i and p_j are the regulation parameters of two different plates, *i* and *j*, respectively [22, 33]. Even though Equation (1.48) is originally derived from the linearized Poisson-Boltzmann equation within the Debye-Hückel approximation, the EDL interaction energy is affected by the regulation parameter based on a nonlinear charge-potential relation. Thus, Equation (1.48) indeed describes the EDL interaction energy of either symmetric or asymmetric plates with realistic charge regulation behaviors, which are determined by pH, total concentration of salts, ionic strength of the electrolyte solution, and the separation distance. This model is also valid for low to high ionic strength of the solution and low to high surface potential cases. The EDL interaction force $F_{\text{EDL,spheres}}(D)$ between two spheres can be obtained by the Derjaguin approximation:

$$F_{\text{EDL,spheres}}\left(D\right) = 2\pi \frac{R_i R_j}{R_i + R_j} W_{\text{EDL,planes}}\left(D\right) \tag{1.49}$$

By incorporating the vdW force from Equation (1.2) and the EDL force from Equation (1.49) into Equation (1.1), the pairwise DLVO interaction force profiles as a variation of pH are obtained for either symmetric or asymmetric spheres. What we are interested are the force profiles for the two different asymmetric cases: 1) a silanol-terminated silica nanoparticle and a PAH/PS particle and 2) an *L*-lysine-covered silica nanoparticle and a PAH/PS particle. Thus, the regulation parameters and the surface potential values for all three symmetric surfaces are required as defined in Equation (48). Additional variables required to compute the regulation parameters of plate *i* and the EDL interaction force between two particles are listed in Table 1.6. The entire calculation procedure of this work is diagrammatically represented in Figure 1.2.

Table 1.6. Variables to calculate nonlinearlized regulation parameters of plates and the EDL interaction forces between particles.

Description of quantity	Symbol	Unit
Regulation parameter for plate *i*	p_i	
Diffuse layer capacitance of plate *i*	$C_{\mathrm{dl},i}$	F
Inner layer capacitance of plate *i*	$C_{\mathrm{in},i}$	F
Binding capacitance of plate *i*	$C_{\mathrm{bi},i}$	F
Stern capacitance of plate *i*	$C_{\mathrm{s},i}$	F
Potential at distance *x* away from the surface of plate *i*	$\psi_{x,i}$	V
Surface potential of plate *i*	$\psi_{\mathrm{o,i}}$	V
Diffuse layer potential at the outer Helmholtz plane for plate *i*	$\psi_{\mathrm{dl},i}$	V
Inverse Debye screening length	κ	m^{-1}
Total bulk molar concentration of electrolytes	C_∞	M
Distance at the outer Helmholtz plane away from surface	δ	m

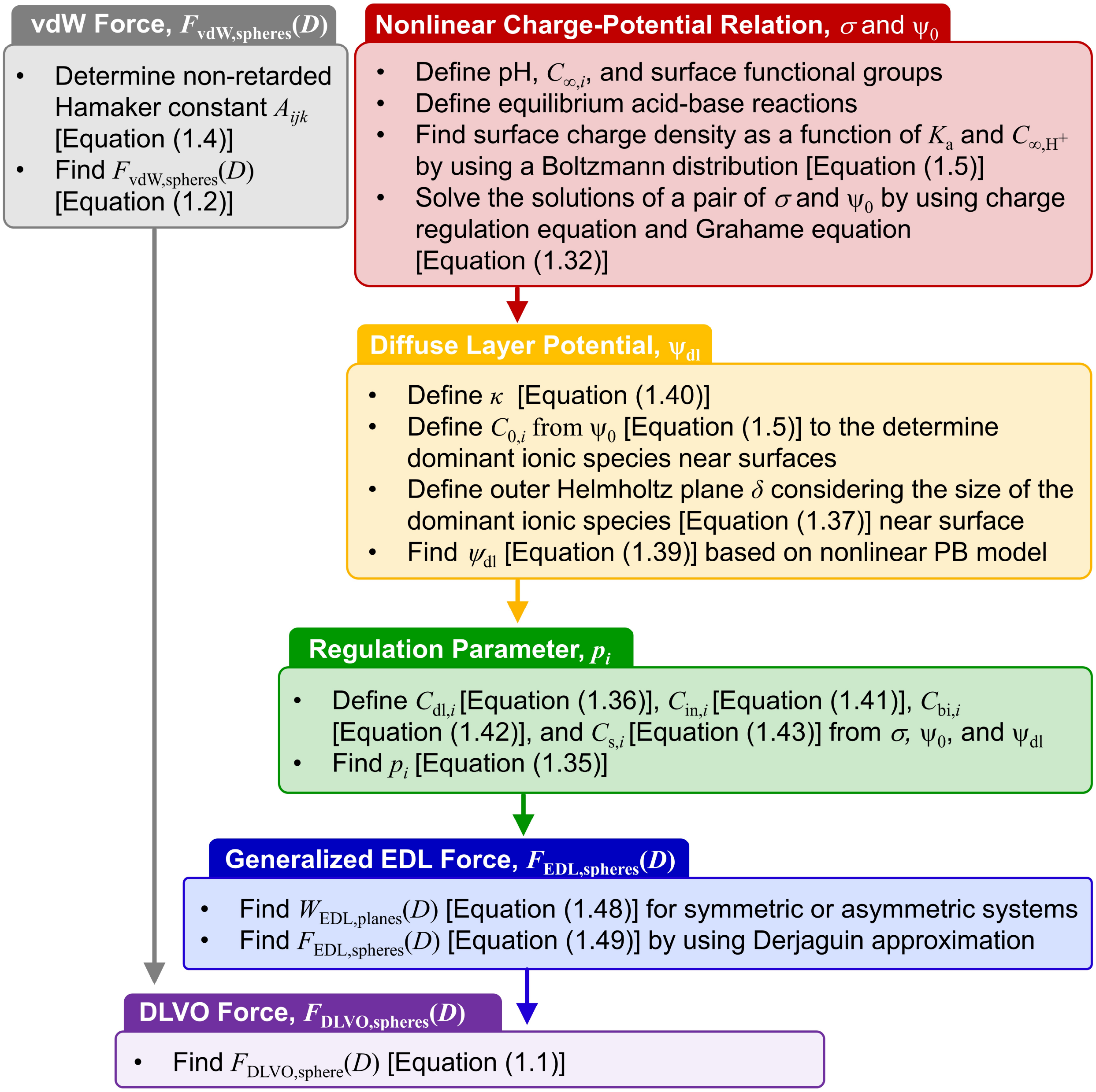

Figure 1.2. Flowchart describing computational algorithm to calculate vdW, generalized EDL, and DLVO interaction forces between particles.

1.4.3. Summary of model contributions

The most recent regulation parameter model is based on a simple charge regulation effect with constant regulation under the Debye-Hückel approximation [21, 22, 28, 29, 31, 70]. It makes use of a mathematical relationship between the regulation parameter and the diffuse layer potential, with values that can be determined by direct measurements of the pairwise interaction force and capacitances C_{dl}, C_{in}, C_{bi}, and C_{s} [29]. For computational simplicity, the Grahame equation is used based on a direct relationship between surface charge density and diffuse layer potential, instead of surface potential. Even though this approach agrees well with experimental results, it has limitations to appropriately describe realistic charge regulation behaviors of a larger variety of colloidal systems.

To properly estimate the pairwise EDL interaction forces under realistic charge regulation behaviors for more practical cases, our proposed model introduces a mathematical procedure to determine the regulation parameter without any experimental measurements. To improve the regulation parameter model, our contributions include (i) a nonlinear relationship between surface charge and surface potential based on the charge regulation effect occurring over a wide range of pH values using nonlinear Poisson-Boltzmann theory, and (ii) a method to define the diffuse layer potential by considering the size of dominant ionic species near surfaces.

First, we show the nonlinear relation between surface charge and surface potential for all possible equilibrium acid-base reactions of a single functional group and multi-functional groups on the surfaces of particles in the pH range from 2 to 12. This method is valid for more practical situations such as low to high pH and low to high electrolyte concentration. Second, considering the size of dominant ions near surfaces allows us to define the diffuse layer potential in the outer Helmholtz plane. The values (surface charge density, surface potential, and diffuse layer potential) determined by these two methods are used to find the regulation parameters, which describe the pairwise EDL interaction forces of particles under a realistic charge regulation effect. If the concentration of particles in solution is dilute, this generalized EDL interaction force model is valid for low to high pH, low to high electrolyte concentration, single to multi-functional surface groups, symmetric systems, and asymmetric systems. This is because the primary assumption of the mathematical description of the pairwise interaction force is that the two interacting particles are not under any external forces [25].

1.5. Results and discussion

1.5.1. Defining morphology and ionizable functional groups of colloidal spheres

An appropriate theoretical description of the interaction energies and forces for spherical particles in suspension, particle morphologies and surface chemistry, is crucial to avoid a significant deviation from real results [23]. First, both the vdW and EDL terms depend on geometry of the particles, which can be defined by size, shape, surface roughness, and density, since Equations (1.2) and (1.49) are the results of Derjaguin approximation [25]. Particularly, the surface roughness must not be ignored for the vdW interaction term since the strength of this interaction extends meaningfully from 0.2 to 1 nm away from the surface [23, 59-61]. Thus, surface roughness of the real spherical particles greater than 1 nm causes uneven vdW interactions between the surface of a sphere and that of another sphere, resulting in a drastic decrease in the pairwise vdW interaction. Second, a deep understanding in protonation and deprotonation of the functional groups on the surface of the colloidal spheres allows defining how many specific chemical groups are ionized and contribute surface charge density at a given pH and ionic strength. Thus, to justify that all the colloidal particles used in this work are ideal for our theoretical model, morphological studies using electron microscopy techniques were completed.

The morphologies of the silanol-terminated silica nanoparticles are shown in the TEM image in Figure 1.3(a). The nanoparticles are spherical and highly monodisperse (diameter: 7.6 ± 0.5 nm). In the early stages of the sol-gel synthesis process, the silica precursor (TEOS) resides in the spherically-shaped hexane colloids, and the NH_4OH basic catalyst is ionized in the water phase. Because the pH of the water phase is 9, the hydroxide ion slowly initiates the hydrolysis of TEOS at the interface between water and hexane. Since the fully hydrolyzed intermediate, an orthosilicic acid ($Si(OH)_4$) is hydrophilic, it moves through the interface from the cyclohexane phase to the water phase. Then, the rapid condensation of silicic acid occurs in the water phase, resulting in the uniform growth of spherical silica nanoparticles.

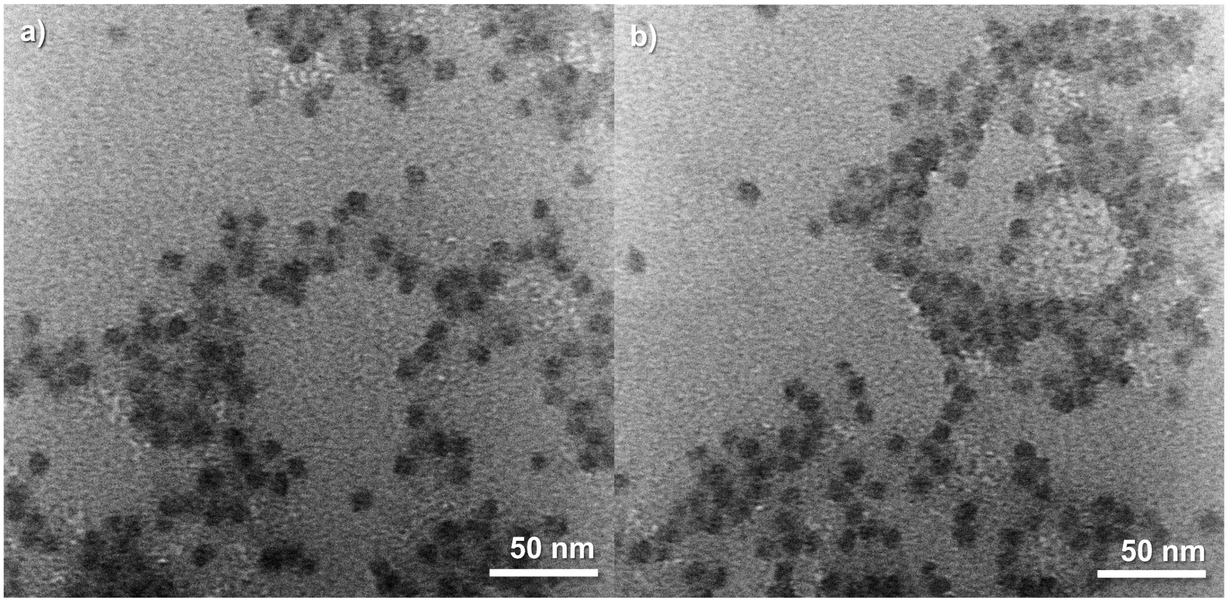

Figure 1.3. Transmission electron micrographs of (a) silanol-terminated silica nanoparticles and (b) *L*-lysine-covered silica nanoparticles.

The TEM image in Figure 1.3(b) presents the *L*-lysine-covered silica nanoparticles synthesized by the *L*-lysine catalyzed sol-gel reaction. The results show that the nanoparticles are highly uniform with a diameter of 7.8 ± 0.4 nm and are spherical as well. The pH of the water solution is between 9 and 10 during the reaction. Within this pH range, all the α-carboxyl groups of *L*-lysine free molecules are deprotonated and exhibit negative charge, whereas almost half of the α-amine groups and half of the ε-amine groups are protonated and are positively charged [77, 79]. These NH_3^+ groups induce the generation of more hydroxide ions, which slowly initiate the hydrolysis of TEOS. The spherical silica spheres then grow by the rapid condensation of silicic acids and the charged *L*-lysine molecules cover the surface of the silica spheres, simultaneously. The mechanism of this *L*-lysine-aided synthesis enables a facile synthesis of highly uniform silica nanoparticles in water [37].

The SEM image at low magnification in Figure 1.4(a) shows that the prepared sulfate-functionalized PS particles by soap-free emulsion polymerization are highly uniform in spherical shape and size (344 ± 1 nm). The closed-packed structure of the particles after a slow dry also supports the high monodispersity of the prepared samples. During the initial stage of the polymerization of styrene monomers, unstable free radicals from the sulfates are generated by thermal decomposition of potassium persulfate in the water phase. The radicals attack the π bonds of the styrene monomers at the styrene/water interface, resulting in the addition of styrene monomer units [88-90], thereby growing the PS chains and resulting in particles that are functionalized with sulfate groups on the surfaces [40]. As shown in Figure A3 in Appendix A, the fractional composition diagram of the sulfate-terminated PS chain indicates that this group exists in a deprotonated form. It also shows that the surface of the PS particle keeps its negative charge at maximum in the pH range from 2 to 12. The pK_a value of -1.5 of the protonated sulfate group on the PS chain was computed using Marvin, a chemistry software of ChemAxon. The SEM micrograph in Figure 1.4(b) and the TEM micrograph in 2(c) show that the sulfate-terminated PS particles have minimal roughness on the surface. The TEM image at high magnification in Figure 1.4(d) confirms that the surface roughness is less than 1 nm.

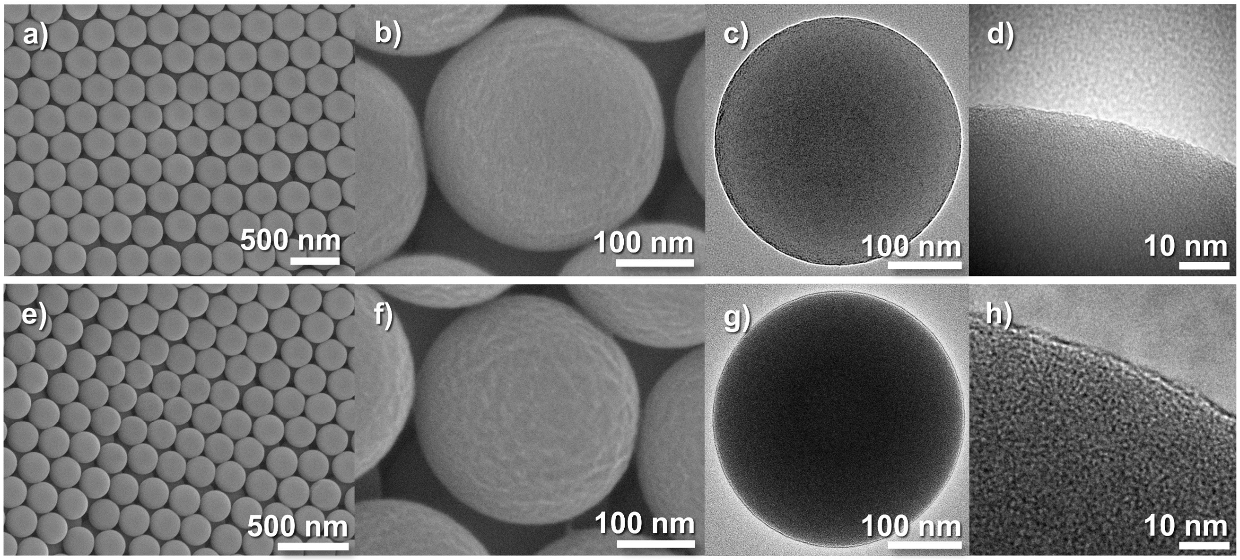

Figure 1.4. (a)-(b) Scanning electron micrographs and (c)-(d) transmission electron micrographs of sulfate-terminated PS particles. (e)-(f) Scanning electron micrographs and (g)-(h) transmission electron micrographs of PAH-coated PS particles.

The SEM micrograph in Figure 1.4(e) shows that the PAH-covered PS particles also have high uniformity in shape and size and exhibit the same close-packed structure after a slow drying procedure. The SEM micrograph in Figure 1.4(f) and the TEM micrographs in Figures 1.4(g) and 2(h) illustrate that the surface roughness of the PAH-covered PS particles is also less than 1 nm. The measured size of the PAH-covered PS particles is 348 ± 1 nm. This indicates that there is an increase in radius of approximately 2 nm after incorporation of the PAH coating. As reported in many studies, a 2 nm thickness of PAH is considered a monolayer. This monolayer is possible at a salt concentration lower than the critical salt concentration [91-93]. Morphologically, the silanol-terminated silica nanoparticles, *L*-lysine-covered silica nanoparticles, and PAH/PS particles, are characterized by their similar size and spherical shape with a smooth surface, thus confirming that it is appropriate to use the non-retarded Hamaker constants from literature and Derjaguin approximation for the pairwise vdW interaction force between spheres.

Figures 1.5(a)-(c) are diagrams representing ionizable functional groups on the surface of the colloidal silica nanoparticles at low, neutral, and high pH, respectively. On the basis of the neutral form of the ionizable surface groups on silica, there are four different types of silanol groups, isolated silanol, geminal silanol, vicinal silanol, and H-bonded silanol [94-100]. Siloxanes are ignored because the colloidal silica nanoparticles in this work never undergo dehydration under drying. At low pH, because of high concentration of protons, most silanol groups keep their protonation state and exhibit neutral charge. A few silanol groups at this low pH are protonated once more and bear positive charge. The sum of these two acid-base equilibrium states of the silanols indicates that the surface charge density of silica nanoparticles can have nearly neutral charge or slightly positive charge depending on ionic strength and solvent types. At neutral pH, the silanols undergo deprotonation due to lower concentration of protons and become silanolates, SiOH, that bear negative charge. At high pH, the extremely low concentration of protons and high concentration of hydroxide ions triggers a full deprotonation of all silanols, resulting in maximum negative charge.

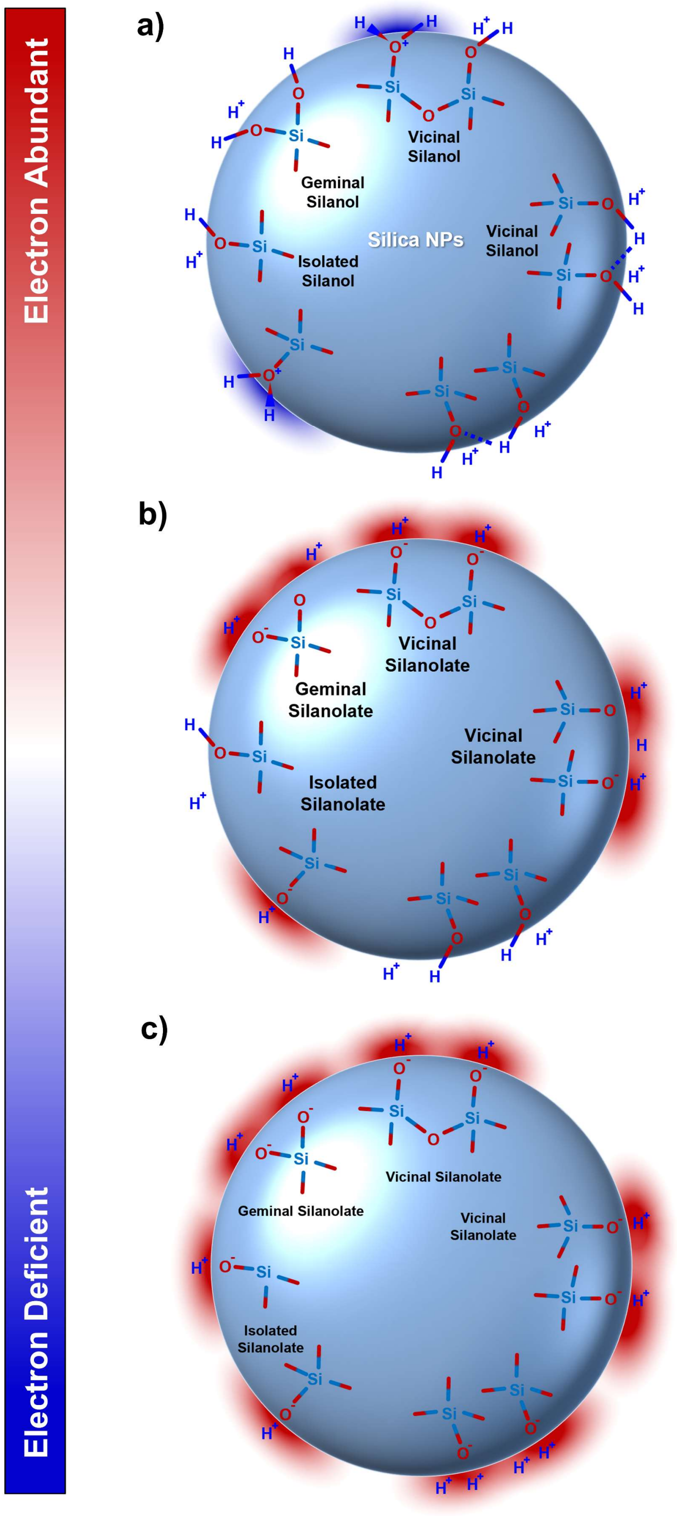

Figure 1.5. Schematic representation of the change in surface charge of silanol-terminated silica nanoparticles by protonation and deprotonation with respect to changes in pH at (a) low pH, (b) neutral pH, and (c) high pH.

Before describing the acid-base equilibrium at the surface of the *L*-lysine-covered silica nanoparticles with respect to pH, we must define which ionizable functional groups contribute to the surface charge density. The *L*-lysine molecule, which covers and protects the silica core has three ionizable groups, namely an α-carboxyl group, an α-amine group, and an ε-amine group [76-79, 82]. Depending on pH, the neutral α-carboxyl group can be transformed to the deprotonated form of COO^- having a negative charge. The α-amine group ($pK_a = 8.95$) and the ε-amine groups ($pK_a = 10.28$) are neutral at high pH. These two functional groups can undergo protonation and bear positive charge at the pH range from low to medium. With this information, we can estimate the desirable configuration of the *L*-lysine at a variety of pH values, characterized by α-carboxyl groups and α-amine groups at the outer surface of the shell, and ε-amine groups bound to the surface of the silica core as depicted in Figure 1.6(a). We need to define a balance in intermolecular forces that forms the core-shell structure of the *L*-lysine-covered silica nanoparticles. We assume that three different interaction forces are present at the following three sites: (i) the interface between the *L*-lysine shell and the silica core surface, (ii) the inside of side chains of the *L*-lysine shell, and (iii) the outer surface of the *L*-lysine shell [76-79].

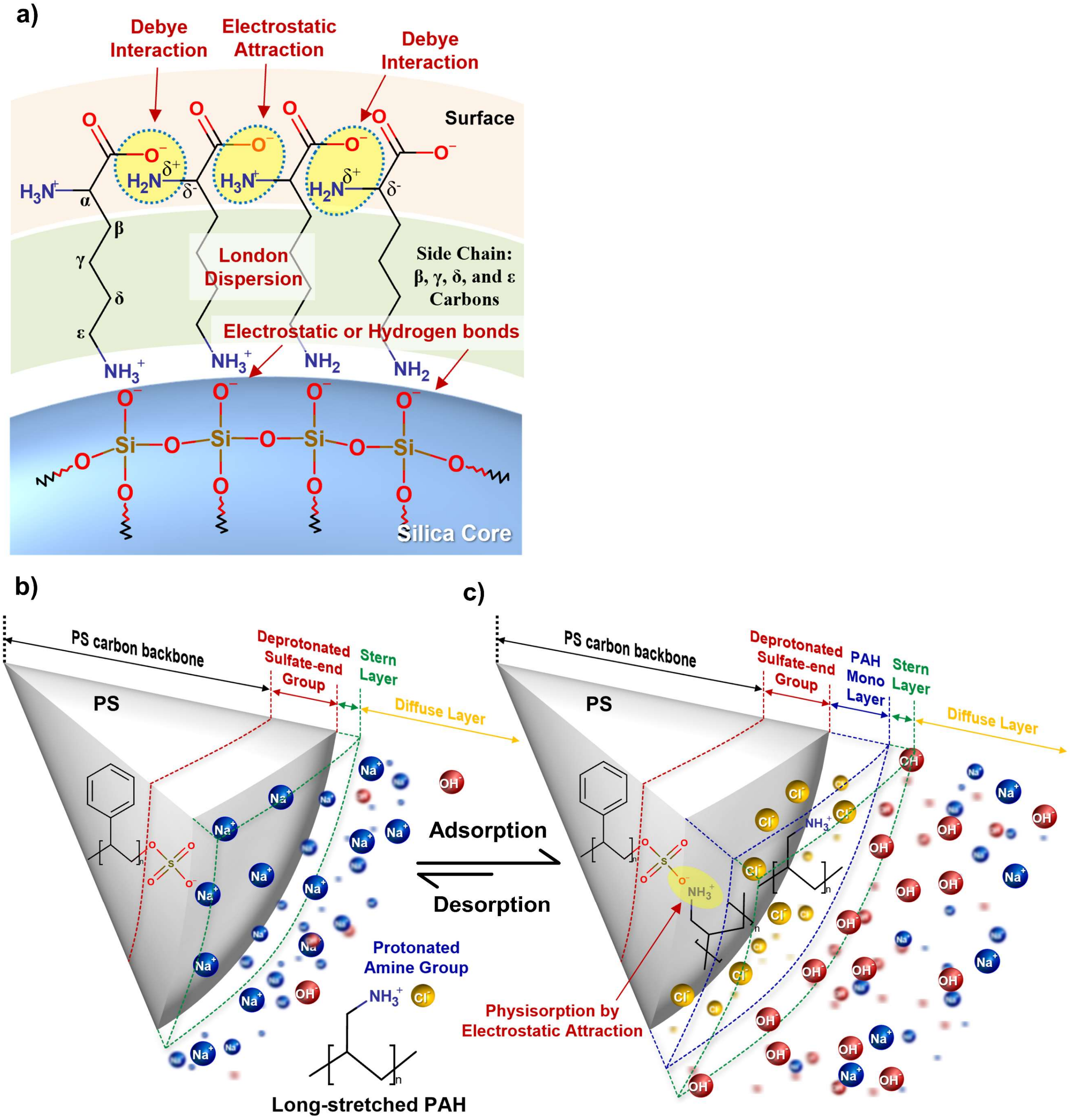

Figure 1.6. (a) Schematic of the structure of the *L*-lysine layer on the silica nanoparticle core and interaction forces that maintain the structure. (b) Structure of coating of PAH chains on sulfate-terminated PS particles.

When it comes to the interaction forces at the interface between the *L*-lysine shell and the silica core, we discuss two different cases. Let us assume that the ε-amine groups of *L*-lysine molecules are interacting with the silica core surface. At the interface, there would be three possible attraction forces: (i) an electrostatic attraction between ε-NH_3^+ of *L*-lysine and SiO^- of the silica core surface, (ii) a dipole-induced dipole attraction (Debye interaction) either between ε-NH_3^+ of *L*-lysine and SiOH of the silica core surface or ε-NH_2 of *L*-lysine and SiO^- of the silica core surface, and (iii) a weak hydrogen bond between ε-NH_2 of *L*-lysine and SiOH of the silica core surface. Because all these three forces would retain the tight bonds between the *L*-lysine shell and the silica core and do not dissipate in a wide range of pH, this configuration of the *L*-lysine molecule in the shell is reasonable. The second case is the α-carbon side with α-amine group and α-carboxyl group of *L*-lysine interacting with the surface of the silica core. Because the α-carboxyl group is deprotonated and bears negative charge, there is repulsion between the α-carbon side and the silica core surface when α-amine is neutral. For the case when the α-amine is protonated and exhibits positive charge, the overall charge of the α-carbon side is neutral. Thus, the α-carbon side of *L*-lysine maintains a distance from the silica surface, while the ε-amine group side favors bonding on the silica surface.

Secondly, there is an instantaneous dipole-induced dipole (London dispersion) attraction force between the side carbon chains from β-carbon to ε-carbon. This intermolecular force is strong enough to hold molecules together at a separation distance less than 0.5 nm. Thus, regardless of the ionic strength of the solution, this type of vdW force can tightly hold the parallelly aligned *L*-lysine molecules in the shell as represented in Figure 1.6(a). Third, at the surface of the *L*-lysine shell, there are three different attraction forces: (i) an electrostatic attractive force between an

α-COO$^-$ of an *L*-lysine and an adjacent α-NH_3^+ of the other *L*-lysine, (ii) a Debye interaction force either between an α-COO$^-$ of an *L*-lysine and an adjacent α-NH_2 of the other *L*-lysine or an α-COOH of an *L*-lysine and an adjacent α-NH_3^+ of the other *L*-lysine. Thus, the balance of all the forces exerted in different regions within the particle favors the desirable configuration of the *L*-lysine shell on the silica core. This configuration is characterized by the ε-amine groups of the *L*-lysine molecules bound to the silica surface. The α-carboxyl groups and the α-amine groups of the *L*-lysine molecules are located at the outer surface of the shell. This justifies the use of the α-carboxyl group and the α-amine group of *L*-lysine as the only ionizable surface groups that participate in the surface charge density of the *L*-lysine-covered nanoparticles.

Figure 1.6(b) illustrates the structure of the sulfate-terminated PS with the distribution of ions (left) and the charge inversion from negative to positive by the physisorption of PAH on the sulfate-ended PS particle at low salt concentration (right) [91-93]. The PS carbon backbone is located inside the core and the sulfate group faces the water phase. The sodium cations from the thermal initiator (*i.e.*, potassium persulfate) are dominant near the surface of this PS particle. Since the PAH-dissolved water solution used for the charge inversion has a very high concentration of salts without adding additional salts, the total concentration of all ionic species during the charge inversion is very low. At a low concentration of salts, there is a lower formation of a counterion cloud (mostly Cl^-) between the protonated amine groups on the side chains of PAH. Thus, the screening effect is negligible in this case. From this, the electrostatic repulsive forces between the protonated amine groups are exerted strongly enough to maintain their spatial arrangement as a long-stretched polyelectrolyte chain instead of a coiled and globular conformation [93]. Also, the protonated amine groups on the side chains of a long-stretched PAH are very strongly attracted to the sulfate groups of the PS particle surface, resulting in an ultra-thin polyelectrolyte coating.

During this attachment procedure, the PAH chains compete with the sodium cations near the PS particle. Because the concentration of PAH used in this work is very high, the positively charged PAH chains are tightly bound on the sulfate group of the PS particle. Meanwhile, the sodium cations, which are bound on the sulfate groups of the PS particle, are displaced from this PAH-coated PS particle. In addition, a redistribution of other ion species also happens during this ion exchange phenomenon. To meet the overall charge balance, more hydroxide ions participate in a cloud of anions together with chloride anions and stay inside of and near the PAH layer. As discussed earlier, since the attached PAH layer is considered a monolayer, we surmise that the potential inside the PAH monolayer is constant anywhere and this PAH layer follows solid-like behavior [93]. With this assumption, we treat the amine groups on this PAH layer as the surface functional groups on a hard particle.

1.5.2. Nonlinear charge regulation relationship between surface charge density and surface potential

In this section, we analyze the changes in both surface charge density and surface potential with respect to pH from the perspective of the Boltzmann distribution of each ionic species on the surface. Surface charge density and surface potential are computed by the charge regulation equations [Equations (1.14), (1.20), and (1.25)] and the Grahame equation [Equation (1.32)] and plotted in Figure 1.7. The raw data for this figure is available in Appendix A. Figure 1.7(a) shows the surface charge density of the silanol-terminated silica nanoparticles, *L*-lysine-covered silica nanoparticles, and PAH/PS particles with respect to pH. Figure 1.7(b) presents the same information with reduced axes for clarity at small values. To discuss further the surface charge density behaviors of these colloidal particles, we explore the shifts of the ionic concentrations in log scale between the bulk solution and the solution on the surface of each particle as a variation of pH, as displayed in Figure 1.8 (raw data information available on page S13 of Supplementary Information). In this figure, we compare the changes in the bulk ionic concentration of each species [Figure 1.8(a)] with the changes in each ionic concentration on the surface of the silanol-terminated silica nanoparticles [Figure 1.8(b)], the *L*-lysine-covered silica nanoparticles [Figure 1.8(c)], and the PAH/PS particles [Figure 1.8(d)]. Each ionic concentration on the surface is computed using the Boltzmann equation [Equation (1.5)] with the calculated surface potential. Each plot is divided into several regions depending on changes in the slope of the ionic concentration with respect to pH.

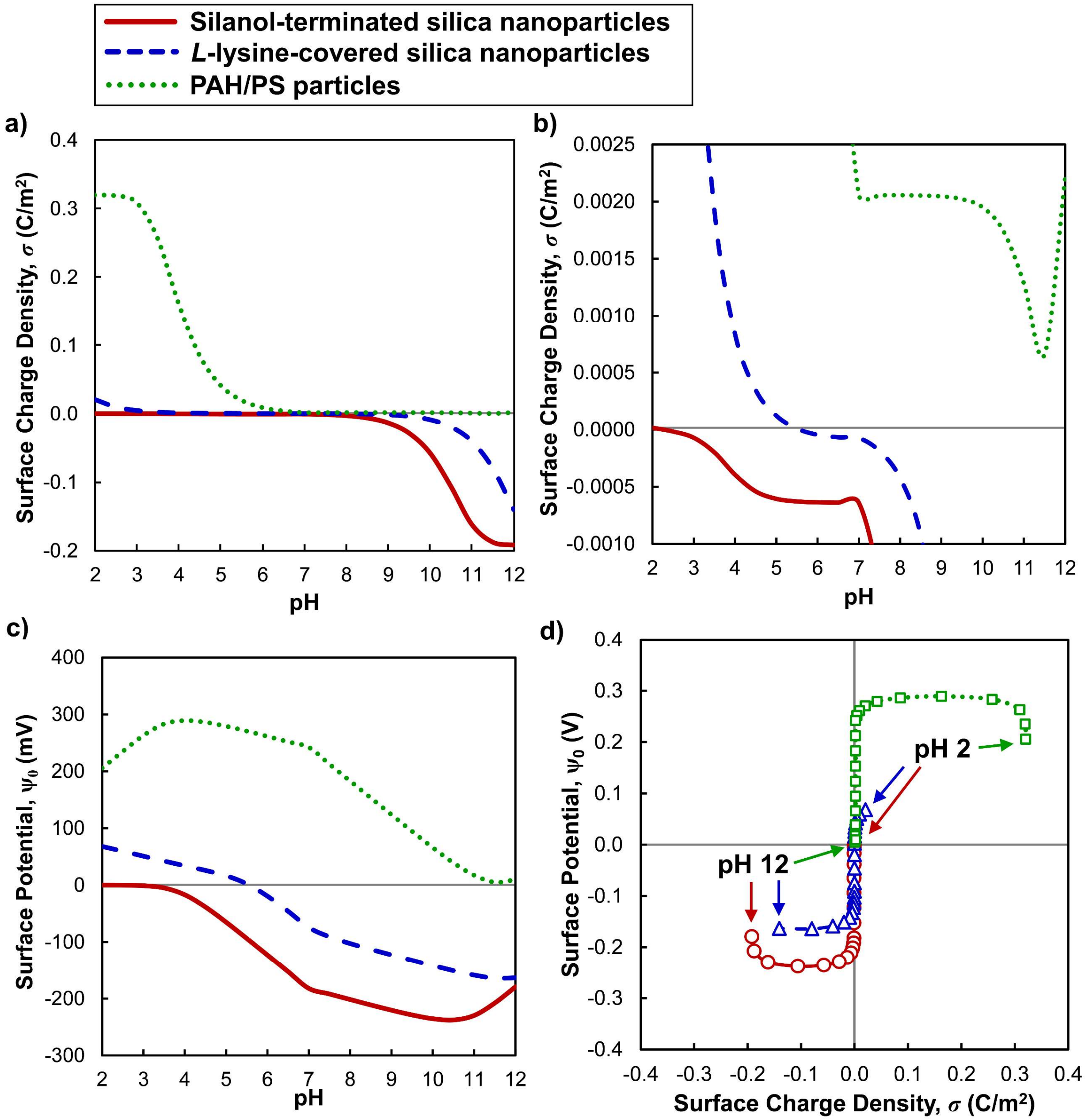

Figure 1.7. (a)-(b) Surface charge density profiles as a function of pH, (c) surface potential distributions as a variation of pH, and (d) surface charge density versus surface potential for silanol-terminated silica nanoparticles, *L*-lysine-covered silica nanoparticles, and PAH/PS particles.

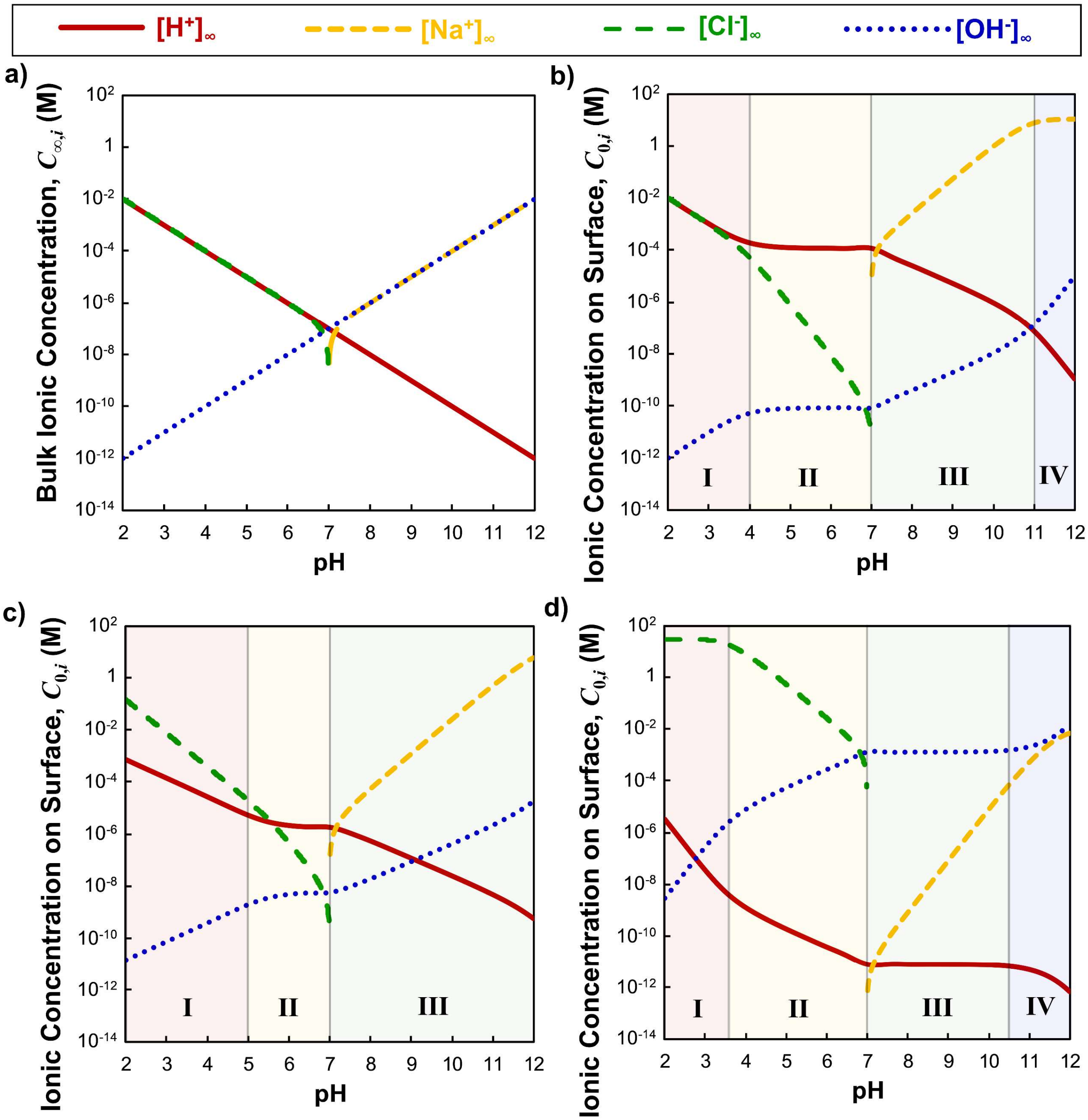

Figure 1.8. Concentration profiles of sodium ions, hydroxide ions, chloride ions, and protons with respect to pH from 2 to 12 for (a) bulk solutions, (b) on the surface of silanol-terminated silica nanoparticles, (c) on the surface of *L*-lysine-covered silica nanoparticles, and (d) on the surface of PAH/PS particles.

Surface charge density of silanol-terminated silica nanoparticles: As seen in Figure 1.7(a), at pH 2 the surface of the silanol-terminated silica nanoparticles is very slightly positive (+0.17 μC/m^2) because a few protonated silanol groups bear positive charge and most of the silanol groups are neutral due to high concentration of protons in the solution. At pH between 2.0 and 2.5, there is a charge inversion from slightly positive to slightly negative with an increase in pH [Figure 1.7(b)]. Region I of Figure 1.8(b) shows that the ionic concentration on the surface is very similar to the behavior shown in Figure 1.8(a) at the same pH range (*i.e.*, from 2 to 4) for $\left[\mathrm{H}^+\right]_0$, $\left[\mathrm{Cl}^-\right]_0$, and $\left[\mathrm{OH}^-\right]_0$. In both figures, the value at pH 2 is the same and the slopes of all three curves point in the same direction for each of the ionic species. This is expected because the rates of change of $\left[\mathrm{H}^+\right]_0$, $\left[\mathrm{Cl}^-\right]_0$, and $\left[\mathrm{OH}^-\right]_0$ on the surface with respect to pH are very close to that of each bulk ionic concentration of the $\left[\mathrm{H}^+\right]_0$, $\left[\mathrm{Cl}^-\right]_0$, and $\left[\mathrm{OH}^-\right]_0$, as seen by comparing Figure 1.7(a) and 4(b). Referring to Figure 1.7(a) from pH 4 to 7, the surface charge density is constant even though the concentration of protons $\left[\mathrm{H}^+\right]_\infty$ in the solution, which decreases with increase in pH, is much lower at pH 7 compared to pH 4. Region II of Figure 1.8(b) shows that the ionic concentration profiles on the surface do not follow the bulk ionic concentration profiles, shown in Figure 1.8(a), between pH 4 and 7. In region II, an increase in pH does not change $\left[\mathrm{H}^+\right]_0$ and $\left[\mathrm{OH}^-\right]_0$, whereas in the bulk the ionic concentration of $\left[\mathrm{H}^+\right]_0$ decreases and that of $\left[\mathrm{OH}^-\right]_0$ increases with increasing pH. Because the density of SiO^- on the silica surface does not change from pH 4 to 7 in Figure 1.7(a), the concentration of the only counterion, H^+, on the silica surface in Region II of Figure 1.8(b) must be constant as well. If $\left[\mathrm{H}^+\right]_0$ is constant, $\left[\mathrm{OH}^-\right]_0$ must also be constant, since the auto-ionization of water molecules obeys pH + pOH = 14 everywhere in the aqueous solution at room temperature. We refer to this as the buffer capacity (*i.e.*, the capacity to protect the volume close to the surface from changes in ionic concentration of protons and hydroxide anions on the surface). On the other hand, $\left[\mathrm{Cl}^-\right]_0$ changes sensitively by the change in pH to meet local charge balance, which shows that this ionic species is not buffered.

From pH 7 to 11 in Figure 1.7(a), as additional NaOH is added to the solution, there is an increase in the absolute value of the surface charge density of the silanol-terminated silica nanoparticles (*i.e.*, the surface charge density becomes more negative). Since this negative surface charge density is high enough to strongly attract more protons and sodium cations near the surface, $\left[\mathrm{H}^+\right]_0$ and $\left[\mathrm{Na}^+\right]_0$ show shifts to higher concentrations when comparing the bulk concentrations in Figure 1.8(a) with those on the surface in Figure 1.8(b). Above pH 11, the surface charge density reaches its maximum (negative) value, which means that all the silanol groups on the surface are fully deprotonated and exert the maximum charge. As plotted in region IV of Figure 1.8(b), $\left[\mathrm{Na}^+\right]_0$ is constant above pH 11. Although more NaOH is added into the solution, the surfaces of the silanol-terminated silica nanoparticles do not accept more sodium cations. Instead, more sensitive changes of $\left[\mathrm{H}^+\right]_0$ and $\left[\mathrm{OH}^-\right]_0$ are the source of the surface buffer capacity of this sodium ion.

Surface charge density of L-lysine-covered silica nanoparticles: In Figure 1.7(a), the surface charge density of the *L*-lysine-covered silica nanoparticles is weakly positive between pH 2 to 5. This is because the surface contains more $\alpha\text{-NH}_3^+$ than $\alpha\text{-COO}^-$ in this acidic environment. Thus, this weakly positive surface charge slightly repels protons and attracts more chloride anions and hydroxide ions near the surface. As seen in region I of Figure 1.8(c), compared to the bulk ionic concentration distributions in Figure 1.8(a), a shift of $\left[\mathrm{H}^+\right]_0$ to a lower concentration and shifts of $\left[\mathrm{Cl}^-\right]_0$ and $\left[\mathrm{OH}^-\right]_0$ to higher concentrations support these ion redistributions. Figure

1.7(b) shows that the surfaces of the *L*-lysine-covered silica nanoparticles undergo a charge inversion from slightly positive to very weakly negative between pH 5 and 6. This indicates that the number of $\alpha\text{-COO}^{-}$ starts slightly exceeding that of $\alpha\text{-NH}_3^+$ in this pH range. However, the overall numbers of both are almost equal. As seen in region II of Figure 1.8(c), both $\left[\text{H}^+\right]_0$ and $\left[\text{OH}^-\right]_0$ are almost constant, even when their bulk concentrations $\left[\text{H}^+\right]_\infty$ and $\left[\text{OH}^-\right]_\infty$, change by two orders of magnitude. Instead, $\left[\text{Cl}^-\right]_0$ changes rapidly, contributing to the buffer capacity for $\left[\text{H}^+\right]_0$ and $\left[\text{OH}^-\right]_0$ near the surface in region II. This indicates that both $\alpha\text{-NH}_3^+$ and $\alpha\text{-COO}^{-}$ on the surface of the *L*-lysine-covered silica nanoparticles are fully ionized and do not accept or lose more protons in this pH range. Incorporation of further NaOH into the solution causes an increase in the negative surface charge density of the *L*-lysine surface above pH 7, as depicted in Figure 1.7(b). At pH 10, as seen in Figure 1.7(a), the surface charge density shows a drastic negative increase. This implies that the $\alpha\text{-NH}_3^+$ starts becoming deprotonated, transitions to $\alpha\text{-NH}_2$, and loses charge in basic conditions, while the $\alpha\text{-COO}^{-}$ stays constant without gain or loss of single protons (this will be discussed further at the end of this sub-section). At high pH, the surface bears enough negative charge density to attract the cations of protons and sodium ions and to repel the hydroxide ion. This is supported by the shifts of both $\left[\text{H}^+\right]_0$ and $\left[\text{Na}^+\right]_0$ to higher concentrations and the shift of $\left[\text{OH}^-\right]_0$ to lower concentration as represented in region III of Figure 1.8(c), compared to the bulk ionic concentration in Figure 1.8(a). The deviations between the ionic concentrations on the surface and the bulk ionic concentrations become larger with an increase in pH.

Surface charge density of PAH/PS particles: As seen in Figure 1.7(a), the surface charge density of the PAH/PS particles is highly positive and constant between pH values of 2 to 3.5. This strongly charged positive surface attracts large amounts of both anionic species of chloride ions and hydroxide ions. Compared to the bulk ionic concentrations in Figure 1.8(a), large shifts of these two ionic concentrations are seen in region I of Figure 1.8(d). At pH 3.5, $\left[\mathrm{Cl}^-\right]_0$ and $\left[\mathrm{OH}^-\right]_0$ are 10^5 times higher than $\left[\mathrm{Cl}^-\right]_\infty$ and $\left[\mathrm{OH}^-\right]_\infty$, respectively. In addition, because this strong positive surface charge pushes the protons away from the surface, the magnitude of $\left[\mathrm{H}^+\right]_0$ is only 10^{-5} of that of $\left[\mathrm{H}^+\right]_\infty$ at the same pH. The plateau of the surface charge density between pH 2 and 3.5 in Figure 1.7(a) indicates that all the amine groups are fully ionized and do not undergo protonation or deprotonation regardless of pH change. In Figure 1.8(d), $\left[\mathrm{Cl}^-\right]_0$ is constant from pH 2 to 3.5, while $\left[\mathrm{H}^+\right]_\infty$ declines from 0.01 M to 3.16×10^{-4} M in the same pH range. Instead, the sensitive changes of $\left[\mathrm{H}^+\right]_0$ and $\left[\mathrm{OH}^-\right]_0$ with respect to changes in pH are the source of the buffer capacity of these chloride anions on the surface.

Returning to Figure 1.7(a), there is a drastic drop in the surface charge density from pH 3.5 to 7. This indicates that the NH_3^+ groups begin deprotonation along with a decrease in the concentration of $\left[\mathrm{H}^+\right]_0$ as described in region II of Figure 1.8(d). As seen in Figure 1.7(b), from pH 7 to 10.5, the surface charge density of the PAH/PS particles is very weakly positive and constant regardless of change in pH. In Figure 1.8(d) $\left[\mathrm{H}^+\right]_0$ and $\left[\mathrm{OH}^-\right]_0$ are also constant in this pH range due to the surface buffer capacity. Instead of changes in these concentrations on the surface, $\left[\mathrm{Na}^+\right]_0$ changes more sensitively to obey local charge balance near the surface in region

III of Figure 1.8(d). From Figure 1.7(b), at pH 10.5, the surface charge density further decreases and finally reaches a minimum value of 6.58×10^{-4} C/m^2 at pH 11.5. From pH 11.5 to 12, the surface charge density slightly increases to 2.20×10^{-3} C/m^2, and from region IV of Figure 1.8(d), the change in each ionic concentration on the surface follows that of the bulk ionic concentration. This is because the almost neutral surface does not effectively attract the counterions or repel the co-ions and is barely involved in charge regulation.

Surface potential of silanol-terminated silica nanoparticles: From Figure 1.7(c), the surface potential of the silanol-terminated silica nanoparticles from pH 2 to 4 is nearly zero because the surface charge density [see Figure 1.7(a)] in this pH range is also very close to zero; and because the high ionic strength of the solution screens the electric field between the silica nanoparticles, nullifying the surface potential. In the pH range from 4 to 7, the magnitude of this negative surface potential increases, even though the negative surface charge density is still extremely weak and constant. This is because the system contains much less ionic strength due to a lower concentration of pH-modifying salts. For an example of the system containing the silica nanoparticles at pH 7 without any additional salts, the Debye length is nearly 1 μm due to the very weak ionic strength of the solution, and the surface potential of this system is barely suppressed by electric field screening. Thus, the surface potential of the silica nanoparticles in the pH between 4 and 7 depends highly on the concentration of salts. Above pH 7, the strength of the surface potential keeps increasing, although a decrease in the ionic strength of the solution contributes to the shrinkage of the Debye length. More specifically, the surface potential from pH 7 to 9 is unexpectedly high, although the negative surface charge density in this pH range is still low. This is because the ionic concentration to screen the electric field between the silica nanoparticles is low in this pH range. From pH 9 to 11, the surface potential increases linearly compared to the large increase in surface charge density from 1.35×10^{-2} to 0.162 C/m^2. We can expect that in this pH range the increased concentration of ions causes effective electric field screening between the silica nanoparticles. At pH 11, the surface charge density does not increase any further because all the silanol groups are fully deprotonated. Above pH 11, the surface potential starts decreasing within the narrowed Debye length from 9.6 nm at pH 11 to 3.0 nm at pH 12 due to the high concentration of salts.

Surface potential of L-lysine-covered silica nanoparticles: As depicted in Figure 1.7(c), the positive surface potential of the *L*-lysine-covered silica nanoparticles decreases from pH 2 to 5.5 and reaches zero at pH 5.5. This is because more α-carboxyl groups of the *L*-lysine shell become deprotonated with an increase in pH. There is a surface potential inversion from slightly positive to negative near pH 5.5, and a subsequent drastic increase of the negative surface potential from pH 5.5 to 7, while the surface charge density of the *L*-lysine-covered silica nanoparticles in Figure 1.7(a) is constant in this same pH range. Above pH 7, the $\alpha\text{-NH}_3^+$ groups start becoming deprotonated with an increase in pH, and the surface exhibits stronger negative charge. This mainly contributes to the increasing negative trend of the surface potential of the *L*-lysine-covered silica nanoparticles above pH 7, especially the shallower slope of the surface potential profile above pH 11 that is mainly caused by the strong ionic strength of the solution.

Surface potential of PAH/PS particles: The strong positive surface charge of PAH/PS particles contributes to their high surface potential value between pH 2 and 4 as plotted in Figure 1.7(c). Because the ionic strength of the solution is reduced to 1/100 from pH 2 to 4, the electric field reaches further with much less attenuation between the PAH/PS particles. As a result, the surface potential increases and reaches its maximum value at pH 4. The positive surface potential decreases with an increase in pH from 4 to 7 mainly because of a sharp drop of the surface charge density. From pH 7 to 10, although the surface charge density is constant, the surface potential keeps decreasing due to an increase in the ionic strength of the solution. Above pH 11, the surface potential approaches zero because the surface charge is also zero. The trend of the computed surface potential profile for each colloidal system with a variation of pH in Figure 1.7(c) is the same as that of our experimentally measured zeta potential profile of each sample in Figure 1.9. Because the ζ-potential should be proportional to the surface potential, this comparison between the computed surface potential profiles and experimentally measured ζ-potential plots validates our nonlinear charge regulation relation between surface charge density and surface potential.

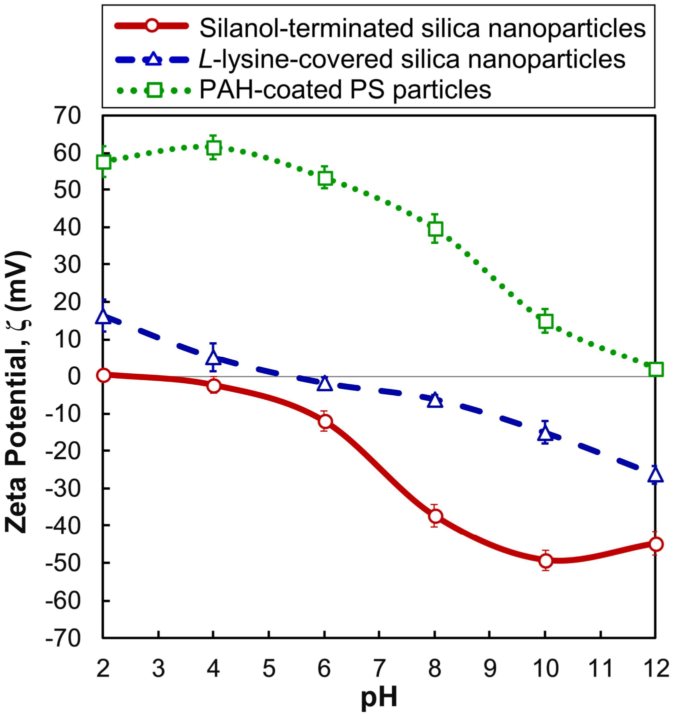

Figure 1.9. Zeta potential profiles as a change of pH for silanol-terminated silica nanoparticles, *L*-lysine-covered silica nanoparticles, and PAH/PS particles.

For purposes of verification of the empirically measured ζ-potential profiles, we measured the distributions of the hydrodynamic sizes for each sample in the same pH range, plotted in Figure

1.10. In Figure 1.10(a), the bimodal size distributions for pH 2 and 4 indicate that the silanol-terminated silica nanoparticles are aggregated because of the weak zeta potential values of 0.4 mV at pH 2 and -2.4 mV at pH 4. Although the zeta potential value of -12 mV at pH 6 is considered too low to maintain colloidal stability for an extended period, the hydrodynamic size distribution at pH 6 shows a good stability because of a high surface potential value of -123 mV from Figure 1.7(c). Even and sharp distributions are seen for pH 8, 10, and 12, thus these systems show excellent stabilities with high ζ-potential values of -59.8, -62.5, and -64.2 mV, respectively. Figure 1.10(b) shows that the *L*-lysine-covered silica nanoparticle systems show good stabilities at pH 2, 8, 10, and 12, while those at pH 4 and 6 have poor colloidal stabilities. For the PAH/PS particle systems, plotted in Figure 1.10(c), the sharp and narrow peaks of the hydrodynamic distributions at pH 2, 4, 6, and 8 indicate their excellent colloidal stabilities, and the strong ζ-potential values at the same pH values in Figure 1.9 support these results. In contrast, one can see the broadened and scattered size distributions at pH 10 and 12. These poor colloidal stabilities are confirmed by the low ζ-potential values of 2.0 mV at pH 10 and 14.0 mV at pH 12. Even though these PAH/PS particles are supposed to exert an additional steric repulsive force, which increases their stability further, the strength of this force vanishes with their zero surface charge densities at this pH range. Thus, experimental ζ-potentials and the hydrodynamic size distributions for all the systems match each other very well and it is appropriate to develop our model further with the computed data of the surface charge density and the surface potential.

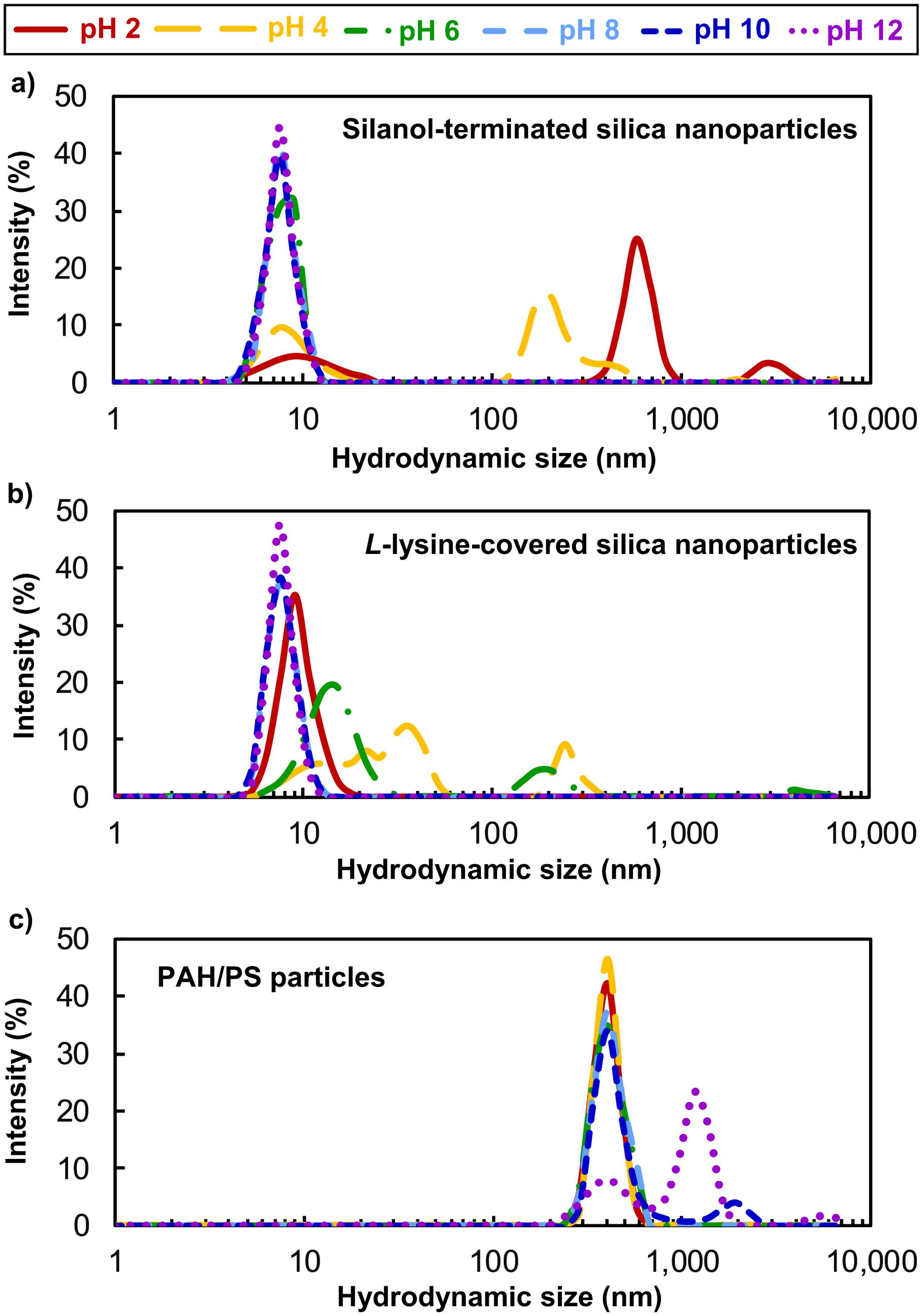

Figure 1.10. Distributions of hydrodynamic sizes of (a) silanol-terminated silica nanoparticles, (b) *L*-lysine-covered silica nanoparticles, and (c) PAH/PS particles measured at pH 2, 4, 6, 8, 10, and 12.

For each of the three colloidal systems, Figure 1.7(d) shows the relationship between the surface charge density and the surface potential. Since these results are based on the nonlinear Poisson-Boltzmann equation with Grahame equation, the profiles generally behave non-linearly and we can specify the surface charge density-surface potential relation as linear or nonlinear depending on the pH and the functional groups on the colloidal surface. First, the σ and ψ_o profile of the silanol-terminated silica nanoparticles is linear from pH 2 to 7 and nonlinear from pH 7 to 12. Second, the profile of the *L*-lysine-covered silica nanoparticles with the amphoteric surface of amine groups and carboxyl groups shows a nonlinear relation from pH 2 to 4, a linear relation from pH 4 to 9, and a nonlinear relation from pH 9 to 12. Third, the profile of the amine-functionalized PAH/PS particles exhibit a nonlinear relation from pH 2 to 7, which becomes linear between pH 7 to 12. For monovalent 1:1 electrolyte systems, such as the ones described in this work, for pH ranges where the σ and ψ_o profiles behave linearly, the colloidal systems have a constant surface charge density and show a drastic change in the surface potential. When the behavior of σ and ψ_o is nonlinear, the surface potential changes along pH less sensitively than the surface charge density.

In order to show that the ionizable surfaces of the colloids are regulated by the ionic concentrations based on the nonlinear Poisson-Boltzmann equation, here we compare the pH-dependent ionization behavior of the functional groups of free molecules and that of the surfaces on each particle. The fractional composition distribution of each functional group in both cases is plotted as a variation of pH in Figure 1.11. The procedures and equations to plot the fractional composition profiles in Figure 1.11 are described in detail from Equations (A4) to (A21) in Appendix A. Figure 1.11(a), (c), and (e) are the fractional composition profiles of silanol molecules, *L*-lysine molecules, and amine groups on the side chain of PAH, respectively. Figure

1.11(b) shows the fractional composition distributions of silanol surface groups, (d) depicts those of α-carboxyl groups and α-amine groups on the surface of the *L*-lysine, and (f) represents those of amine groups of PAH chains attached on PS particles. Comparing Figure 1.11(a) and (b), it is noted that the pH range where the ionization of the silanol surface group occurs experiences a shift to the right *(i.e.*, higher pH). From Figure 1.11(c) and (d), we see that the ionizable pH range of the α-carboxyl group of the *L*-lysine layer undergoes a positive shift, whereas the pH range for ionization of the α-amine group of the *L*-lysine shows a negative shift. Comparison of Figure 1.11(e) and (f) indicates that the pH range of the ionization of the amine group of PAH shows a negative shift. From this analysis, it is obvious that the pH-dependent ionization tendency of the functional groups on the colloidal surfaces is very different from the functional groups of the free molecules. This is because the ionizations of functional groups of free molecules, compared to those on colloidal surfaces, are regulated by different concentrations of ions even at the same pH of the system. As discussed before, the ionic concentration at a distance away from the surface is governed by Boltzmann's equation [Equation (1.5)]. On the other hand, the ionizable free molecules are controlled by the bulk ionic concentration. From the analysis of the plots in Figure 1.11, we can generalize the trends of the shifts of the fractional composition distribution of ions with pH. When the functional groups undergo ionization on the surface, the negatively ionizable functional group on the surface become negatively charged at higher pH, compared to that in the free molecules. In contrast, the positively ionizable functional groups on the surface become positively charged at lower pH, compared to the free molecules. Since these shifts are primarily caused by the difference in proton concentration at the particle surface and far away from the particle, these results support our nonlinear charge regulation model governed by pH and total salt concentration of the solution.

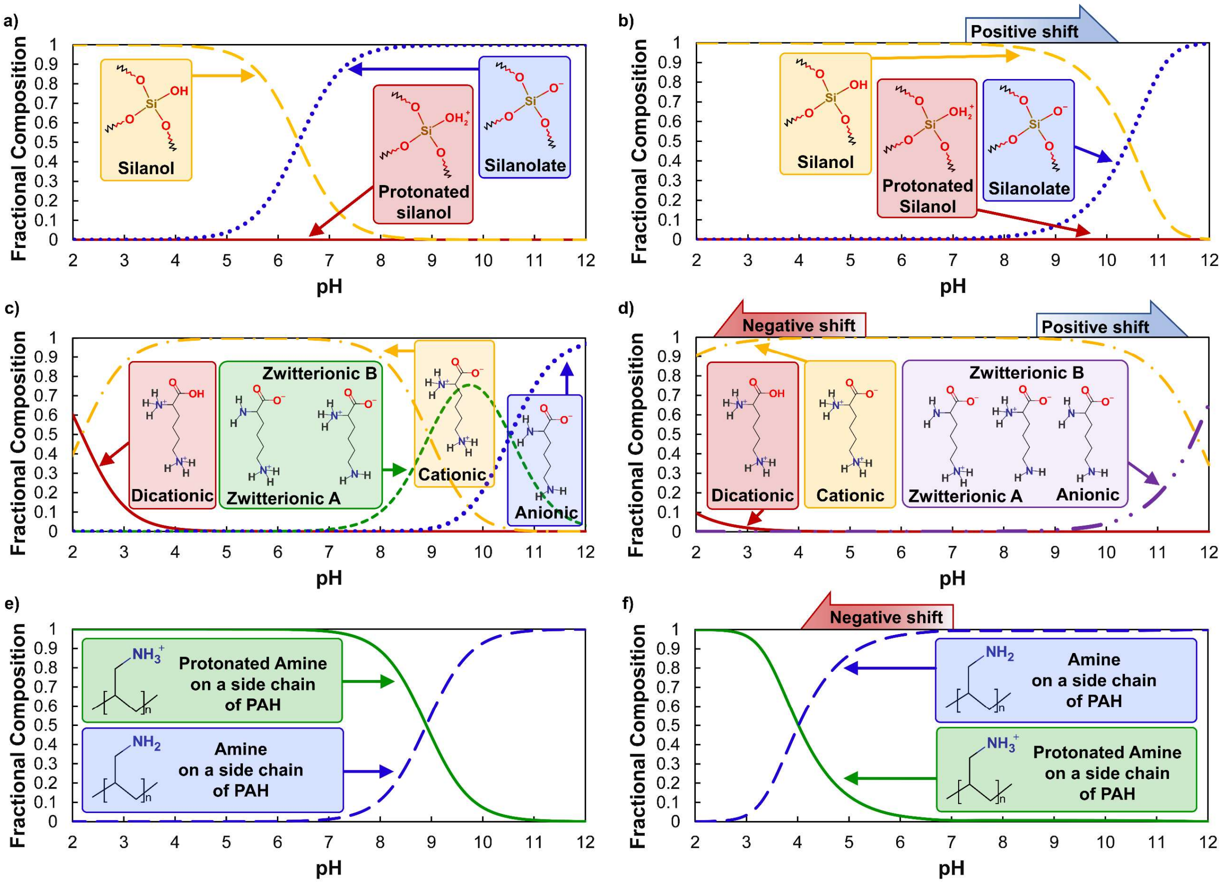

Figure 1.11. Fractional composition distributions of (a) silanol groups of free molecules, (b) silanol groups on the surface of silica nanoparticles, (c) free *L*-lysine molecules, (d) *L*-lysine layer on the silica nanoparticles, (e) amine groups of free PAH chains, and (f) amine groups of PAH coated on PS particles. The negatively chargeable functional groups show positive shift, and the positively ionizable functional groups undergo negative shift.

1.5.3. Regulation parameter under nonlinear charge regulation relation

As discussed in section 3, to define the regulation parameter under nonlinear charge regulation for each material, the diffuse layer potential at the outer Helmholtz plane should be determined [101,102]. Figure 1.12(a) illustrates how the dominant ionic species, Na$^+$ and OH$^-$, are distributed away from the isolated silanol-terminated silica nanoparticles at pH 12. Figure 1.12(b) depicts the EDL structure at pH 12 in terms of the potential profile and the dominant counterion (Na$^+$) concentration profile away from the surface of the silanol-terminated silica nanoparticles. The potential profile is plotted by using Equation (1.39) with the computed values of $\psi_{o,silica}$ from the data of Figure 1.7(c) and κ from Equation (1.40). The counterion (Na^+) concentration distribution is created by using the Boltzmann equation [Equation (1.5)]. The designated inner Helmholtz plane (0.134 nm), outer Helmholtz plane (0.560 nm), and Debye length (3.05 nm) are theoretically determined, and the shear plane (2.58 nm) is determined from the empirically measured ζ-potential value (Figure 1.9). From Figure 1.12(b), the potential distribution of a charged silica nanoparticle in a solution with high salt concentration tends to drop drastically within 1 nm from its surface due to a thin Debye length caused by high ionic strength. Because this case indicates that even a 0.1 nm difference in the outer Helmholtz plane location results in a large deviation in the diffuse layer potential, the accurately determined outer Helmholtz plane location for every case guarantees a reliable regulation parameter value.

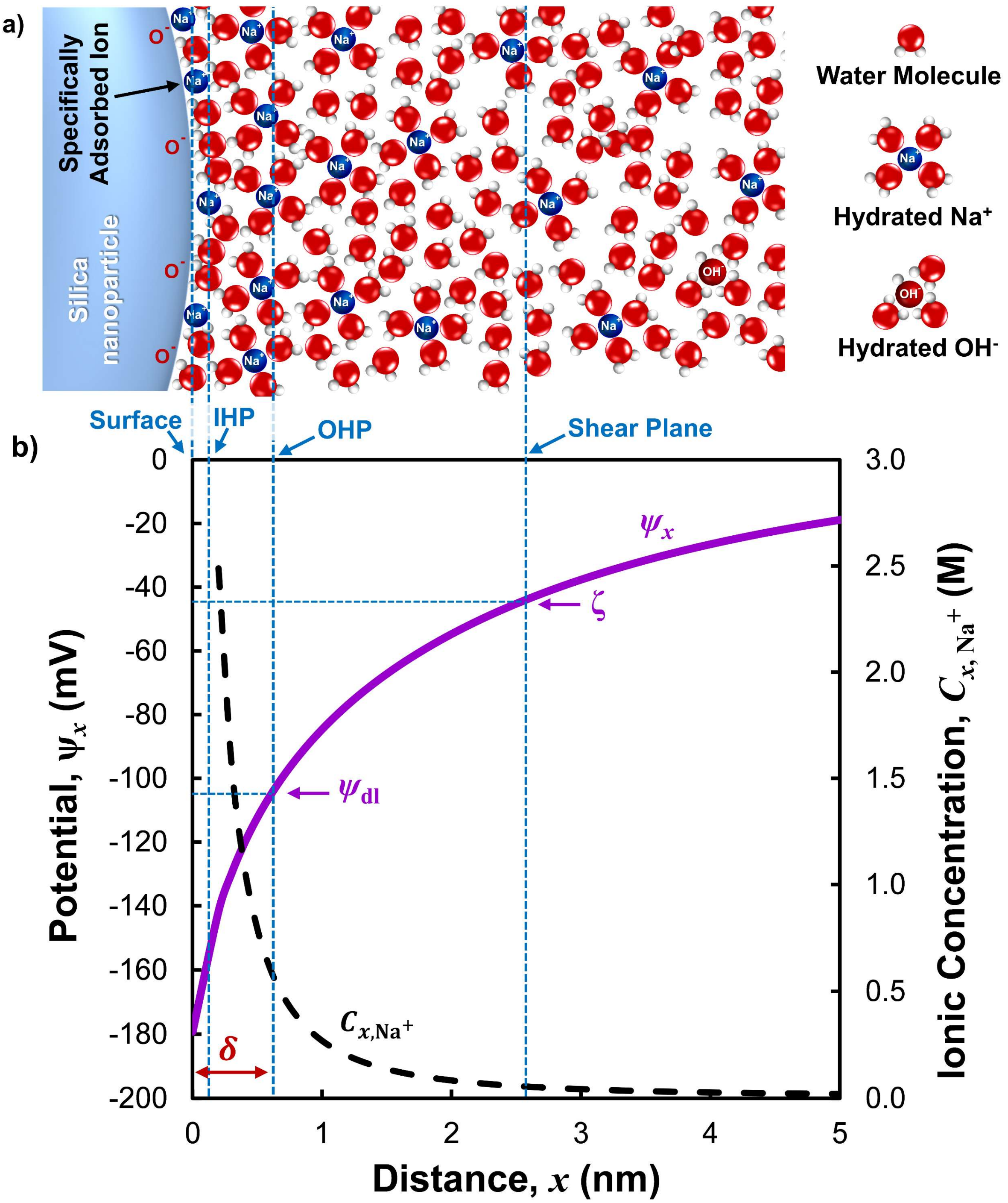

Figure 1.12. (a) An illustration of the electrical double layer structure of a silanol-terminated silica nanoparticle aqueous solution at pH 12 based on (b) a potential profile and a dominant counterion (sodium cation) concentration distribution as function of distance from the surface of the silica nanoparticles.

As depicted in Figure 1.12(b), the position of the outer Helmholtz plane is a sum of the diameter of the water molecule layer and the radius of the hydrated counterion [Equation (1.40)]. The dominant counterions near the surfaces of the silanol-terminated silica nanoparticles, the *L*-lysine-covered silica nanoparticles, and the PAH/PS particles at pH 2, 4, 6, 8, 10, and 12 are determined from Figure 1.8(b), (c), and (d), respectively. These dominant counterions and the outer Helmholtz plane locations are summarized in Table 1.5. The outer Helmholtz plane locations are used to calculate the diffuse layer potentials to obtain the regulation parameters. For pH 2, 4, 6, 8, 10, and 12, the potential distributions of the isolated silanol-terminated silica nanoparticles is provided in Figure 1.13(a)-(c), the *L*-lysine-covered silica nanoparticles in Figure 1.13(f)-(g), and the PAH/PS particles in Figure 1.13(d)-(e). When it comes to the ionic concentration distributions as a function of the distance away from the surface, we provide only the case of the silanol-terminated silica nanoparticles at each pH as shown in Figure 1.14.

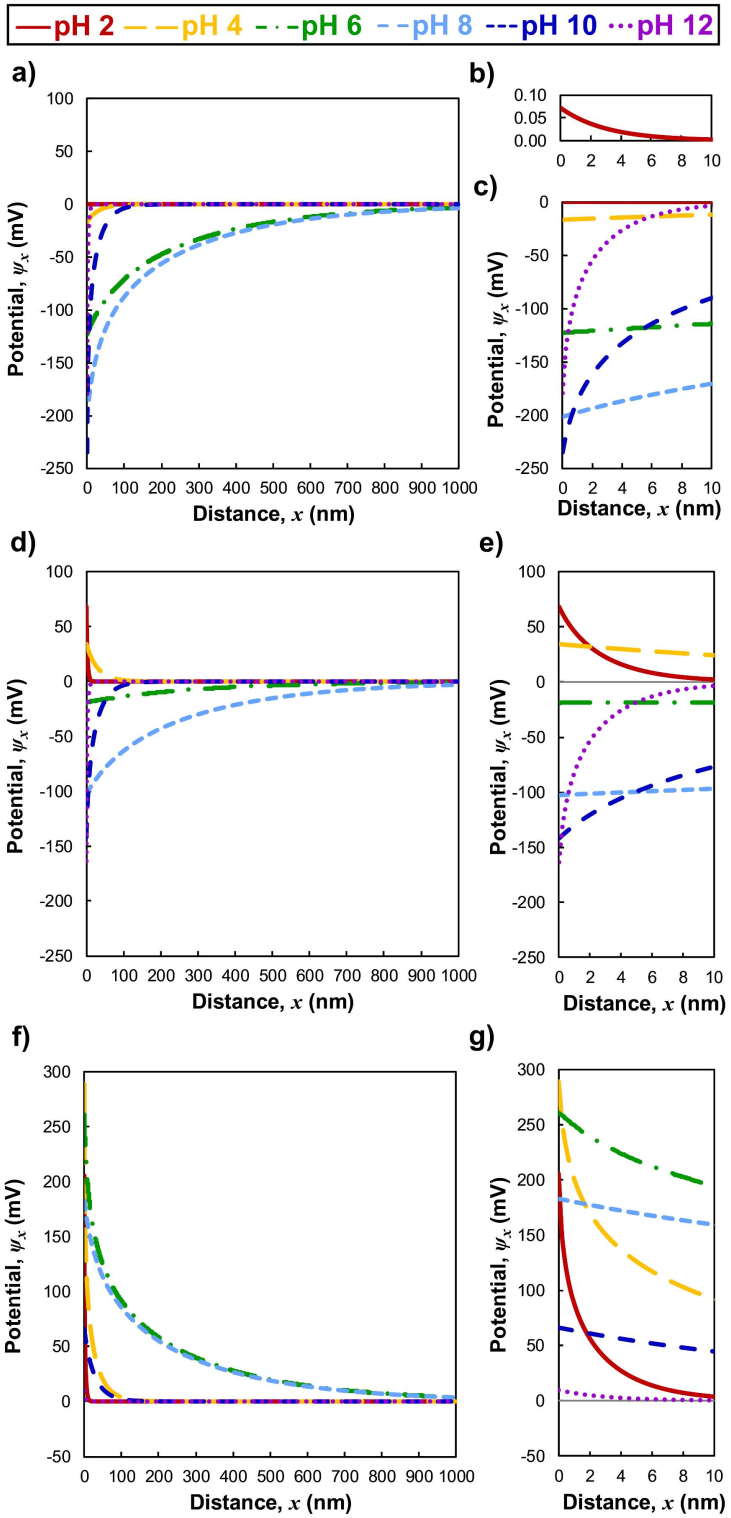

Figure 1.13. (a) Potential profiles of silanol-terminated silica nanoparticles at a distance from 0 to 1000 nm, (b) and (c) at a distance from 0 to 10 nm, (d) potential profiles of *L*-lysine-covered silica nanoparticles at a distance from 0 to 1000 nm, (e) at a distance from 0 to 10 nm, (f) potential profiles of PAH/PS particles at a distance from 0 to 1000 nm, and (g) at a distance from 0 to 10 nm.

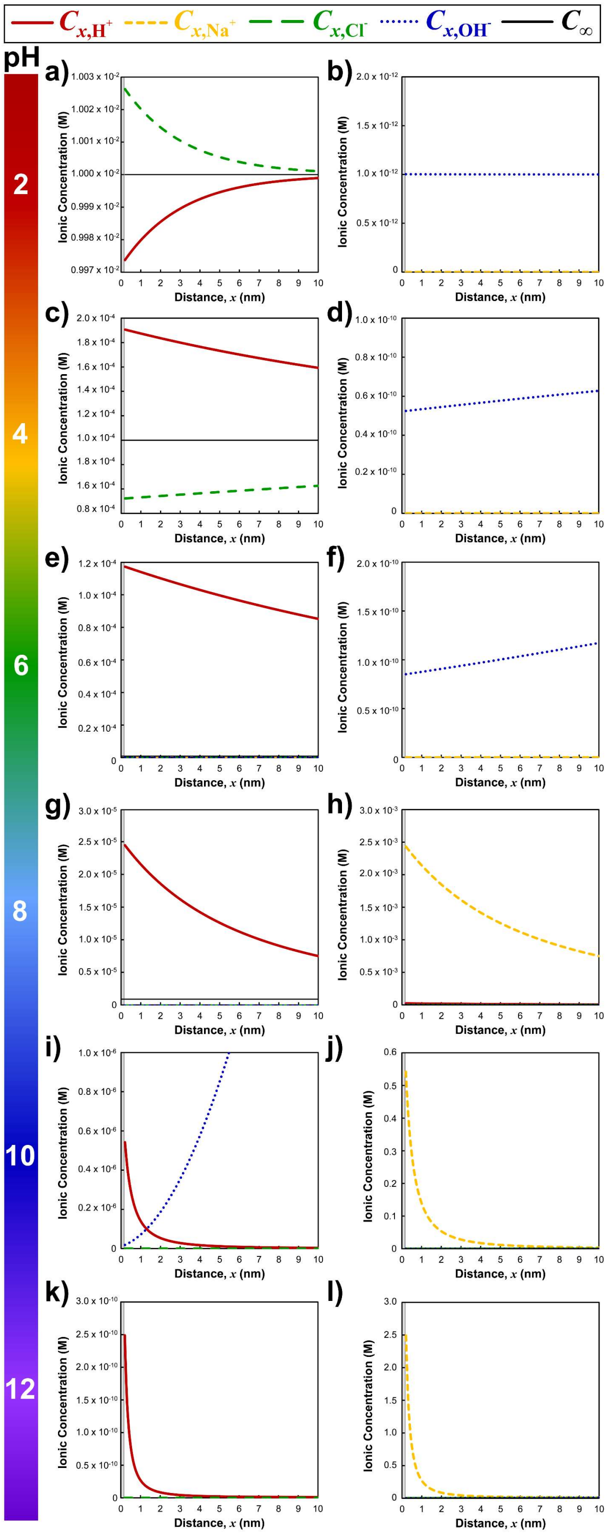

Figure 1.14. Concentration profiles of H$^+$, Na$^+$, Cl$^-$, OH$^-$, and bulk electrolyte for silanol-terminated silica nanoparticles (a), (b) at pH 2, (c), (d) at pH 4, (e), (f) at pH 6, (g), (h) at pH 8, (i), (j) at pH 12, (k), and (l) at pH 12.

The nonlinear relation between the surface charge density and the surface potential in Figure 1.7(d) is valid for isolated surfaces such as in an extremely dilute solution. This limited charge regulation model only considers pH and total salt concentration. In real situations, the separation distance between immersed surfaces varies by interparticle interactions and Brownian motion. This indicates that the charge regulation model, which only considers pH and total salt concentration, fails to describe the realistic behaviors of the surface charge density and the surface potential of the approaching particles. When the separation distance decreases, the modified electric field triggers redistribution of ionic concentration near surfaces to obey the local charge neutrality between the surfaces. These repositioned ions force the changes in acid-base equilibrium of the surface functional groups, and this protonation or deprotonation causes a change in surface charge density as well as potential profile, including surface potential. This changed potential profile between the particles directly alters the electric field between them. As a result, the sum of the force from this modified electric field and vdW force primarily determines the next movements of the two colloidal particles. The cycle of these consecutive events occurs continuously until the system reaches thermodynamic equilibrium. Thus, if we can mathematically explain how both surface charge density and surface potential of the approaching particles behave, we will more accurately predict the behaviors of most practical colloidal particles of both symmetric and asymmetric systems.

A regulation parameter is a key tool to describe how both the surface charge and the surface potential change upon approach of the two surfaces [21, 22]. Figure 1.15(a) presents the variation of regulation parameter profiles obtained from Equations (1.35), (1.36), (1.41), (1.42), and (1.43). When the system has a p_i value of unity, the surface charge density of the particle surface is constant regardless of the redistribution of charges when the two particles are moving closer to each other. In contrast, the surface potential is constant for a p_i value of zero. However, the system with $p_i = 1$ or 0 is unrealistic because the redistribution of ions must occur for particles that are approaching. In most realistic situations, the surface charge density and the surface potential are not constant when the separation distance approaches zero. Thus, the regulation parameter value should be between 1 and 0. We discuss how p_i changes for each symmetric system with respect to pH and generalize this phenomenon.

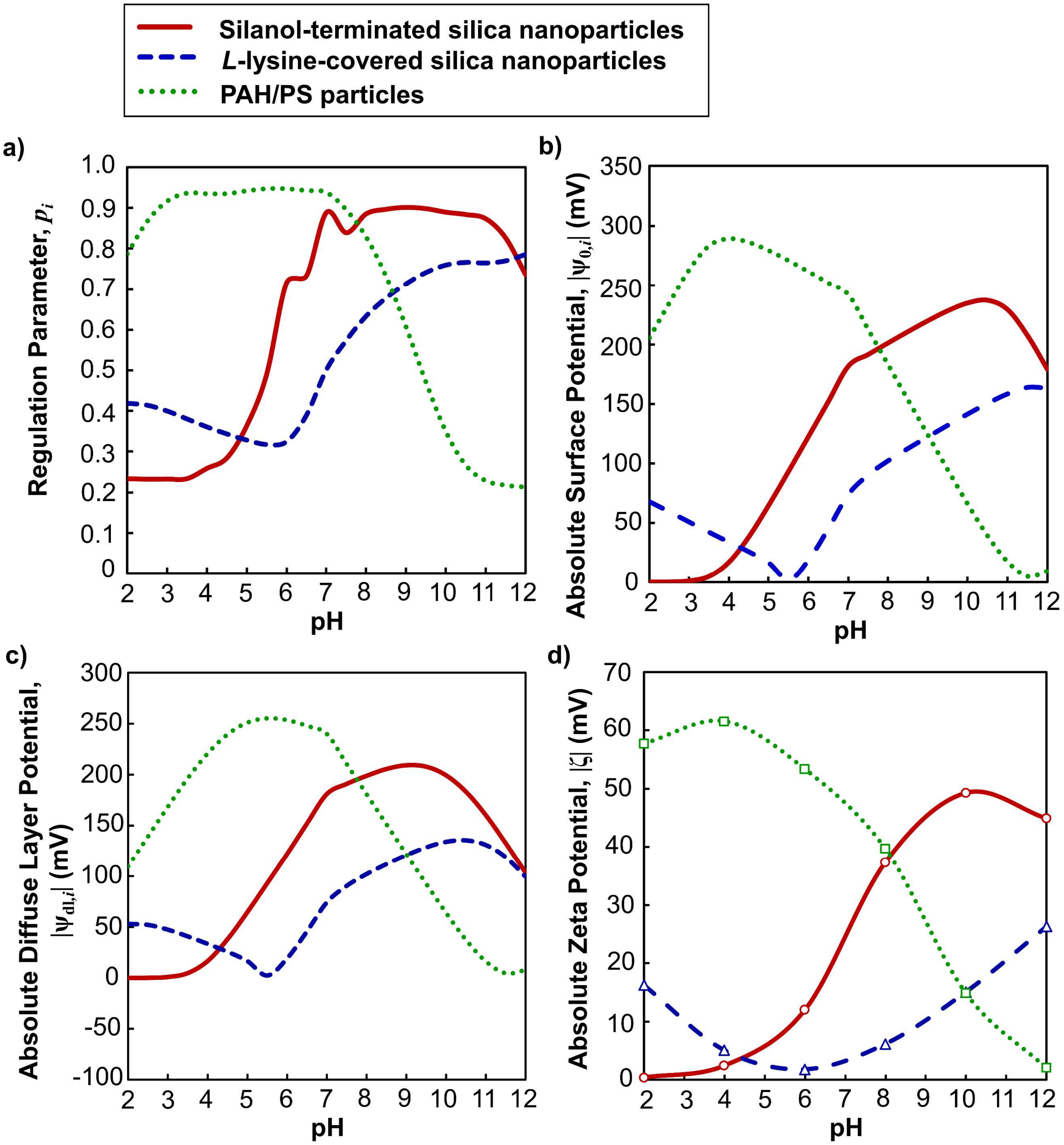

Figure 1.15. (a) Regulation parameter, (b) absolute surface potential, (c) absolute diffuse layer potential, and (d) absolute ζ-potential profiles (based on measurements) for the silanol-terminated silica nanoparticles, *L*-lysine-covered silica nanoparticles, and PAH/PS particles with respect to changes in pH.

The behavior of the regulation parameter in the silanol-terminated silica nanoparticles is categorized into four regions along pH, from 2 to 4, 4 to 7, 7 to 11, and 11 to 12. These pH ranges are the same as we defined for ionic concentration profiles in Figure 1.8(b). In the pH range from 2 and 4, $p_i = 0.22$ at a surface charge density of 0 [see Figure 1.7(a)]. In the pH range from 4 to 7 where both surface charge density and ionic strength are weak, p_i drastically increases with an increase in pH and reaches a value of 0.86 at pH 7. From pH 7 to 11, both surface charge density and surface potential become stronger with constant p_i of 0.86. This shows that the surface charge density changes minimally for the particles upon approach in this pH range. Above pH 11, p_i decreases and reaches 0.74 at pH 12. This reduction in the value of p_i indicates that the surface charge density becomes more sensitive to the redistributed charges when the two silanol-terminated silica nanoparticles come closer.

The regulation parameter behavior of the *L*-lysine silica nanoparticles is divided into three pH ranges, 2 to 6, 6 to 10, and 10 to 12. These pH ranges differ from those designated (pH 2 to 5, 5 to 7, and 7 to 12) in Figure 1.8(c). This difference is discussed later. At pH values from 2 to 6, p_i decreases as the surface charge density decreases from a positive value to zero [see Figure 1.7(a)]. At pH values from 6 to 10, p_i increases as the negative surface charge density becomes stronger. Above pH 10, p_i stays constant at a value of 0.75.

The slope of the regulation parameter of PAH/PS particles varies at four different pH ranges, 2 to 3, 3 to 7, 7 to 11, and 11 to 12. In the pH range of 2 and 3 where the high surface charge density value is constant at high ionic strength, p_i increases from 0.8 to 0.92. In this range, the strong surface charge density is constant for the approaching particles. In the pH range from 3 to 7, the constant p_i indicates that the surface charge density of the PAH/PS particles changes minimally when the separation distance approaches zero. There is a significant drop of the p_i value from pH 7 to 11 as the surface charge density becomes nearly zero [see Figure 1.7(a)]. From pH 11 to 12, the constant p_i at 0.2 and the nearly zero surface charge density indicate that the surface potential undergoes small changes and the surface charge density is constant near zero for the approaching PAH/PS particles.

In order to justify that the computed p_i values generalize the EDL interaction energy and force for both symmetric and asymmetric colloidal systems, the regulation parameters for all the symmetric cases must be governed by the nonlinear relation between the surface charge density and the surface potential. The pH range of each regulation parameter of the silanol-terminated silica nanoparticles and the PAH/PS particles is divided the same as the pH ranges we defined for the surface charge density [Figure 1.7(a)], the surface potential [Figure 1.7(c)], and the ionic concentration on the surface [Figure 1.8(b) and (d)]. However, the pH ranges for the regulation parameter of the *L*-lysine-covered silica nanoparticles are 2 to 6, 7 to 10 and 10 to 12, which are different from the pH ranges of 2 to 5, 5 to 7 and 7 to 12 of the surface charge density [Figure 1.7(a)], the surface potential [Figure 1.7(c)], and the ionic concentration on the surface [Figure 1.8(c)]. With a premise that the regulation parameter cannot be negative, the trends of the regulation parameter behaviors [Figure 1.15(a)] are similar to the absolute values of the computed surface potential profiles [Figure 1.15(b)], the absolute values of the calculated diffuse layer potential [Figure 1.15(c)], and the absolute values of empirically measured zeta potentials [Figure 1.15(d)] for all three symmetric surfaces. This is solid evidence to theoretically and experimentally support the validation of this regulation parameter. The absolute surface potential profiles in Figure 1.15(b) are determined by taking absolute values of the surface potential data from Figure 1.7(c). The absolute potential diagrams in Figure 1.15(c) are calculated by taking absolute values of the computed potential [Equation (1.39)] at the outer Helmholtz plane determined in Table 1.5. Taking absolute values of the experimentally measured ζ-potential values in Figure 1.9 gives the absolute ζ-potential distributions in Figure 1.15(d).

From this analysis, we can conclude the following three general assessments. First, for the particles consisting of a single type of ionizable functional group on the surface, the trend of the regulation parameter with variation of pH follows both the absolute values of the theoretically computed surface potentials and those of empirically measured ζ-potentials. Thus, without regulation parameter information, the charge regulation behavior of the particles upon approach is roughly expected from either surface potential or ζ-potential values. Second, the comparisons of surface charge density [Figure 1.7(a)], ionic concentration on the surface [Figure 1.8(b), (c), and (d)], and regulation parameters [Figure 1.15(a)], reveals the following correlations. As ionic strength increases, p_i decreases. As surface charge density increases, p_i increases. When both ionic strength and surface charge density increase, p_i is constant regardless of change in pH. Third, from the case of *L*-lysine, which has an amphoteric surface having two different charges, we can flexibly design the surface of particles, which is characterized by a specific charge regulation behavior. This can be achieved by a combination of two or more different types of functional groups on the surface of the particles.

1.5.4. Pairwise DLVO interaction forces

Figures 1.16(a)-(f) illustrate SEM images of the morphology of the deposited silanol-terminated silica nanoparticles on the PAH/PS particles with respect to pH. The morphology of these inorganic-organic composite particles are characterized by coverage of the silanol-terminated silica nanoparticles on PAH/PS particles and the presence of homoaggregation (aggregation with the same types of colloids) of the silanol-terminated silica nanoparticles. As seen in Figures 1.16(a)-(f), the degree of coverage increases from the extreme pH (2 and 12) to neutral pH, and the homoaggregation of the silanol-terminated silica nanoparticles is observed at pH 2 and 4. The combination of these two phenomena determines their morphologies, namely homoaggregated silanol-terminated silica nanoparticles at pH 2 and 4, homoagglomerated (agglomeration with the same types of colloids) silanol-terminated silica nanoparticles at pH 6, densely-packed silanol-terminated silica nanoparticles at pH 8, and isolated silanol-terminated silica nanoparticles with small coverage at pH 10 and 12. Thus, to describe these two phenomena, namely the coverage and homoaggregation, we scrutinize the two different pairwise interactions: (i) an interaction between a silanol-terminated silica nanoparticle and a PAH/PS particle as depicted in Figure 1.16(g) and (ii) an interaction between two silanol-terminated silica nanoparticles as illustrated in Figure 1.16(k).

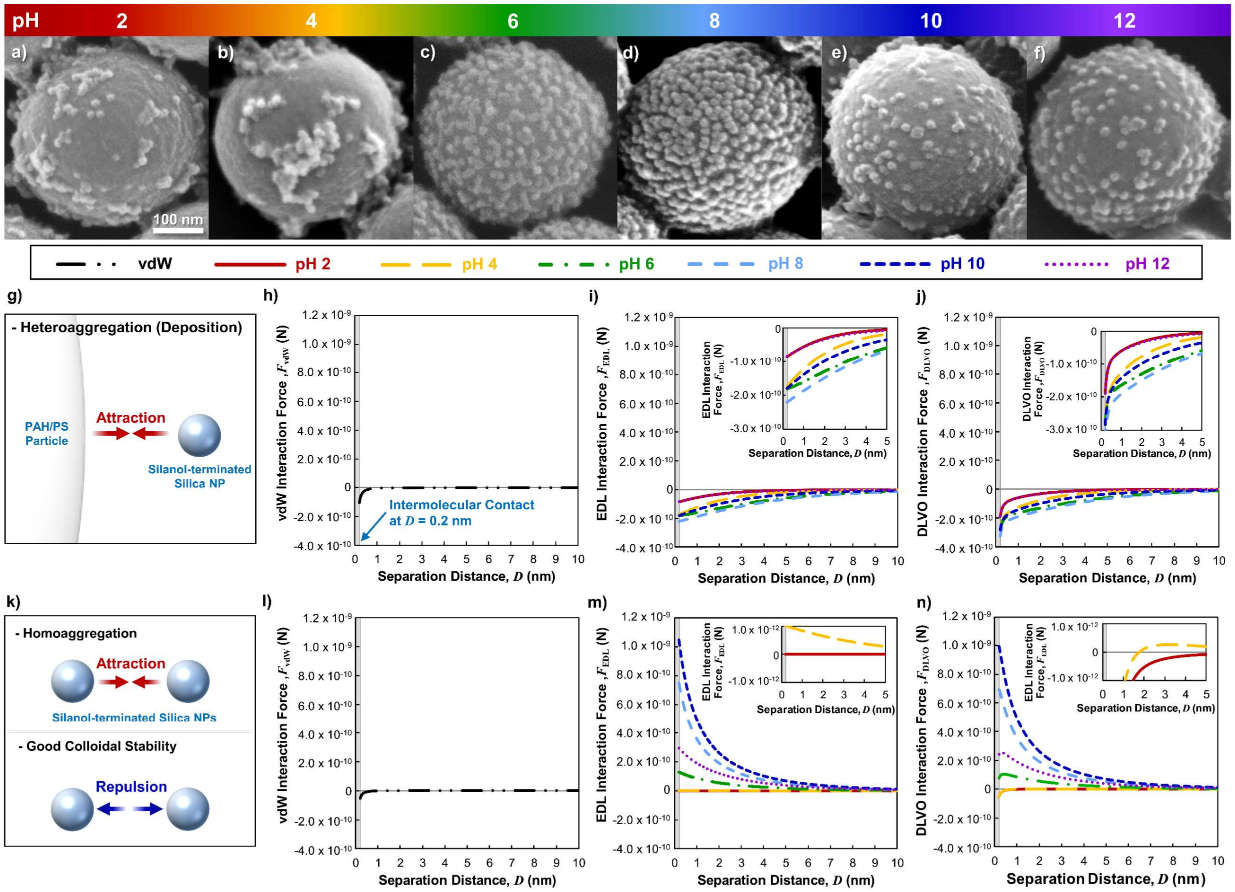

Figure 1.16. Scanning electron micrographs of silanol-terminated silica nanoparticles deposited on PAH/PS particles prepared at (a) pH 2, (b) pH 4, (c) pH 6, (d) pH 8, (e) pH 10, and (f) pH 12. (g) Scheme of interactions between a silanol-terminated silica nanoparticle and a PAH/PS particle. (h) Pairwise vdW interaction force profile, (i) pairwise EDL interaction force profile, and (j) pairwise DLVO interaction force profile for a silanol-terminated silica nanoparticle and a PAH/PS particle as a function of the separation distance with respect to pH. (k) Scheme of interactions between two silanol-terminated silica nanoparticles. (l) Pairwise vdW interaction force profile, (m) pairwise EDL interaction force profile, and (n) pairwise DLVO interaction force profile for two silanol-terminated silica nanoparticles as a function of the separation distance with respect to pH.

The degree of coverage is directly related to the heteroaggregation (aggregation with more than two different types of colloids) between silanol-terminated silica nanoparticles and PAH/PS particles. Thus, we investigate the pairwise DLVO interaction between these asymmetric particles to explain this phenomenon. Figure 1.16(h) shows the vdW interaction force profile [Equation (1.2)], Figure 1.16(i) presents the EDL interaction force profiles [Equation (1.49)] based on the regulation parameter we obtained earlier, and Figure 1.16(j) displays the DLVO interaction force [Equation (1.1)] profiles. As seen in Figure 1.16(h), the vdW force is constant regardless of the pH and the ionic strength of solution. Its attraction force becomes stronger at separation distances smaller than 0.5 nm, while it is very weak when that separation distance is greater. As plotted in Figure 1.16(i), the EDL interaction force between the silanol-terminated silica nanoparticle and the PAH/PS particle is attractive in the entire pH range because of their oppositely charged surfaces. Overall, the magnitude of the pairwise EDL attractive force between the asymmetric surfaces is the strongest at pH 6 and 8, medium at pH 4 and 10, and weakest at pH 2 and 12. For pH values between 6 and 8, these strongest attraction forces originate from the higher surface potentials of both silanol-terminated silica nanoparticles and PAH/PS, as shown in Figure 1.7(c). The next strong attraction forces at pH 4 and 10 are primarily determined by the weakest value of the regulation parameter of the silanol-terminated silica nanoparticle or the PAH/PS particle. For example, at pH 4 the regulation parameter of the silanol-terminated silica nanoparticles is 0.25 while that of the PAH/PS particles is 0.92. Moreover, at pH 10 the regulation parameter of the silanol-terminated silica nanoparticles is 0.88, but that of PAH/PS is 0.38. Likewise, the weakest attractive EDL forces seen at pH 2 and 12 are determined by the small regulation parameter value of the silanol-terminated silica nanoparticles at pH 2 ($p_i = 0.24$) and that of the PAH/PS particle at pH 12 ($p_i = 0.2$). From this analysis, we conclude that one surface having a smaller value of regulation parameter mainly limits the magnitude of the EDL interaction force. Figure 1.16(j) displays the DLVO interaction forces for these asymmetric surfaces. If one compares Figure 1.16(h), (i), and (j), the EDL attraction forces are dominant along the separation distance, while the relatively weak vdW force is only meaningful at the separation distance less than 0.5 nm. Thus, the EDL attraction force dominantly triggers the silanol-terminated silica nanoparticle and the

PAH/PS particle to approach each other. Once they are in intermolecular contact at D = 0.2 nm, this EDL interaction force mainly holds these two particles together. In addition to this, the vdW force contributes to holding the silanol-terminated silica nanoparticle on the PAH/PS particle more tightly. If we take a closer look at both Figures 1.16(a)-(f) and 10(j), the coverage trend of the silanol-terminated silica nanoparticles on the PAH/PS particle matches well as pH is varied. The degree of nanoparticle coverage is proportional to the magnitude of the attractive DLVO force. The strongest DLVO force profiles at pH 6 and 8 agree with the highest coverage of the silanol-terminated silica nanoparticles on the PAH/PS particle. The medium strength of the DLVO forces at pH 4 and 10 is correlated to the medium coverage of the nanoparticles. The weakest DLVO forces at pH 2 and 12 correspond with the lowest coverage of the silica nanoparticles. Thus, to increase the coverage of these silanol-terminated silica nanoparticles on the PAH/PS particles, we can increase the value of the regulation parameter.

The second factor that affects the morphology of these inorganic/organic nanocomposite particles is homoaggregation of the silanol-terminated silica nanoparticles. As illustrated in Figure 1.16(k), these particles undergo homoaggregation under attractive forces, while exhibiting good colloidal stability under repulsive force. This trend can be explained by the DLVO interaction force profiles for the two symmetric silanol-terminated silica nanoparticles. Figure 1.16(l) represents the vdW interaction force [Equation (1.2)], Figure 1.16(m) displays the EDL interaction force [Equation (1.49)], and Figure 1.16(n) shows the DLVO interaction force [Equation (1.1)] profiles. As seen in Figure 1.16(l), at intermolecular contact, the vdW force between the two silanol-terminated silica nanoparticles is also constant regardless of pH and ionic strength of the solution. Its magnitude is almost half of the vdW force between the silanol-terminated silica nanoparticles and the PAH/PS particle, compared with Figures 1.16(h) and (l). This attractive vdW force is only valid when the separation distance is less than 0.3 nm. This is mainly because higher numbers of atoms can be instantaneously polarized in the large PAH/PS particle and can exert London dispersion forces between the small nanoparticle and the large PAH/PS particle. Figure 1.16(m) shows that the EDL force for these symmetric surfaces increases in order from pH 2, 4, 6, 12, 8, and 10. This tendency agrees with the regulation parameter profile for the silanol-terminated silica nanoparticles as displayed in Figure 1.15(a). As discussed earlier, the surface charge density of the silanol-terminated silica nanoparticles increases as pH increases. The regulation parameter considers that the surface potential drops with respect to the ionic strength of the solution so that the surface at pH 12 shows attenuated repulsive force. As displayed in Figure 1.16(n), the overall DLVO interaction force profiles for this symmetric system with respect to pH are dominantly governed by the EDL interaction force profiles. In this case, the physically meaningful role of the vdW force is to offset the very weak repulsive EDL force at pH 2 and 4 and change it to an attractive force as confirmed in Figure 1.16(n). This result supports the homoaggregation of the silanol-terminated silica nanoparticles seen in the SEM images for pH 2 and 4 in Figures 1.16(a)-(f). If we look at the SEM image for pH 6, most silanol-terminated silica nanoparticles are partially in contact with each other although the DLVO profile for this pH shows repulsive force. This is because when more nanoparticles are attached to the other surface, the redistribution of ionic species occurs, resulting in changes of both surface charge density and surface potential. Thus, the actual strength of this repulsive force between the silica nanoparticles, which are attached on the PAH/PS particle, should be attenuated from the computed DLVO force. The total repulsive force at intermolecular contact for pH 6 is not strong enough to isolate all the attached silanol-terminated silica nanoparticles on the PAH/PS particle. The other DLVO profiles at pH 8, 10, and 12 show strong repulsive forces so that all the attached silanol-terminated silica nanoparticles on the

PAH/PS particles are likely to be isolated as confirmed in the SEM images for pH 8, 10, and 12 in Figures 1.16(a)-(f).

Figures 1.17(a)-(f) illustrate a series of SEM images showing the changes in the morphology of the deposited *L*-lysine-covered silica nanoparticles on the PAH/PS particle with respect to pH. As discussed earlier, the change in these morphologies can be explained by both the degree of the *L*-lysine-covered silica nanoparticle coverage on PAH/PS and the homoaggregation of the *L*-lysine-covered silica nanoparticles. As seen in Figures 1.17(a)-(b), the deposition of the *L*-lysine-covered silica nanoparticles does not occur at pH 2 and 4. According to the SEM images, the degree of coverage increases in order of 12, 6, 10, and 8. Weak homoaggregation of the *L*-lysine-covered silica nanoparticles creates clustering at pH 6 [Figure 1.17(c)] and bridging at pH 8 [Figure 1.17(d)]. These changes in morphology with pH are summarized in Table 1.7. We find that there is no *L*-lysine-covered silica nanoparticle deposition at pH 2 and 4, clustered *L*-lysine-covered silica nanoparticles at pH 6, densely-packed *L*-lysine-covered silica nanoparticles with slight homoagglomeration at pH 8, and isolated nanoparticles with smaller coverage at pH 10 and 12. In order to explain this change in morphology, we explore the two different pairwise interactions: (i) an interaction between an *L*-lysine-covered silica nanoparticle and a PAH/PS particle as depicted in Figure 1.17(g) and (ii) an interaction between two *L*-lysine-covered silica nanoparticles as illustrated in Figure 1.17(k).

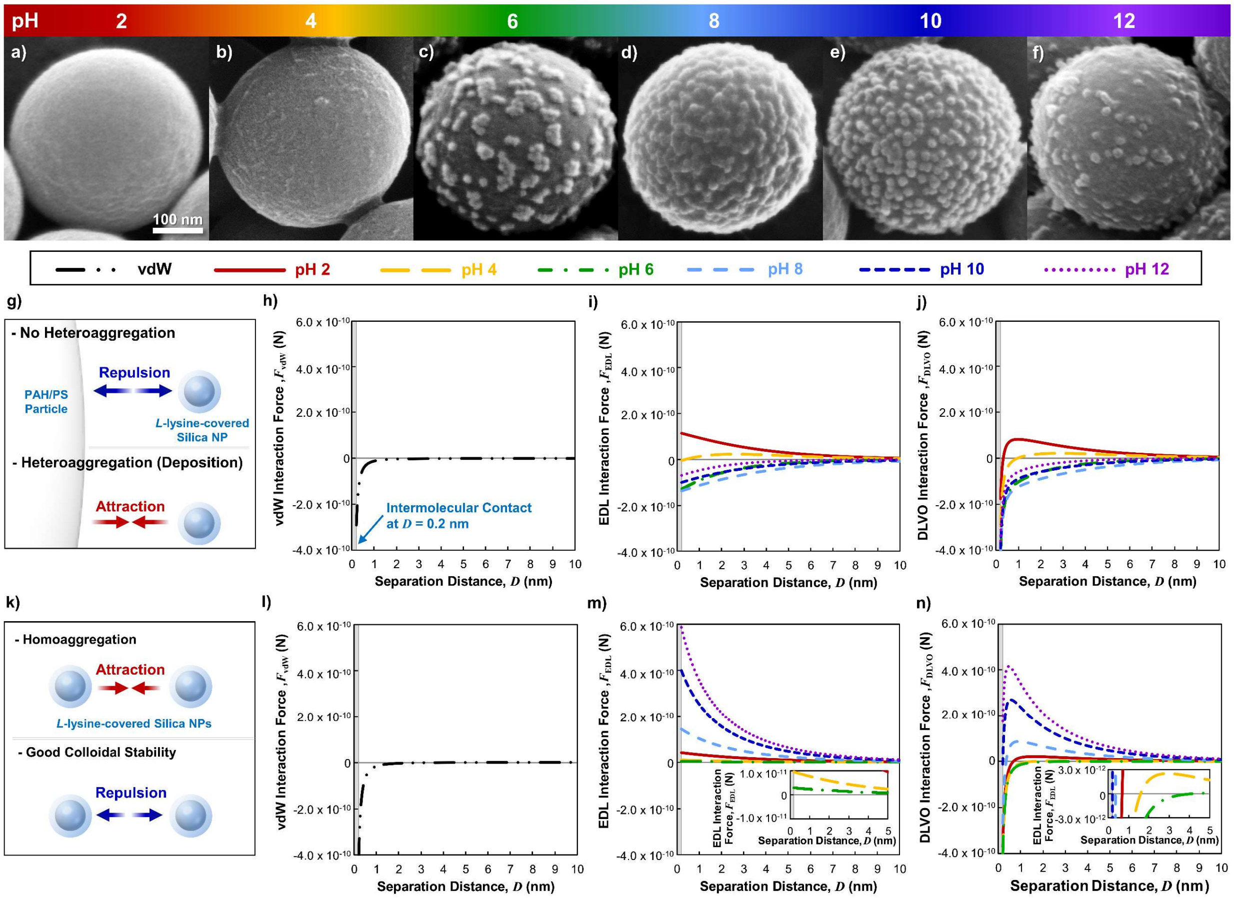

Figure 1.17. Scanning electron micrographs of *L*-lysine-covered silica nanoparticles deposited on PAH/PS particles prepared at (a) pH 2, (b) pH 4, (c) pH 6, (d) pH 8, (e) pH 10, and (f) pH 12. (g) Scheme of interactions between a *L*-lysine-covered silica nanoparticle and a PAH/PS particle. (h) Pairwise vdW interaction force profile, (i) pairwise EDL interaction force profile, and (j) pairwise DLVO interaction force profile for an *L*-lysine-covered silica nanoparticle and a PAH/PS particle as a function of the separation distance with respect to pH. (k) Scheme of interactions between two *L*-lysine-covered silica nanoparticles. (l) Pairwise vdW interaction force profile, (m) pairwise EDL interaction force profile, and (n) pairwise DLVO interaction force profile for two *L*-lysine-covered silica nanoparticles as a function of the separation distance with respect to pH.

Table 1.7. Summary of deposition behavior of silanol-terminated silica nanoparticles on PAH/PS and *L*-lysine-covered silica nanoparticles on PAH/PS with respect to pH of solutions.

pH	(1) Silanol-terminated silica nanoparticles on PAH/PS			(2) *L*-lysine-covered silica nanoparticles on PAH/PS		
	Silanol-terminated silica nano-particles (a)	Silanol-terminated silica nano-particles and PAH/PS (b)	Coverage	*L*-lysine-covered silica nano-particles (a)	*L*-lysine-covered silica nano-particles and PAH/PS (b)	Coverage
2	Homo-aggregation	Hetero-aggregation	Low	Repulsion	Repulsion	None
4	Homo-aggregation		Low	Homo-aggregation	Repulsion	None
6	Homo-agglomeration		High	Homo-aggregation	Hetero-aggregation	Medium
8	Isolated		High	Homo-agglomeration	Hetero-aggregation	High
10	Isolated		Medium	Isolated	Hetero-aggregation	High
12	Isolated		Medium	Isolated	Hetero-aggregation	Low

(a) Colloidal stability behavior between small silica nanoparticles
(b) Colloidal stability behavior between a large PAH/PS particle and small silica nanoparticles

The degree of coverage of the *L*-lysine-covered silica nanoparticles on PAH/PS is described by the pairwise DLVO interaction force of these asymmetric particles. Figure 1.17(h) displays the vdW interaction force [Equation (1.2)], Figure 1.17(i) represents the EDL interaction force [Equation (1.49)] based on the regulation parameter, and Figure 1.17(j) plots the DLVO interaction force [Equation (1.1)] profile. As seen in Figure 1.17(h), the attractive vdW force starts increasing at D = 1 nm, and its magnitude at intermolecular contact is two times higher than the vdW force between the silanol-terminated silica nanoparticle and the PAH/PS particle [see Figure 1.16(h)]. The large difference in these vdW forces originates from the fact that more atoms of the *L*-lysine layer undergo instantaneous dipole-induced dipole forces than those of silica. Because the amphoteric surface of the *L*-lysine can have positive, neutral, and negative charge depending on pH [see Figure 1.7(a)], the EDL interaction force profiles between the *L*-lysine-covered silica nanoparticles and PAH/PS particle at pH 2 and 4 are attractive, and those at pH 6, 8, 10, and 12 are repulsive as plotted in Figure 1.17(i). If we take a closer look at the most interesting EDL interaction force profile at pH 4, this weak repulsive force becomes weaker as the separation distance approaches zero. This indicates that our nonlinear charge regulation model describes the attenuation of the surface charge density, which is caused by the redistribution of ionic species when these two asymmetric particles are approaching. For the attractive EDL interaction forces, their strength increases in order of pH 12, 6, 10, and 8. As seen in Figure 1.17(j), the DLVO interaction force profiles for separation distances larger than 0.5 nm are dominantly governed by the EDL interaction forces, whereas those at the separation distance less than 0.5 nm are mostly governed by the strong vdW forces. The repulsive DLVO forces at pH 2 and 4 agree with a lack of deposition of the *L*-lysine-covered silica nanoparticles on the PAH/PS particle, as seen in Figures 1.16(a)-(b). Because the vdW force is constant regardless of pH of the solution, the tendency of the strength of the DLVO interaction force depends on the EDL interaction force, and the magnitude of the attractive DLVO force also increases in order of pH 12, 6, 10, and 8. This trend of the attraction force profiles show good agreements with the degree of coverage of the *L*-lysine-covered silica nanoparticles on the PAH/PS particles as confirmed in the SEM images for pH 6, 8, 10, and 12 of Figures 1.17(c)-(f).

The homoaggregation of the *L*-lysine-covered silica nanoparticles occurs when there is attraction between these as illustrated in the inset of Figure 1.17(k). In contrast, when there is a strong repulsion between them, they show good colloidal stability. Figure 1.17(l) presents the vdW interaction force [Equation (1.2)], Figure 1.17(m) shows the EDL interaction force [Equation (1.49)], and Figure 1.17(n) shows the DLVO interaction force [Equation (1.1)] profiles. As seen in Figure 1.17(l), the attractive vdW force starts rising at D = 1.1 nm, and its magnitude at intermolecular contact (D = 0.2 nm) is seven times higher than the vdW force between the silanol-terminated silica nanoparticles [see Figure 1.16(l)]. As explained earlier, this difference is due to the high density of atoms of the *L*-lysine layer. The EDL repulsive force plotted in Figure 1.17(m) increases in order of pH 6, 4, 2, 8, 10, and 12. This trend for the symmetric *L*-lysine-covered silica nanoparticles matches the corresponding regulation parameter as plotted in Figure 1.15(a). Although the EDL interaction force seems dominant across all separation distance ranges as comparing Figures 1.17(m) and (n), the degree of contribution of each vdW and EDL interaction force to the DLVO interaction force profile is different depending on the pH of the solution and the separation distance. For pH 4 and 6, the vdW forces start effectively affecting these two symmetric surfaces at a separation distance of 2.8 nm and 5 nm, respectively, where the derivatives of the DLVO forces with respect to the separation distance are zero. For pH 2, 8, 10, and 12, these symmetric particles are primarily governed by the vdW force at a separation distance less than 0.5 nm. For the samples having deposited *L*-lysine silica nanoparticles, the DLVO interaction force increases in order of 6, 8, 10, and 12. The DLVO force profile at pH 6 shows attractive force and agrees with the clustered *L*-lysine-covered silica nanoparticles on the PAH/PS particle in the SEM images of Figure 1.17(a)-(f). Although the DLVO profile for pH 8 shows weak repulsive force, its value is not enough to prevent the homoaggregation of the *L*-lysine-covered silica nanoparticles when many of them are attached on the PAH/PS particle, forming dense packing and connections between them on the PAH/PS particle. As discussed earlier, this is because the substrate particle, which has small particles attached, loses surface charge density because of the redistribution of ions. Both DLVO force profiles of pH 10 and 12 [Figure 1.17(n)] show strong repulsion so that the deposited *L*-lysine-covered silica nanoparticles are isolated on the PAH/PS particle.

In summary, our modified EDL model is based on a regulation parameter that describes realistic charge regulation. The pairwise DLVO interaction force profile, based of this modified EDL model, effectively describes both symmetric and asymmetric particles. Since this regulation parameter describes realistic charge regulation phenomena depending on pH, total salt concentration, ionic strength, and separation distance, our EDL model is extended to mathematically explain practical situations such as low and high ionic strength and low and high surface potential cases. This single DLVO model can describe both the heteroaggregation between a silica nanoparticle and a PAH/PS particle and homoaggregation between two identical silica nanoparticles. This analysis explains the deposition behavior of silanol-terminated silica nanoparticles and *L*-lysine-covered silica nanoparticles on amine-functionalized PAH/PS particles with respect to pH. In addition, we also see the possibility for flexibly designing the particle surface to control charge regulation behavior. This can be achieved by combinations of multi-functional groups on the particle surfaces. Thus, we propose that this regulation parameter model, under the nonlinear charge regulation relation and the ionic size-determined diffuse layer potential, generalizes pairwise EDL interaction force and energy for both symmetric and asymmetric surfaces and extends its applications for low to high ionic strength and low to high surface potential cases.

1.6. Conclusions

In this study, we introduced an experimental method and a modified DLVO model to elucidate and predict mechanisms that can finely control the morphologies of inorganic nanoparticles physically deposited on the surface of submicron-sized organic particles in a water solution. To compare the results of the experiments with the theoretical values from our model, we prepared silanol-terminated silica nanoparticles and amphoteric *L*-lysine-covered silica nanoparticles. Also, PAH monolayer-coated polystyrene sub-micrometer particles were prepared as a substrate. The two different types of silica nanoparticles were physisorbed onto the PAH/PS particles at different pH conditions, and morphologies were analyzed by scanning electron microscopy. To theoretically characterize the difference in the deposition behaviors of these two types of silica particles to PAH/PS particles, we describe heteroaggregation between a silica particle and a polystyrene particle and homoaggregation between two identical silica particles. To illustrate these two phenomena mathematically, we used a modified DLVO model, which describes pairwise interactions for both symmetric and asymmetric surfaces. In the vdW interaction force term, the surface roughness of the particles greatly influences the classical London dispersion force, thus verification of the surfaces of the synthesized particles was done by scanning and transmission electron microscopy to minimize the error caused by significant roughness of the particle surfaces. To develop our EDL interaction model, the nonlinear charge regulation relation between surface charge density and surface potential was described by defining the acid-base reaction of the functional groups on the colloidal surface with respect to pH. Compared to previously reported regulation parameter models [21, 22, 26-28], we theoretically calculated a constant regulation parameter for each case based on the nonlinear charge regulation of surface charge density and surface potential. Then, the pairwise EDL interaction force was generalized by introducing the regulation parameter, which describes the realistic charge regulation phenomenon as a function of pH, total salt concentration, ionic strength of the solution, and the separation distance. We found that the trend of this regulation parameter can be roughly estimated by the absolute values of theoretically calculated surface potentials and diffuse layer potentials, as well as the absolute values of experimentally measured ζ-potentials. We expect that one can design the desired charge regulation behaviors of colloidal systems at specific pH values by placing more than two different types of functional groups on the colloidal particles. The sum of the vdW and the EDL interaction forces for both symmetric and asymmetric surfaces describes the pH-dependency of the deposition behaviors of inorganic nanoparticles on sub-micrometer organic substrate particles. Thus, we propose that the regulation parameter based on our nonlinear charge regulation model generalizes the EDL interaction term so that the DLVO model describes both symmetric and asymmetric surfaces, as well as low to high ionic strength and low to high potential cases. This model is expected to contribute to the design of organic/inorganic hybrid nanoparticles, which have the potential to solve problems in a variety of applications.

1.7. Chapter 1: Acknowledgements

This work was supported by a grant from the National Science Foundation (No. 1911372) and funding from the UC-Mexico Initiative of the University of California Office of the President.

Chapter 1, in part, has been submitted for submission for publication of the material as it may appear in Journal of Colloid and Interface Science, 2021, Choi, Seongcheol; Vazquez-Duhalt, Rafael; Graeve, Olivia A. The dissertation author was the primary investigator and author of this material.

Chapter 2

Effect of Initial Reaction Rate Gradient and Casimir-Lifshitz Force on Gold Coating Behavior on Positively Charged Polystyrene Particles under Potential Distribution

2.1. Abstract

We propose the mathematical analyses to support the behaviors of gold coating on the amine-functionalized polystyrene (PS) particles depending on the concentration of *L*-ascorbic acid. The perspectives of this description include the initial generation rate gradient of Au(I) complex and the Casimir-Lifshitz interaction force profile between particles under the potential distribution governed by charge regulation. To observe the difference in the morphology of the deposited gold layer on the PS particles, gold coating was performed on poly(allylamine) hydrochloride (PAH) covered PS particles with tetrachloroauric(III) acid trihydrate at various concentration of *L*-ascorbic acid. The initial reaction rate profile based on the ionic concentration gradient determined by charge regulation enables us to compare and guess the chances of the generation of nucleation of gold at specific distance away from the surface of the PS particles. Based on this, the Casimir-Lifshitz force between a PAH/PS particle and a growing gold nanocluster is investigated to explain the deposition of the gold nanoclusters on the PAH/PS particles and the agglomeration of the gold nanoclusters. The morphological analysis of the synthesized gold-coated PAH/PS particles shows that the proposed mathematical analyses well describe the gold coating behaviors on the positively charged dielectric colloidal particles.

2.2. Introduction

Gold-coated dielectric colloidal particles have received considerable attentions due to their potential applications in biosensor [103], catalyst [104], molecular imaging [105, 106], surface-enhanced Raman scattering (SERS) [107-110], and photothermal cancer therapy [111-115]. The properties of the gold-coated dielectric colloidal particles such as chemical, electronic, mechanical, optical, and thermal properties are tunable depending on the thickness and the morphology of the gold shell [109, 110, 116-120]. There has been considerable effort devoted to decrease the thickness of the gold shell on the dielectric particles as thin as nanoscale because it provides an extra degree of freedom to design and control their properties. The achieved minimum thickness of a transition metal layer such as gold on the amorphous dielectric colloidal has been reported as about 10 nm [121], and it appears to have been little progress in how to reduce their gold shell thickness further yet. On the other hand, it has been reported that the thickness of the gold layer on Fe_3O_4 substrate nanoparticles can be achieved as thin as a few nanometers with very uniform surface [122-127]. In the case of gold coating on crystalline Fe_3O_4 nanoparticles, since autocatalytic reduction may occur uniformly with the Fe atom at the surface with the reduced form of the precursor and the reducing agent at very high rate, a uniform coating layer on the Fe_3O_4 core can be achieved as thin as a few nanometers. However, it seems very difficult to generate a uniform transition metal shell on the surface of amorphous dielectric particles as thin as several nanometers because the autocatalytic reduction does not occur right at the surface of the amorphous dielectric materials.

When it comes to the methods of how to synthesize thin and uniform transition metal coating on the amorphous dielectric colloidal particles, there are a direct coating method [109, 110, 118, 119, 128-130] and a seeded method [107, 113, 116, 117, 119-121, 130] in general. The core strategy of the direct coating method on amorphous dielectric material particles is to use opposite surface charge of the dielectric material to the charge of the reduced precursor of the transition metal [131]. This method promotes the nucleation and the growth of transition metal intensively near the surface of the dielectric colloidal particles because of high concentrations of the reduced forms of the precursor and the reducing agent around their surface. In case of the seeded method, the decorated transition metal nanoclusters on the dielectric particles plays a role as autocatalytic surface so the decorated metal nanoclusters grow at fast pace and then become a shell. However, the reported analysis of the mechanism for the transition metal coating on the amorphous dielectric particles is lack of the insights into the reaction rate gradient along the distance from the surface of the dielectric particles. This reaction rate gradient is directly caused by the ionic concentration gradient governed by potential distribution in the colloidal system. To overcome the limit of the 10 nm thickness of the transition metal coating on the amorphous dielectric colloidal particles, we need to scrutinize how the reaction rate is determined by the ionic concentration gradient under the potential distribution in the system. On top of this, the movement behaviors of the generated transition metal nanoclusters may allow us to interpretate the morphology of the transition metal coating.

In this study, we mathematically describe the mechanism of how the morphologies of the gold-coated shell on the amine-functionalized PS particles change depending on a variation of the concentration of the reducing agent, *L*-ascorbic acid. Our viewpoint of the gold coating behavior is based on one-dimensionally analysis along the distance from the surface of the PS particle under potential distribution governed by charge regulation model in terms of following two: 1) the initial generation rate of Au(I) complex and 2) the Casimir-Lifshitz interaction force between particles. First, the initial reaction rate varies along the distance away from the PS particle surface due to the concentration gradient of all ions under potential distribution generated between the positively charged PS particles. By comparing the initial reaction rates at different concentration of *L*-ascorbic acid along the distance away from the PS particle, the trends of the nucleation of gold and the growth gold nanoclusters can be roughly predicted. Second, the Casimir-Lifshitz interaction force is used to explain the deposition of the generated or growing gold nanoclusters onto the PS particles and the agglomeration of the gold nanoclusters depending on the concentration of *L*-ascorbic acid. Casimir-Lifshitz interaction is the unified description of van der Waals (vdW) and Casimir interactions [132]. It explains the pair-wise particle interaction in terms of zero-point energy and quantum fluctuation of the electromagnetic field. Because the growing gold nanoclusters are uncharged, so the Casimir-Lifshitz force is the only interaction between particles in this system. To consider the electric field shielding effect [25,132-134] determined by the total concentration gradient of all free ions in our system, we introduced the improved Casimir-Lifshitz force model which shows a reduction in the entropic term of Casimir-Lifshitz force. So, based on the calculation results of the initial generation rate of Au(I) complex and the Casimir-Lifshitz force between particles, we analyze the change in morphologies of the synthesized gold coating on PS particles in a variation of the concentration of *L*-ascorbic acid.

2.3. Experimental Methodology

Materials: Styrene (≥99%, 1% of 4-tert-butylcatechol included as a stabilizer), sodium hydroxide (NaOH, >98%, pellets), potassium persulfate (≥99.0%), poly(allylamine) hydrochloride (PAH, M_w: 5,000-15,000 g/mol), *L*-ascorbic acid (≥99%), and tetrachloroauric(III) acid trihydrate ($HAuCl_4 \cdot 3H_2O$, ≥99.9%) were purchased from Sigma-Aldrich (St. Louis, MO).

All chemicals except styrene were used as received without further purification. Deionized water was used in all experiments.

Synthesis of sulfate-ended polystyrene particles: Sulfate-ended anionic polystyrene (PS) particles were prepared by soap-free emulsion polymerization [40]. To get rid of an inhibitor (4-tert-butylcatechol), styrene was washed with 1.0 M NaOH aqueous solution 4 times and then dried with magnesium sulfate. 10 g of the purified styrene monomer was vigorously stirred with 190 g of water in a reactor under nitrogen atmosphere at 75°C. After 1 h, 10 g of water with 0.10 g of potassium persulfate was injected into the reactor to thermally initiate the chain-growth polymerization. The reaction solution was incubated for 24 h and then washed 7 times with an excessive amount of water by using a sequence of ultrasonication and centrifugation. Finally, this purified PS particle suspension was diluted to 0.10 wt.% with water and redistributed by ultrasonication for 15 min.

Preparation of PAH-covered PS particles: To prepare PAH-covered PS (PAH/PS) particle suspension, 1.0 mL of 20 wt.% PAH water solution was mixed with 30.0 mL of the 0.10 wt.% PS particle suspension [41-45]. The solution was stirred vigorously for 24 h at room temperature. This mixture was micro-filtered 5 times with an excessive amount of water by using a cellulose acetate membrane filter (pore size: 0.20 μm, Advantec MFS, Inc., Dublin, CA) to eliminate free PAH molecules. The washed PAH/PS particle suspension was diluted to 0.01 wt.% with water.

Preparation of gold-coated PS particles: To investigate the mechanism of gold coating behaviors on the amine-functionalized dielectric submicron particles, 6 different concentrations (100, 10.0, 5.00, 2.50, 1.00, and 0.50 mM) of *L*-ascorbic acid water solution were prepared. 100 μL of the 0.01 wt.% PAH/PS suspension was poured into 25 mL of the different concentration of the *L*-ascorbic acid solution. For the gold precursor, 25 mM of $HAuCl_4$ aqueous solution was prepared. All the prepared stock solutions were incubated at room temperature for 1 h before the gold coating reaction. To initiate the gold coating reaction, 150 μL of the 25 mM $HAuCl_4$ stock solution was injected into the mixture of the PAH/PS particles suspension and the *L*-ascorbic acid solution [129]. The synthesis conditions of the gold coating on PAH/PS particles are listed in Table 2.1. The reaction is done within 1 min. The reacted solution was redispersed in a ultrasonication bath for 10 mins and microfiltered by using a cellulose acetate membrane filter. Then, the filtered solid contents were transferred to water. This sequence of the washing procedures was performed 4 times, and then the solid contents were redispersed in water using ultrasonication for 10 min.

Table 2.1. Synthesis conditions of gold coating on PAH-covered polystyrene particles.

Sample	PAH/PS Suspension (100 μL)	*L*-ascorbic acid Solution (25 mL)	$HAuCl_4$ Solution (150 μL)
1	0.01 wt.%	100 mM	25 mM
2		10.0 mM	
3		5.00 mM	
4		2.50 mM	
5		1.00 mM	
6		0.50 mM	

Characterization: For all the characterizations, every prepared sample was vacuum dried at room temperature for one week to remove water contents. A field emission scanning electron microscope (FE-SEM, Zeiss Sigma 500, Carl Zeiss AG, Oberkochen, Germany) was performed to image the morphology of the prepared particles. The dried samples for SEM were not sputter-coated to avoid even a very small distortion of the original morphology of the gold-coated PS particles. A transmission electron microscope (TEM, JEOL 1200 EX II, JEOL Ltd., Tokyo, Japan) was used to further observe the morphology of each particle sample.

2.4. Theoretical Model

To describe the detailed mechanism of the gold coating behaviors on the amine-functionalized dielectric submicron colloidal particles with changes in the concentration of *L*-ascorbic acid, we develop the following two models: 1) relative initial reaction rate profiles away from the particle surface and 2) Casimir-Lifshitz force between particles through medium under ionic concentration distributions. The relative initial reaction rate profile model is a tool to estimate the difference in the reduction rate of Au(III) chloride complex, the nucleation rate, and the growth rate of gold away from the surface of the cationic PS particles. The Casimir-Liftshitz force model is used to describe the nucleation of gold near and far away from the cationic PS particles. Both models consider the ionic concentration gradient based on charge regulation and potential profiles near the surface of the substrate particle. Thus, we can describe the obvious difference in gold coating behaviors between near the cationic surface and away from the surface.

2.4.1. Relative initial reaction rate profile

To estimate the difference in the reduction rate of Au(III) chloride complex, the nucleation rate, and the growth rate of gold away from the surface of the cationic PS particles, we introduce the relative initial reaction rate profile for the reduction of Au(III) to Au(I) chloride complex. We start developing the model from the charge regulation model [29-31, 66-71, 74] to evaluate surface charge density and surface potential of the cationic PS particles. With a pair of the surface charge density and the surface potential, we can define potential profiles and ionic concentration profiles. Then, we approximate the reaction rate distributions in terms of Au(I) chloride complex from these ionic concentration profiles.

2.4.1.1. Initial fractional composition of L-ascorbic acid and Au(III) complex

When the gold precursor stock solution is poured into the *L*-ascorbic acid solution containing PAH/PS particles, we can imagine that a very complicated series of phenomena occur simultaneously. This may include the reaction of the gold precursor and the reducing agents, the acid-base equilibrium reactions of ionizable substances, the development of EDL structure near solid surface, the concentration gradient of all ionic species, etc. Such these phenomenon affect each other and becomes even much more complicated. Our strategy to analyze the gold coating behaviors on the amine-functionalized PS partices is to compare the initial reaction rates along the distance away from the surface. This is because the initial value is generally the simplist data we can obtain. To start developing our model, we first should estimate the initial fractional composition of the *L*-ascorbic acid and the Au(III) complex of the reaction mixture. For a purpose of the model simplification, we surmize that the acid-base reaction reaches nearly close to the equilibrium state fast enough. In addition to this, the contribution of the proton concentration change due to the association and dissociation of the amine group on the PAH/PS particle is ignored because it is very low compared to that of the reductant and gold precursor as seen in Table 2.2. In order to determine the initial fractional compositions of the *L*-ascorbic acid and the gold precursor participating in the reaction, we need to determine the acid-base equilibrium reaction for each substance and then relate how these two substances affect each other.

Table 2.2. The total concentrations of PAH/PS particles, HAuCl4, and *L*-ascorbic acid in the reaction mixture.

Sample	PAH/PS (g/L)	$C_{\mathrm{HAuCl_4}}$ (M)	$C_{L\text{-AA}}$ (M)
1	3.9604×10^{-7}	1.48515×10^{-4}	9.901×10^{-2}
2			9.901×10^{-3}
3			4.950×10^{-3}
4			2.475×10^{-3}
5			9.901×10^{-4}
6			4.950×10^{-4}

L-ascorbic acid undergoes the following two equilbrium acid-base reactions:

$$L\text{-AscH}_2 \overset{K_{\mathrm{a}_1}}{\rightleftharpoons} L\text{-AscH}^- + \mathrm{H}^+ \tag{2.1a}$$

$$L\text{-AscH}^- \overset{K_{\mathrm{a}_2}}{\rightleftharpoons} L\text{-Asc}^{2-} + \mathrm{H}^+ \tag{2.1b}$$

where K_{a_1} = $10^{-4.12}$ and K_{a_2} = $10^{-11.51}$ [135] are the acid dissociation constants of the reaction Equations (2.1a) and (2.1b), respectively. These acid dissociation contants are written as:

$$K_{\mathrm{a}_1} = \frac{\left[L\text{-AscH}^-\right]_\infty \left[\mathrm{H}^+\right]_\infty}{\left[L\text{-AscH}_2\right]_\infty} \tag{2.2a}$$

$$K_{\mathrm{a}_2} = \frac{\left[L\text{-Asc}^{2-}\right]_\infty \left[\mathrm{H}^+\right]_\infty}{\left[L\text{-AscH}^-\right]_\infty} \tag{2.2b}$$

where $[L\text{-AscH}_2]_\infty$, $\left[L\text{-AscH}^-\right]_\infty$, and $\left[L\text{-Asc}^{2-}\right]_\infty$ are the bulk concentrations of $L\text{-AscH}_2$, $L\text{-AscH}^-$, and $L\text{-Asc}^{2-}$. The symbol $x = \infty$ indicates that the concentration of any substances at *x* are far away from the isolated charged PAH/PS particles. From Equations (2.2a) and (2.2b), we can define the fractions of all available forms of *L*-ascorbic acid in a function of the concentration of proton as:

$$\alpha_{\infty,L\text{-AscH}_2} = \frac{\left[\mathrm{H}^+\right]_\infty^2}{K_{a_1}K_{a_2} + K_{a_1}\left[\mathrm{H}^+\right]_\infty + \left[\mathrm{H}^+\right]_\infty^2} \tag{2.3a}$$

$$\alpha_{\infty,L\text{-AscH}^-} = \frac{K_{a_1}\left[\mathrm{H}^+\right]_\infty}{K_{a_1}K_{a_2} + K_{a_1}\left[\mathrm{H}^+\right]_\infty + \left[\mathrm{H}^+\right]_\infty^2} \tag{2.3b}$$

$$\alpha_{\infty,L\text{-Asc}^{2-}} = \frac{K_{a_1}K_{a_2}}{K_{a_1}K_{a_2} + K_{a_1}\left[\mathrm{H}^+\right]_\infty + \left[\mathrm{H}^+\right]_\infty^2} \tag{2.3c}$$

where $\alpha_{\infty,L\text{-AscH}_2}$, $\alpha_{\infty,L\text{-AscH}^-}$, $\alpha_{\infty,L\text{-Asc}^{2-}}$ are the fractions of $L\text{-AscH}_2$, $L\text{-AscH}^-$, and $L\text{-Asc}^{2-}$. When both *L*-ascorbic acid and $\mathrm{HAuCl_4}$ exist in an aqueous solvent, the ratio of the protons generated by the deprotonation of *L*-ascorbic acid is defined as $\beta_{\infty,\mathrm{H}^+}$. From Equations (2.1a) and (1b), we know that the $L\text{-AscH}^-$ loses 1 proton and $L\text{-Asc}^{2-}$ loses 2 protons. So, using the Equations (2.3b) and (2.3c), $\beta_{\infty,\mathrm{H}^+}$ can be expressed as the fractions of each forms of *L*-ascorbic acid:

$$\beta_{\infty,\mathrm{H}^+} = \alpha_{\infty,L\text{-AscH}^-} + 2\alpha_{\infty,L\text{-Asc}^{2-}} \tag{2.4}$$

For efficient computations, we define the boundary condition for $\beta_{\infty,\mathrm{H}^+}$ as $0 \le \beta_{\infty,\mathrm{H}^+} \le 2$. Since not only *L*-ascorbic acid but also the gold precursor contributes to the total proton concentration, the concentration of proton from $\mathrm{HAuCl_4}$ should be considered as well.

When $\mathrm{HAuCl_4}$ is dissolved in water, it loses a proton and becomes $\mathrm{AuCl_4^-}$ [136, 137]. Its degree of hydrolysis is determined by the concentrations of protons and chloride anions in the solution [137]. Since the solution mixture used in this experiment is acidic, it is assumed that the Au(III) complex undergoes the following six acid-base equilibrium reactions during the entire reaction:

$$\mathrm{AuCl_4^- + H_2O \overset{K_{a_3}}{\rightleftharpoons} AuCl_3(H_2O) + Cl^-} \tag{2.5a}$$

$$\mathrm{AuCl_3(H_2O) \overset{K_{a_4}}{\rightleftharpoons} AuCl_3(OH)^- + H^+} \tag{2.5b}$$

$$\mathrm{AuCl_3(OH)^- + H_2O \overset{K_{a_5}}{\rightleftharpoons} AuCl_2(OH)(H_2O) + Cl^-} \tag{2.5c}$$

$$\mathrm{AuCl_2(OH)(H_2O) \overset{K_{a_6}}{\rightleftharpoons} AuCl_2(OH)_2^- + H^+} \tag{2.5d}$$

$$\mathrm{AuCl_2(OH)_2^- + H_2O \overset{K_{a_7}}{\rightleftharpoons} AuCl(OH)_3^- + Cl^- + H^+} \tag{2.5e}$$

$$\mathrm{AuCl(OH)_3^- + H_2O \overset{K_{a_8}}{\rightleftharpoons} Au(OH)_4^- + Cl^- + H^+} \tag{2.5f}$$

where $K_{a_3} = 3.98 \times 10^{-6}$, $K_{a_4} = 0.25$, $K_{a_5} = 0.36 \times 10^{-2}$, $K_{a_6} = 2.81 \times 10^{-5}$, $K_{a_7} = 8.91 \times 10^{-9}$, and $K_{a_8} = 1.0 \times 10^{-10}$ are the acid dissociation constants for the reaction Equations (2.5a) to (2.5f), respectively [137]. From these, the fractions of the possible forms of Au(III) complex ions are written in a function of the concentration of proton and chloride anions as:

$$\alpha_{\infty,\mathrm{AuCl_4^-}} = \frac{\left[\mathrm{H^+}\right]_\infty^4 \left[\mathrm{Cl^-}\right]_\infty^4}{L_\infty} \tag{2.6a}$$

$$\alpha_{\infty,\mathrm{AuCl_3(H_2O)}} = \frac{K_{a_3}\left[\mathrm{H^+}\right]_\infty^4 \left[\mathrm{Cl^-}\right]_\infty^3}{L_\infty} \tag{2.6b}$$

$$\alpha_{\infty,\mathrm{AuCl_3(OH)^-}} = \frac{K_{a_3}K_{a_4}\left[\mathrm{H^+}\right]_\infty^3 \left[\mathrm{Cl^-}\right]_\infty^3}{L_\infty} \tag{2.6c}$$

$$\alpha_{\infty,\mathrm{AuCl_2(OH)(H_2O)}} = \frac{K_{a_3}K_{a_4}K_{a_5}\left[\mathrm{H^+}\right]_\infty^3 \left[\mathrm{Cl^-}\right]_\infty^2}{L_\infty} \tag{2.6d}$$

$$\alpha_{\infty,\mathrm{AuCl_2(OH)_2^-}} = \frac{K_{a_3}K_{a_4}K_{a_5}K_{a_6}\left[\mathrm{H^+}\right]_\infty^2\left[\mathrm{Cl^-}\right]_\infty^2}{L_\infty} \tag{2.6e}$$

$$\alpha_{\infty,\mathrm{AuCl(OH)_3^-}} = \frac{K_{a_3}K_{a_4}K_{a_5}K_{a_6}K_{a7}\left[\mathrm{H^+}\right]_\infty\left[\mathrm{Cl^-}\right]_\infty}{L_\infty} \tag{2.6f}$$

$$\alpha_{\infty,\mathrm{Au(OH)_4^-}} = \frac{K_{a_3}K_{a_4}K_{a_5}K_{a_6}K_{a_7}K_{a_8}}{L_\infty} \tag{2.6g}$$

where $\alpha_{\infty,\mathrm{AuCl_4^-}}$, $\alpha_{\infty,\mathrm{AuCl_3(H_2O)}}$, $\alpha_{\infty,\mathrm{AuCl_3(OH)^-}}$, $\alpha_{\infty,\mathrm{AuCl_2(OH)(H_2O)}}$, $\alpha_{\infty,\mathrm{AuCl_2(OH)_2^-}}$, and $\alpha_{\infty,\mathrm{AuCl(OH)_3^-}}$ are the fractions of $\mathrm{AuCl_4^-}$, $\mathrm{AuCl_3(H_2O)}$, $\mathrm{AuCl_3(OH)^-}$, $\mathrm{AuCl_2(OH)(H_2O)}$, $\mathrm{AuCl_2(OH)_2^-}$, and $\mathrm{AuCl(OH)_3^-}$, respectively. $\left[\mathrm{Cl^-}\right]_\infty$ is the concentration chloride anions of the bulk solution. And, L_∞ is defined as:

$$\begin{aligned} L_\infty = {} & K_{a_3}K_{a_4}K_{a_5}K_{a_6}K_{a_7}K_{a_8} + K_{a_3}K_{a_4}K_{a_5}K_{a_6}K_{a_7}\left[\mathrm{H^+}\right]_\infty\left[\mathrm{Cl^-}\right]_\infty \\ & + K_{a_3}K_{a_4}K_{a_5}K_{a_6}\left[\mathrm{H^+}\right]_\infty^2\left[\mathrm{Cl^-}\right]_\infty^2 + K_{a_3}K_{a_4}K_{a_5}\left[\mathrm{H^+}\right]_\infty^3\left[\mathrm{Cl^-}\right]_\infty^2 \\ & + K_{a_3}K_{a_4}\left[\mathrm{H^+}\right]_\infty^3\left[\mathrm{Cl^-}\right]_\infty^3 + K_{a_3}\left[\mathrm{H^+}\right]_\infty^4\left[\mathrm{Cl^-}\right]_\infty^3 + \left[\mathrm{H^+}\right]_\infty^4\left[\mathrm{Cl^-}\right]_\infty^4 \end{aligned} \tag{2.6h}$$

As mentioned earlier, $\mathrm{HAuCl_4}$ is basically ionized by releasing one proton. And, Equations from (2.5a) to (2.5f) show us the number of protons and chloride anions generated during the acid-base equilibrium reations of the Au(III) complex. The ratio of the protons contributed by $\mathrm{HAuCl_4}$ is defined as $\gamma_{\infty,\mathrm{H^+}}$, which can be expressed in terms of Equations from (2.6a) to (2.6g) as:

$$\begin{aligned} \gamma_{\infty,\mathrm{H^+}} = {} & \alpha_{\infty,\mathrm{AuCl_4^-}} + \alpha_{\infty,\mathrm{AuCl_3(H_2O)}} + 2\alpha_{\infty,\mathrm{AuCl_3(OH)^-}} + 2\alpha_{\infty,\mathrm{AuCl_2(OH)(H_2O)}} + 3\alpha_{\infty,\mathrm{AuCl_2(OH)_2^-}} \\ & + 4\alpha_{\infty,\mathrm{AuCl(OH)_3^-}} + 5\alpha_{\infty,\mathrm{Au(OH)_4^-}} \end{aligned} \tag{2.7}$$

From Equations (2.5a) to (2.5f), the boundary condition for $\gamma_{\infty,\mathrm{H^+}}$ is defined as $1 \le \gamma_{\infty,\mathrm{H^+}} \le 5$. Another relation we can define is the concentration of chloride anions dissociated from $\mathrm{HAuCl_4}$

during its hydrolysis. The ratio of the generated chloride anions is defined as $\gamma_{\infty,\mathrm{Cl}^-}$. From Equations (2.5a) to (2.5f), $\gamma_{\infty,\mathrm{Cl}^-}$ can be written in terms of the fractions of Au(III) complex as:

$$\begin{aligned}\gamma_{\infty,\mathrm{Cl}^-} = {} & \alpha_{\infty,\mathrm{AuCl_3(H_2O)}} + \alpha_{\infty,\mathrm{AuCl_3(OH)^-}} + 2\left(\alpha_{\infty,\mathrm{AuCl_2(OH)(H_2O)}} + \alpha_{\infty,\mathrm{AuCl_2(OH)_2^-}}\right) + 3\alpha_{\infty,\mathrm{AuCl(OH)_3^-}} \\ & + 4\alpha_{\infty,\mathrm{Au(OH)_4^-}}\end{aligned} \tag{2.8}$$

The boundary condition of beta is defined as $0 \le \beta_{\infty,\mathrm{Cl}^-} \le 4$.

The total concentration of protons of the bulk solution is the sum of the concentrations of protons from *L*-ascorbic acid and $\mathrm{HAuCl_4}$ and written as:

$$\left[\mathrm{H^+}\right]_\infty = \left[\mathrm{H^+}\right]_{\infty,L\text{-AA}} + \left[\mathrm{H^+}\right]_{\infty,\mathrm{HAuCl_4}} \tag{2.9}$$

where $\left[\mathrm{H^+}\right]_{\infty,L\text{-AA}}$ and $\left[\mathrm{H^+}\right]_{\infty,\mathrm{HAuCl_4}}$ are the concentrations of protons generated from *L*-ascorbic acid and $\mathrm{HAuCl_4}$, respectively. To express Equation (2.9) in a function of the concentration of protons and chloride ions, Equation (2.9) is converted into the form of $\beta_{\infty,\mathrm{H^+}}$ and $\gamma_{\infty,\mathrm{H^+}}$ and rearranged as:

$$\beta_{\infty,\mathrm{H^+}}\left[L\text{-AA}\right] + \gamma_{\infty,\mathrm{H^+}}\left[\mathrm{HAuCl_4}\right] - \left[\mathrm{H^+}\right]_\infty = 0 \tag{2.10}$$

where $\left[L - \mathrm{AA}\right]$ and $\mathrm{HAuCl_4}$ are the concentrations of the *L*-ascorbic acid and $\mathrm{HAuCl_4}$ participated in the reaction, respectively. The relation of $\gamma_{\infty,\mathrm{Cl}^-}$, $\mathrm{HAuCl_4}$, and $\left[\mathrm{Cl^-}\right]_\infty$ for the gold precursor is expressed as:

$$\gamma_{\infty,\mathrm{Cl}^-}\left[\mathrm{HAuCl_4}\right] - \left[\mathrm{Cl^-}\right]_\infty = 0 \tag{2.11}$$

If we define the left terms of Equations (2.10) and (2.11) as functions of $\left[\mathrm{H^+}\right]_\infty$ and $\left[\mathrm{Cl^-}\right]_\infty$, a pair of roots of $\left[\mathrm{H^+}\right]_\infty$ and $\left[\mathrm{Cl^-}\right]_\infty$, can be solved by finding a point where both of these functions equal to zero on the intersection line of the two curved surfaces of these two functions. From the calculated $\left[\mathrm{H}^{+}\right]_{\infty}$, the theoretical pH value of each experimental condition can be determined. The fractional composition of the *L*-ascorbic acid is acquired from Equations from (2.3a) to (2.3c) using the computed $\left[\mathrm{H}^{+}\right]_{\infty}$. The fractional composition of Au(III) complex is determined by using the computed pair of $\left[\mathrm{H}^{+}\right]_{\infty}$ and $\left[\mathrm{Cl}^{-}\right]_{\infty}$ in Equations (2.6a) to (2.6g). The computed initial concentrations of all molecules including available forms of *L*-ascorbic acid and HAuCl_4 for the change in the concentration of *L*-ascorbic acid obey the overall charge balance and are listed with the theoretical initial pH in Table 2.3. A water molecule is excluded in all equations because it is solvent [138].

Table 2.3. The computed initial concentrations (M) of all molecules including available forms *i* of *L*-ascorbic acid and $HAuCl_4$ with a change in the concentration of *L*-ascorbic acid with the theoretical initial pH of the mixture.

Sample #	1	2	3	4	5	6
L-ascorbic acid (M)	9.901×10^{-2}	9.901×10^{-3}	4.950×10^{-3}	2.475×10^{-3}	9.901×10^{-4}	4.950×10^{-4}
pH	2.54	3.00	3.12	3.23	3.35	3.41
i	$C_{\infty,i}$ (M)					
H^+	2.85×10^{-3}	9.99×10^{-4}	7.55×10^{-4}	5.87×10^{-4}	4.49×10^{-4}	3.89×10^{-4}
Cl^-	2.73×10^{-4}	2.81×10^{-4}	2.83×10^{-4}	2.85×10^{-4}	2.86×10^{-4}	2.86×10^{-4}
OH^-	3.51×10^{-12}	1.00×10^{-11}	1.32×10^{-11}	1.70×10^{-11}	2.23×10^{-11}	2.57×10^{-11}
L-$AscH_2$	9.64×10^{-2}	9.20×10^{-3}	4.45×10^{-3}	2.20×10^{-3}	8.47×10^{-4}	4.14×10^{-4}
L-$AscH^-$	2.57×10^{-3}	7.00×10^{-4}	4.52×10^{-4}	2.84×10^{-4}	1.43×10^{-4}	8.08×10^{-5}
L-Asc^{2-}	2.78×10^{-12}	2.16×10^{-12}	1.85×10^{-12}	1.49×10^{-12}	9.85×10^{-13}	6.42×10^{-13}
$AuCl_4^-$	7.71×10^{-6}	2.91×10^{-6}	2.22×10^{-6}	1.74×10^{-6}	1.32×10^{-6}	1.13×10^{-6}
$AuCl_3(H_2O)$	1.12×10^{-7}	4.11×10^{-8}	3.12×10^{-8}	2.42×10^{-8}	1.84×10^{-8}	1.58×10^{-8}
$AuCl_3(OH)^-$	9.86×10^{-6}	1.03×10^{-5}	1.03×10^{-5}	1.03×10^{-5}	1.02×10^{-5}	1.01×10^{-5}
$AuCl_2(OH)(H_2O)$	1.30×10^{-4}	1.32×10^{-4}	1.31×10^{-4}	1.30×10^{-4}	1.29×10^{-4}	1.18×10^{-4}
$AuCl_2(OH)_2^-$	1.28×10^{-6}	3.71×10^{-6}	4.89×10^{-6}	6.24×10^{-6}	8.06×10^{-6}	9.23×10^{-6}
$AuCl(OH)_3^-$	1.47×10^{-8}	1.18×10^{-7}	2.04×10^{-7}	3.32×10^{-7}	5.59×10^{-7}	7.39×10^{-7}
$Au(OH)_4^-$	1.89×10^{-12}	4.20×10^{-11}	9.54×10^{-11}	1.99×10^{-10}	4.36×10^{-10}	6.64×10^{-10}

2.4.1.2. Initial potential profile and initial ionic concentration profile

The phenomenon that the ionizable chemical species on the surface are regulated by the concentration of all ionic species near its surfaces is called charge regulation [29-31, 66-71, 74]. The concentration profile $C_{x,i}$ of each ionic species at the distance *x* away from the surface is governed by a Boltzmann equation [25]:

$$C_{x,i} = C_{\infty,i}\, e^{-\frac{z_i q \Psi_x}{k_B T}} \tag{2.12}$$

where $C_{\infty,i}$ is the bulk molar concentration of an ion *i*, z_i is valence of *i*, *q* is the elementary charge, ψ_x is the potential at *x*, $\mathrm{k_B}$ is Boltzmann's constant, and *T* is the absolute temperature. Equation (2.12) tells us that the concentrations of any ionic species near the surface can be determined if we know the surface potential. When the two PS particles stay far away in solution, we say that these two particles are isolated. In this situation, we can mathematically describe the surface charge density and the surface potential governed by the charge regulation [29-31, 66-71, 74]. With a pair of the surface charge density and the surface potential, we can define the local density of each ion near the surface [25]. To do so, we start building the model from the charge regulation of the surface by proton concentration on surface.

For the immersed PAH/PS particles in electrolyte solution, the amine groups on their surfaces undergo protonation and deprotonation depending on the local concentration of protons near the surfaces. The local area of the protonated amine group is positively charged whereas that of the unreacted amine group stays neutral. This acid-base equilibrium reaction occurring at the surface of the PAH/PS particles is defined as:

$$\mathrm{NH_3^+} \overset{K_{\mathrm{a_9}}}{\rightleftharpoons} \mathrm{NH_2} + \mathrm{H^+} \tag{2.13}$$

$K_{\mathrm{a_9}} = 10^{-8.9}$ [83] is an acid dissociation constant of Equation (2.13) and written as:

$$K_{\mathrm{a_9}} = \frac{[\mathrm{NH_2}]_0 \left[\mathrm{H^+}\right]_0}{\left[\mathrm{NH_3^+}\right]_0} \tag{2.14}$$

$[\mathrm{NH_2}]_0$ and $\left[\mathrm{NH_3^+}\right]_0$ are the surface site densities of $\mathrm{NH_2}$ and $\mathrm{NH_3^+}$, respectively. $\left[\mathrm{H^+}\right]_0$ is the concentration of protons at the interface between the surface and the liquid. The surface charge density σ of the ionizable amine group can be expressed in a function of the proton concentration at surface/liquid interface as:

$$\sigma = q\mathrm{N}_{\mathrm{A}}N_{\mathrm{total,PAH/PS}}\frac{\left[\mathrm{H}^{+}\right]_{0}}{K_{\mathrm{a}_1}+\left[\mathrm{H}^{+}\right]_{0}} \tag{2.15}$$

where N_{A} is Avogadro constant, and $N_{\mathrm{total,PAH/PS}} = 3.32 \times 10^{-6}$ mol/m^2 [85] is the total number site density of the amine group on the surface of PAH/PS particles. By using Equation (2.12), the surface charge σ in Equation (2.15) can be expressed in terms of the proton concentration of the bulk solution $\left[\mathrm{H}^{+}\right]_{0}$ and surface potential ψ_0 as:

$$\sigma = q\mathrm{N}_{\mathrm{A}}N_{\mathrm{total,PAH/PS}}\frac{\left[\mathrm{H}^{+}\right]_{\infty}e^{-\frac{q\psi_0}{\mathrm{k_B}T}}}{K_{\mathrm{a}_1}+\left[\mathrm{H}^{+}\right]_{\infty}e^{-\frac{q\psi_0}{\mathrm{k_B}T}}} \tag{2.16}$$

According to the charge regulation, the second relationship between surface charge density and surface potential is that the concentration of total ions in the surface influences these two values. Poisson's equation describes the Laplacian of the potential and the concentration of each ion at distance *x* away from surface as [25]:

$$\frac{\mathrm{d}^2\psi}{\mathrm{d}x^2} = -\frac{z_i q C_{x,i}}{\varepsilon_0\varepsilon_{\mathrm{m}}} \tag{2.17}$$

where ε_0 is the permittivity of vacuum and ε_{m} is the relative permittivity of medium m (m = water in this case) at room temperature. Because the ionic concentration obeys the Boltzmann's distribution, the combination of Equations (2.12) and (2.17) brings the Poisson-Boltzmann equation [25]:

$$\frac{\mathrm{d}^2\psi}{\mathrm{d}x^2} = -\frac{q\mathrm{N}_{\mathrm{A}}}{\varepsilon_0\varepsilon_{\mathrm{m}}}\sum_i z_i C_{\infty,i}e^{-\frac{z_i q\psi_x}{\mathrm{k_B}T}} \tag{2.18}$$

For the two isolated symmetric surfaces in solution, we say the distance *D* between these surfaces goes infinity ($D\to\infty$) and $x = D/2$ is the point at mid-plane between them. A sequence of differentiating Equation (2.12) and integrating it between $C_{D/2,i}$ (the ionic concentration at the mid-plane) and $C_{x,i}$ (the ionic concentration at *x*) brings the following relation [25]:

$$C_{x,i} = C_{\infty,i} + \frac{\varepsilon_0 \varepsilon_{\mathrm{m}}}{2\mathrm{k_B}T}\left(\frac{d\psi}{dx}\right)_x^2 \tag{2.19}$$

The second relationship between surface charge density and surface potential can be derived from Equations (2.12) and (2.19) and is called the Grahame equation [25, 29-31, 66-71, 74]:

$$\sigma = \sqrt{8\varepsilon_0\varepsilon_{\mathrm{m}}\mathrm{k_B}T\mathrm{N_A}C_\infty \times 10^3}\ \sinh\left(\frac{q\psi_0}{2\mathrm{k_B}T}\right) \tag{2.20}$$

By solving Equations (2.16) and (2.20), a pair of roots of surface charge density and surface potential can be obtained for the change in concentration of *L*-ascorbic acid. The results of this calculation are summarized in a Table 2.4.

Table 2.4. Surface charge density, surface potential, and Debye length based on charge regulation model in a change of the concentration of *L*-ascorbic acid.

Sample #	pH	$C_{L\text{-AA}}$ (M)	λ_{D} (nm)	σ (C/m^2)	ψ_0 (V)
1	2.54	9.901×10^{-2}	5.7	0.319	0.238
2	3.00	9.901×10^{-3}	9.6	0.310	0.263
3	3.12	4.950×10^{-3}	11.1	0.303	0.269
4	3.23	2.475×10^{-3}	12.5	0.294	0.274
5	3.35	9.901×10^{-4}	14.3	0.280	0.278
6	3.41	4.950×10^{-4}	15.4	0.272	0.281

A sequence of rearranging of Equation (2.19) and integrating it in terms of *x* results in the potential profile at a distance *x* away from the surface [25]:

$$\psi_x = \frac{2\mathrm{k_B}T}{q} \ln\left[\frac{1+\left\{\tanh\left(\frac{q\psi_0}{4\mathrm{k_B}T}\right)\right\}e^{-\kappa x}}{1-\left\{\tanh\left(\frac{q\psi_0}{4\mathrm{k_B}T}\right)\right\}e^{-\kappa x}}\right] \tag{2.21}$$

where κ is the inverse Debye screening length expressed as [25]:

$$\kappa = \sqrt{\frac{\sum_i q^2 z_i^2 C_{\infty,i} \mathrm{N_A} \times 10^3}{\varepsilon_0 \varepsilon_\mathrm{m} \mathrm{k_B} T}} \tag{2.22}$$

The concentrations of all defined ionic species from Table 2.3 are used for the sigma term in Equation (2.22). The calculated Debye length $\lambda_\mathrm{D} = 1/\kappa$ are listed in Table 2.4. The potential distribution of Equation (2.21) is determined by the charge-regulated surface potential. By using Equation (2.12) with the concentration of each ionic species *i* from Table 2.3 and the computed potential profile from Equation (2.21), we obtain the concentration distribution of each ionic species *i* at distance *x* away from the PAH/PS particle surface. When it comes to the noncharged substances such as $L\text{-AscH}_2$, $\mathrm{AuCl_3(H_2O)}$, and $\mathrm{AuCl_3(OH)(H_2O)}$, we surmize that the concentrations of these uncharged forms are constant everywhere even within EDL.

At this point, we notice that the changed fractional composition of the ionic species inside the EDL can act as an extra driving force for further acid-base equilibrium reaction. If we compare the ratio of the solution volume within Debye length to the solution volume beyond Debye length, its ratio varies from 1.27×10^{-11} to 3.62×10^{-11} in the experimental conditions of this work. In addition to this, the Debye length varies from 5.7 to 15.4 nm depending on the concentration of *L*-ascorbic acid of this work. This means that the ions and the noncharged substances outside the EDL can travel very short distances quickly and act as a buffer. Thus, even though the additional acid-base equilibrium reaction occurs within EDL, we can assume that the concentrations of all species determined beyond Debye length and the potential gradient within Debye length govern the entire system.

2.4.1.3. Relative initial reaction rate profile for reduction of Au(III) complex to Au(I) chloride complex

The reduction of Au(III) complex by *L*-ascorbic acid results in the formation of gold [48, 49]. We introduce the Finke-Watzky model [139, 140] to specifically understand this reaction. The overall reaction can be broken down into three stages: 1) formation of Au(I) chloride complex ion by the reduction of Au(III) complex ions, 2) nucleation of gold ,and 3) autocatalytic surface growth of gold [136, 137, 139, 140].

In the first stage, various forms of Au(III) complex anions $\mathrm{AuCl_{4-y}(OH)_y^-}$ (y = 1, 2, 3, 4) are reduced by the neutral form ($L\text{-AscH}_2$) and the form with -1 charge ($L\text{-AscH}^-$) of *L*-ascorbic acid [141]. And Au(I) chloride complex anions ($\mathrm{AuCl_2^-}$) are the products in this step. For acidic solution, all possible irreversible reactions in the first stage are defined as follows [49]:

$$\mathrm{AuCl_4^-} + L\text{-}\mathrm{AscH_2} \xrightarrow{k_1} \mathrm{AuCl_2^-} + \mathrm{DHA} + 2\mathrm{Cl^-} + 2\mathrm{H^+} \tag{2.23a}$$

$$\mathrm{AuCl_4^-} + 2L\text{-}\mathrm{AscH^-} \xrightarrow{k_2} \mathrm{AuCl_2^-} + 2\mathrm{DHA} + 2\mathrm{Cl^-} \tag{2.23b}$$

$$\mathrm{AuCl_3(OH)^-} + L\text{-}\mathrm{AscH_2} \xrightarrow{k_3} \mathrm{AuCl_2^-} + \mathrm{DHA} + \mathrm{Cl^-} + \mathrm{H^+} + \mathrm{H_2O} \tag{2.23c}$$

$$\mathrm{AuCl_3(OH)^-} + 2L\text{-}\mathrm{AscH^-} + \mathrm{H^+} \xrightarrow{k_4} \mathrm{AuCl_2^-} + 2\mathrm{DHA} + \mathrm{Cl^-} + 2\mathrm{H_2O} \tag{2.23d}$$

$$\mathrm{AuCl_2(OH)_2^-} + L\text{-}\mathrm{AscH_2} \xrightarrow{k_5} \mathrm{AuCl_2^-} + \mathrm{DHA} + 2\mathrm{H_2O} \tag{2.23e}$$

$$\mathrm{AuCl_2(OH)_2^-} + 2L\text{-}\mathrm{AscH^-} + 2\mathrm{H^+} \xrightarrow{k_6} \mathrm{AuCl_2^-} + 2\mathrm{DHA} + 4\mathrm{H_2O} \tag{2.23f}$$

where k_1 , k_2 , k_3 , k_4 , k_5 ,and k_6 denote rate constants of reactions from Equations (2.23a) to (2.23f). The byproduct, dehydroascorbic acid (DHA), in the reactions of the first stage is an oxidized form of *L*-ascorbic acid [137]. This stage ends when either the Au(III) complex anions or the two active forms of *L*-ascorbic acid becomes deficient.

The second stage corresponds to nucleation of gold. In this step, the Au(I) chloride anion intermediate is reduced by *L*-ascorbic acid and becomes a single gold atom. The step for the formation of nulcei is defined as [137]:

$$\mathrm{AuCl_2^-} + \frac{1}{2}L\text{-}\mathrm{AscH_2} \xrightarrow{k_7} \mathrm{Au} + \frac{1}{2}\mathrm{DHA} + 2\mathrm{Cl^-} + \mathrm{H^+} \tag{2.24a}$$

$$\mathrm{AuCl_2^-} + L\text{-}\mathrm{AscH^-} \xrightarrow{k_8} \mathrm{Au} + \mathrm{DHA} + 2\mathrm{Cl^-} \tag{2.24b}$$

where k_7 and k_8 are the rate constants of the reactions of Equations (2.24a) and (2.24b), respectively. It is known that the rate of nuclei formation is slow [137, 139, 140].

The third stage corresponds to autocatalytic growth of gold. At the very beginning of this step, the single gold atom catalyze the reduction of an Au(I) chloride anion by *L*-ascorbic acid and then becomes $\mathrm{Au_2}$. This procedure can be defined as [137]:

$$\mathrm{AuCl_2^-} + \frac{1}{2}L\text{-}\mathrm{AscH_2} + \mathrm{Au} \xrightarrow{k_9} \mathrm{Au_2} + \frac{1}{2}\mathrm{DHA} + 2\mathrm{Cl^-} + \mathrm{H^+} \tag{2.25a}$$

$$\mathrm{AuCl_2^-} + L\text{-}\mathrm{AscH^-} + \mathrm{Au} \xrightarrow{k_{10}} \mathrm{Au_2} + \mathrm{DHA} + 2\mathrm{Cl^-} \tag{2.25b}$$

where k_9 and k_{10} are the reaction rate constants of Equations (2.25a) and (2.25b), respectively.

The product $\mathrm{Au_2}$ has more surface area, and its electronic structures change. Because of these, it catalyzes the reduction of $\mathrm{AuCl_2^-}$ at different rate and becomes $\mathrm{Au_3}$. Thus, the reaction rate constants for the third state may vary with the number of atoms of the growing gold. The growth of gold proceeds by this chain reactions at the chaning reaction rate until the system uses up either $\mathrm{AuCl_2^-}$ or *L*-ascorbic acid. The reaction equations of the Finke-Watzky two step mechanism for all size of gold products can be generalized. So, the reaction equations in the second and the third stages can be redefined as:

$$\mathrm{AuCl_2^-} + \frac{1}{2}L\text{-}\mathrm{AscH_2} + \mathrm{Au}_{n-1} \xrightarrow{k_{\mathrm{Au}_n}} \mathrm{Au}_n + \frac{1}{2}\mathrm{DHA} + 2\mathrm{Cl^-} + \mathrm{H^+} \tag{2.26a}$$

$$\mathrm{AuCl_2^-} + L\text{-}\mathrm{AscH^-} + \mathrm{Au}_{n-1} \xrightarrow{k'_{\mathrm{Au}_n}} \mathrm{Au}_n + \mathrm{DHA} + 2\mathrm{Cl^-} \tag{2.26b}$$

where k_{Au_n} and k'_{Au_n} are the rate constants of reaction Equations (2.26a) and (2.26b), respectively. These constants vary depending on *n*, which indicates the number of reactions which the Au_n product experiences. When the gold nucleus undergoes a series of these reactions *n* times, it finally bcomes Au_n. This expression can define not only the Finke-Watzky two step mechanism but also further growth of gold in terms of *n*.

The overall reaction rate of these three stages must be determined experimentally [50]. However, nothing is known about how to experimentally measure the reaction rate within the EDL of the surface of colloidal particles. We need to develop a strategy to guess reaction rates to describe the gold coating behaviors based on this Finke-Watzky two step mechanism.

If we take a close look at Equations (2.23a) to (2.23f), $\mathrm{AuCl_2^-}$ is the product of all these reaction equations in the first stage. In addition to this, $\mathrm{AuCl_2^-}$ participates as a reactant in Equation (26a) and (26b) of the second and the third stages. Because $\mathrm{AuCl_2^-}$ exists as an intermediate of the entire reaction, we can use the reaction rate in terms of the initial concentration of $\mathrm{AuCl_2^-}$ to guess the trend of each stage during the gold coating procedure. Overall, the concentration of $\mathrm{AuCl_2^-}$ is proportional to the rate of its formation in the first stage and inversely proportional to its consumption rate in the second and the third stages. To make the model simpler, it is necessary to discuss each step of the gold synthesis more specifically.

Only the first stage proceeds for the very short time at the beginning of the whole process of gold synthesis whereas the second and the third stages are inactive [142]. Therefore, if we only consider the reactions only at the very beginning of this first stage, the reaction rate in terms of $AuCl_2^-$ becomes very simple. When the concentration of $AuCl_2^-$ is locally greater than the saturation concentration, nucleation of gold begins. At the very beginning of the second stage, the initial reaction rate of nucleation is proportional to the concentration of $AuCl_2^-$, which is produced in the first stage. Since the third step is an autocatalytic reaction, the reaction in this stage takes place very quickly when nuclei of gold are formed in the second stage. Once the growth of gold occurs, $AuCl_2^-$ is consumed very quickly while it is produced from the reduction of Au(III) complex [137]. This results in the decrease in the concentration of $AuCl_2^-$ intermediate. When its concentration becomes lower than the saturation concentration for nucleation, the second stage terminates [142]. After this, the reactions only in the first and the third stages proceed.

From this discussion, it seems promising to consider only the reactions between the beginning of the first stage and the initial stage of the nucleation for the purpose of model simplification. Since we know the initial concentration gradient of all ionic species, we can define the ratio of the initial reaction rate of the formation of $AuCl_2^-$ at distance x away from the PAH/PS particle surface. With this ratio of the initial reaction rates, we can compare the local concentration of $AuCl_2^-$ at any point x away from the surface. In addition to this, we can guess the initial rate of nucleation of gold because it is proportional to the concentration of $AuCl_2^-$.

Thus, we propose that the ratio of the initial reaction rate of the formation of $AuCl_2^-$ at distance away from its surface can describe the gold coating behavior on the amine-functionalized

PS particle. From Equations (2.23a) to (2.23f), the initial reaction rate of the formation of $\mathrm{AuCl_2^-}$ at x away from the surface of PAH/PS particle, $r_{\mathrm{AuCl_2^-},x,t=0}$, is defined as:

$$\begin{aligned} r_{\mathrm{AuCl_2^-},x,t=0} = & \left[\mathrm{AuCl_4^-}\right]_{x,t=0}\left(k_1\left[L\text{-}\mathrm{AscH_2}\right]_{x,t=0} + k_2\left[L\text{-}\mathrm{AscH^-}\right]_{x,t=0}^2\right) \\ & + \left[\mathrm{AuCl_3(OH)^-}\right]_{x,t=0}\left(k_3\left[L\text{-}\mathrm{AscH_2}\right]_{x,t=0} + k_4\left[L\text{-}\mathrm{AscH^-}\right]_{x,t=0}^2\left[\mathrm{H^+}\right]_{x,t=0}\right) \\ & + \left[\mathrm{AuCl_2(OH)_2^-}\right]_{x,t=0}\left(k_5\left[L\text{-}\mathrm{AscH_2}\right]_{x,t=0} + k_6\left[L\text{-}\mathrm{AscH^-}\right]_{x,t=0}^2\left[\mathrm{H^+}\right]_{x,t=0}^2\right) \end{aligned} \quad (2.27)$$

where t is time. Because each rate constant of Equation (2.23a) to (2.23f) cannot be experimentally determined, we assume that $k_1 = k_3 = k_5 = 1\ \mathrm{M \cdot s^{-1}}$, $k_2 = 1\ \mathrm{M^{-2} \cdot s^{-1}}$, and $k_4 = k_6 = 1\ \mathrm{M^{-3} \cdot s^{-1}}$ for the purpose of simplification. Dividing the initial reaction rate profiles by the minimum initial reaction rate value at $x = 1$ μm for the L-ascorbic acid concentration of 4.950×10^{-4} M gives the ratio of the initial reaction rate distributions of $\mathrm{AuCl_2^-}$. The constants and the symbols used in this section are listed in Table 2.5.

Table 2.5. Variables and constants used to estimate the initial reaction rate of the formation of Au(I) chloride complex.

Description of quantity	Symbol	Value $^{(a)}$
Absolute temperature	T	298.15 K
Acid dissociation constant of reaction Equation (2.1a)	K_{a_1}	$10^{-4.12}$ [66]
Acid dissociation constant of reaction Equation (2.1b)	K_{a_2}	$10^{-11.51}$ [66]
Acid dissociation constant of reaction Equation (2.5a)	K_{a_3}	3.98×10^{-6} [137]
Acid dissociation constant of reaction Equation (2.5b)	K_{a_4}	0.25 [137]
Acid dissociation constant of reaction Equation (2.5c)	K_{a_5}	0.36×10^{-2} [137]
Acid dissociation constant of reaction Equation (2.5d)	K_{a_6}	2.81×10^{-5} [137]
Acid dissociation constant of reaction Equation (2.5e)	K_{a_7}	8.91×10^{-9} [137]
Acid dissociation constant of reaction Equation (2.5f)	K_{a_8}	10^{-10} [137]
Acid dissociation constant of reaction Equation (2.14)	K_{a_8}	$10^{-8.9}$ [83]
Avogadro's number	N_A	$6.02214076 \times 10^{-23}$ mol^{-1}
Boltzmann constant	k_B	1.380649×10^{-23} J/K
Bulk molar concentration of ionic species i	$C_{\infty,i}$	M
Distance away from the surface	x	m
Distance between the surface of two particles	D	m
Elementary charge	q	$1.602176634 \times 10^{-19}$ C
Molar concentration of ionic component i at distance x away from the surface	$C_{x,i}$	M
Permittivity of vacuum	ε_0	8.854×10^{-12} F/m
Potential at distance x away from the surface	ψ_x	V
Relative permittivity of a medium m at room temperature	ε_m	
Total number of ionizable site density of PAH layer	$N_{total,PAH/PS}$	3.32×10^{-6} mol/m^2 [85]
Surface charge density	σ	C/m^2
Surface Potential	ψ_0	V
Valence of ionic species i	z_i	

$^{(a)}$ Only units are listed for variables

2.4.2. Casimir-Lifshitz force

Since the surfaces of the gold-coating and gold nanoclusters synthesized in this experiment are electrically neutral, the primary interaction force between two gold particles or between a gold particle and a PAH/PS particle is the Casimir-Lifshitz force. For gold nanoparticles generated or being growing at the distance x away from the PAH/PS surface, the

Casimir-Lifshitz interaction between the particles is determined depending on the size and the location of the particles, the distance between the particles, and ionic concentration of the medium. This occurs during or even after the reaction. The Casimir-Lifshitz force is the most advanced form of the vdW force and accurately describes retardation effect [132]. This force triggers the movement of all the colloids in the system. This phenomenon makes the differences in the morphology of the gold coating on PAH/PS surface. We can guess the positions of the generated gold nanoclusters away from the surface of the PAH/PS particle from the relative initial reaction rate profile computed in the previous section. If we can expect the movement direction of these gold nanoclusters by using the Casimir-Lifshitz force between the particles, we can better understand the gold coating behaviors on the positively charged dielectric particles.

With the frequency-dependent dielectric response functions of two spherical particles and a medium over a wide range of frequency, we can express the Casimir-Lifshitz force between the two particles as a function of distance [25, 132-134, 143-150]. Since gold nanoparticles growing have different electric structures depending on the total number of gold atoms, the dielectric response functions of the gold nanoparticles keep changing during synthesis. In addition to this, because gold nanoclusters without surface treatment have no colloidal stability, it is very difficult to experimentally measure adsorption spectrum of the uncharged gold nanoclusters in water. Therefore, in order to obtain the Casimir-lifshitz force profile between the two gold nanoclusters including different numbers of Au atom, their dielectric response function was calculated from the simulated photo-absorption spectra.

2.4.2.1. Photo-absorption spectrum of gold nanoclusters by real-time propagation TDDFT

The photo-absorption spectra of the gold nanoclusters were simulated using the real-time propagation of time-dependent density-functional theory (TDDFT) code [151-153] implemented in the open-source quantum chemistry software, GPAW (grid-based projector-augmented wave method) [154], with the linear combination of atomic orbitals (LCAO) mode [155]. Eight different sizes of Au_n nanoclusters (number of Au atoms, n = 1, 2, 3, 4, 13, 55, 147, and 309), which are based on space group of $Fm\bar{3}m$ (225) and lattice constant of 4.08 Å were, constructed by using the open-source software, Atomic Simulation Environment (ASE) [156]. The core criterion of the representative structure of each Au_n nanocluster is that the nanocluster favors minimum surface energy during growth. In case of n = 13, 55, 147, and 309, the nanoclusters follow an icosahedron with I_h symmetry [157-162]. The geometries of the Au_n nanoclusters used for the real-time propagation TDDFT simulation are visualized by using PyMOL in Figure 2.1. Each Au_n nanocluster was placed into a cubic unit cell with minimum vacuum size around the system $d_{\mathrm{vac}} = 6$ Å. To approximate the exchange and correlation for the optical properties of gold nanoclusters, the adiabatic Gritsenko-van Leeuwen-van Lenthe-Baerends-solid-correlation (GLLB-sc) functional was used with the real-space grid spacing $h_{\mathrm{rgs}} = 0.3$ Å. P-valence basis set for Au were used to improve density of states of the unoccupied states [151]. To reduce computational cost, 18 basis functions including 5d, 6s, 6p, and forbidden bands per Au atom were selected. For proper convergence of the ground-state calculation of each gold nanocluster during the self-consistency cycle, the selected input parameters (linear mixing coefficient, number of old densities, and weight) of the density mixer listed in Table 2.6. were used with the convergence tolerance of 10^{-12}. To ensure the trend of the results, the band gap information was obtained by analyzing projected density of states (PDOS) of each Au_n nanocluster. The real-time propagation TDDFT simulation was performed in the x direction for 30 fs using time steps of 10 as [151-155]. The simulated results were convoluted by a Gaussian broadening with 0.1 eV full width at half maximum (FWHM) from 0 to 30 eV with energy resolution of 0.01 eV. The photo-absorption spectra of GPAW package are expressed as dipole strength function in Hartree atomic unit system.

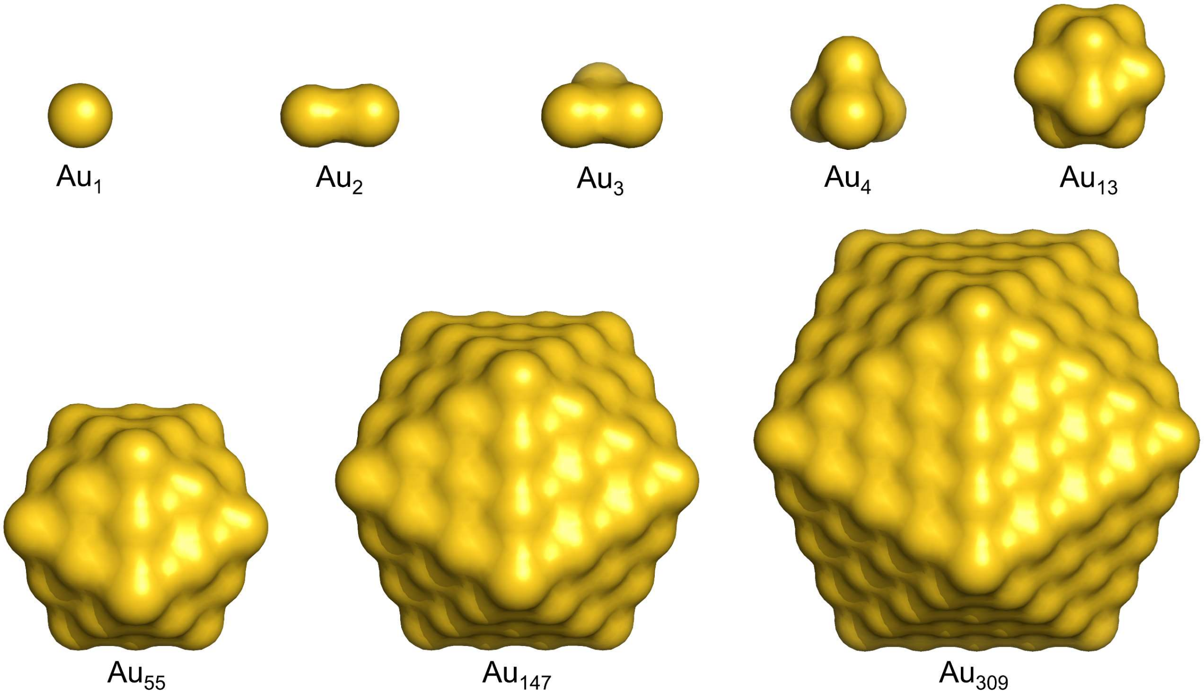

Figure 2.1. Visualized geometries of Au_n nanoclusters constructed for the real-time propagation of TDDFT simulation.

Table 2.6. Calculation parameters for time-propagation time-dependent density functional theory simulation.

Au_n	Linear mixing coefficient	Number of old density	Weight	Number of bands
Au_1	0.05	1.0	1.0	18
Au_2	0.05	1.0		36
Au_3	0.05	1.0		54
Au_4	0.05	1.0		72
Au_{13}	0.25	1.0		234
Au_{55}	0.02	5.0		990
Au_{147}	0.02	5.0		2646
Au_{309}	0.02	5.0		5562

2.4.2.2. Extinction coefficient

The simulated dipole strength function $S(\omega)$ result in the atomic units can be converted to the optical absorption cross-section $\sigma_{\text{abs}}(\omega)$ by using the following relation:

$$\sigma_{\text{abs}}(\omega) = \frac{\pi h c r_e}{q} S(\omega) \tag{2.28}$$

where ω is the angular frequency, h is the Planck constant, and c is the speed of light. And r_e is the classical electron radius defined as:

$$r_e = \frac{q^2}{4\pi\varepsilon_0 m_e c^2} \tag{2.29}$$

where m_e is the electron mass. The absorption coefficient $\alpha_{\text{abs}}(\omega)$ can be expressed from the optical absorption cross-section $\sigma_{\text{abs}}(\omega)$ as:

$$\alpha_{\text{abs}}(\omega) = \frac{\sigma_{\text{abs}}(\omega)}{V_{\text{vdW}}} \tag{2.30}$$

where V_{vdW} is the vdW volume. At this normalization stage, the definition of the volume of the nanocluster can be critial to the dielectric response function at Matsubara frequencies. To minimize the errors, we use vdW volume in stead of the volume of quasi-spherical model. We defined the vdW surfaces of the Au*n* nanoclusters with polygon mesh by using PyMol based on the metallic radius of 144 pm and the vdW radius of 166 pm for gold. Then, the vdW volume of each nanocluster was computed from this vdW surface as listed in Table 2.7. The extinction coefficient $k(\omega)$ can be calculated from the absorption coefficient $\alpha_{\text{abs}}(\omega)$ by using the following relation:

$$k(\omega) = \frac{c}{2\omega} \alpha_{\text{abs}}(\omega) \tag{2.31}$$

Table 2.7. Polygon mesh data and computed van der Waals (vdW) volumes of the structured gold nanospheres based on metallic radius of 144 pm and vdW radius of 166 pm.

Au_n	Vertices	Faces	Volume (m^3)
Au_1[(a)]	N/A	N/A	1.9161×10^{-29}
Au_2	1,788	596	3.8973×10^{-29}
Au_3	2,436	812	5.9397×10^{-29}
Au_4	2,940	980	7.8862×10^{-29}
Au_{13}	6,900	2,300	2.6151×10^{-28}
Au_{55}	18,168	6,056	1.0892×10^{-27}
Au_{147}	34,764	11,588	2.8670×10^{-27}
Au_{309}	56,688	18,896	5.9603×10^{-27}

(a) Volume of a sphere with vdW radius of gold.

2.4.2.3. Loss factor

The imaginary part of the dielectric response function $\varepsilon''(\omega)$ (also called loss factor) can be computed from the following equation [132]:

$$\varepsilon''(\omega) = 2n(\omega)k(\omega) \tag{2.32}$$

where $n(\omega)$ is refractive index in a function of angular frequency. The refractive index $n(\omega)$ and the extinction coefficient $k(\omega)$ are the real part and the imaginary part of the complex refractive index $\tilde{n}(\omega)$, respectively. This relation is defined as [132]:

$$\tilde{n}(\omega) = n(\omega) + ik(\omega) \tag{2.33}$$

This tells us that $n(\omega)$ and $k(\omega)$ are Hilbert transform pairs. Thus, we can calculate $n(\omega)$ by using the Kramers-Kronig relation defined as:

$$n(\omega) = 1 + \frac{1}{\pi} P \int_{-\infty}^{+\infty} \frac{k(\omega')}{\omega' - \omega} \mathrm{d}\omega' \tag{2.34}$$

where *P* is Cauchy principal value for integrals with divergences [163-165]. To ensure the result accuracy of this transform, the data for $k(\omega)$ should include the frequency range from zero to infinity. Because the domain of the dipole strength function we acquired from real-time propagation TDDFT simulation is from 0 to 30 eV with the resolution of 0.01 eV, this transform is valid. The loss factor $\varepsilon''(\omega)$ for each Au$_n$ nanocluster was determined using Equation (2.32) with the calculation results from Equations (2.31) and (2.34).

For the comparison purpose, the loss factor of bulk gold was computed based on Hubbard-corrected local density approximation (LDA+U) [166] implemented in GPAW [167]. The whole calculation for the DFT and the dielectric response of the bulk Au [168] was performed by using the modified Python scripts from the online example code [169]. The self-consistent cycle was performed on sparse 16 × 16 × 16 k-point grid sampling of Brillouin zone for the unit cell of Au (lattice constant: 4.08 Å, space group: $\mathrm{Fm\bar{3}m}$ (225)) with the 32 basis functions and a plane wave cutoff energy of 400 eV. The fractional occupancy of states was established by using Fermi-Dirac distribution with the smearing of the occupation number of 0.10 eV. The excitation energy was estimated by non-self-consistent field method with Brillouin zone sampled by k-point grid of density 35 points/ Å^3. For the calculation procedure of the dielectric function of bulk gold, the damping parameter of 0.0267 eV and Hubbard correction U of 2.0 eV were selected to fit the results to the most cited experimental data [170].

2.4.2.4. Dielectric response function at Matsubara frequencies

Complex frequency $\tilde{\omega}$ is used to express both sinusoidal oscillation and exponential increment or decrement of the electromagnetic radiation as [132]:

$$\tilde{\omega} = \omega + i\xi \tag{2.35}$$

In Equation (2.35), ω indicates the real part of radial frequency, and ξ is imaginary part of radial frequency (also called Matsubara frequency) [132]. By using Kramers-Kronig relation the dielectric function at Matsubara frequency $\varepsilon(i\xi_m)$ is defined as:

$$\varepsilon(i\xi_m) = 1 + \frac{2}{\pi} P \int_0^{+\infty} \frac{\omega \varepsilon''(\omega)}{\omega^2 + \xi_m^2} \mathrm{d}\omega \tag{2.36}$$

where $i\xi_m = i2\pi \mathrm{k_B} Tm / \hbar$ is Matsubara frequency, m is zero or a positive integer, and $\hbar$ is the reduced Planck constant [59, 61, 132-134, 144-150]. The dielectric functions at imaginary frequencies for Au$_n$ nanoclusters and bulk gold were obtained by using Equation (2.36) with the computed loss factor values. The dielectric response function at imaginary frequencies for PS was computed from the measured extinction coefficient values and the extrapolated data of PS from other literature [171]. The complex refractive index data of water [172] was used to obtain the dielectric response function at Matsubara frequencies.

2.4.2.5. Casimir-Lifshitz force between particles across medium

The Casimir-Lifshitz interaction force $F_{ijk,\mathrm{SS}}$ between the two spherical particles i and k crossing medium j is defined as [132]:

$$F_{ijk,\mathrm{SS}}(D, R_i, R_k) = \frac{2\pi R_i R_k}{R_i + R_k} G_{ijk,\mathrm{PP}}(D) \tag{2.37}$$

where R_i and R_k are the radii of the sphere i and k. The radii for the Au$_n$ nanoclusters and the PS particle used to compute the Casimir-Lifshitz force are listed in Table 2.8. $G_{ijk,\mathrm{PP}}$ is the Casimir-Liftshitz interaction energy of the two plates i and k across the medium j and defined as [132, 143]:

$$G_{ijk,\mathrm{PP}}(D) = -\frac{A_{ijk}(D)}{12\pi D^2} \tag{2.38}$$

A_{ijk} is Hamaker coefficient in a function of D defined as [132, 143]:

$$A_{ijk}(D) = -\frac{3\mathrm{k_B} T}{2} \sum_{m=0}^{\infty}{}' \int_{r_m}^{\infty} p \ln[(1 - \overline{\Delta}_{ij} \overline{\Delta}_{kj} e^{-p})(1 - \Delta_{ij} \Delta_{kj} e^{-p})] \mathrm{d}p \tag{2.39}$$

where $\overline{\Delta}$ and Δ are transverse magnetic mode (TM) and transverse electric mode (TE), respectively. TM and TE are defined as [132]:

$$\text{TM:} \quad \overline{\Delta}_{ij} = \frac{s_j(\xi_m)\varepsilon_i(\xi_m) - s_i(\xi_m)\varepsilon_j(\xi_m)}{s_j(\xi_m)\varepsilon_i(\xi_m) + s_i(\xi_m)\varepsilon_j(\xi_m)} \tag{2.40}$$

$$\text{TE:} \quad \Delta_{ij} = \frac{s_j(\xi_m) - s_i(\xi_m)}{s_j(\xi_m) + s_i(\xi_m)} \tag{2.41}$$

where s_i is written as [143]:

$$s_i = \sqrt{p^2 + \left(\frac{2\xi_m D}{c}\right)^2 \left[\varepsilon_i(\xi_m) - \varepsilon_j(\xi_m)\right]} \tag{2.42}$$

The symbol ' in the sigma in Equation (2.39) indicates that the $m = 0$ term is to be multiplied by 1/2. This zero-frequency term without electrostatic screening effect is simplified as [143]:

$$A_{ijk,m=0}(D) = -\frac{3\mathrm{k_B}T}{4}\int_0^\infty p\ln\left(1 - \overline{\Delta}_{ij}\overline{\Delta}_{kj}e^{-p}\right)\mathrm{d}p \tag{2.43}$$

For the zero-frequency term, the static dielectric constants $\varepsilon(0)$ of all Au$_n$ nanoclusters and water were calculated with the refractive index and the extinction coefficient functions by using the following relation [143]:

$$\varepsilon(0) = \left[n(\omega)\right]^2 + \left[k(\omega)\right]^2 \tag{2.44}$$

The static dielectric constant for PS was obtained from other literature. The static dielectric constants ($m = 0$) for all materials used in this work are summarized in Table 2.9.

Table 2.8. Radii of Au$_n$ nanoclusters and PS particles used to compute Casimir-Lifshitz forces.

	Au$_1$	Au$_2$	Au$_3$	Au$_4$	Au$_{13}$	Au$_{55}$	Au$_{147}$	Au$_{309}$	PAH/PS
Radius (nm)	0.166[a]	0.210[b]	0.242[b]	0.266[b]	0.397[b]	0.638[b]	0.881[b]	1.12[b]	174[c]

[a] vdW radius of gold.
[b] Radii calculated by assuming that all Au$_n$ nanoclusters are spherical and their volumes follow the vdW volume listed in Table 2.7.
[c] Measured by using SEM.

Table 2.9. Static dielectric constants $\varepsilon(0)$ for Au$_n$ nanoclusters, PS, and water used to compute the zero-frequency term of Casimir-Lifshitz force.

	Au$_1$	Au$_2$	Au$_3$	Au$_4$	Au$_{13}$	Au$_{55}$	Au$_{147}$	Au$_{309}$	PS	Water
$\varepsilon(0)$	1.856[a]	1.628[a]	1.983[a]	1.892[a]	1.649[a]	0.550[a]	0.843[a]	1.703[a]	2.45[b]	78.30[b]

[a] Calculated from computed $n(0)$ and $k(0)$ of each component by using Equation (2.44).
[b] Calculated from the PS [171] and water [172] data of other literature.

Because the zero-frequency contribution to Casimir-Lifshitz force is an electrostatic interaction, in the medium containing free charges this entropic term becomes screened due to polarization of the free charges [25, 132-134]. The zero-frequency term screened by the free charges in the medium is written as:

$$A_{ijk,m=0}(D) = -\frac{3\mathrm{k_B}T}{4}\int_0^{\infty} p\ln(1-\overline{\Delta}_{ij,\mathrm{screened}}\overline{\Delta}_{kj,\mathrm{screened}}e^{-s})\mathrm{d}p \tag{2.45}$$

where $\overline{\Delta}_{\mathrm{screened}}$ is the screened TM and defined as:

$$\overline{\Delta}_{ij,\mathrm{screened}} = \frac{p\varepsilon_i(0) - s\varepsilon_j(0)}{p\varepsilon_i(0) + s\varepsilon_j(0)} \tag{2.46}$$

where s is in charge of the electrostatic screening effect [132]. When the gold nanoclusters and coatings are formed around the PS particle surface, the interaction between these gold particles experience the different strength of the electrostatic screening effect depending on ionic concentration gradient due to the potential changes from PS surface. If the centers of the two uncharged spherical particles *i* (radius: R_i) and *k* (radius: R_k) are at x_i and x_k away from the surface of the charged surface, respectively, the distance *D* is written as:

$$D = \left(x_k - R_k\right) - \left(x_i + R_i\right) \tag{2.47}$$

The *s* term in Equation (2.46) describes the change in electrostatic screening effect due to the ionic concentration gradient between the two gold nanoparticles and is defined as:

$$s = \left[p^2 + 4\left(\int_{x_i + R_i}^{x_k - R_k} \kappa_x \mathrm{d}x\right)^2 \right]^{1/3} \tag{2.48}$$

where κ_x is the specific inverse Debye length at *x* between two uncharged particles and expressed as:

$$\kappa_x = \sqrt{\frac{\sum_i q^2 z_i^2 C_{x,i} \mathrm{N_A} \times 10^3}{\varepsilon_0 \varepsilon_\mathrm{m} \mathrm{k_B} T}} \tag{2.49}$$

This modified inverse Debye length is introduced to apply the changes in electrostatic screening due to the ionic concentration gradient at any points in the system containing the charged surface. The Casimir-Lifshitz interaction force between the two gold nanoclusters across the water medium with a change in ionic concentration due to the charged surface by charge regulation was computed by using Equation (2.37) with the electrostatic screened zero-frequency term of Equation (2.45). The variables and the constants used to compute the Casimir-Lifshitz force are listed in Table 2.10. All calculations for Casimir-Lifshitz force were scripted in Python and accelerated by high performance computing using a Just-in-Time (JIT) compilation and parallelization in Numba [173].

Table 2.10. Variables and constants used to calculate Casmir-Lifshitz force.

Description of quantity	Symbol	Value [(a)]
Center point of sphere *i* away from the surface	x_i	m
Complex frequency	$\tilde{\omega}$	
Electron mass	m_e	$9.1093837015 \times 10^{-31}$ kg
Imaginary part of angular frequency	ξ	rad/s
Minimum vacuum size around the system	d_vac	6 Å
Planck constant	h	$6.62607015 \times 10^{-34}$ J·Hz^{-1}
Radius of sphere *i*	R_i	m
Real-space grid spacing	h_rgs	0.3 Å
Real part of angular frequency	ω	rad/s
Reduced Planck constant	$\hbar$	$1.054571817 \times 10^{-34}$ J·s
Speed of light in vacuum	c	299,792,458 m/s

(a) Only units are listed for variables.

2.5. Results and Discussion

To describe the gold coating behaviors on the amine-functionalized PS particles to the concentration with a change in the concentration of *L*-ascorbic acid, we develop our discussions in the following three parts: 1) comparison of initial reaction rate profiles, 2) Casimir-Lifshitz force to evaluate the movement direction of the generated gold nanoclusters in the initial stage, and 3) further discussions of the gold coating phenomenon with morphological analysis.

2.5.1. Initial reaction rate

Because the slow rate of nucleation of Au at the beginning of the reaction determines the overall reaction rate, this nucleation rate has a great influence on the shape of the gold coating on the positively charged dielectric particles. To predict the nucleation rates of gold in a function of distance *x* away from the positively charged PS particle surface, we first analyze the initial ionic concentration gradient under the EDL structure based on the charge regulation model. And then, we explain which reactions dominantly contribute the local nucleation of gold by analyzing the ratio of the initial reaction rate profile to the minimum reaction rate value.

2.5.1.1. Fractional compositions of L-ascorbic acid and Au(III) complex

In order to construct the charge-regulated EDL structure, the initial bulk concentrations of all ionic species from *L*-ascorbic acid and Au(III) complex should be defined first. This enables us to calculate the inverse debye screening length participating in Equation (2.21). The fractional compositions of *L*-ascorbic acid and Au(III) complex are plotted in Figures 2.2(a) and 2.2(b), respectively, in a function of the initial concentration of *L*-ascorbic acid of the reaction solution.

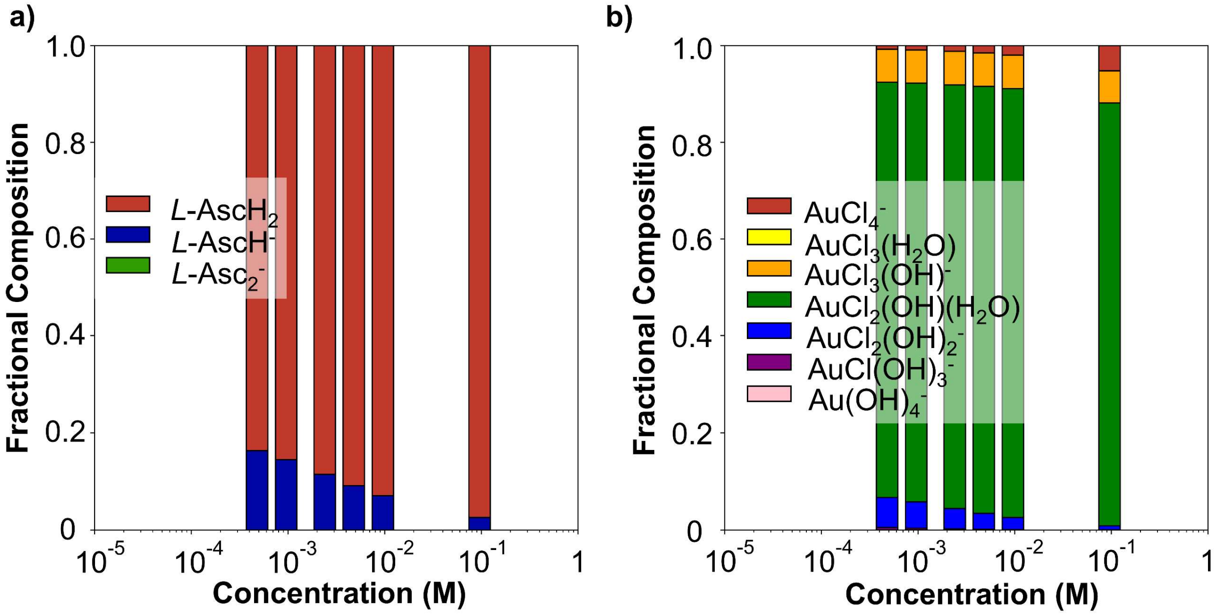

Figure 2.2. Fractional compositions of all possible forms of (a) *L*-ascorbic acid and (b) Au(III) complex in a variation of the initial concentration of *L*-ascorbic acid.

The fractional composition of *L*-ascorbic acid in Figure 2.2(a) was determined by using Equations (2.3a) to (2.3c) with the concentrations of proton listed in Table 2.3. First, as the initial concentration of *L*-ascorbic acid of the reaction solution increases, the pH of the solution decreases. As seen in Figure 2.3, only two forms of *L*-ascorbic acid, *L*-AscH$_2$ and *L*-AscH$^-$, exist in acidic solution. The reaction solution without any further pH adjustment must be acidic because each HAuCl$_4$ molecule bears one proton in the reaction system. Although the factional composition of

AscH$^-$ decreases when the concentration of *L*-ascorbic acid increases in the solution, the total amount of *L*-AscH$^-$ inceases resulting in more concentration of proton in the whole system. Second, as seen in Figure 2.2(a), when the concentration of *L*-ascorbic acid increases in the system, the fraction of *L*-AscH$_2$ increases while the fraction of *L*-AscH$^-$ decreases. This trend exactly follows the fractional composition distributions of *L*-ascorbic acid plotted in Figure 2.3. So, we know that the two existing forms, *L*-AscH$_2$ and *L*-AscH$^-$, in the system can directly reduce Au(III) complex in our system.

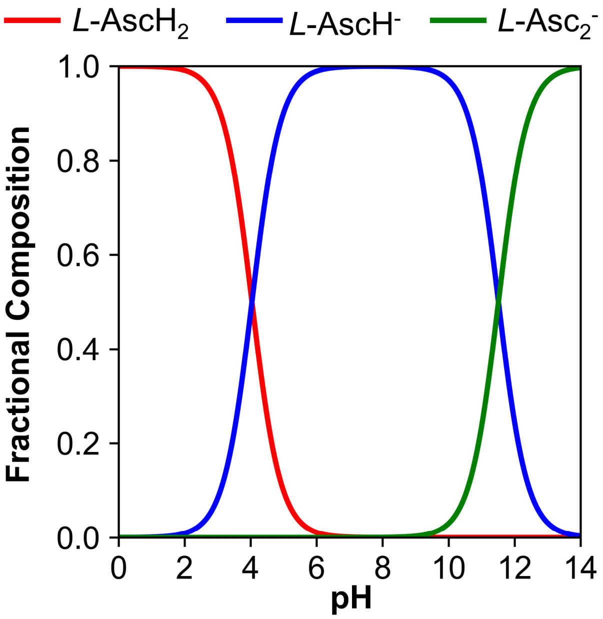

Figure 2.3. Fractional composition of all available forms of *L*-ascorbic acid in a change of pH.

The fractional composition of all the available forms of Au(III) complex was plotted in Figure 2.2(b) by using Equations (2.6a) to (2.6g) with the computed concentrations of proton and chloride anion from Table 2.3. As defined in the equalibrium reactions in Equations (2.5a) to (2.5f), Au(III) complex can exists as seven different forms. Five forms are negatively charged: $AuCl_4^-$, $AuCl_3(OH)^-$, $AuCl_2(OH)_2^-$, $AuCl(OH)_3^-$, and $Au(OH)_4^-$. And, two forms are neutral: $AuCl_3(H_2O)$

and $AuCl_2(OH)(H_2O)$. First, as seen in Figure 2.2(b), as the concentration of *L*-ascorbic acid increases, the sum of the proportions of all the available negative forms decreases. In the pH range between 2.54 and 3.41, the majorities of the active negative forms of Au(III) complex are $AuCl_4^-$, $AuCl_3(OH)^-$, and $AuCl_2(OH)_2^-$. These negatively charged forms directly participate in the initial reaction of the nucleation and the growth of gold. Specifically, the proportion of $AuCl_4^-$ increases with an increment of the concentration of *L*-ascorbic acid while the fractions of $AuCl_3(OH)^-$ and $AuCl_2(OH)_2^-$ tend to decrease. Second, the majority of the gold complex for all cases exists as a neutral form of $AuCl_2(OH)(H_2O)$. As the concentration of *L*-ascorbic acid increases, the fraction of $AuCl_2(OH)(H_2O)$ increases. This neutral form is not the direct source for the Finke-Watzky two-step reaction. Thus, in our experiments, only about 10% of Au(III) complex participate in the initial reaction. When the composition balance collapeses or the pH and the concentration of Cl^- of the solution change after the reaction starts, the neutral form $AuCl_2(OH)(H_2O)$ (90% of Au(III) complex) starts becoming the negatively charged forms $AuCl_4^-$, $AuCl_3(OH)^-$, and $AuCl_2(OH)_2^-$.

Figures 2.4(a), 2.4(b), 2.4(c), and 2.4(d) show the fractional distributions of Au(III) complex when 0.001, 0.01, 0.1, and 1 M of Cl^- is added , repectively. These fractional profiles show peak-shift to the higher pH with an increase in the concentration of Cl^-. In addition to this, the proportions of all forms vary depending on the concentrations of Cl^- as well as pH. In acidic evironments, the majority of Au(III) complex exists as an inactive neutral form $AuCl_2(OH)(H_2O)$ at the low concentration of Cl^-. In contrast, most of Au(III) complex under the high concentration of Cl^- are the negatively charged forms which can directly participate in the initial reactions. This tells us that we can control the fraction of the active Au(III) complex forms in the initial reaction rate by adding chloride containing salts such as NaCl or KCl.

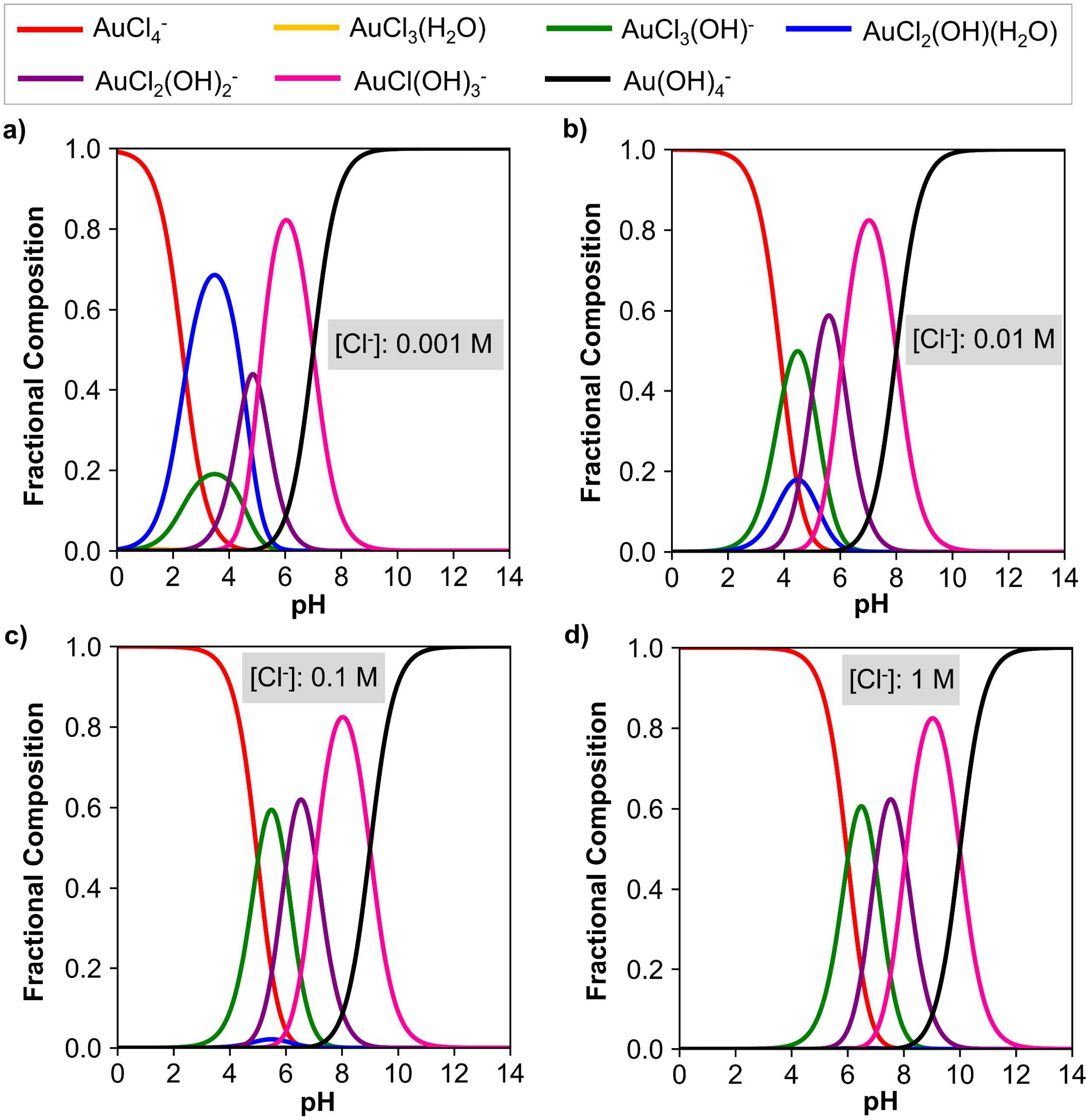

Figure 2.4. Fractional composition of all available forms of Au(III) complex in a change of pH at the concentration of chloride anion of (a) 0.001, (b) 0.01, (c) 0.1, and (d) 1 M.

As we have discussed so far, through this fractional composition analysis, we can predict which form is directly involved in the initial two-step reaction of gold nucleation and growth depending on the concentration of *L*-ascorbic acid. The bulk concentrations of all possible forms of *L*-ascorbic acid and Au(III) complex were calculated from the results of the fractional compositions and listed in Table 2.3.

2.5.1.2. EDL based on charge regulation

The surface charge density and the surface potential of the PAH/PS particles based on charge regulation are plotted in a function of the concentration of *L*-ascorbic acid in Figure 2.5(a). The surface charge density increases with an increment of the concentration of *L*-ascorbic acid. As mentioned earlier, as the concentration of *L*-ascorbic acid increases, the bulk concentration of protons in the system also increases. This increased concentration of protons causes more amounts of the amine groups of the PAH chain on the PS particle to be protonated and ionized, resulting in a stronger positive surface charge of the PAH/PS particles at low pH. In contrast, the surface potential of the PAH/PS particles falls with an increment in the concentration of *L*-ascorbic acid. As seen in Equation (2.20), the surface potential is proportional to the surface charge density when the concentrations of ions are constant. As the concentration of *L*-ascorbic acid increases, not only the concentration of hydrogen but also all the ionic concentrations of *L*-ascorbic acid and Au(III) complex increase. Since this increased total ionic concentration triggers a stronger electric field screening effect between the two charged PAH/PS particles, the potential becomes lowered everywhere between the particles. Thus, the charge regulation model well describes a realstic trade-off relation between the surface charge density and the surface potential in a function of the concentration of *L*-ascorbic acid.

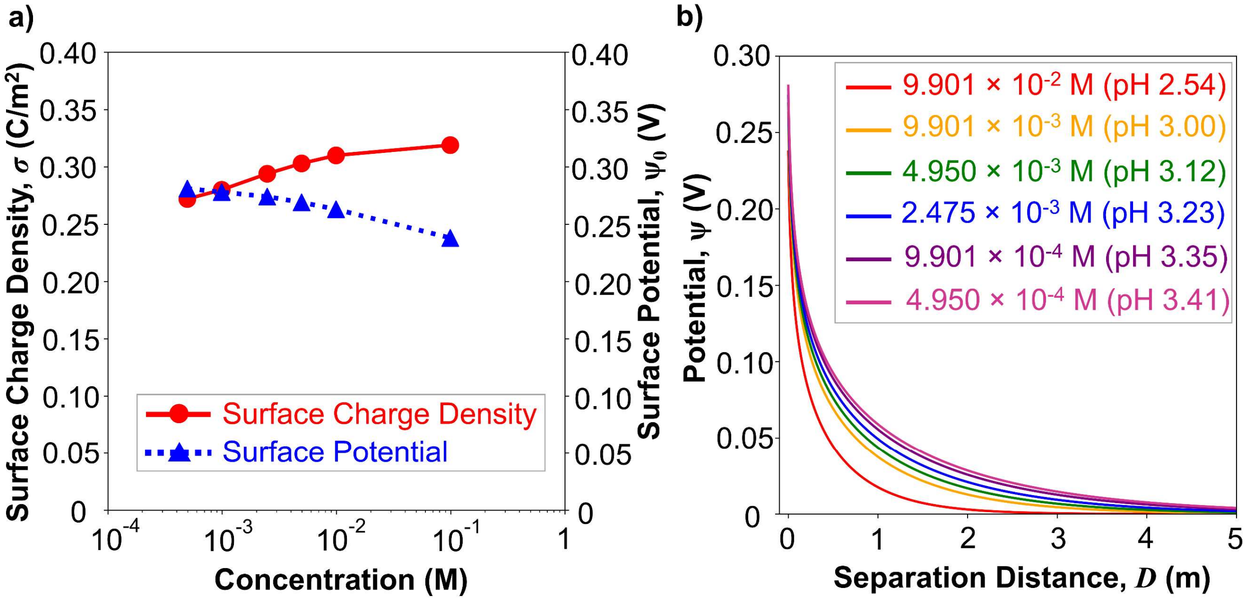

Figure 2.5. (a) surface charge density and the surface potential of the PAH/PS particles and (b) potential distributions at the distance away from the surface of PAH/PS particle in a change of *L*-ascorbic acid.

Figure 2.5(b) shows the potential distributions at the distance away from the surface of the PAH/PS particle for the different concentration of *L*-ascorbic acid. These EDL structures were determined by using Equation (2.21) with the surface potential and the inverse Debye length values from Table 2.4. The potential profiles in Figure 2.5(b) show that the strength of the potential weakens and the thickness of the EDL becomes thinner as the concentration of *L*-ascorbic acid increases. This is because that the densed ions of *L*-ascorbic acid and Au(III) complex screen the electric field between the charged PAH/PS particles stronger. The computed surface charge density and surface potential values of the PAH/PS particles from Table 2.4 indicate that the PAH/PS particles show an excellent colloidal stability for all the cases in the acidic environment. This means that each PAH/PS particle is well isolated so the EDL structures described in Figure 2.5(b) are only valid at the beginning of the gold coating reaction.

2.5.1.3. Initial ionic concentration profiles

The initial concentration profiles of 13 molecules except water at the distance *x* away from the surface of PAH/PS particles at the various concentrations of *L*-ascorbic acid are plotted in Figures 2.6(a) to 2.6(f). The Debye length for each system is displayed as well. To scrutinize the initial concentration gradient of each component, we will develop our discussion in the following order: 1) overall trends of all components and 2) detailed analysis on the initial concentrations of the forms of *L*-ascorbic acid and Au(III) complex participating the reaction.

A proton is the only positively charged free molecule in this system. The concentration of the proton is constant when it is far away from the surface of the PAH/PS particle. However, it exponentially decreases within the Debye length in all cases because the PAH/PS particle has a very strong positive surface charge in acidic solution as we discussed earlier. These protons are in equilibrium with the other nine different negative charges: OH^-, Cl^-, *L*-$AscH^-$, *L*-Asc^{2-}, $AuCl_4^-$, $AuCl_3(OH)^-$, $AuCl_2(OH)_2^-$, $AuCl(OH)_3^-$, and $Au(OH)_4^-$. The concentrations of all these negative charges skyrocket within the EDL due to the driving force to obey the local charge balance near the positively charged surface of the PAH/PS particle. On the other hand, the concentration of each anion is constant when it is far away from the surface. Lastly, there are three neutral forms: *L*-$AscH_2$, $AuCl_3(H_2O)$, and $AuCl_2(OH)(H_2O)$. Since these forms are neutral, their concentrations are constant everywhere and not directly affected by the charged surface.

As defined in Equations (2.23a) to (2.23f) and Equations (2.24a) and (2.24b), the forms of *L*-ascorbic acid that actually act as reducing agents in the reduction of Au(III) complex and Au(I) complex are *L*-$AscH_2$ and *L*-$AscH^-$. Since the other form *L*-Asc^{2-} is fully deprotonated, it does not function as a reducing agent. So, only both *L*-$AscH_2$ and *L*-$AscH^-$ forms are discussed. As seen in Figures 2.6(a) to 2.6(f), the concentration of *L*-$AscH_2$ increases in proportion to the amount of the *L*-ascorbic acid added. Since *L*-$AscH_2$ is neutral, its concentration for each case is constant regardless of distance away from the surface of the PAH/PS particle. The concentrations of *L*-AscH$^-$ in Figures 2.6(a) to 2.6(f) are constant and lower than the concentrations of *L*-AscH$_2$ when they are far away from the surface. However, the concentration of *L*-AscH$^-$ skyrockets in all cases when it approaches the positive surface of PAH/PS particle. The difference in the concentrations of *L*-AscH$^-$ between near the positive surface and outside the EDL is huge. For the case at the *L*-ascorbic acid concentration of 9.901×10^{-2} M in Figure 2.6(a), the concentration of *L*-AscH$^-$ outside the EDL is 10^{-3}M whereas the concentration of *L*-AscH$^-$ on the surface is 10 M. So, the concentration of *L*-AscH$^-$ near the surface is about 10,000 times higher than that far away from the surface. If the concentration of *L*-ascorbic acid is small in such a case (4.950×10^{-4} M) in Figure 2.6(f), the concentration of *L*-AscH$^-$ outside the EDL is about 10^{-4} M while that near the surface is 10 M. In this case, the concentration of *L*-AscH$^-$ in this case is about 100,000 times higher than that far away from the surface. That is, the difference in the concentration ratio of *L*-AscH$^-$ between near the surface and far away from the surface is much larger at low concentration of *L*-ascorbic acid than at high concentration. Due to this dramatic change in the concentration of *L*-AscH$^-$ depending on the location, the dominant form of *L*-ascorbic acid that actually participates the reduction of Au(III) or Au(I) complex is *L*-AscH$_2$ or *L*-AscH$^-$. The points at which the dominant form of *L*-ascorbic acid is reversed are 2 nm in Figures 2.6(a), 5 nm in 3(b), 8 nm in 3(c), 10 nm in 3(d), 12 nm in 3(e), and 14 nm in 3(f). We call these points as component determination points. Beyond this point, the neutral form *L*-AscH$_2$ dominates the reduction reaction whereas the negative form *L*-AscH$^-$ primarily participates the reduction within this point.

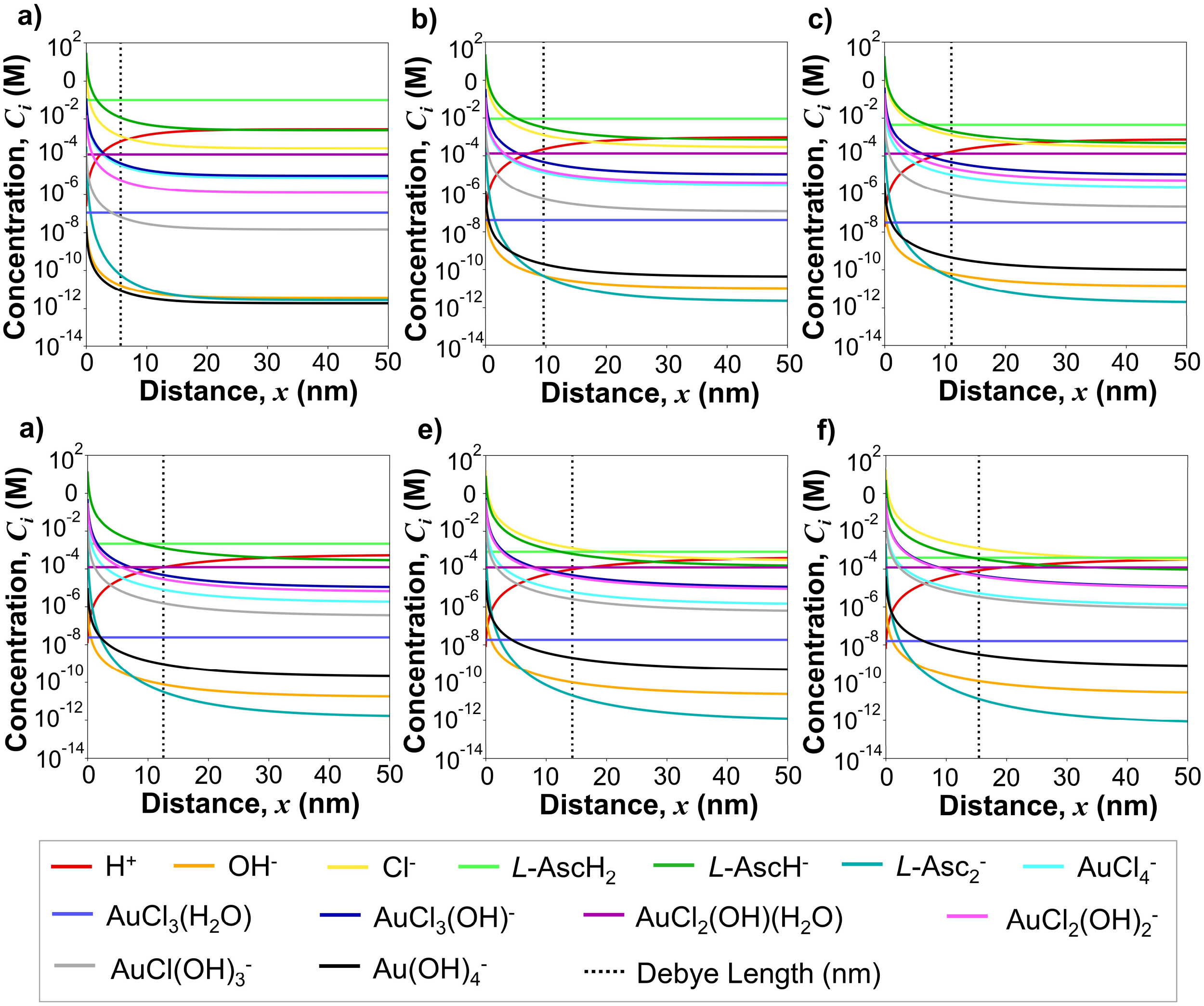

Figure 2.6. Initial concentration profiles of H^+, OH^-, Cl^-, L-$AscH_2$, L-$AscH^-$, L-Asc_2^-, $AuCl_4^-$, $AuCl_3(H_2O)$, $AuCl_3(OH)^-$, $AuCl_2(OH)(H_2O)$, $AuCl_2(OH)_2^-$, $AuCl(OH)_3^-$, and $Au(OH)_4^-$ at the distance x from the PAH/PS particle surface at L-ascorbic acid concentration of (a) 9.901×10^{-2}, (b) 9.901×10^{-3}, (c) 4.950×10^{-3}, (d) 2.475×10^{-3}, (e) 9.901×10^{-4}, and (f) 4.950×10^{-4} M.

As we discussed in Figure 2.2(b), although $AuCl_2(OH)(H_2O)$ does not directly participate in the reduction reaction, about 90% of the Au(III) complex exist in the form of $AuCl_2(OH)(H_2O)$ at the beginning of the reaction in all experiments of this work. As shown in Figures 2.6(a) to 2.6(f), its concentration is constant regardless of distance. In addition, since the amount of gold precursors added in in all cases is the same, all of these six experiments have almost the same concentrations of $AuCl_2(OH)(H_2O)$ as listed in Table 2.3.

In an acidic environment, there are three negatively charged forms of Au(III) complex which actually participate in the reduction reaction: $AuCl_4^-$, $AuCl_3(OH)^-$, and $AuCl_2(OH)_2^-$. The portion of all these three species only takes up about 10% for all cases. The concentration of each anion increases drastically inside the EDL as it approaches the positively charged surface of the PAH/PS particle as shown in Figures 2.6(a) to 2.6(f). At the concentration of *L*-ascorbic acid of 9.901×10^{-2} M, the concentrations of $AuCl_4^-$, $AuCl_3(OH)^-$, and $AuCl_2(OH)_2^-$ near the surface are about 1,000 times higher than those far away the surface as seen in Figure 2.6(a). At the concentration of *L*-ascorbic acid of 4.950×10^{-4} M, the concentrations of these three anions near the surface is about 10,000 higher than the anion concentrations far away from the surface as shown in Figure 2.6(f). Therefore, as the concentration of *L*-ascorbic acid increases in the system, the difference in the concentration ratio between near the particle surface and the outside of the EDL tends to become larger.

The proportion of the concentrations of these three negative charges varies depending on the concentration of *L*-ascorbic acid. First of all, among the three negative charges participating in the reaction, $AuCl_3(OH)^-$ shows the highest concentration in all experimental conditions. In Figure 2.6(a), the sum of the concentrations of $AuCl_4^-$ and $AuCl_3(OH)^-$ takes up about 96% of the sum of the concentrations of $AuCl_4^-$, $AuCl_3(OH)^-$, and $AuCl_2(OH)_2^-$. In Figures 2.6(b) and 2.6(c), the sum of $AuCl_3(OH)^-$ and $AuCl_2(OH)_2^-$ concentrations takes up about 83% and 82% of the total concentration of the three anions, respectively. In Figures 2.6(d), 2.6(e), and 2.6(f), the sum of $AuCl_3(OH)^-$ and $AuCl_2(OH)_2^-$ concentrations is about 90%, 93%, and 94% of the sum of the concentrations of the three anions, respectively. Therefore, the change in the concentration of *L*-ascorbic acid affects the pH and the total ionic concentration. As a result, this determines the dominant forms of the Au(III) complex participating in the reduction reaction.

2.5.1.4. Comparison of initial reaction rate profiles

Figure 2.7(a) shows the ratio of each initial reaction rate profiles of AuCl$_2^-$ to the minimum initial reaction rate at 1 μm for *L*-ascorbic acid concentration of 4.950 × 10^{-4} M. Unless otherwise mentioned, we call this ratio of the initial reaction rate as initial reaction rate for convenience. For each *L*-ascorbic acid concentration, the initial reaction rate of AuCl$_2^-$ is constant outside the Debye screening length. When the point of interest approaches to the surface, the initial reaction rate of AuCl$_2^-$ starts increasing. Within Debye screening length, the initial reaction rate of AuCl$_2^-$ tends to exponentially increase for all cases in acidic environment. Based on these trends of the initial reaction rate of AuCl$_2^-$,we will describe how the generation rate of gold nucleation varies locally inside and outside of Debye screening length at different concentration of *L*-ascorbic acid.

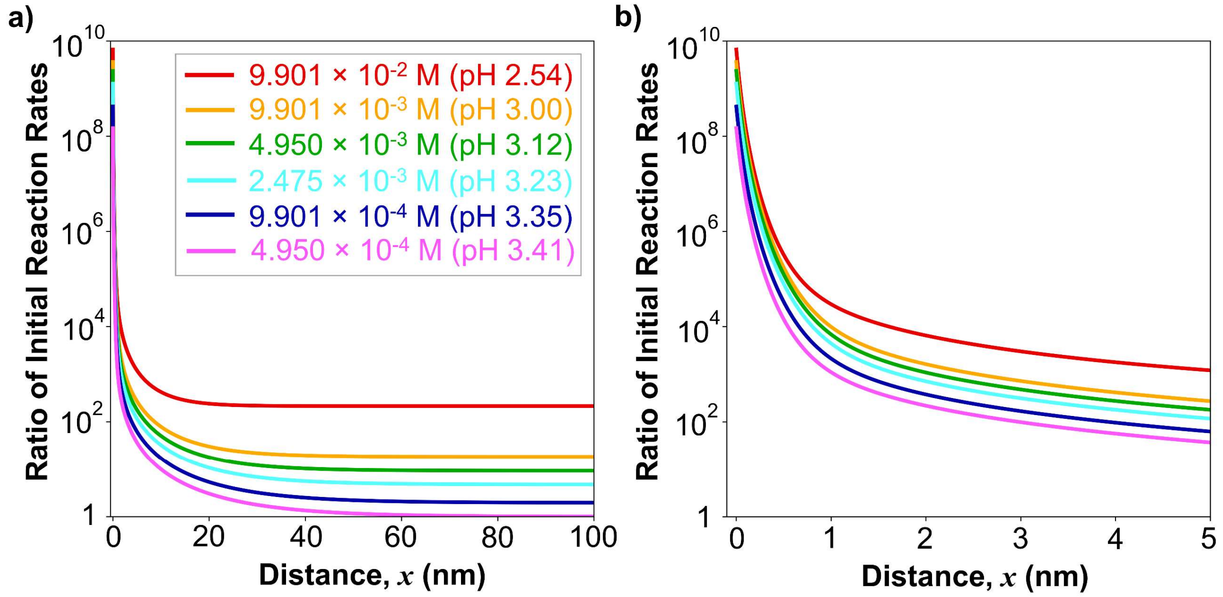

Figure 2.7. Ratio profiles of initial reaction rates in terms of AuCl$_2^-$ at various concentration of *L*-ascorbic acid in the distance range of (a) 0 to 100 nm and (b) 0 to 5 nm.

The initial reaction rate of $AuCl_2^-$ outside the Debye screening length is proportional to the *L*-ascorbic acid concentration as seen in Figure 2.7(a). For example, at the concentration of *L*-ascorbic acid of 4.950×10^{-4} M, the initial reaction rate outside the EDL is 1, so the probability of gold nucleation is expected to be relatively very low due to the initial reaction rate of $AuCl_2^-$ formation. At the concentration of *L*-ascorbic acid of 9.901×10^{-2} M, the initial reaction rate is 300. In this case, we can expect that the concentration of $AuCl_2^-$ rapidly reaches the critical concentration for gold nucleation, resulting in relatively high probability of gold nucleation outside of the Debye screening length. This indicates that the probability of generation of free gold particles outside the EDL is relatively high if the concentration of *L*-ascorbic acid added to the reaction is high. Conversely, if the concentration of *L*-ascorbic acid added is low, the probability of free gold particles being formed outside the EDL is low.

As shown in Figure 2.7(a), the initial rate of $AuCl_2^-$ formation rapidly increases as it approaches the surface within the Debye screening length, and this rate is proportional to the *L*-ascorbic acid concentration. The Debye screening length becomes shorter as the concentration of *L*-ascorbic acid increases. In other words, the location where the reaction rate starts increasing exponentially tends to be closer to the surface as the concentration of *L*-ascorbic acid increases. Figure 2.7(b) shows the initial reaction rate profile at the different concentration of *L*-ascorbic acid from the surface to 2 nm in more detail. When it is very close to the surface, the initial reaction rate of $AuCl_2^-$ sckyrockets and proportional to the the concentration of *L*-ascorbic acid. For example, at the concentration of *L*-ascorbic acid of 9.901×10^{-2} M, the initial rate of $AuCl_2^-$ formation on the surface is 9×10^9, which is about 10^7 times of the rate outside the EDL. In the case of the concentration of *L*-ascorbic acid of 9.901×10^{-2} M, the initial rate of $AuCl_2^-$ formation on the surface is 2×10^8, which is about 2×10^8 times of the rate outside the EDL. As shown in Figure 2.7(a), all experiments show these huge differences in the initial reaction rates between near the surface and far from the EDL. This indicates that the probability of gold nucleation near the positively charged particle surface is overwhelmingly higher than that far away the EDL. In fact, when the reaction starts, the highly populated reactants near the surface are rapidly consumed due to the very high reaction rate at the initial stage. After this, the local charge balance inside the EDL rapidly collapses, and then the reagent molecules existing outside the EDL move to the positively charged particle surface by diffusion. The driving force of this mass transport is the equilibrium force to restore the charge balance inside the EDL.

Figures 2.8(a) to 2.8(f) show the contribution profile of each reduction reaction of Au(III) complex corresponding to Equations (2.23a) to (2.23f) at the distance away from the surface at the different concentration of *L*-ascorbic acid. For all six reactions from Equations (2.23a) to (2.23f), each contribution tends to increase as it is close to the surface. This trend is consistent with the behavior of the concentration profile and the initial reaction rate as previously discussed. In all cases, the reaction of Equation (2.23b) is dominant within 1 nm from the surface, and near the surface $AuCl_2^-$ is primarily generated by the reaction of Equation (2.23b). Comparing Figures 2.8(a) to 2.8(f), at the distance of 1 nm or more from the surface, the dominant reactions that contribute the most to the initial reaction rate vary depending on the concentration of *L*-ascorbic acid. As seen in Figure 2.8(a), the reactions of Equations (2.23a) and (2.23c) are dominant at distances greater than 1 nm at the concentration of *L*-ascorbic acid of 9.901×10^{-2} M. As plotted in Figures 2.8(b), 2.8(c), and 2.8(d), the generation of $AuCl_2^-$ at the distance greater than 1 nm is governed by the reaction of Equation (2.23c) at the concentrations of *L*-ascorbic acid are 9.901×10^{-3}, 4.950×10^{-3}, and 2.475×10^{-3} M, respectively. Figures 2.8(e) and 2.8(f) show that the reactions of both Equations (2.23c) and (2.23e) mostly determine the formation of $AuCl_2^-$ at a distance greater than 1 nm when the concentration of *L*-ascorbic acid is relatively low at 9.901×10^{-4} and 4.950×10^{-4} M, respectively. Lastly, the reactions of Equations (2.23d) and (2.23f) have little effect on the generation of $AuCl_2^-$ everywhere for all cases. As discussed from this analysis, the dominant reaction type can vary depending on the concentration of *L*-ascorbic acid and the distance from the surface of the particles. In particular, the reason why the dominant reaction also varies depending on the distance is that the contribution of the reaction of Equation (2.23b) changes the most drastically with a distance. As mentioned earlier, the reaction of Equation (2.23b) dominates within 1 nm. However, for example, the contribution from the reaction of Equation (2.23b) at the distance of 5 nm or more can be ignored.

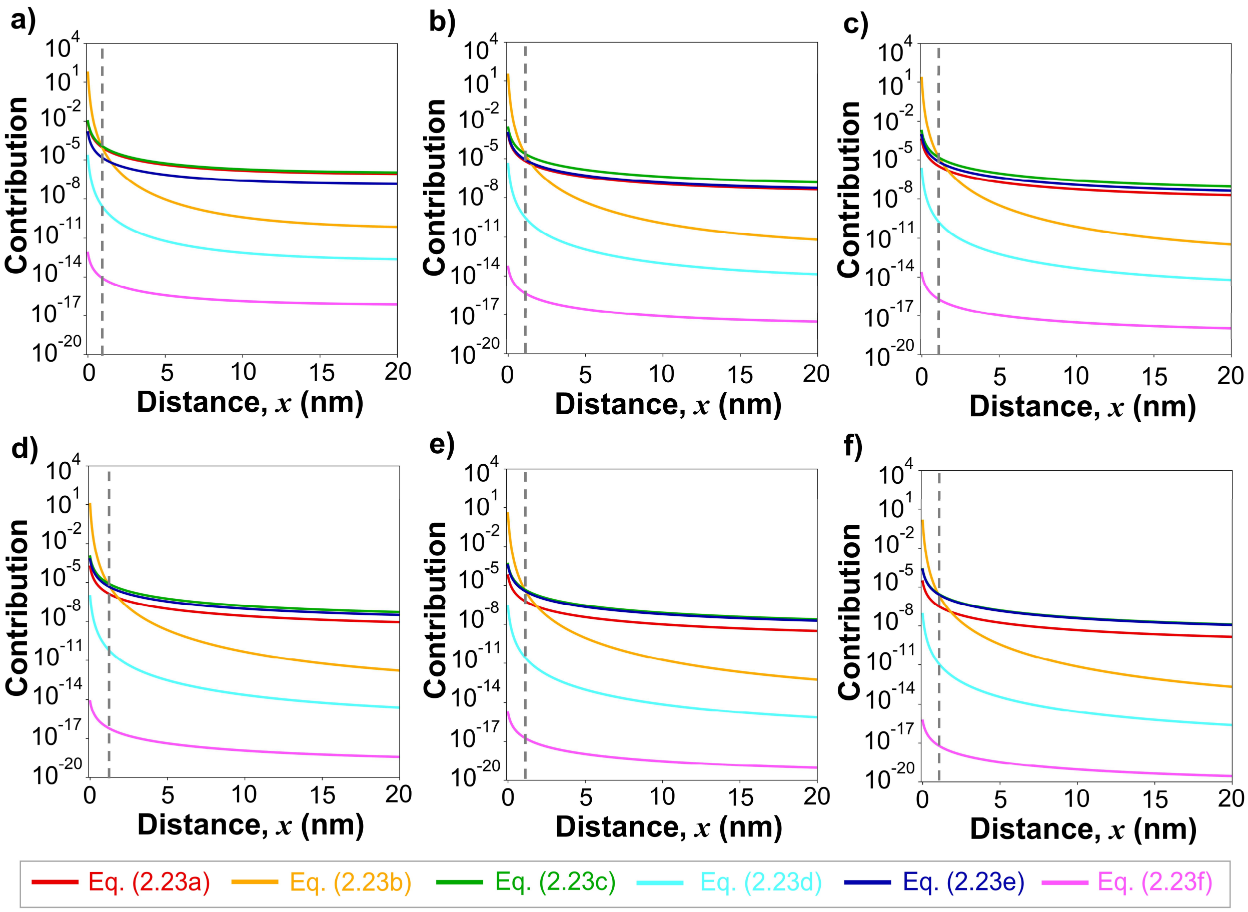

Figure 2.8. Contribution profiles of the reduction reactions of Au(III) complex corresponding to Equation (2.23a) to (2.23f) at the distance x from the PAH/PS particle surface at *L*-ascorbic acid concentration of (a) 9.901 × 10^{-2}, (b) 9.901 × 10^{-3}, (c) 4.950 × 10^{-3}, (d) 2.475 × 10^{-3}, (e) 9.901 × 10^{-4}, and (f) 4.950× 10^{-4} M.

So far, we described the initial reaction rate profile at distance away from the surface of the PAH/PS particle based on the defined concentration gradient of all types of molecules except water. For this, the EDL was constructed using the charge regulation model, and then the ionic concentration distribution from the particle surface was defined. The local concentration of $AuCl_2^-$ increases in proportion to the initial reaction rate defined in this discussion. And, when the local concentration of $AuCl_2^-$ reaches the critical concentration, the nucleation of gold occurs locally. Since the generation rate of nucleation is proportional to the concentration of $AuCl_2^-$, we assume that the local probability of the generation of nucleation can be roughly compared with the initial generation rate of $AuCl_2^-$. Figures 2.7(a) to 2.7(f) tell us that the probability of the generation of gold nucleation is the highest near surface and the lowest far away from the surface. The result of the nucleation is single atom. It becomes nanoclusters at the beginning of the growth and then nanoparticles after further growth. If this single atom or nanocluster grows only on the surface of the PAH/PS particles, we call it gold coating. Otherwise, the generated gold nucleation or gold nanoclusters far away from the surface may affect the morphology of the gold on the PAH/PS particle. Therefore, describing the movement of the generated gold atom and nanoclusters will give a better understanding of the behavior of the gold coating. In the next section, with the nucleation generation scenario based on the initial reaction rate defined, movement behavior of the generated nucleation and the growing nanoclusters will be described.

2.5.2. Deposition of gold nanoclusters on the PAH/PS particle by Casimir-Lifshitz force

To numerically explain how the generated gold nanoclusters are deposited on the PAH/PS particle during the synthesis, we first define the dielectric response function at imaginary frequency for all materials in the system. Then, we will determine the movement behaviors of the growing Au_n nanoclusters by describing Casimir-Lifshitz force between a PAH/PS particle and a Au_n nanocluster through water medium at ionic concentration gradient. Because there is no charge on the bare Au_n nanoclusters, we surmise that the Casimir-Lifshitz force is the only valid force in the system. Other forces such as hydration force, depletion force, etc. are ignored in this work.

2.5.2.1. Dielectric response function at Matsubara frequencies

The dipole strength functions as photo-absorption spectra by real-time propagation TDDFT simulation were obtained as seen in Figures 2.9. And, then the loss factor spectra in

Figure 2.10 were calculated from them. The data for bulk gold, PS, and water were extracted from other literatures [170-172].

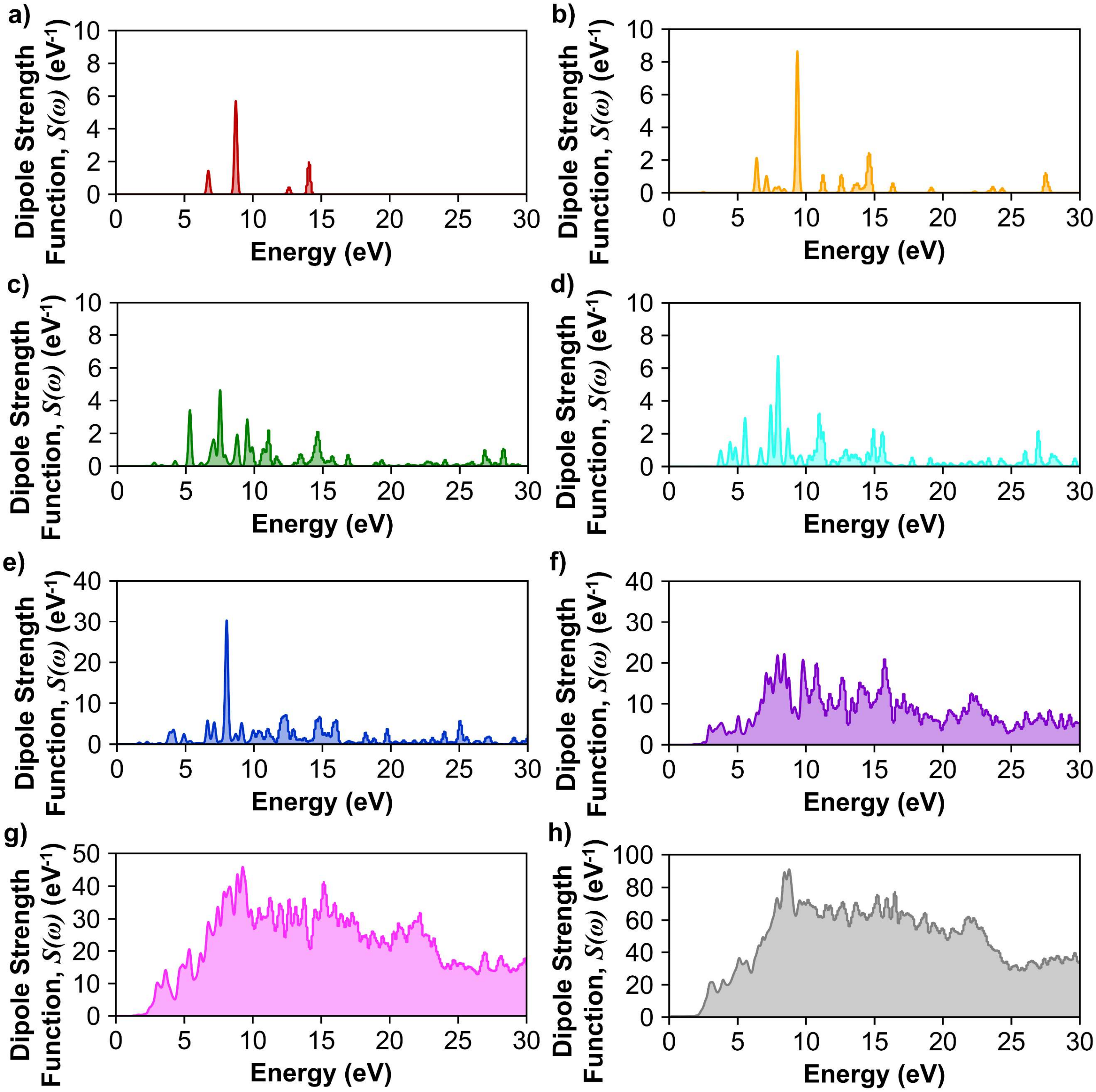

Figure 2.9. Results of the dipole strength function by real-time propagation TDDFT simulation of (a) Au_1, (b) Au_2, (c) Au_3, (d) Au_4, (e) Au_{13}, (f) Au_{55}, (g) Au_{147}, and (h) Au_{309}.

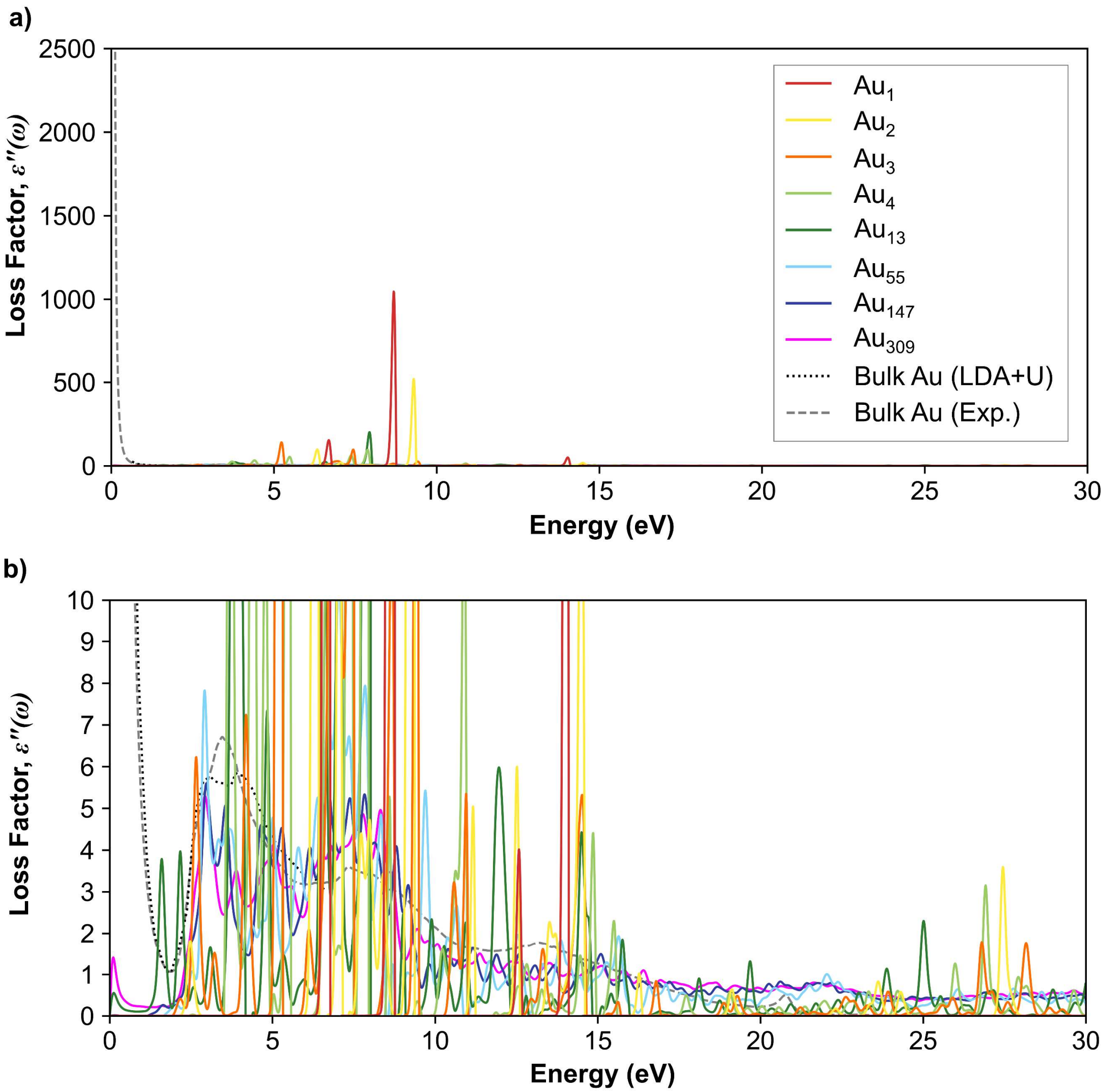

Figure 2.10. Loss factor spectra of Au$_n$ simulated by real-time propagation TDDFT, bulk Au computed by LDA+U method, and bulk Au experimentally measured by other literature at (a) large scale and (b) magnified scale.

Figure 2.11(a) shows the dielectric response function at imaginary frequency for the following materials: Au_1, Au_2, Au_3, Au_4, Au_{13}, Au_{55}, Au_{147}, Au_{309}, bulk gold, PS, and water. As seen in Figure 2.11(a), the dielectric response profiles at Matsubara frequencies of all Au$_n$ are far much lower than that of bulk gold. This is because the optical properties of the Au$_n$ nanoclusters are determined by their discretized orbital energy levels whereas that of the bulk gold is governed by the continuous bands of energy levels. Figure 2.11(b) is the magnified plot of Figure 2.11(a) with a smaller y-axis scale, and Figure 2.11(c) shows the enlarged range of the imaginary frequency between 10^{16} and 10^{18} rad/s. Comparing Figures 2.11(b) and 2.11(c) tells us that the tendency of dielectric response function at imaginary frequency depending on the number of Au atoms *n* is different in the frequency ranges based on 10^{16} rad/s. As seen in Figure 2.11(b), the dependency of the dielectric response functions on the number of Au atoms appears to be random in the imaginary frequency range lower than 10^{16} rad/s. On the other hand, the dielectric response function is proportional to n in the imaginary frequency range higher than that as shown in Figure 2.11(c). If we recall the definition of the Matsubara frequency, $i\xi_m = i2\pi k_B Tm/\hbar$, we can see the sampling frequency is intensively distributed at the higher imaginary frequency. Therefore, the sum of the dielectric response function of Au_n over the entire imaginary frequency range is proportional to the number of Au atoms *n*.

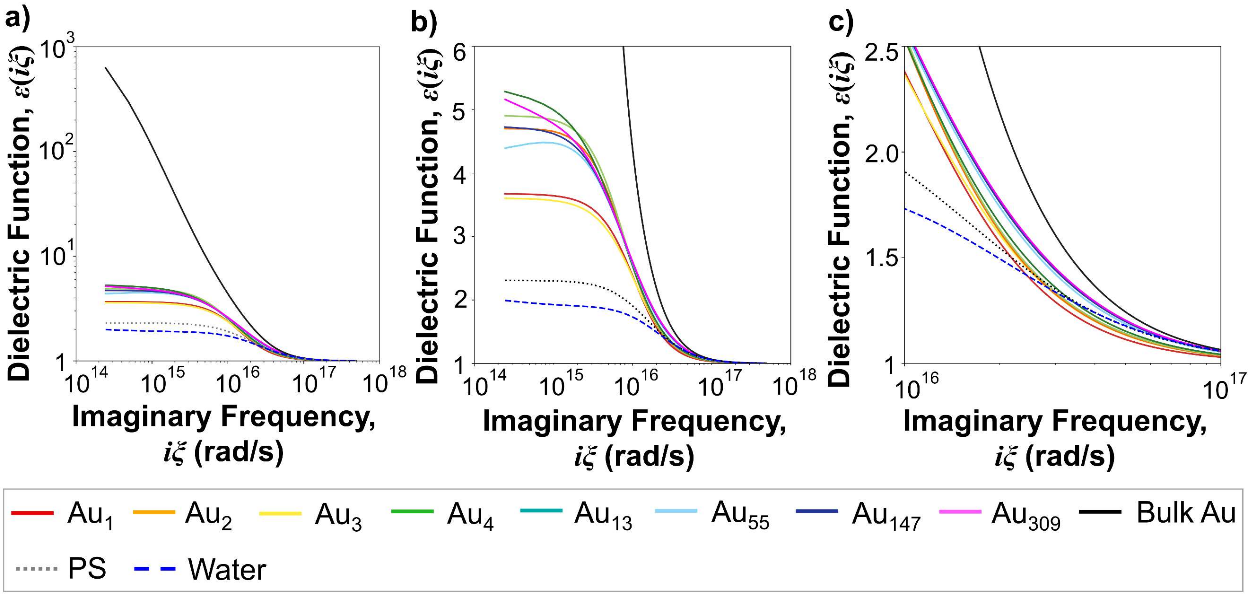

Figure 2.11. Computed dielectric response function at Matsubara frequency of Au_1, Au_2, Au_3, Au_4, Au_{13}, Au_{55}, Au_{147}, Au_{309}, bulk gold, PS, and water for $m = 1$ to 2000 in (a) large scale, (b) enlarged scale in the y-axis, and (c) imaginary frequency range between 10^{16} and 10^{17} rad/s.

To validate the trend of the computed dielectric response function at Matsubara frequency, the highest occupied molecular orbital and lowest unoccupied molecular orbital (HOMO-LUMO) near the fermi level is investigated from the PDOS distributions of all the Au_n nanoclusters in Figure 2.12. From the PDOS data, the HOMO-LUMO energy gaps of Au_n nanoclusters are plotted in Figure 2.13. The result shows that the HOMO-LUMO energy gap of an Au_n nanocluster increases as the number of Au atoms n decreases. Therefore, it can be said that the tendency of the computed dielectric response functions at Matsubara frequencies for the Au_n nanoclusters is reliable.

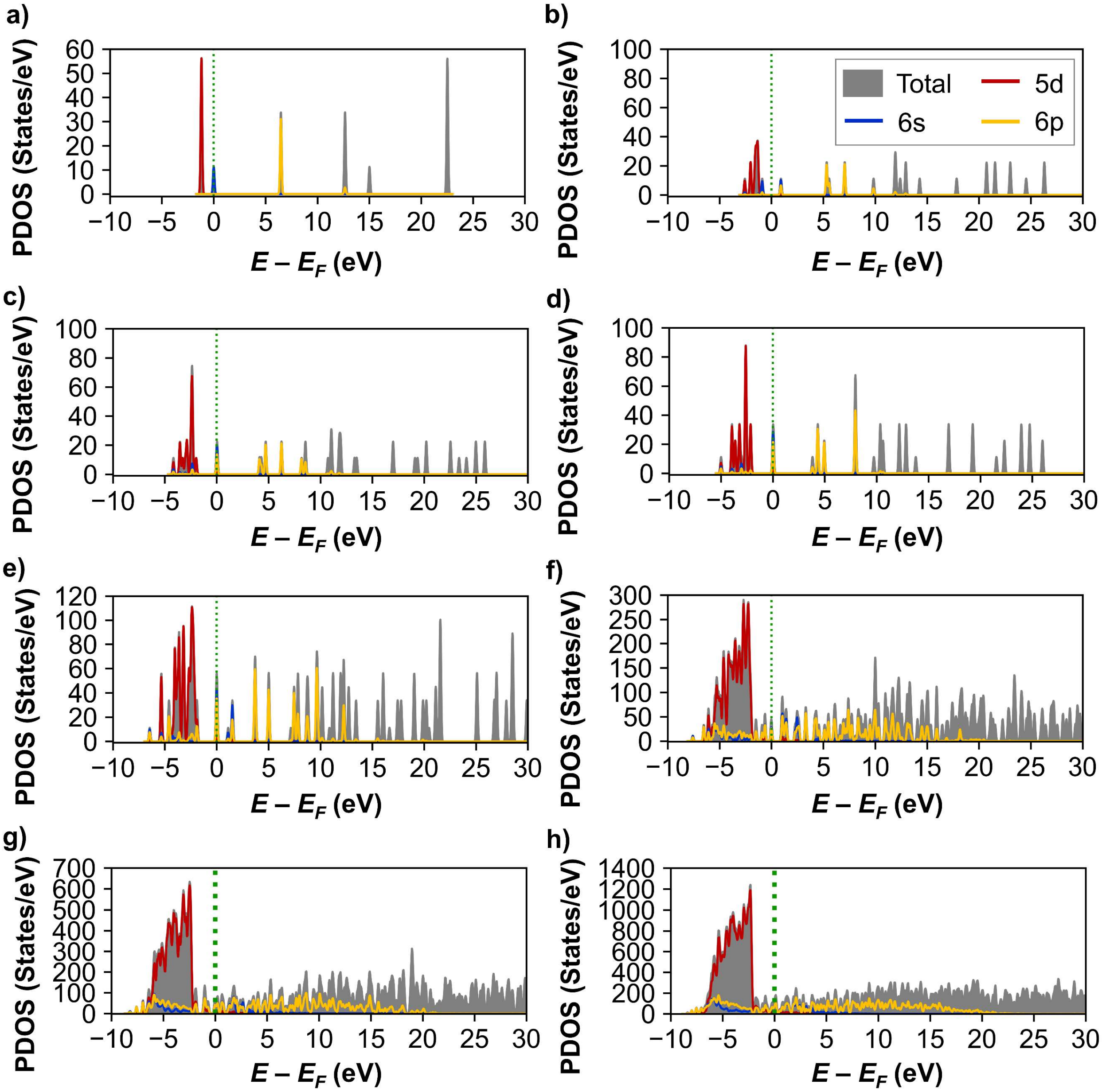

Figure 2.12. Computed results of projected density of states distributions for (a) Au$_1$, (b) Au$_2$, (c) Au$_3$, (d) Au$_4$, (e) Au$_{13}$, (f) Au$_{55}$, (g) Au$_{147}$, and (h) Au$_{309}$.

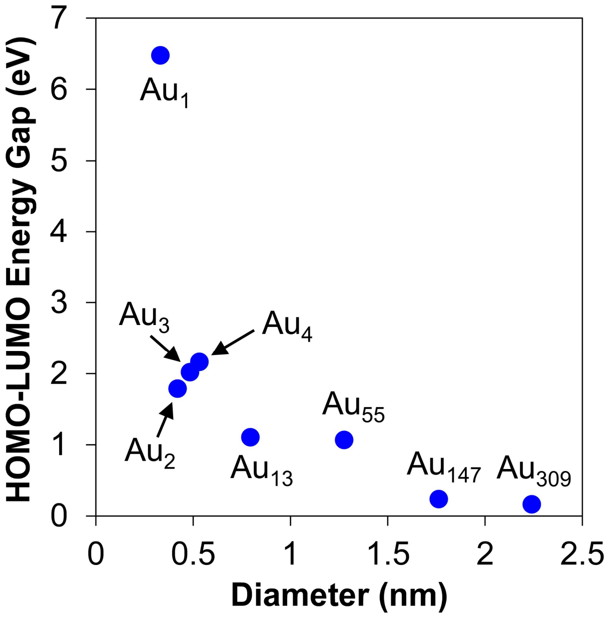

Figure 2.13. Highest occupied molecular orbital and lowest unoccupied molecular orbital (HOMO-LUMO) energy gap of the Au$_n$ nanoclusters from the projected density of states data.

One can qualitatively evaluate whether the Casimir-Lifshitz interaction force between two particles i and k across a medium j is attractive or repulsive by using, $-(\varepsilon_i - \varepsilon_j)(\varepsilon_k - \varepsilon_j)$, a multiplication of the terms with differences in dielectric response function over the entire spectrum range of Matsubara frequency [25, 132-134, 143-150]. For example, if $\varepsilon_i > \varepsilon_k > \varepsilon_j$, the force is attraction because the result value is negative. When $\varepsilon_i > \varepsilon_j > \varepsilon_k$, the value is positive, so the force is repulsive. Since the dielectric response profiles for all the solid materials in Figure 2.11(b) are higher than that of water, we can predict that the interaction force between any two particles across water is always an attraction in this system.

2.5.2.2. Casimir-Lifshitz force between a PAH/PS particle and an Au$_n$ nanocluster across water

The computed results of the Casimir-Lifshitz force between a PAH/PS particle (i) and each Au$_n$ nanocluster (k) across water (j) at different concentration of *L*-ascorbic acid are summarized in Figure 2.14. The force profiles of the cases with Au$_1$, Au$_2$, Au$_3$, Au$_4$, Au$_{13}$, Au$_{55}$, Au$_{147}$, and

Au_{309} as the particle *k* are shown in Figures 2.14(a), 7(b), 7(c), 7(d), 7(e), 7(f), 7(g), and 7(h), respectively.

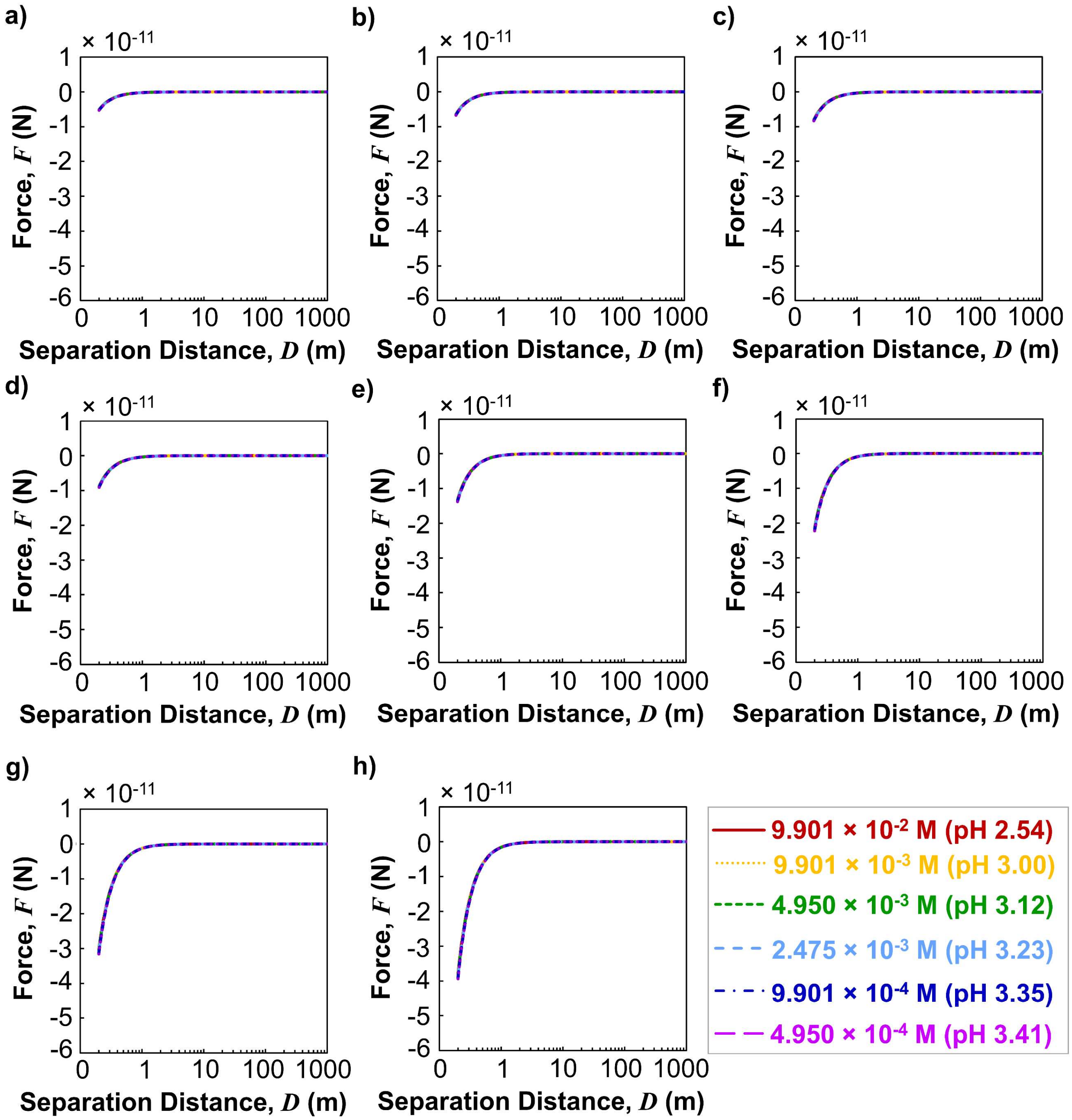

Figure 2.14. Computed Casimir-Lifshitz interaction force profiles between a PAH/PS particle and a Au_n nanocluster across water medium at various concentration of *L*-ascorbic acid: (a) Au_1, (b) Au_2, (c) Au_3, (d) Au_4, (e) Au_{13}, (f) Au_{55}, (g) Au_{147}, and (h) Au_{309}.

As seen in each plot of Figure 2.14, it appears that the change in the concentration of *L*-ascorbic acid has little effect on the Casimir-Lifshitz interaction force between the PAH/PS particle and each Au_n in the acidic pH range from 2.54 to 3.41. To investigate how the entropic term of the Casimir-Lifshitz force is attenuated by the electric field shielding effect, the percent differences in the Casimir-Lifshitz force profile at between the *L*-ascorbic acid concentration of 9.901×10^{-2} M and the rests are plotted in Figure 2.15. Figures 2.15(a) to 2.15(h) correspond to the cases for the particle *k* is Au_1 to Au_{309}, respectively. First, the difference in Casimir-Lifshitz force shown in Figures 2.15(a) to 2.15(h) is about 0.5% to 5% for the separation distance below 200 nm. This is because the zero-frequency term, which is necessarily an electrostatic force, is weakened due to the electric field screening by the concentration gradient of ions near the positively charged PAH/PS particle surface. The Casimir-Lifshitz force at a distance larger than 200 nm is constant regardless of the concentration of *L*-ascorbic acid in the pH range between 2.54 and 3.41. Second, comparing Figures 2.15(a) to 2.15(h), the effect of the *L*-ascorbic acid concentration on the difference in the Casimir-Lifshitz force between the PAH/PS and the gold nanocluster at the distance less than 200 nm decreases with an increment in the size of the Au_n nanoclusters. In all cases, the difference in the Casimir-Lifshitz force depending on the *L*-ascorbic acid concentration is less than 5% within the separation distance of 200 nm. Above the separation distance of 200 nm, the difference in the forces is less than 0.1 %. Therefore, as mentioned above, it can be said that the effect of the concentration of *L*-ascorbic acid on the Casimir-Lifshitz force between the PS the Au_n nanocluster is little over all the range of the separation distance.

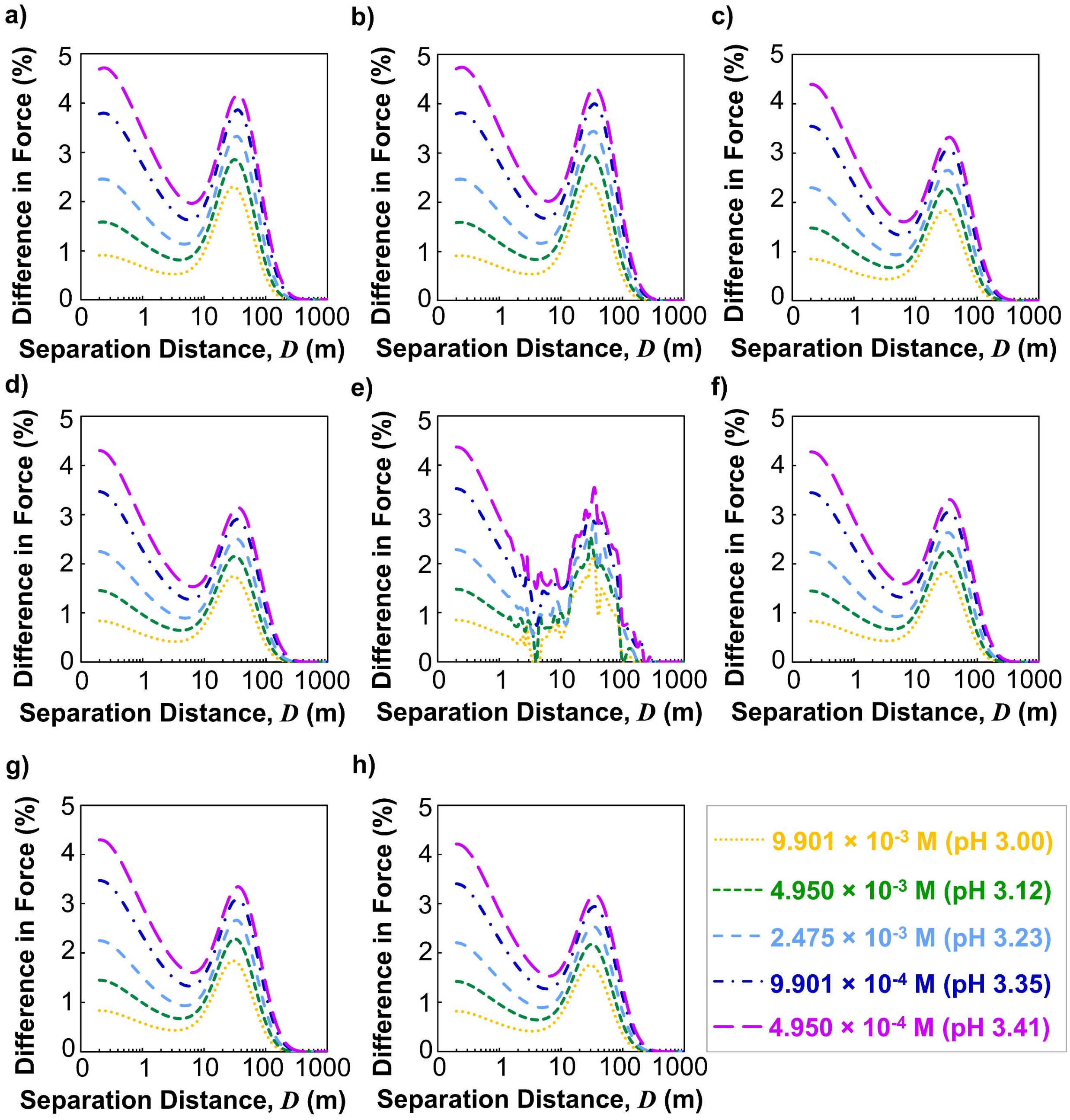

Figure 2.15. Percentage difference profiles in Casimir-Lifshitz interaction force at between *L*-ascorbic acid concentration of 9.901 × 10^{-2} M and the other concentrations: (a) Au_1, (b) Au_2, (c) Au_3, (d) Au_4, (e) Au_{13}, (f) Au_{55}, (g) Au_{147}, and (h) Au_{309} as a particle *k*.

In the earlier discussion, we explained that the nucleation and the growth of gold intensively occurs at a very high reaction rate near the positively charged surface of the PS particle by the concentrated ions around it. Comparing the Casimir-Lifshitz force profiles from a) to h) in Figure 2.14, the force between the PAH/PS particle and the Au_n increases as n increases. This indicates that the attractive force with the PAH/PS particle and the Au_n nanocluster increases during the synthesis because the gold nucleation (Au_1) generated around the PAH/PS surface grows and increases its size. Therefore, the growing Au_n nanocluster moves toward the PAH/PS particle at accelerated speed. And it is deposited on the PAH/PS surface. These deposited gold nanoclusters keep growing until the reaction ends and become a shell on the PAH/PS particle.

2.5.3. Effect of L-ascorbic acid concentration on morphology of gold coating

To analyze the experimental results of the variation in the morphology of the coated gold on the PAH/PS particles with a change of the concentration of *L*-ascorbic acid, the earlier discussions on the initial reaction rate gradient and the Casimir-Lifshitz interaction force are used. The initial reaction rate gradient under the EDL numerically explains that the nucleation and the growth of gold intensively occurs near the positively charged surface of the PAH/PS particle. In addition, the procedure of the deposition of the growing gold nanoclusters on the surface of the PAH/PS particles during the synthesis was computationally described by the Casimir-Lifshitz force between them. In this section, we scrutinize the morphological difference in the gold coating on the PAH/PS particles with a change in *L*-ascorbic acid concentration by the SEM analysis in the perspectives of the initial reaction rate and the Casimir-Lifshitz force. Moreover, the agglomeration of the bare gold nanoclusters which might occurs in the real experiments will be explained.

Figures 2.16(a) to 2.16(f) show SEM images (100k x) of the morphologies of the gold-coated PAH/PS particles at the concentrations of *L*-ascorbic acid of 9.901×10^{-2}, 9.901×10^{-3}, 4.950×10^{-3}, 2.475×10^{-3}, 9.901×10^{-4}, and 4.950×10^{-4} M, respectively. And Figures 2.17(a) to

10(f) are the magnified SEM images (200k x) of each sample to observe the detailed morphologies of the surface of the gold coating at the same conditions. The morphology variation of the gold coating on the PAH/PS depending on *L*-ascorbic acid concentration will be explained by these SEM images in terms of the nucleation of gold.

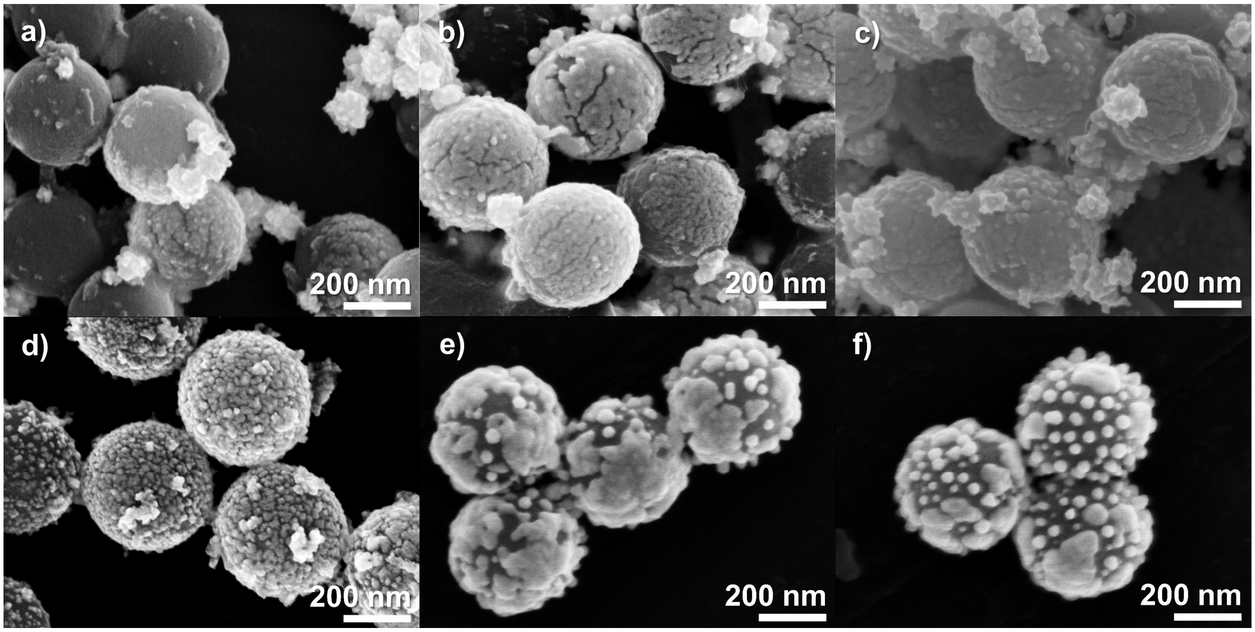

Figure 2.16. Scanning electron micrographs at 100,000x magnification of the gold-coated PAH/PS particles prepared at *L*-ascorbic acid concentration of (a) 9.901×10^{-2}, (b) 9.901×10^{-3}, (c) 4.950×10^{-3}, (d) 2.475×10^{-3}, (e) 9.901×10^{-4}, and (f) 4.950×10^{-4} M.

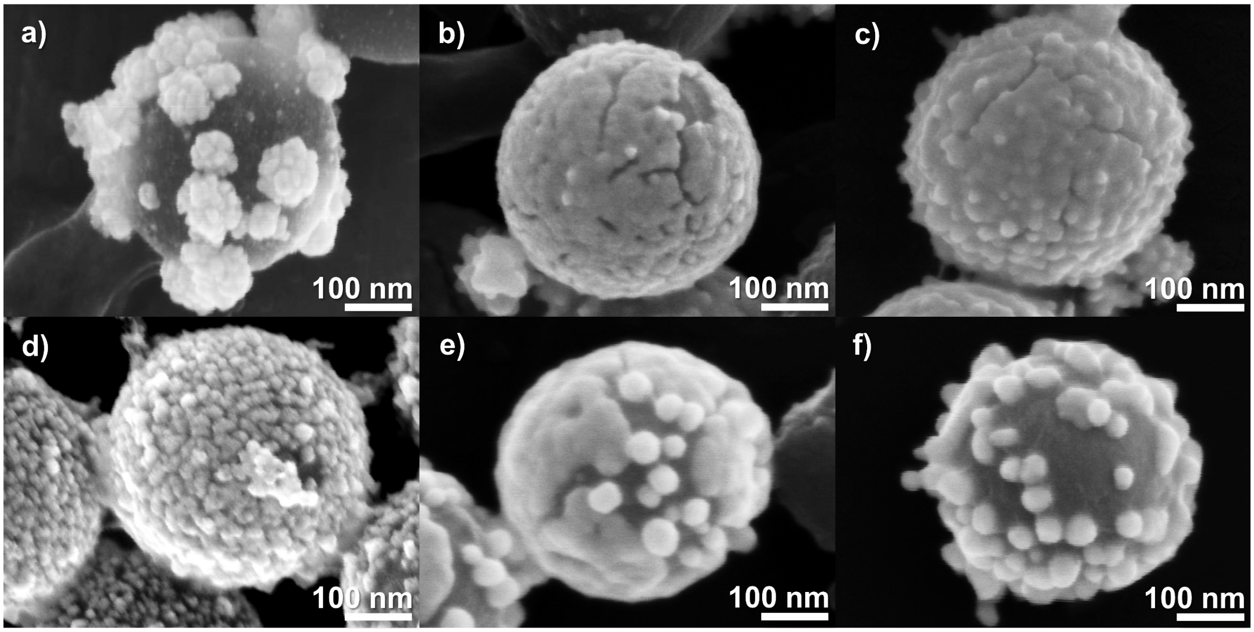

Figure 2.17. Scanning electron micrographs at 200,000x magnification of the representative gold-coated PAH/PS particle synthesized at *L*-ascorbic acid concentration of (a) 9.901 × 10^{-2}, (b) 9.901 × 10^{-3}, (c) 4.950 × 10^{-3}, (d) 2.475 × 10^{-3}, (e) 9.901 × 10^{-4}, and (f) 4.950× 10^{-4} M.

First, we start our discussion with the generation of the gold nucleation near the PAH/PS particle surface at the different concentration of *L*-ascorbic acid. Referring to Figure 2.16(a), gold coating is hardly observed on the surface of most PAH/PS particles despite of the highest concentration of *L*-ascorbic acid of the system. A few PAH/PS particles are coated with gold on one side, such as Janus particles. On top of that, agglomerated gold nanoparticles with a size of about 100 nm are observed. They are stick together with each other or decorated on the surface of the PAH/PS particles. As seen in the magnified SEM image of this sample in Figure 2.17(a), one can see the very small gold nanoclusters (very small bright spots) are deposited on the PAH/PS particle surface between the decorated gold agglomerates. These tiny and densely distributed gold nanoclusters indicate that the gold nucleation occurs very actively around the PAH/PS particles. This is consistent with the highest ratio of the initial reaction rate profile near the surface of the PAH/PS particle as seen in Figures 2.7(a) and 2.7(b). However, Figures 2.16(a) and 2.17(a) indicate that most of the reactants are used to form gold agglomerates instead of these deposited gold nanoclusters. Comparing Figures 2.17(a) to 2.17(f), the size of the gold nanoparticles grown after being deposited on the surface of the PAH/PS particles by Casimir-Lifshitz attractive force is inversely proportional to the *L*-ascorbic acid concentration. In the cases of Figures 2.17(b), 2.17(c), and 2.17(d), the number of generated gold nucleation near the surface of the PAH/PS particle appears to be enough to generate the thin gold layer with high coating coverage on the PAH/PS particle. The coated gold observed in Figures 2.17(b) and 2.17(c) is a shell, whereas small gold particles are uniformly deposited in Figure 2.17(d). In the cases of Figures 2.17(e) and 2.17(f), the number of deposited gold particles is small, the size of the grown gold coating is large, and the coverage is low due to the small amount of nucleation of gold near the surface. From this SEM image analysis, we can see that the rate of nucleation generation near the PAH/PS surface, which depends on the *L*-ascorbic acid concentration, affects the variation of the morphology of gold coating in the positively charged PS particles.

Second, the dependency of the *L*-ascorbic acid concentration on the generation of the gold agglomerates and the degree of the gold coating coverage are discussed in terms of the nucleation of gold in the regions away from the PAH/PS surface. As seen in Figure 2.7(a), the ratio of the initial reaction rate profile becomes constant as it moves away from the PAH/PS particle surface. That is, the nucleation rate of gold outside the EDL is constant as well away from the PAH/PS particle surface. If the reaction rate outside the EDL reaches the critical concentration fast enough to cause the nucleation of gold, then the growth rate of the gold is also very high by the autocatalytic reduction over the entire system. This means that the consumption of the reactants in the whole system also occurs very fast. In this case, the entire reaction is quickly terminated without sufficient mass transfer of the negatively charged reactants towards the positively charged

PAH/PS particle. Therefore, in the gold coating synthesis at the highest concentration (9.901×10^{-2} M) of *L*-ascorbic acid in our experiments, many gold nanoparticles generated far away from the PAH/PS particles quickly consume the reactants by the autocatalytic reduction. Because of this, the gold nanoclusters deposited on the PAH/PS particle surface are not supplied with enough reactants. In other words, the transition metal coating strategy by using highly concentrated ionic reactants near the counter-charged substrate particle does not work at the very high concentration of *L*-ascorbic acid. In addition, when bare gold nanoparticles grow everywhere away from the PAH/PS particles, they undergo agglomeration quickly due to the attractive force between these gold nanoparticles. As shown in Figure 2.16(a), these gold agglomerates are attached on the PAH/PS particles or other gold agglomerates by the attraction. Therefore, the deposited tiny gold nanoclusters on the PAH/PS particles, low gold coating coverage, and gold agglomerates are observed in the case of synthesis at such a high concentration of *L*-ascorbic acid, as seen in Figures 2.16(a) and 2.17(a).

The gold agglomerates are observed in Figures 2.16(b), 2.16(c), and 2.16(d) as well, whereas they are not seen in Figures 2.16(e) and 2.16(f). Therefore, if the concentration of *L*-ascorbic acid is less than 9.901×10^{-4} M, it can be inferred that the generation rate of the Au(I) complex is not sufficient for the nucleation of gold in the regions far away from the PAH/PS particle. From this, we can say that the gold agglomerates are hardly generated at the regions where the ratio of the initial reaction rate shown in Figure 2.7(a) is less than about 10. Comparing Figures 2.16(a), 2.16(b), 2.16(c), and 2.16(d), the size of the gold agglomerates is smaller, as the concentration of *L*-ascorbic acid decreases. Moreover, the gold agglomerates are seen less. This means that the more amount of the reduced form of the gold precursor is consumed for the growth of the deposited gold on the PAH/PS particle surface at lower concentration of *L*-ascorbic acid.

The trend of the amount of gold coating on the PAH/PS particle supports this statement in the next discussion with SEM images. Looking at Figures 2.16(a) to 2.16(c), since the coverage of the thin gold coating increases inversely proportional to the *L*-ascorbic acid concentration, the amount of the gold coating on the PAH/PS particle increases. And, from Figures 2.16(d) to 2.16(f), it can be seen that a sufficient amount of gold is generated on the PAH/PS particles because the thickness of the coated gold increases despite of the decrease in the coating coverage.

By using our model to estimate the relative rate of the gold nucleation along the distance away from the PAH/PS particle in a change of the concentration of *L*-ascorbic acid, we have discussed the mechanisms of 1) the variation in the morphology of the gold coating on the PAH/PS particles and 2) the formation of the gold agglomerates. In addition, the deposition behavior of the growing gold nanoclusters onto the PAH/PS particle was explained by Casimir-Lifshitz interaction force profiles. As discussed in the SEM analysis, the computational results of these two models well describe the change in the morphology of the gold coating on the PAH/PS particles. However, our model has a limitation to explain the exact behaviors of the growth stage of the gold since that tool to estimate the relative reaction rate is only valid for the very initial stage of the reaction as mentioned in the theoretical section.

To sum up, we developed the numerical models to describe the gold coating behaviors on the positively charged dielectric particles in terms of the initial reaction rate and the Casimir-Lifshitz force under the potential governed by charge regulation. First, the concentrations of all molecules present in the system except for water were numerically defined considering the concentrations of *L*-ascorbic acid and $HAuCl_4$ used for the synthesis of the gold coating and the acid dissociation constants for all possible equilibrium equations. Based on charge regulation model with these data, the surface charge density and the surface potential of the charged PAH/PS particles were defined and then the computation for the potential distribution was performed. The result allows us to obtain the concentration gradients of forms of the molecules except water under potential. Based on this, the ratio of the initial reaction rate profile depending on the distance away from the surface of the charged PAH/PS particle was defined by all possible reaction equations of the reduced forms of the gold precursor. By comparing the ratios of the initial reaction rates, we can roughly evaluate the amount of nucleation of gold at the specific distance under the different concentration of *L*-ascorbic acid. Based on this information, the deposition behaviors of the generated or growing gold nanoclusters on the PAH/PS particles was computationally described by using the Casimir-Lifshitz force. To obtain Casimir-Lifshitz force, the dielectric response functions at Matsubara frequency of the growing gold nanoclusters at different sizes were calculated from the real-time propagation TDDFT simulation. Moreover, the attenuation of the entropic term of the Casimir-Lifshitz force under the EDL due to the electric field shielding effect was introduced into the existing model. The numerical results show that the movement of the growing gold nanoclusters towards the positively charged substrate particles are accelerated because the attractive force between the PAH/PS and the growing gold nanocluster becomes stronger with an increase in the size of the gold nanocluster. In the SEM analysis, these two numerical models well explain the variation in the gold coating morphology which prepared at different concentration of *L*-ascorbic acid in our experiments. Therefore, we propose that our numerical models well describe the direct coating behaviors of transition metals on the charged dielectric colloidal particles. It is expected that these models in our new perspectives will help to guide new directions to achieve a few nanometers thick transition metal coatings on dielectric particles in the future.

2.6. Conclusions

We introduced the mathematical analyses to explain the gold coating behaviors onto the amine-functionalized PAH/PS particles at different concentration of *L*-ascorbic acid in the perspective of the nucleation of gold by using the initial reaction rate and the Casimir-Lifshitz force under the potential distribution governed by charge regulation. To verify the computed data based on our model with the experimental results, the gold coated PAH/PS particles were synthesized by using a direct coating method. The concept of the ratios of the initial reaction rates allows us to a rough estimation of the nucleation rate of gold away from the PAH/PS particle surface at a various concentration of *L*-ascorbic acid. This provides an insight of where the nucleation of gold intensively occurs and agglomeration of gold nanoclusters. On top of that, our analysis of the Casimir-Lifshitz force between the PAH/PS particle and the growing gold nanocluster indicates that the generated or growing gold nanoclusters near the PAH/PS particles move towards the positively charged PAH/PS substrate at accelerated speed. This is because that the strength of the attraction force between them also increases with an increment of the size of the gold nanocluster. Our discussion on the SEM analysis concludes that our models in terms of the generation of gold nucleation well describe the gold coating behaviors on the positively charged dielectric particles under potential distribution despite the limited analysis of the growing stage of the gold coating procedure. Compared to the conventional approaches to analyze the gold coating behaviors reported by other literatures [109, 110, 118, 119, 128-130], our model considers the sophisticated and realistic physical phenomena in the colloidal system including charge regulation, acid-base equilibrium of functional groups, EDL structure, ionic concentration gradients, interaction force between particles based on thermal fluctuations of the electromagnetic field, electric field shielding effect, retardation effect, etc. For the future work, we can extend the application of our models to a various combinations of transition metal shell and dielectric particle core. Moreover, a computational investigation on the transition metal coating with more than two different types of functional groups such as thiol and amine groups on the dielectric substrate particles may give us an insight to better design the experiment strategy for the ultrathin transition metal coating on the dielectric colloids. Thus, we propose that the ratio of the initial reaction rate and the Casimir-Lifshitz force profiles, based on the charge regulation model and the potential distribution, elucidate the transition metal coating behavior on the functionalized dielectric colloidal particles.

2.7. Chapter 2: Acknowledgements

This work was supported by a grant from the National Science Foundation (No. 1911372) and funding from the UC-Mexico Initiative of the University of California Office of the President.

Chapter 2, in part is currently being prepared for submission for publication of the material. Choi, Seongcheol; Vazquez-Duhalt, Rafael; Graeve, Olivia A. The dissertation author was the primary investigator and author of this material.

Chapter 3

Summary and Future Work

In this dissertation, the behaviors of silica nanoparticle deposition and gold coating on positively charged PS particles were investigated in detail by using mathematical models based on realistic phenomena inside the colloidal suspension such as charge regulation, potential distribution, ionic concentration gradient, electric field shielding effect, interaction force, etc.

In Chapter 1, the behavior of silica nanoparticles on the positively charged PS particles at different pH was numerically described using modified DLVO pairwise interaction force. In particular, the EDL interaction force term includes regulation parameter, which is based on the nonlinear charge regulation relation between surface charge density and surface potential, to consider the redistribution of ions (Figure 3.1) for the two approaching particles. Surprisingly, the numerical result of this model shows the attenuation of the EDL interaction force caused by this redistribution of ions. This mathematical model well explains the morphological difference of the deposited silica nanoparticles on the PAH/PS particles in a wide range of pH. Moreover, this modified DLVO interaction model can explain pairwise interaction of particles for a different pH, high and low ionic concentration, various functional groups on particle surface, and a wide range of particle size.

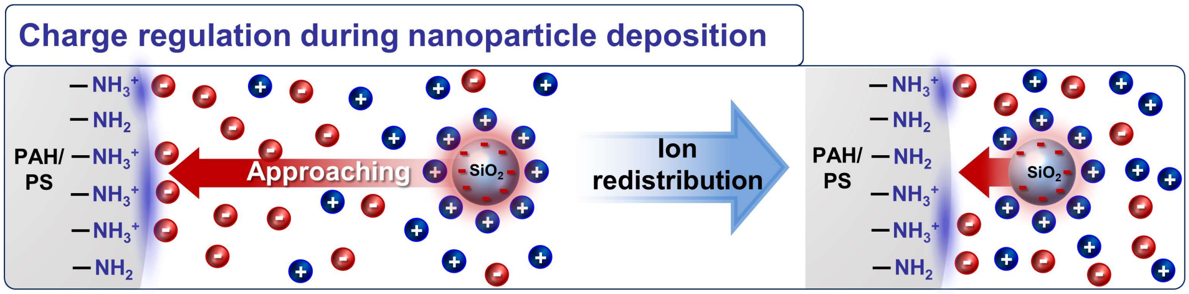

Figure 3.1. Scheme of redistribution of ions during silica nanoparticle deposition onto particle substate.

However, this model is only valid for dilute colloidal suspension because it describes physical property value with respect to one-dimensional distance between two particles. To overcome this disadvantage, we expect that this issue would be solved by extending the model to three-dimensional space and considering the many body interactions. In Figure 3.2, the surface plots show the computational results of the two-dimensional potential when many silanol-terminated silica nanoparticles are nearby a PAH/PS particle at pH 10 in water. Figure 3.2(a) indicates potential surface plot before deposition of silica nanoparticles on the PAH/PS, and Figure 3.2(b) shows the changed potential gradient when the deposition is done. In both figures, the sign of the potential between the PAH/PS particle and the silica particle is opposite, which means an attraction force is applied between them. In this case, the greater the difference in potential, the greater the attractive force is exerted on both. When it comes to the interaction between a silanol-terminated silica nanoparticle and a PAH/PS particle, the force is repulsion because both potentials are negative. This two-dimensional analysis of potential gradient shows that the analysis in higher dimension can be a very intuitive tool to describe physical phenomenon.

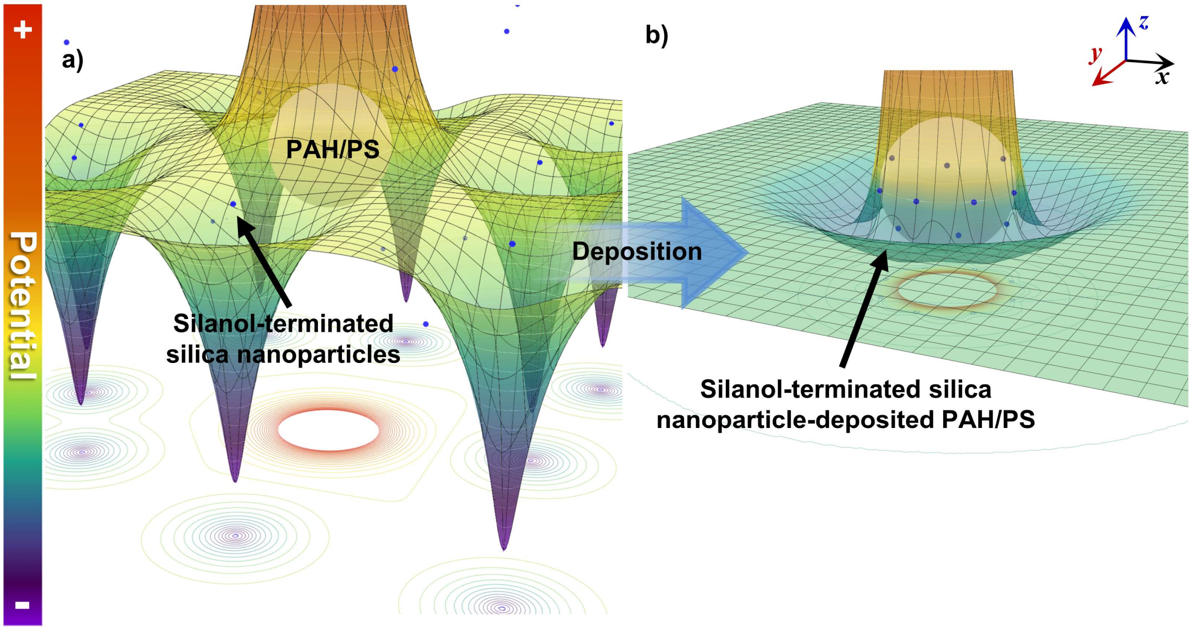

Figure 3.2. Two-dimensional potential surface plots (a) when silica nanoparticles are away from the PAH/PS particle and (b) when silica nanoparticles are deposited on the PAH/PS particle.

In chapter 2, mathematical models were presented to describe the c gold coating behavior on PAH/PS particles at different concentration of *L*-ascorbic acid. This model predicts the initial reaction rate from the concentration gradient of the ionized reactants near the positively charged PAH/PS particles. It allows us to compare the relative nucleation rates of gold in functions of a distance away from the PAH/PS particle surface and concentration of *L*-ascorbic acid. In addition, it is also possible to predict whether agglomeration of gold nanoclusters occurs or not with this method. On top of that, the direct deposition of growing gold particles on the PAH/PS substrate was described using Casimir-Lifshitz force considering the concentration gradient of ions. Lastly, the SEM analysis shows that these models well explain the gold coating behavior of the positively charged PS particles.

To describe gold coating behavior more accurately, the rate constant of reaction must be defined through experimental measurements. However, due to the technological limitations of mankind, it is impossible to measure the reaction rate depending on the distance around the PS particle in time at nano-scale distance. Therefore, a relative initial reaction rate was introduced by assuming the rate constants of each reaction as an arbitrary unit value in this study. In the middle of the reaction, when gold grows on the PS surface, the area of the charged PAH/PS surface decreases since the degree of gold coating coverage increases. Thus, various physical properties, which are defined for the initial stage of the reaction such as ionic concentration gradient and potential distribution differ from the initial conditions, are not the same anymore in the middle of the reaction. Therefore, this model can only predict the initial stage of the overall reaction and has limitations in explaining the growth of gold. Therefore, we need to investigate further to overcome these barriers.

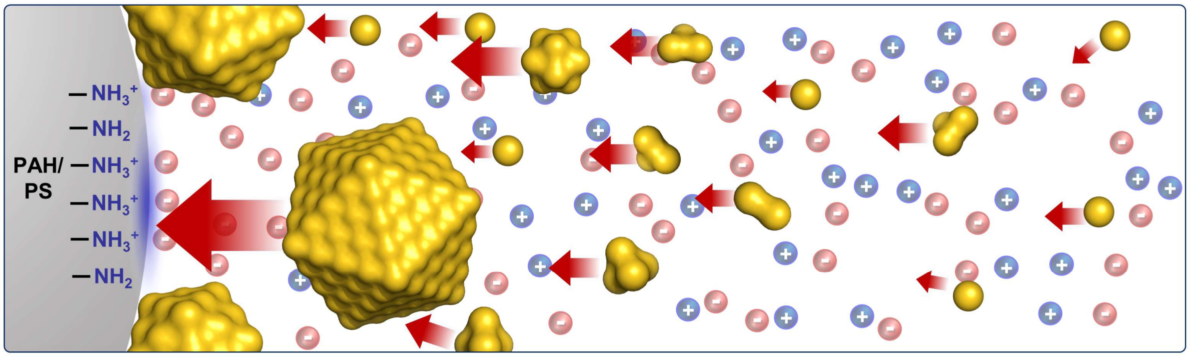

Figure 3.3. An illustration of the growing golds near the positively charged surface of polystyrene particle and the direction of their movements.

Appendix A

Fractional composition distributions of sulfate-terminated PS chains:

The fractional composition profiles of a sulfate group terminated at the end of a PS chain is calculated based on the following equilibrium acid-base reaction:

$$\mathrm{SO_3(OH)} \overset{K_{a_6}}{\rightleftharpoons} \mathrm{SO_4^- + H^+} \tag{A1}$$

where K_{a_6} is the acid dissociation constant of $10^{1.5}$ (computed using Marvin from ChemAxon). The fraction (α_i) of each component i on the basis of Equation (A1) are defined as:

$$\alpha_{\mathrm{SO_3(OH)}} = \frac{\left[\mathrm{H^+}\right]_\infty}{K_{a_6} + \left[\mathrm{H^+}\right]_\infty} \tag{A2}$$

$$\alpha_{\mathrm{SO_4^-}} = 1 - \alpha_{\mathrm{SO_3(OH)}} \tag{A3}$$

where $\alpha_{\mathrm{SO_3(OH)}}$ and $\alpha_{\mathrm{SO_4^-}}$ are the fractions of the protonated sulfate and the sulfate at the end of the PS chains, respectively. Equations (A2) and (A3) are used to plot the fractional composition distributions of the sulfate-terminated PS chains in Figure A1.

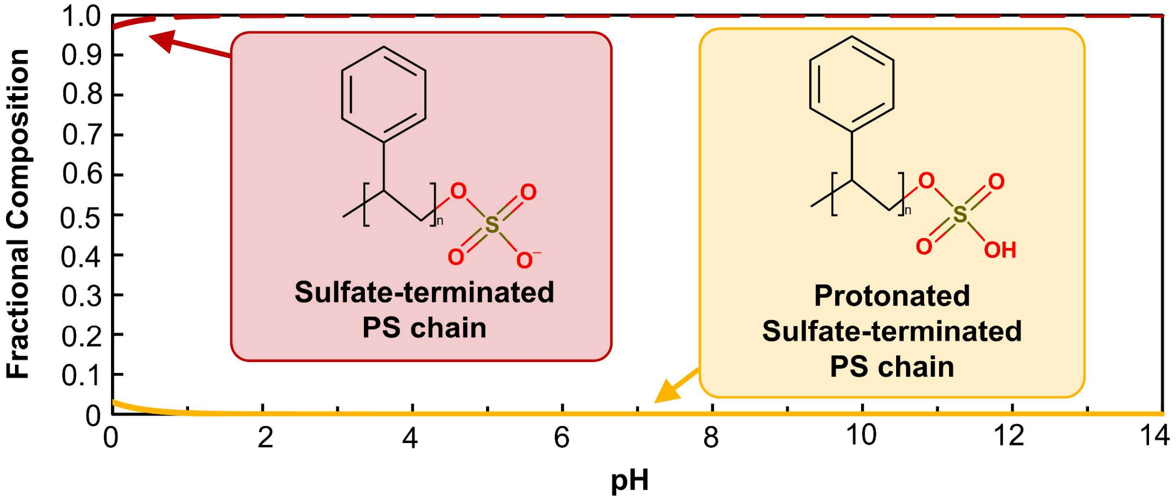

Figure A1. Fractional composition distributions of sulfate-terminated PS chains.

Appendix B

Raw data for Figures 1.7(a), 1.7(c) and 1.7(d):

Table B1. Data for Figures 1.7(a), 1.7(c) and 1.7(d).

Figure 1.7(a)			
pH	Surface charge density, σ (C/m^2) silanol-terminated silica nanoparticles	Surface charge density, σ (C/m^2) *L*-lysine-covered silica nanoparticles	Surface charge density, σ (C/m^2) PAH/PS particles
2.0	1.65×10^{-5}	2.05×10^{-2}	3.20×10^{-1}
2.5	-1.64×10^{-5}	9.51×10^{-3}	3.19×10^{-1}
3.0	-7.11×10^{-5}	4.32×10^{-3}	3.10×10^{-1}
3.5	-1.99×10^{-4}	1.93×10^{-3}	2.58×10^{-1}
4.0	-3.94×10^{-4}	8.39×10^{-4}	1.63×10^{-1}
4.5	-5.41×10^{-4}	3.48×10^{-4}	8.62×10^{-2}
5.0	-6.06×10^{-4}	1.22×10^{-4}	4.24×10^{-2}
5.5	-6.29×10^{-4}	9.74×10^{-6}	2.02×10^{-2}
6.0	-6.37×10^{-4}	-4.49×10^{-5}	9.47×10^{-3}
6.5	-6.39×10^{-4}	-6.68×10^{-5}	4.42×10^{-3}
7.0	-6.40×10^{-4}	-7.44×10^{-5}	2.06×10^{-3}
7.5	-1.38×10^{-3}	-1.87×10^{-4}	2.06×10^{-3}
8.0	-2.96×10^{-3}	-4.23×10^{-4}	2.06×10^{-3}
8.5	-6.34×10^{-3}	-9.25×10^{-4}	2.05×10^{-3}
9.0	-1.35×10^{-2}	-2.00×10^{-3}	2.05×10^{-3}
9.5	-2.82×10^{-2}	-4.30×10^{-3}	2.02×10^{-3}
10.0	-5.70×10^{-2}	-9.20×10^{-3}	1.95×10^{-3}
10.5	-1.06×10^{-1}	-1.95×10^{-2}	1.75×10^{-3}
11.0	-1.62×10^{-1}	-4.05×10^{-2}	1.29×10^{-3}
11.5	-1.87×10^{-1}	-7.99×10^{-2}	6.58×10^{-4}
12.0	-1.92×10^{-1}	-1.41×10^{-1}	2.20×10^{-3}

Figure 1.7(c)

pH	Surface potential, ψ_o (mV) silanol-terminated silica nanoparticles	Surface potential, ψ_o (mV) *L*-lysine-covered silica nanoparticles	Surface potential, ψ_o (mV) PAH/PS particles
2.0	0.072	68.110	205.565
2.5	-0.128	59.708	234.979
3.0	-0.985	51.043	262.957
3.5	-4.897	42.460	283.133
4.0	-16.960	34.167	289.072
4.5	-38.440	26.004	285.986
5.0	-65.02	16.667	279.068
5.5	-93.703	2.399	270.517
6.0	-122.955	-19.216	261.263
6.5	-152.455	-45.754	251.673
7.0	-181.985	-74.285	241.947
7.5	-191.799	-90.646	212.365
8.0	-201.496	-102.502	182.801
8.5	-211.064	-112.773	153.245
9.0	-220.233	-122.579	123.767
9.5	-228.637	-132.249	94.482
10.0	-235.173	-141.657	65.848
10.5	-237.387	-150.626	39.115
11.0	-229.526	-158.488	17.459
11.5	-207.630	-163.899	5.116
12.0	-179.228	-163.294	9.595

Figure 1.7(d)						
pH	Surface charge density, σ (C/m^2) silanol-terminated silica nanoparticles	Surface potential, ψ_o (mV) silanol-terminated silica nanoparticles	Surface charge density, σ (C/m^2) *L*-lysine-covered silica nanoparticles	Surface potential, ψ_o (mV) *L*-lysine-covered silica nanoparticles	Surface charge density, σ (C/m^2) PAH/PS particles	Surface potential, ψ_o (mV) PAH/PS particles
2.0	1.65×10^{-5}	0.072	2.05×10^{-2}	68.110	3.20×10^{-1}	205.565
2.5	-1.64×10^{-5}	-0.128	9.51×10^{-3}	59.708	3.19×10^{-1}	234.979
3.0	-7.11×10^{-5}	-0.985	4.32×10^{-3}	51.043	3.10×10^{-1}	262.957
3.5	-1.99×10^{-4}	-4.897	1.93×10^{-3}	42.460	2.58×10^{-1}	283.133
4.0	-3.94×10^{-4}	-16.960	8.39×10^{-4}	34.167	1.63×10^{-1}	289.072
4.5	-5.41×10^{-4}	-38.440	3.48×10^{-4}	26.004	8.62×10^{-2}	285.986
5.0	-6.06×10^{-4}	-65.072	1.22×10^{-4}	16.667	4.24×10^{-2}	279.068
5.5	-6.29×10^{-4}	-93.703	9.74×10^{-6}	2.399	2.02×10^{-2}	270.517
6.0	-6.37×10^{-4}	-122.955	-4.49×10^{-5}	-19.216	9.47×10^{-3}	261.263
6.5	-6.39×10^{-4}	-152.455	-6.68×10^{-5}	-45.754	4.42×10^{-3}	251.673
7.0	-6.40×10^{-4}	-181.985	-7.44×10^{-5}	-74.285	2.06×10^{-3}	241.947
7.5	-1.38×10^{-3}	-191.799	-1.87×10^{-4}	-90.646	2.06×10^{-3}	212.365
8.0	-2.96×10^{-3}	-201.496	-4.23×10^{-4}	-102.502	2.06×10^{-3}	182.801
8.5	-6.34×10^{-3}	-211.064	-9.25×10^{-4}	-112.773	2.05×10^{-3}	153.245
9.0	-1.35×10^{-2}	-220.233	-2.00×10^{-3}	-122.579	2.05×10^{-3}	123.767
9.5	-2.82×10^{-2}	-228.637	-4.30×10^{-3}	-132.249	2.02×10^{-3}	94.482
10.0	-5.70×10^{-2}	-235.173	-9.20×10^{-3}	-141.657	1.95×10^{-3}	65.848
10.5	-1.06×10^{-1}	-237.387	-1.95×10^{-2}	-150.626	1.75×10^{-3}	39.115
11.0	-1.62×10^{-1}	-229.526	-4.05×10^{-2}	-158.488	1.29×10^{-3}	17.459
11.5	-1.87×10^{-1}	-207.630	-7.99×10^{-2}	-163.899	6.58×10^{-4}	5.116
12.0	-1.92×10^{-1}	-179.228	-1.41×10^{-1}	-163.294	2.20×10^{-3}	9.595

Appendix C

Derivation of fractional composition equations used for Figure 1.11:

Fractional Composition Diagrams of Free Silanol Molecules

This section introduces the procedures and equations to plot the fractional composition profiles in Figure 1.11. The fractions of the components ($\mathrm{SiOH_2^+}$, SiOH, and $\mathrm{SiO^-}$) for free silanol groups are based on Equations (1.8a) and (1.8b) and defined as:

$$\alpha_{\mathrm{SiOH_2^+}} = \frac{\left[\mathrm{H^+}\right]_\infty^2}{K_{\mathrm{a_1}}K_{\mathrm{a_2}} + K_{\mathrm{a_1}}\left[\mathrm{H^+}\right]_\infty + \left[\mathrm{H^+}\right]_\infty^2} \tag{A4}$$

$$\alpha_{\mathrm{SiOH}} = \frac{K_{\mathrm{a_1}}\left[\mathrm{H^+}\right]_\infty}{K_{\mathrm{a_1}}K_{\mathrm{a_2}} + K_{\mathrm{a_1}}\left[\mathrm{H^+}\right]_\infty + \left[\mathrm{H^+}\right]_\infty^2} \tag{A5}$$

$$\alpha_{\mathrm{SiO^-}} = \frac{K_{\mathrm{a_1}}K_{\mathrm{a_2}}}{K_{\mathrm{a_1}}K_{\mathrm{a_2}} + K_{\mathrm{a_1}}\left[\mathrm{H^+}\right]_\infty + \left[\mathrm{H^+}\right]_\infty^2} \tag{A6}$$

where $\alpha_{\mathrm{SiOH_2^+}}$, α_{SiOH}, and $\alpha_{\mathrm{SiO^-}}$ are the fractions of the protonated silanol, the silanol, and the silanolate of the free molecules having a silanol group, respectively. Equations (A4), (A5), and (A6) are used to plot the factional composition diagrams of the silanol groups of free molecules as shown in Figure 1.11 (a).

Fractional Composition Diagrams of Surface Silanol on Silica Nanoparticles

The fractions of the species (SiOH_2^+, SiOH, and SiO^-) of silanol groups on the surface of silica nanoparticles can be defined by replacing $\left[\mathrm{H}^+\right]_\infty$ of Equations (A4), (A5), and (A6) with $\left[\mathrm{H}^+\right]_0$ and using Boltzmann Equation [Equation (1.5)], resulting in the following equations:

$$\alpha_{\mathrm{SiOH}_2^+,\mathrm{surface}} = \frac{\left[\mathrm{H}^+\right]_\infty^2 e^{-\frac{2q\psi_0}{\mathrm{k_B}T}}}{K_{\mathrm{a}_1}K_{\mathrm{a}_2} + K_{\mathrm{a}_1}\left[\mathrm{H}^+\right]_\infty e^{-\frac{q\psi_0}{\mathrm{k_B}T}} + \left[\mathrm{H}^+\right]_\infty^2 e^{-\frac{2q\psi_0}{\mathrm{k_B}T}}} \tag{A7}$$

$$\alpha_{\mathrm{SiOH},\mathrm{surface}} = \frac{K_{\mathrm{a}_1}\left[\mathrm{H}^+\right]_\infty e^{-\frac{q\psi_0}{\mathrm{k_B}T}}}{K_{\mathrm{a}_1}K_{\mathrm{a}_2} + K_{\mathrm{a}_1}\left[\mathrm{H}^+\right]_\infty e^{-\frac{q\psi_0}{\mathrm{k_B}T}} + \left[\mathrm{H}^+\right]_\infty^2 e^{-\frac{2q\psi_0}{\mathrm{k_B}T}}} \tag{A8}$$

$$\alpha_{\mathrm{SiO}^-,\mathrm{surface}} = \frac{K_{\mathrm{a}_1}K_{\mathrm{a}_2}}{K_{\mathrm{a}_1}K_{\mathrm{a}_2} + K_{\mathrm{a}_1}\left[\mathrm{H}^+\right]_\infty e^{-\frac{q\psi_0}{\mathrm{k_B}T}} + \left[\mathrm{H}^+\right]_\infty^2 e^{-\frac{2q\psi_0}{\mathrm{k_B}T}}} \tag{A9}$$

where $\alpha_{\mathrm{SiOH}_2^+,\mathrm{surface}}$, $\alpha_{\mathrm{SiOH},\mathrm{surface}}$, and $\alpha_{\mathrm{SiO}^-,\mathrm{surface}}$ are the fractions of the protonated silanol, the silanol, and the silanolate on the surface of the silica nanoparticles, respectively. Equations (A7), (S8), and (S9), are used to create the fractional composition profiles of the silanol groups of the silica nanoparticles as seen in Figure 1.11 (b).

Fractional Composition Diagrams of Free *L*-lysine Molecules

Depending on ionizations of the three functional groups ($\alpha\text{-NH}_2, \alpha\text{-COOH}$, and $\varepsilon\text{-NH}_2$), *L*-lysine will have five different forms, namely dicationic, cationic, zwitterionic form A, zwitterionic form B, and cationic, as shown in Figures 1.11(c) and 1.11(d). The equilibrium acid-base reaction equation for $\varepsilon\text{-NH}_2$ is defined by:

$$\varepsilon\text{-NH}_3^+ \overset{K_{a_7}}{\rightleftharpoons} \varepsilon\text{-NH}_2 + \text{H}^+ \tag{A10}$$

where K_{a_7} is $10^{-10.53}$ [174]. From Equations (1.15a), (1.15b), and (A10), the fractions of different forms of free *L*-lysine molecules can be defined as:

$$\alpha_{\text{Dicationic},L\text{-lysine}} = \frac{\left[\text{H}^+\right]_\infty^3}{K_{a_3}K_{a_4}K_{a_7} + K_{a_3}K_{a_4}\left[\text{H}^+\right]_\infty + K_{a_3}\left[\text{H}^+\right]_\infty^2 + \left[\text{H}^+\right]_\infty^3} \tag{A11}$$

$$\alpha_{\text{Cationic},L\text{-lysine}} = \frac{K_{a_3}\left[\text{H}^+\right]_\infty^2}{K_{a_3}K_{a_4}K_{a_7} + K_{a_3}K_{a_4}\left[\text{H}^+\right]_\infty + K_{a_3}\left[\text{H}^+\right]_\infty^2 + \left[\text{H}^+\right]_\infty^3} \tag{A12}$$

$$\alpha_{\text{Zwitterionic A},L\text{-lysine}} + \alpha_{\text{Zwitterionic B},L\text{-lysine}} = \frac{K_{a_3}K_{a_4}\left[\text{H}^+\right]_\infty}{K_{a_3}K_{a_4}K_{a_7} + K_{a_3}K_{a_4}\left[\text{H}^+\right]_\infty + K_{a_3}\left[\text{H}^+\right]_\infty^2 + \left[\text{H}^+\right]_\infty^3} \tag{A13}$$

$$\alpha_{\text{Anionic},L\text{-lysine}} = \frac{K_{a_3}K_{a_4}K_{a_7}}{K_{a_3}K_{a_4}K_{a_7} + K_{a_3}K_{a_4}\left[\text{H}^+\right]_\infty + K_{a_3}\left[\text{H}^+\right]_\infty^2 + \left[\text{H}^+\right]_\infty^3} \tag{A14}$$

where $\alpha_{\text{Dicationic},L\text{-lysine}}$, $\alpha_{\text{Cationic},L\text{-lysine}}$, $\alpha_{\text{Zwitterionic A},L\text{-lysine}} + \alpha_{\text{Zwitterionic B},L\text{-lysine}}$, and $\alpha_{\text{Anionic},L\text{-lysine}}$ are the fractions of dicationic form, cationic form, sum of zwitterionic forms A and B, and cationic form of *L*-lysine, respectively. The factional composition diagrams of *L*-lysine are plotted in Figure 1.11(c) by using Equations (A11), (A12), (A13), and (A14).

Fractional Composition Diagrams of Surface *L*-lysine on Silica Nanoparticles

The fractions of the species (dicationic form, cationic form, and sum of zwitterionic A, zwitterionic B, and anoionic forms) of the *L*-lysine layer on the silica nanoparticles can be derived from Equations (1.15a) and (1.15b). Replacing $\left[\text{H}^+\right]_\infty$ with $\left[\text{H}^+\right]_0$ and using the Boltzmann equation [Equation (1.5)] results in:

$$\alpha_{\text{Dicationic},L\text{-lysine,surface}} = \frac{\left[\mathrm{H}^+\right]_\infty^2 e^{-\frac{2q\psi_0}{\mathrm{k_B}T}}}{K_{\mathrm{a}_3}K_{\mathrm{a}_4} + K_{\mathrm{a}_3}\left[\mathrm{H}^+\right]_\infty e^{-\frac{q\psi_0}{\mathrm{k_B}T}} + \left[\mathrm{H}^+\right]_\infty^2 e^{-\frac{2q\psi_0}{\mathrm{k_B}T}}} \tag{A15}$$

$$\alpha_{\text{Cationic},L\text{-lysine,surface}} = \frac{K_{\mathrm{a}_3}\left[\mathrm{H}^+\right]_\infty e^{-\frac{q\psi_0}{\mathrm{k_B}T}}}{K_{\mathrm{a}_3}K_{\mathrm{a}_4} + K_{\mathrm{a}_3}\left[\mathrm{H}^+\right]_\infty e^{-\frac{q\psi_0}{\mathrm{k_B}T}} + \left[\mathrm{H}^+\right]_\infty^2 e^{-\frac{2q\psi_0}{\mathrm{k_B}T}}} \tag{A16}$$

$$\alpha_{\text{Zwitterionic A},L\text{-lysine,surface}} + \alpha_{\text{Zwitterionic B},L\text{-lysine,surface}} + \alpha_{\text{Anionic},L\text{-lysine,surface}} = \\ = \frac{K_{\mathrm{a}_3}K_{\mathrm{a}_4}}{K_{\mathrm{a}_3}K_{\mathrm{a}_4} + K_{\mathrm{a}_3}\left[\mathrm{H}^+\right]_\infty e^{-\frac{q\psi_0}{\mathrm{k_B}T}} + \left[\mathrm{H}^+\right]_\infty^2 e^{-\frac{2q\psi_0}{\mathrm{k_B}T}}} \tag{A17}$$

where $\alpha_{\text{Dicationic},L\text{-lysine,surface}}$, $\alpha_{\text{Cationic},L\text{-lysine,surface}}$, and $\alpha_{\text{Zwitterionic A},L\text{-lysine,surface}} + \alpha_{\text{Zwitterionic B},L\text{-lysine,surface}}$ $+\alpha_{\text{Anionic},L\text{-lysine,surface}}$ are the fractions of dicationic, cationic, and sum of zwitterionic A, zwitterionic B, and anionic form of the surface of the *L*-lysine layer on the silica nanoparticles, respectively. The fractional composition distributions of the surface of *L*-lysine-covered silica nanoparticles are plotted in Figure 1.11 (d) by using Equations (A15), (A16), and (A17).

Fractional Composition Diagrams of Amine of Free PAH Chains

The fractions of the protonated amine ($\alpha_{\mathrm{NH_3^+}}$) and the amine ($\alpha_{\mathrm{NH_2}}$) of free PAH chains can be derived by using Equation (1.21) and defined as:

$$\alpha_{\mathrm{NH_3^+}} = \frac{\left[\mathrm{H}^+\right]_\infty}{K_{\mathrm{a}_5} + \left[\mathrm{H}^+\right]_\infty} \tag{A18}$$

$$\alpha_{\mathrm{NH_2}} = 1 - \alpha_{\mathrm{NH_3^+}} \tag{A19}$$

The fractional composition profiles are plotted in Figure 1.11(e) using Equations (A18) and (S19).

Fractional Composition Diagrams of Surface Amine on PAH/PS Particles

Replacing $\left[\mathrm{H}^+\right]_\infty$ of Equations (A18) and (A19) with $\left[\mathrm{H}^+\right]_0$ and then using the Boltzmann equation [Equation (1.5)] results in:

$$\alpha_{\mathrm{NH}_3^+,\mathrm{surface}} = \frac{\left[\mathrm{H}^+\right]_\infty e^{-\frac{q\psi_0}{\mathrm{k_B}T}}}{K_{\mathrm{a}_5} + \left[\mathrm{H}^+\right]_\infty e^{-\frac{q\psi_0}{\mathrm{k_B}T}}} \tag{A20}$$

$$\alpha_{\mathrm{NH}_2,\mathrm{surface}} = 1 - \alpha_{\mathrm{NH}_3^+,\mathrm{surface}} \tag{A21}$$

where $\alpha_{\mathrm{NH}_3^+,\mathrm{surface}}$ and $\alpha_{\mathrm{NH}_2,\mathrm{surface}}$ are the fractions of the protonated amine group and the amine group on the surface of the PAH/PS particles, respectively.

BIBLIOGRAPHY

[1] Zhang, Z.; Zhang, P.; Wang, Y.; Zhang, W. Recent Advances in Organic-inorganic Well-Defined Hybrid Polymers Using Controlled Living Radical Polymerization Techniques. *Polym. Chem.* **2016**, *7* (24), 3950-3976.

[2] Lee, J.; Hong, C. K.; Choe, S.; Shim, S. E. Synthesis of Polystyrene/Silica Composite Particles by Soap-Free Emulsion Polymerization Using Positively Charged Colloidal Silica. *J. Colloid Interface Sci.* **2007**, *310* (1), 112-120.

[3] Tan W.K.; Araki Y.; Yokoi A.; Kawamura G.; Matsuda A.; Muto H. Micro- and Nano-assembly of Composite Particles by Electrostatic Adsorption. *Nanoscale Res. Lett.* **2019**, *14*, 297-305.

[4] Hood, M.; Mari, M.; Muñoz-Espí, R. Synthetic Strategies in the Preparation of Polymer/Inorganic Hybrid Nanoparticles. *Materials* **2014**, *7* (5), 4057-4087.

[5] Caruso F.; Lichtenfeld H.; Giersig M.; Mohwald H. Electrostatic Self-Assembly of Silica Nanoparticle-Polyelectrolyte Multilayers on Polystyrene Latex Particles. *J. Am. Chem. Soc.* **1998**, *120*, 8523-8524.

[6] Landon, P.B.; Mo, A.H.; Zhang, C.; Emerson, C.D.; Printz, A.D.; Gomez, A.F.; DeLaTorre, C.J.; Colburn, D.A.M.; Anzenberg, P.; Eliceiri, M.; O'Connell, C.; Lal, R. Designing Hollow Nano Gold Golf Balls. *ACS Appl. Mater. Interfaces* **2014**, *6* (13), 9937-9941.

[7] Satoh, H.; Yabu, H. One-Pot Preparation of Organic-Inorganic Composite Microspheres Comprising Silica Nanoparticles and End-Functionalized Polymers. *Macromol. Mater. Eng.* **2015**, *301* (3), 279-286.

[8] Suhendi, A.; Nandiyanto, A. B. D.; Ogi, T.; Okuyama, K. Agglomeration-Free Core-Shell Polystyrene/Silica Particles Preparation Using an Electrospray Method and Additive-Free Cationic Polystyrene Core. *Mater. Lett.* **2013**, *91*, 161-164.

[9] Fischer, V.; Bannwarth, M.B.; Jakob, G.; Landfester, K.; Muñoz-Espí, R. Luminescent and Magnetoresponsive Multifunctional Chalcogenide/Polymer Hybrid Nanoparticles. *J. Phys. Chem. C* **2013**, *117* (11), 5999-6005.

[10] Lu, Y.; Mei, Y.; Drechsler, M.; Ballauff, M. Thermosensitive Core-Shell Particles as Carriers for Ag Nanoparticles: Modulating the Catalytic Activity by a Phase Transition in Networks. *Angew. Chem. Int. Ed.* **2006**, *45* (5), 813-816.

[11] Tian, C.; Mao, B.; Wang, E.; Kang, Z.; Song, Y.; Wang, C.; Li, S. Simple Strategy for Preparation of Core Colloids Modified with Metal Nanoparticles. *J. Phys. Chem. C* **2007**, *111* (9), 3651-3657.

[12] Schrinner, M.; Ballauff, M.; Talmon, Y.; Kauffmann, Y.; Thun, J.; Moller, M.; Breu, J. Single Nanocrystals of Platinum Prepared by Partial Dissolution of Au-Pt Nanoalloys. *Science* **2009**, *323* (5914), 617-620.

[13] Fischer, V.; Lieberwirth, I.; Jakob, G.; Landfester, K.; Muñoz-Espí, R. Metal Oxide/Polymer Hybrid Nanoparticles with Versatile Functionality Prepared by Controlled Surface Crystallization. *Adv. Funct. Mater.* **2012**, *23* (4), 451-466.

[14] Yang, Z.; Niu, Z.; Lu, Y.; Hu, Z.; Han, C.C. Templated Synthesis of Inorganic Hollow Spheres with a Tunable Cavity Size onto Core–Shell Gel Particles. *Angew. Chem. Int. Ed.* **2003**, *42* (17), 1943-1945.

[15] Xu, Z.; Xia, A.; Wang, C.; Yang, W.; Fu, S. Synthesis of Raspberry-like Magnetic Polystyrene Microspheres. *Mater. Chem. Phys.* **2007**, *103* (2-3), 494-499.

[16] Feyen, M.; Weidenthaler, C.; Schüth, F.; Lu, A.-H. Regioselectively Controlled Synthesis of Colloidal Mushroom Nanostructures and Their Hollow Derivatives. *J. Am. Chem. Soc.* **2010**, *132* (19), 6791–6799.

[17] Negrete-Herrera, N.; Putaux, J.-L.; David, L.; Haas, F.D.; Bourgeat-Lami, E. Polymer/Laponite Composite Latexes: Particle Morphology, Film Microstructure, and Properties. *Macromol. Rapid Commun.* **2007**, *28* (15), 1567-1573.

[18] Reculusa, S.; Mingotaud, C.; Bourgeat-Lami, E.; Duguet, E.; Ravaine, S. Synthesis of Daisy-Shaped and Multipod-like Silica/Polystyrene Nanocomposites. *Nano Lett.* **2004**, *4* (9), 1677-1682.

[19] Fukui, Y.; Fujimoto, K. Bio-Inspired Nanoreactor Based on a Miniemulsion System to Create Organic-inorganic Hybrid Nanoparticles and Nanofilms. *J. Mater. Chem. A* **2012**, *22* (8), 3493.

[20] Hamberger, A.; Ziener, U.; Landfester, K. Encapsulation of In Situ Nanoprecipitated Inorganic Materials in Confined Geometries Into a Polymer Shell Using Inverse Miniemulsion. *Macromol. Chem. Phys.* **2013**, *214* (6), 691-699.

[21] Trefalt, G.; Szilagyi, I.; Borkovec, M. Poisson–Boltzmann Description of Interaction Forces and Aggregation Rates Involving Charged Colloidal Particles in Asymmetric Electrolytes. *J. Colloid Interface Sci.* **2013**, *406*, 111-120.

[22] Trefalt, G.; Ruiz-Cabello, F.J.M.; Borkovec, M. Interaction Forces, Heteroaggregation, and Deposition Involving Charged Colloidal Particles. *J. Phys. Chem. B* **2014**, *118*, 6346-6355.

[23] Elzbieciak-Wodka, M.; Popescu, M.N.; Ruiz-Cabello, F.J.M.; Trefalt, G.; Maroni, P.; Borkovec, M. Mearsurements of dispersion forces between colloidal latex particles with

the atomic force microscope and comparison with Lifshitz theory. *J. Chem. Phys.* **2014**, *140*, 104906.

[24] Ninham, B.W. On Progress in Forces since the DLVO Theory. *Adv. Colloid Interface Sci.* **1999**, *83* (1-3), 1-17.

[25] Israelachvili, J.N. *Intermolecular and Surface Forces*; Elsevier, 2011.

[26] Behrens, S.H.; Borkovec, M. Electrostatic Interaction of Colloidal Surfaces with Variable Charge. *J. Phys. Chem. B* **1999**, *103* (15), 2918–2928.

[27] Popa, I.; Sinha, P.; Finessi, M.; Maroni, P.; Papastavrou, G.; Borkovec, M. Importance of Charge Regulation in Attractive Double-Layer Forces between Dissimilar Surfaces. *Phys. Rev. Lett.* **2010**, *104* (22).

[28] Montes Ruiz-Cabello, F.J.; Trefalt, G.; Maroni, P.; Borkovec, M. Electric Double-Layer Potentials and Surface Regulation Properties Measured by Colloidal-Probe Atomic Force Microscopy. *Phys. Rev. E* **2014**, *90* (1).

[29] Smith, A.; Maroni, P.; Borkovec, M.; Trefalt, G. Measuring Inner Layer Capacitance with the Colloidal Probe Technique. *Colloids and Interfaces* **2018**, *2* (4), 65.

[30] Smith, A.M.; Borkovec, M.; Trefalt, G. Forces between Solid Surfaces in Aqueous Electrolyte Solutions. *Adv. Colloid Interface Sci.* **2020**, *275*, 102078.

[31] Uzelac, B.; Valmacco, V.; Trefalt, G. Interactions between Silica Particles in the Presence of Multivalent Coions. *Soft Matter* **2017**, *13* (34), 5741-5748.

[32] Behrens, S.H.; Borkovec, M. Exact Poisson-Boltzmann Solution for the Interaction of Dissimilar Charge-Regulating Surfaces. *Phys. Rev. E* **1999**, *60* (6), 7040-7048.

[33] Carnie, S.L.; Chan, D.Y.C. Interaction Free Energy between Plates with Charge Regulation: A Linearized Model. *J. Colloid Interface Sci.* **1993**, *161* (1), 260-264.

[34] Wang J.; Sugawara-Narutaki A.; fukao M.; Yokoi T.; Shimojima A.; Okubo T.; Two-phase Synthesis of Monodisperse Silica Nanospheres with Amines or Ammonia Catalyst and Their Controlled Self-Assembly. *ACS Appl. Mater. Interfaces* **2011**, *3*, 1538-1544.

[35] Quan B.; Lee C.; Yoo J.S.; Piao Y. Facile scalable synthesis of highly monodisperse small silica nanoparticles using alkaline buffer solution and their application for efficient sentinel lymph node mapping. *J. Mater. Chem. B* **2017**, *5*, 586-594.

[36] Yokoi, T.; Sakamoto, Y.; Terasaki, O.; Kubota, Y.; Okubo, T.; Tatsumi, T. Periodic Arrangement of Silica Nanospheres Assisted by Amino Acids. *J. Am. Chem. Soc.* **2006**, *128*, 13664-13665.

[37] Davis T.M.; Snyder M.A.; Krohn J.E.; Tsapatsis M. Nanoparticles in Lysine-Silica Sols. Chem. Mater. 2006, 18, 5814-5816.

[38] Yokoi, T.; Iwama, M.; Watanabe, R.; Sakamoto, Y.; Terasaki, O.; Kubota, Y.; Kondo, J.N.; Okubo, T.; Tatsumi, T. Synthesis of well-ordered nanospheres with uniform mesopores assisted by basic amino acids. *Stud. Surf. Sci. Catal.* **2007**, *170*, 1774-1780.

[39] Hartlen, K.D.; Athanasopoulos A.P.T.; Kitaev, V. Facile Preparation of Highly Monodisperse Small Silica Spheres (15 to > 200 nm) Suitable for colloidal Templating and Formation of Ordered Arrays. *Langmuir* **2008**, *24*, 1714-1720.

[40] Breite, D.; Went, M.; Prager, A.; Schulze, A. Tailoring Membrane Surface Charges: A Novel Study on Electrostatic Interactions during Membrane Fouling. *Polymers* **2015**, *7* (10), 2017-2030.

[41] Rojas, O.J.; Ernstsson, M.; Neuman, R.D.; Claesson, P.M. Effect of Polyelectrolyte Charge Density on the Adsorption and Desorption Behavior on Mica. *Langmuir* **2002**, *18* (5), 1604-1612.

[42] Gong, H.; Garcia-Turiel, J.; Vasilev, K.; Vinogradova, O.I. Interaction and Adhesion Properties of Polyelectrolyte Multilayers. *Langmuir* **2005**, *21* (16), 7545-7550.

[43] Dressick, W.J.; Wahl, K.J.; Bassim, N.D.; Stroud, R.M.; Petrovykh, D.Y. Divalent-Anion Salt Effects in Polyelectrolyte Multilayer Depositions. *Langmuir* **2012**, *28* (45), 15831-15843.

[44] Hierrezuelo, J.; Sadeghpour, A.; Szilagyi, I.; Vaccaro, A.; Borkovec, M. Electrostatic Stabilization of Charged Colloidal Particles with Adsorbed Polyelectrolytes of Opposite Charge. *Langmuir* **2010**, *26* (19), 15109-15111.

[45] Feldötö, Z.; Varga, I.; Blomberg, E. Influence of Salt and Rinsing Protocol on the Structure of PAH/PSS Polyelectrolyte Multilayers. *Langmuir* **2010**, *26* (22), 17048-17057.

[46] Ridley, R.E.; Fathi-Kelly, H.; Kelly, J.P.; Vasquez, V.R.; Graeve, O.A. Predicting the Size of Salt-Containing Aqueous Na-AOT Reverse Micellar Water-in-Oil Microemulsions with Consideration for Specific Ion Effects. *J. Colloid Interface Sci.* **2021**, *586*, 830-835.

[47] Ridley, R.E.; Alvarado, E.; Mrse, A.A.; Vasquez, V.R.; Graeve, O.A. Phase Stability and Miscibility in Ethanol/AOT/n-Heptane Systems: Evidence of Multilayered Cylindrical and Spherical Microemulsion Morphologies. *Langmuir* **2020**, *36* (38), 11274-11283.

[48] Cahill, J.T.; Ruppert, J.N.; Wallis, B.; Liu, Y.; Graeve, O.A. Development of Mesoporosity in Scandia-Stabilized Zirconia: Particle Size, Solvent, and Calcination Effects. *Langmuir* **2014**, *30* (19), 5585-5591.

[49] Vargas-Consuelos, C.I.; Seo, K.; Camacho-López, M.; Graeve, O.A. Correlation between Particle Size and Raman Vibrations in WO_3 Powders. *J. Phys. Chem. C* **2014**, *118* (18), 9531-9537.

[50] Graeve, O.A.; Fathi, H.; Kelly, J.P.; Saterlie, M.S.; Sinha, K.; Rojas-George, G.; Kanakala, R.; Brown, D.R.; Lopez, E.A. Reverse Micelle Synthesis of Oxide Nanopowders: Mechanisms of Precipitate Formation and Agglomeration Effects. *J. Colloid Interface Sci.* **2013**, *407*, 302-309.

[51] Saterlie, M.S.; Sahin, H.; Kavlicoglu, B.; Liu, Y.; Graeve, O.A. Surfactant Effects on Dispersion Characteristics of Copper-Based Nanofluids: A Dynamic Light Scattering Study. *Chem. Mater.* **2012**, *24* (17), 3299-3306.

[52] Fathi, H.; Kelly, J.P.; Vasquez, V.R.; Graeve, O.A. Ionic Concentration Effects on Reverse Micelle Size and Stability: Implications for the Synthesis of Nanoparticles. *Langmuir* **2012**, *28* (25), 9267-9274.

[53] Saterlie, M.; Sahin, H.; Kavlicoglu, B.; Liu, Y.; Graeve, O. Particle Size Effects in the Thermal Conductivity Enhancement of Copper-Based Nanofluids. *Nanoscale Res. Lett.* **2011**, *6* (1), 217.

[54] Vasquez, V.R.; Williams, B.C.; Graeve, O.A. Stability and Comparative Analysis of AOT/Water/Isooctane Reverse Micelle System Using Dynamic Light Scattering and Molecular Dynamics. *J. Phys. Chem. B* **2011**, *115* (12), 2979-2987.

[55] Sinha, K.; Pearson, B.; Casolco, S.R.; Garay, J.E.; Graeve, O.A. Synthesis and Consolidation of $BaAl_2Si_2O_8$:Eu: Development of an Integrated Process for Luminescent Smart Ceramic Materials. *J. Am. Ceram. Soc.* **2009**, *92* (11), 2504-2511.

[56] Sinha, K.; Kavlicoglu, B.; Liu, Y.; Gordaninejad, F.; Graeve, O.A. A Comparative Study of Thermal Behavior of Iron and Copper Nanofluids. *J. Appl. Phys.* **2009**, *106* (6), 064307.

[57] Graeve O.A.; Sinha K. Dynamic Light Scattering Study of Reverse Micellar Systems for the Synthesis of Iron-Based Nanofluids. *Int. J. Mod. Phys. B* **2007**, *21* (28n29), 4774-4781.

[58] Hamaker H.C. The London-van der Waals attraction between spherical particles. *Physica* **1937**, *4* (10), 1058-1072.

[59] Priye, A.; Marlow, W. H. Computations of Lifshitz-van der Waals interaction energies between irregular particles and surfaces at all separations for resuspension modelling. *J. Phys. D: Appl. Phys.* **2013**, *46*, 425306.

[60] Svetovoy, V. B.; Palasantzas G. Influence of surface roughness on dispersion forces. *Adv. Colloid Interface Sci.* **2015**, *216*, 1-19.

[61] Eom, N.; Parsons, D. F.; Craig, V. S. J. Roughness in Surface Force Measurements: Extension of DLVO Theory to Describe the Forces between Hafnia Surface. *J. Phys. Chem. B* **2017**, *121*, 6442-6453.

[62] Leite, F. L.; Bueno, C. C.; Da Róz, A. L.; Ziemath, E. C.; Oliveira, O. N., Jr. Theoretical Models for Surface Forces and Adhesion and Their Measurement Using Atomic Force Microscopy. *Int. J. Mol. Sci.* **2012**, *13*, 12773-12856.

[63] French, R. H.; Winey, K. I.; Yang, M. K.; Qiu, W. Optical Properties and van Der Waals-London Dispersion Interactions of Polystyrene Determined by Vacuum Ultraviolet Spectroscopy and Spectroscopic Ellipsometry. *Aust. J. Chem.* **2007**, *60* (4), 251.

[64] Engh, R. A.; Huber, R. Accurate Bond and Angle Parameters for X-Ray Protein Structure Refinement. *Acta Crystallogr. A* **1991**, *47* (4), 392-400.

[65] Grimann, M.; Fuhrmann-Lieker, T. Biological Photonic Crystals. *Organic and Hybrid Photonic Crystals*; Springer International Publishing: 2015; pp 57-74.

[66] Barisik, M.; Atalay, S.; Beskok, A.; Qian, S. Size Dependent Surface Charge Properties of Silica Nanoparticles. *J. Phys. Chem. C* **2014**, *118* (4), 1836-1842.

[67] Atalay, S.; Ma, Y.; Qian, S. Analytical Model for Charge Properties of Silica Particles. *J. Colloid Interface Sci.* **2014**, *425*, 128-130.

[68] Boon, N.; van Roij, R. Charge Regulation and Ionic Screening of Patchy Surfaces. *J. Chem. Phys.* **2011**, *134* (5), 54706.

[69] Yeh, L.-H.; Xue, S.; Joo, S.W.; Qian, S.; Hsu, J.-P. Field Effect Control of Surface Charge Property and Electroosmotic Flow in Nanofluidics. *J. Phys. Chem. C* **2012**, *116* (6), 4209-4216.

[70] Trefalt, G.; Behrens, S.H.; Borkovec, M. Charge Regulation in the Electrical Double Layer: Ion Adsorption and Surface Interactions. *Langmuir* **2015**, *32* (2), 380-400.

[71] Cloarec, J.-P.; Chevalier, C.; Genest, J.; Beauvais, J.; Chamas, H.; Chevolot, Y.; Baron, T.; Souifi, A. pH Driven Addressing of Silicon Nanowires onto Si_3N_4/SiO_2 Micro-Patterned Surfaces. *Nanotechnology* **2016**, *27* (29), 295602.

[72] Ovanesyan, Z.; Aljzmi, A.; Almusaynid, M.; Khan, A.; Valderrama, E.; Nash, K. L.; Marucho, M. Ion-ion Correlation, Solvent Excluded Volume and pH Effects on Physicochemical Properties of Spherical Oxide Nanoparticles. *J. Colloid Interface Sci.* **2016**, *462*, 325-333.

[73] Avni, Y.; Andelman, D.; Podgornik, R. Charge Regulation with Fixed and Mobile Charged Macromolecules. *Curr. Opin. Electrochem.* **2019**, *13*, 70-77.

[74] Ozcelik, H.G.; Barisik, M. Electric Charge of Nanopatterned Silica Surfaces. *Phys. Chem. Chem. Phys.* **2019**, *21* (14), 7576-7587.

[75] Gambino, G. L.; Lombardo, G. M.; Grassi, A.; Marletta, G. Molecular Modeling of Interactions Betweenl-Lysine and a Hydroxylated Quartz Surface. *J. Phys. Chem. B* **2004**, *108* (8), 2600-2607.

[76] Yokoi, T.; Wakabayashi, J.; Otsuka, Y.; Fan, W.; Iwama, M.; Watanabe, R.; Aramaki, K.; Shimojima, A.; Tatsumi, T.; Okubo, T. Mechanism of Formation of Uniform-sized Silica Nanospheres Catalyzed by Basic Amino Acids. *Chem. Mater.* **2009**, *21*, 3719-3729.

[77] Kitadai, N.; Yokoyama, T.; Nakashima, S. ATR-IR Spectroscopic Study of *L*-lysine Adsorption on Amorphous Silica. *J. Colloid Interface Sci.* **2009**, *329* (1), 31-37.

[78] Li, X.; Shantz, D. F. PFG NMR studies of lysine-silica solutions. *J. Colloid Interface Sci.* **2012**, *383*, 19-27.

[79] Guo, C.; Holland, G. P. Investigating Lysine Adsorption on Fumed Silica Nanoparticles. *J. Phys. Chem. C* **2014**, *118*, 25792-25801.

[80] Hiemstra, T.; Van Riemsdijk, W. H.; Bolt, G. H. Multisite Proton Adsorption Modeling at the Solid/Solution Interface of (Hydr)oxides: A New Approach. *J. Colloid Interface Sci.* **1989**, *133* (1), 91-104.

[81] Sonnefeld, J.; Löbbus, M.; Vogelsberger, W. Determination of Electric Double Layer Parameters for Spherical Silica Particles under Application of the Triple Layer Model Using Surface Charge Density Data and Results of Electrokinetic Sonic Amplitude Measurements. *Colloids Surf. A* **2001**, *195* (1-3), 215-225.

[82] Flower D. R. Vaccines: Data and Databases. *Bioinformatics for Vaccinology*; John Wiley & Sons, Ltd: 2008; pp 113-165.

[83] Dickhaus, B.N.; Priefer, R. Determination of Polyelectrolyte pK_a Values Using Surface-to-Air Tension Measurements. *Colloids Surf. A* **2016**, *488*, 15-19.

[84] Bharti, B. Surfactant Adsorption and Aggregate Structure at Silica Nanoparticles. *Adsorption, Aggregation and Structure Formation in Systems of Charged Particles*; Springer International Publishing: 2014; pp 47-61.

[85] Zhang, Y.; Fry, C.G.; Pedersen, J.A.; Hamers, R.J. Dynamics and Morphology of Nanoparticle-Linked Polymers Elucidated by Nuclear Magnetic Resonance. *Anal. Chem.* **2017**, *89* (22), 12399-12407.

[86] Chan, D. Y. C.; Mitchell, D. J.; Ninham, B. W.; Pailthorpe, B. A. Solvent Structure in Particle Interactions. Low Pressure Effects and Analytic Limits. Journal of the Chemical Society, *J. Chem. Soc., Faraday Trans. 2* **1980**, *76*, 776.

[87] Nakamura, M.; Sato, N.; Hoshi, N.; Sakata, O. Outer Helmholtz Plane of the Electrical Double Layer Formed at the Solid Electrode-Liquid Interface. *ChemPhysChem* **2011**, *12* (8), 1430-1434.

[88] Goodall, A. R.; Wilkinson, M. C.; Hearn, J. Mechanism of Emulsion Polymerization of Styrene in Soap-Free Systems. *J. Polym. Sci. Polym. chem.***1977**, *15* (9), 2193-2218.

[89] Chang, H.-S.; Chen, S.-A. Kinetics and Mechanism of Emulsifier-Free Emulsion Polymerization. II. Styrene/Water Soluble Comonomer (Sodium Methallyl Sulfonate) System. *J. Polym. Sci. Polym. chem.* **1988**, *26* (4), 1207-1229.

[90] Chiu, W.-Y.; Shih, C.-C. A Study of the Soap-Free Emulsion Polymerization of Styrene. *J. Appl. Polym. Sci.* **1986**, *31* (7), 2117-2128.

[91] Dubas, S. T.; Schlenoff, J. B. Factors Controlling the Growth of Polyelectrolyte Multilayers. *Macromolecules* **1999**, *32* (24), 8153-8160.

[92] Porus, M.; Maroni, P.; Borkovec, M. Structure of Adsorbed Polyelectrolyte Monolayers Investigated by Combining Optical Reflectometry and Piezoelectric Techniques. *Langmuir* **2012**, *28* (13), 5642-5651.

[93] Stoll, S.; Chodanowski, P. Polyelectrolyte Adsorption on an Oppositely Charged Spherical Particle. Chain Rigidity Effects. *Macromolecules* **2002**, *35* (25), 9556-9562.

[94] Zhuravlev, L. T. The Surface Chemistry of Amorphous Silica. Zhuravlev Model. *Colloids Surf. A* **2000**, *173* (1-3), 1-38.

[95] Sulpizi, M.; Gaigeot, M.-P.; Sprik, M. The Silica-Water Interface: How the Silanols Determine the Surface Acidity and Modulate the Water Properties. *J. Chem. Theory Comput.* **2012**, *8* (3), 1037-1047.

[96] Kim, S.; Stébé, M.-J.; Blin, J.-L.; Pasc, A. pH-Controlled Delivery of Curcumin from a Compartmentalized Solid Lipid Nanoparticle@mesostructured Silica Matrix. *J. Mater. Chem. B* **2014**, *2* (45), 7910-7917.

[97] Gierada, M.; Petit, I.; Handzlik, J.; Tielens, F. Hydration in Silica Based Mesoporous Materials: A DFT Model. *Phys. Chem. Chem. Phys.* **2016**, *18* (48), 32962-32972.

[98] Comas-Vives, A. Amorphous SiO_2 Surface Models: Energetics of the Dehydroxylation Process, Strain, Ab Initio Atomistic Thermodynamics and IR Spectroscopic Signatures. *Phys. Chem. Chem. Phys.* **2016**, *18* (10), 7475-7482.

[99] Pfeiffer-Laplaud, M.; Gaigeot, M.-P. Electrolytes at the Hydroxylated (0001) α-Quartz/Water Interface: Location and Structural Effects on Interfacial Silanols by DFT-Based MD. *J. Phys. Chem. C* **2016**, *120* (26), 14034-14047.

[100] Dalstein, L.; Potapova, E.; Tyrode, E. The Elusive Silica/Water Interface: Isolated Silanols under Water as Revealed by Vibrational Sum Frequency Spectroscopy. *Phys. Chem. Chem. Phys.* **2017**, *19* (16), 10343–10349.

[101] Brown, M. A.; Abbas, Z.; Kleibert, A.; Green, R. G.; Goel, A.; May, S.; Squires, T. M. Determination of Surface Potential and Electrical Double-Layer Structure at the Aqueous Electrolyte-Nanoparticle Interface. *Phys. Rev. X* **2016**, *6* (1).

[102] Jalil, A. H.; Pyell, U. Quantification of Zeta-Potential and Electrokinetic Surface Charge Density for Colloidal Silica Nanoparticles Dependent on Type and Concentration of the Counterion: Probing the Outer Helmholtz Plane. *J. Phys. Chem. C* **2018**, *122* (8), 4437-4453.

[103] Zhu, R.; Feng, H.; Li, Q.; Su, L.; Fu, Q.; Li, J.; Song, J.; Yang, H. Asymmetric Core-Shell Gold Nanoparticles and Controllable Assemblies for SERS Ratiometric Detection of MicroRNA. *Angew. Chem. Int. Ed.* **2021**, *60* (22), 12560-12568.

[104] Sun, L.; Jiang, L.; Zhang, J.; Murayama, T.; Zhang, M.; Zheng, Y.; Su, H.; Qi, C. Preparation of Polyaniline Microtubes as the Gold Catalyst Support with Improved Catalytic Performances for the Reduction of Nitrophenols. *Top. Catal.* **2020**, *64* (3-4), 215-223.

[105] Loo, C.; Hirsch, L.; Lee, M.-H.; Chang, E.; West, J.; Halas, N.; Drezek, R. Gold Nanoshell Bioconjugates for Molecular Imaging in Living Cells. *Opt. Lett.* **2005**, *30* (9), 1012.

[106] Muñoz-Ortiz, T.; Hu, J.; Ortgies, D.H.; Shrikhande, S.; Zamora-Perez, P.; Granado, M.; González-Hedström, D.; Fuente-Fernández, M.; García-Villalón, Á.L.; Andrés-Delgado, L.; Martín Rodríguez, E.; Aguilar, R.; Alfonso, F.; García Solé, J.; Rivera Gil, P.; Jaque, D.; Rivero, F. Molecular Imaging of Infarcted Heart by Biofunctionalized Gold Nanoshells. *Adv. Healthc. Mater.* **2021**, *10* (10), 2002186.

[107] Wang, W.; Cai, W.; Yang, Y.; Li, H.; Cong, M.; Chen, T. Controlled Growth of Metal Nanoparticles on Amino-Functionalized Polystyrene Microspheres and Their Application in Surface-Enhanced Raman Spectroscopy. *Mater. Chem. Phys.* **2013**, *142* (2-3), 756-762.

[108] Mir-Simon, B.; Morla-Folch, J.; Gisbert-Quilis, P.; Pazos-Perez, N.; Xie, H.; Bastús, N.G.; Puntes, V.; Alvarez-Puebla, R.A.; Guerrini, L. SERS Efficiencies of Micrometric Polystyrene Beads Coated with Gold and Silver Nanoparticles: The Effect of Nanoparticle Size. *J. Opt.* **2015**, *17* (11), 114012.

[109] Zhang, J.; Liu, J.; Wang, S.; Zhan, P.; Wang, Z.; Ming, N. Facile Methods to Coat Polystyrene and Silica Colloids with Metal. *Adv. Funct. Mater.* **2004**, *14* (11), 1089-1096.

[110] Lee, J.-H.; Mahmoud, M.A.; Sitterle, V.B.; Sitterle, J.J.; Meredith, J.C. Highly Scattering, Surface-Enhanced Raman Scattering-Active, Metal Nanoparticle-Coated Polymers

Prepared via Combined Swelling-Heteroaggregation. *Chem. Mater.* **2009**, *21* (23), 5654-5663.

[111] Gobin, A.M.; Lee, M.H.; Halas, N.J.; James, W.D.; Drezek, R.A.; West, J.L. Near-Infrared Resonant Nanoshells for Combined Optical Imaging and Photothermal Cancer Therapy. *Nano Lett.* **2007**, *7* (7), 1929-1934.

[112] Santra, T.S.; Kar, S.; Chen, T.-C.; Chen, C.-W.; Borana, J.; Lee, M.-C.; Tseng, F.-G. Near-Infrared Nanosecond-Pulsed Laser-Activated Highly Efficient Intracellular Delivery Mediated by Nano-Corrugated Mushroom-Shaped Gold-Coated Polystyrene Nanoparticles. *Nanoscale* **2020**, *12* (22), 12057-12067.

[113] Zhang, H.; Zhang, Y.; Wu, C.; Tan, H.; Wang, S.; Zhang, B.; Zhang, Q. Preparation and Photothermal Study of Polystyrene Coated with Gold Nanoshell Composite Particles. *J. Mater. Sci.* **2017**, *52* (11), 6581-6590.

[114] Rastinehad, A.R.; Anastos, H.; Wajswol, E.; Winoker, J.S.; Sfakianos, J.P.; Doppalapudi, S.K.; Carrick, M.R.; Knauer, C.J.; Taouli, B.; Lewis, S.C.; Tewari, A.K.; Schwartz, J.A.; Canfield, S.E.; George, A.K.; West, J.L.; Halas, N.J. Gold Nanoshell-Localized Photothermal Ablation of Prostate Tumors in a Clinical Pilot Device Study. *Proc. Natl. Acad. Sci. U.S.A.* **2019**, *116* (37), 18590-18596.

[115] Simón, M.; Jørgensen, J.T.; Norregaard, K.; Kjaer, A. 18F-FDG Positron Emission Tomography and Diffusion-Weighted Magnetic Resonance Imaging for Response Evaluation of Nanoparticle-Mediated Photothermal Therapy. *Sci. Rep.* **2020**, *10* (1).

[116] Shi, W.; Sahoo, Y.; Swihart, M.T.; Prasad, P.N. Gold Nanoshells on Polystyrene Cores for Control of Surface Plasmon Resonance. *Langmuir* **2005**, *21* (4), 1610-1617.

[117] Khlebtsov, B.N.; Khanadeyev, V.A.; Ye, J.; Mackowski, D.W.; Borghs, G.; Khlebtsov, N. G. Coupled Plasmon Resonances in Monolayers of Metal Nanoparticles and Nanoshells. *Phys. Rev. B* **2008**, *77* (3), 035440.

[118] Jang, S.G.; Kim, S.-H.; Lee, S.Y.; Jeong, W.C.; Yang, S.-M. Facile Synthesis of Core-Shell and Janus Particles via 2-D Dendritic Growth of Gold Film. *J. Colloid Interface Sci.* **2010**, *350* (2), 387-395.

[119] Dobrowolska, P.; Krajewska, A.; Gajda-Rączka, M.; Bartosewicz, B.; Nyga, P.; Jankiewicz, B. Application of Turkevich Method for Gold Nanoparticles Synthesis to Fabrication of SiO_2@Au and TiO_2@Au Core-Shell Nanostructures. *Materials* **2015**, *8* (6), 2849-2862.

[120] Mann, D.; Nascimento-Duplat, D.; Keul, H.; Möller, M.; Verheijen, M.; Xu, M.; Urbach, H.P.; Adam, A.J.L.; Buskens, P. The Influence of Particle Size Distribution and Shell Imperfections on the Plasmon Resonance of Au and Ag Nanoshells. *Plasmonics* **2017**, *12* (3), 929-945.

[121] Sauerbeck, C.; Haderlein, M.; Schürer, B.; Braunschweig, B.; Peukert, W.; Klupp Taylor, R.N. Shedding Light on the Growth of Gold Nanoshells. *ACS Nano* **2014**, *8* (3), 3088-3096.

[122] Wang; Luo, J.; Fan, Q.; Suzuki, M.; Suzuki, I.S.; Engelhard, M.H.; Lin, Y.; Kim, N.; Wang, J.Q.; Zhong, C.-J. Monodispersed Core-Shell Fe_3O_4@Au Nanoparticles. *J. Phys. Chem. B* **2005**, *109* (46), 21593-21601.

[123] Xu, Z.; Hou, Y.; Sun, S. Magnetic Core/Shell Fe_3O_4/Au and Fe_3O_4/Au/Ag Nanoparticles with Tunable Plasmonic Properties. *J. Am. Chem. Soc.* **2007**, *129* (28), 8698-8699.

[124] Goon, I. Y.; Lai, L. M.H.; Lim, M.; Munroe, P.; Gooding, J.J.; Amal, R. Fabrication and Dispersion of Gold-Shell-Protected Magnetite Nanoparticles: Systematic Control Using Polyethyleneimine. *Chem. Mater.* **2009**, *21* (4), 673-681.

[125] Jin, Y.; Jia, C.; Huang, S.-W.; O'Donnell, M.; Gao, X. Multifunctional Nanoparticles as Coupled Contrast Agents. *Nat. Commun.* **2010**, *1* (1).

[126] Moraes Silva, S.; Tavallaie, R.; Sandiford, L.; Tilley, R.D.; Gooding, J.J. Gold Coated Magnetic Nanoparticles: From Preparation to Surface Modification for Analytical and Biomedical Applications. *Chem. Commun.* **2016**, *52* (48), 7528-7540.

[127] Nguyen, T.; Mammeri, F.; Ammar, S. Iron Oxide and Gold Based Magneto-Plasmonic Nanostructures for Medical Applications: A Review. *Nanomaterials* **2018**, *8* (3), 149.

[128] Landon, P.B.; Mo, A.H.; Zhang, C.; Emerson, C.D.; Printz, A.D.; Gomez, A.F.; DeLaTorre, C.J.; Colburn, D.A.M.; Anzenberg, P.; Eliceiri, M.; O'Connell, C.; Lal, R. Designing Hollow Nano Gold Golf Balls. *ACS Appl. Mater. Interfaces* **2014**, *6* (13), 9937-9941.

[129] Bao, H.; Bihr, T.; Smith, A.-S.; Klupp Taylor, R.N. Facile Colloidal Coating of Polystyrene Nanospheres with Tunable Gold Dendritic Patches. *Nanoscale* **2014**, *6* (8), 3954-3966.

[130] Choma, J.; Dziura, A.; Jamioła, D.; Nyga, P.; Jaroniec, M. Preparation and Properties of Silica-Gold Core-Shell Particles. *Colloids Surf. A* **2011**, *373* (1-3), 167-171.

[131] Thanh, N.T.K.; Maclean, N.; Mahiddine, S. Mechanisms of Nucleation and Growth of Nanoparticles in Solution. *Chem. Rev.* **2014**, *114* (15), 7610-7630.

[132] Parsegian, V.A. *Van Der Waals Forces: A Handbook for Biologists, Chemists, Engineers, and Physicists*; Cambridge University Press: 2005.

[133] Geyer, B.; Klimchitskaya, G.L.; Mohideen, U.; Mostepanenko, V.M. Comment on "Precision Measurement of the Casimir-Lifshitz Force in a Fluid." *Phys. Rev. A* **2008**, *77* (3), 036102.

[134] Munday, J.N.; Capasso, F.; Parsegian, V.A.; Bezrukov, S.M.Measurements of the Casimir-Lifshitz Force in Fluids: The Effect of Electrostatic Forces and Debye Screening. *Phys. Rev. A* **2008**, *78* (3), 032109.

[135] Kumler, W.D.; Daniels, T.C. Titration Curves and Dissociation Constants of *L*-Ascorbic Acid (Vitamin C) and Diethyl Dihydroxymaleate. *J. Am. Chem. Soc.* **1935**, *57* (10), 1929-1930.

[136] Luty-Błocho, M.; Pacławski, K.; Wojnicki, M.; Fitzner, K. The Kinetics of Redox Reaction of Gold(III) Chloride Complex Ions with *L*-Ascorbic Acid. *Inorg. Chim. Acta* **2013**, *395*, 189-196.

[137] Luty-Błocho, M.; Wojnicki, M.; Fitzner, K. Gold Nanoparticles Formation via Au(III) Complex Ions Reduction with *L*-Ascorbic Acid. *Int. J. Chem. Kinet.* **2017**, *49* (11), 789-797.

[138] Levenspiel, O. *Chemical Reaction Engineering*; John Wiley & Sons, 1998.

[139] Watzky, M.A.; Finke, R.G. Transition Metal Nanocluster Formation Kinetic and Mechanistic Studies. A New Mechanism When Hydrogen Is the Reductant: Slow, Continuous Nucleation and Fast Autocatalytic Surface Growth. *J. Am. Chem. Soc.* **1997**, *119* (43), 10382-10400.

[140] Morris, A.M.; Watzky, M.A.; Agar, J.N.; Finke, R.G. Fitting Neurological Protein Aggregation Kinetic Data via a 2-Step, Minimal/"Ockham's Razor" Model: The Finke-Watzky Mechanism of Nucleation Followed by Autocatalytic Surface Growth. *Biochemistry* **2008**, *47* (8), 2413-2427.

[141] Mironov, I.V.; Makotchenko, E.V. The Hydrolysis of $AuCl_4^-$ and the Stability of Aquachlorohydroxocomplexes of Gold(III) in Aqueous Solution. *J. Solution Chem.* **2009**, *38* (6), 725-737.

[142] Cao, G. *Nanostructures & Nanomaterials*; Imperial College Press: 2004.

[143] Dagastine, R.R.; Prieve, D.C.; White, L.R. The Dielectric Function for Water and Its Application to Van der Waals Forces. *J. Colloid Interface Sci.* **2000**, *231* (2), 351-358.

[144] van Zwol, P.J.; Palasantzas, G.; De Hosson, J.Th.M. Influence of Dielectric Properties on van Der Waals/Casimir Forces in Solid-Liquid Systems. *Phys. Rev. B* **2009**, *79* (19), 195428.

[145] Milling, A.; Mulvaney, P.; Larson, I. Direct Measurement of Repulsive van Der Waals Interactions Using an Atomic Force Microscope. *J. Colloid Interface Sci.* **1996**, *180* (2), 460-465.

[146] Lee, S.; Sigmund, W.M. Repulsive van Der Waals Forces for Silica and Alumina. *J. Colloid Interface Sci.* **2001**, *243* (2), 365-369.

[147] Boström, M.; Sernelius, B. E.; Brevik, I.; Ninham, B. W. Retardation Turns the van Der Waals Attraction into a Casimir Repulsion as Close as 3 nm. *Phys. Rev. A* **2012**, *85* (1), 010701.

[148] Boström, M.; Ninham, B.W.; Brevik, I.; Persson, C.; Parsons, D.F.; Sernelius, B.E. Ultrathin Metallic Coatings Can Induce Quantum Levitation between Nanosurfaces. *Appl. Phys. Lett.* **2012**, *100* (25), 253104.

[149] Boström, M.; Sernelius, B.E.; Baldissera, G.; Persson, C.; Ninham, B.W. Casimir-Lifshitz Interaction between ZnO and SiO_2 nanorods in Bromobenzene Turns Repulsive at Intermediate Separations Due to Retardation Effects. *Phys. Rev. A* **2012**, *85* (4).

[150] Esteso, V.; Carretero-Palacios, S.; Míguez, H. Casimir-Lifshitz Force Based Optical Resonators. *J. Phys. Chem. Lett.* **2019**, *10* (19), 5856-5860.

[151] Kuisma, M.; Sakko, A.; Rossi, T.P.; Larsen, A.H.; Enkovaara, J.; Lehtovaara, L.; Rantala, T. T. Localized Surface Plasmon Resonance in Silver Nanoparticles: Atomistic First-Principles Time-Dependent Density-Functional Theory Calculations. *Phys. Rev. B* **2015**, *91* (11), 115431.

[152] Rossi, T.P.; Lehtola, S.; Sakko, A.; Puska, M.J.; Nieminen, R.M. Nanoplasmonics Simulations at the Basis Set Limit through Completeness-Optimized, Local Numerical Basis Sets. *J. Chem. Phys.* **2015**, *142* (9), 094114.

[153] Rossi, T.P.; Kuisma, M.; Puska, M.J.; Nieminen, R.M.; Erhart, P. Kohn-Sham Decomposition in Real-Time Time-Dependent Density-Functional Theory: An Efficient Tool for Analyzing Plasmonic Excitations. *J. Chem. Theory Comput.* **2017**, *13* (10), 4779-4790.

[154] Enkovaara, J.; Rostgaard, C.; Mortensen, J.J.; Chen, J.; Dułak, M.; Ferrighi, L.; Gavnholt, J.; Glinsvad, C.; Haikola, V.; Hansen, H.A.; Kristoffersen, H.H.; Kuisma, M.; Larsen, A.H.; Lehtovaara, L.; Ljungberg, M.; Lopez-Acevedo, O.; Moses, P.G.; Ojanen, J.; Olsen, T.; Petzold, V.; Romero, N.A.; Stausholm-Møller, J.; Strange, M.; Tritsaris, G.A.; Vanin, M.; Walter, M.; Hammer, B.; Häkkinen, H.; Madsen, G.K.H.; Nieminen, R.M.; Nørskov, J.K.; Puska, M.; Rantala, T.T.; Schiøtz, J.; Thygesen, K.S.; Jacobsen, K.W. Electronic Structure Calculations with GPAW: A Real-Space Implementation of the Projector Augmented-Wave Method. *J. Phys. Condens. Matter* **2010**, *22* (25), 253202.

[155] Larsen, A.H.; Vanin, M.; Mortensen, J.J.; Thygesen, K.S.; Jacobsen, K.W. Localized Atomic Basis Set in the Projector Augmented Wave Method. *Phys. Rev. B* **2009**, *80* (19), 195112.

[156] Hjorth Larsen, A.; Jørgen Mortensen, J.; Blomqvist, J.; Castelli, I.E.; Christensen, R.; Dułak, M.; Friis, J.; Groves, M.N.; Hammer, B.; Hargus, C.; Hermes, E.D.; Jennings, P.C.; Bjerre Jensen, P.; Kermode, J.; Kitchin, J.R.; Leonhard Kolsbjerg, E.; Kubal, J.; Kaasbjerg, K.; Lysgaard, S.; Bergmann Maronsson, J.; Maxson, T.; Olsen, T.; Pastewka, L.; Peterson, A.; Rostgaard, C.; Schiøtz, J.; Schütt, O.; Strange, M.; Thygesen, K.S.; Vegge, T.; Vilhelmsen, L.; Walter, M.; Zeng, Z.; Jacobsen, K.W. The Atomic Simulation Environment-a Python Library for Working with Atoms. *J. Phys. Condens. Matter* **2017**, *29* (27), 273002.

[157] Schmid, G. The Relevance of Shape and Size of Au_{55} Clusters. *Chem. Soc. Rev.* **2008**, *37* (9), 1909.

[158] He, Y.; Zeng, T. First-Principles Study and Model of Dielectric Functions of Silver Nanoparticles. *J. Phys. Chem. C* **2010**, *114* (42), 18023-18030.

[159] Jin, R.; Zhu, Y.; Qian, H. Quantum-Sized Gold Nanoclusters: Bridging the Gap between Organometallics and Nanocrystals. *Chem. Eur. J.* **2011**, *17* (24), 6584-6593.

[160] Myshlyavtsev, A.V.; Stishenko, P.V. Relative Stability of Icosahedral and Cuboctahedral Metallic Nanoparticles. *Adsorption* **2013**, *19* (2-4), 795-801.

[161] Schneider, C.M.; Cölfen, H. Formation of Nanoclusters in Gold Nucleation. *Crystals* **2020**, *10* (5), 382.

[162] Li, H.; Li, L.; Pedersen, A.; Gao, Y.; Khetrapal, N.; Jónsson, H.; Zeng, X.C. Magic-Number Gold Nanoclusters with Diameters from 1 to 3.5 nm: Relative Stability and Catalytic Activity for CO Oxidation. *Nano Lett.* **2014**, *15* (1), 682-688.

[163] Peiponen, K.-E.; Lucarini, V.; Vartiainen, E.M.; Saarinen, J.J. Kramers-Kronig Relations and Sum Rules of Negative Refractive Index Media. *Eur. Phys. J. B* **2004**, *41* (1), 61-65.

[164] Watts, B. Calculation of the Kramers-Kronig Transform of X-Ray Spectra by a Piecewise Laurent Polynomial Method. *Opt. Express* **2014**, *22* (19), 23628.

[165] Whittaker, K.A.; Keaveney, J.; Hughes, I.G.; Adams, C.S. Hilbert Transform: Applications to Atomic Spectra. *Phys. Rev. A* **2015**, *91* (3), 032513.

[166] Anisimov, V.I.; Zaanen, J.; Andersen, O.K. Band Theory and Mott Insulators: Hubbard *U* instead of Stoner *I*. *Phys. Rev. B* **1991**, *44* (3), 943-954.

[167] Dudarev, S.L.; Botton, G.A.; Savrasov, S.Y.; Humphreys, C.J.; Sutton, A.P. Electron-Energy-Loss Spectra and the Structural Stability of Nickel Oxide: An LSDA+U Study. *Phys. Rev. B* **1998**, *57* (3), 1505-1509.

[168] Avakyan, L.; Durimanov, V.; Nemesh, D.; Srabionyan, V.; Ihlemann, J.; Bugaev, L. Theoretical Approach for Calculation of Dielectric Functions of Plasmonic Nanoparticles of Noble Metals, Magnesium and Their Alloys. *Opt. Mater.* **2020**, *109*, 110264.

[169] Avakyan, L.; Durimanov, V.; Nemesh, D.; Srabionyan, V.; Ihlemann, J.; Bugaev, L. Data, Python Script and Results for Calculation of Dielectric Functions of Plasmonic Nanoparticles of Noble Metals, Magnesium and Their Alloys, 2020.

[170] Johnson, P.B.; Christy, R.W. Optical Constants of the Noble Metals. *Phys. Rev. B* **1972**, *6* (12), 4370-4379.

[171] Inagaki, T.; Arakawa, E.T.; Hamm, R.N.; Williams, M.W. Optical Properties of Polystyrene from the Near-Infrared to the X-Ray Region and Convergence of Optical Sum Rules. *Phys. Rev. B* **1977**, *15* (6), 3243-3253.

[172] Segelstein, D.J. *The Complex Refractive Index of Water.* Master's Thesis, University of Missouri-Kansas City, Kansas City, MO, 1981.

[173] Lam, S.K.; Pitrou, A.; Seibert, S. Numba: A LLVM-Based Python JIT Compiler. In *Proceedings of the Second Workshop on the LLVM Compiler Infrastructure in HPC - LLVM '15*; ACM Press, New York, 2015, pp 1-6.

[174] Ito, A.; Hattori, M.; Yoshida, T.; Takahashi, K. Contribution of the Net Charge to the Regulatory Effects of Amino Acids and ε-Poly(*L*-Lysine) on the Gelatinization Behavior of Potato Starch Granules. *Biosci. Biotechnol. Biochem.* **2006**, *70* (1), 76-85.